Weld line Charpy toughness investigations on High Frequency Induction (HFI) welded pipes and exploration of a method to achieve toughness improvements

By Sam Baker

Swansea University
College of Engineering

Submitted to Swansea University in fulfilment of the requirements for the degree of
Doctor of Philosophy

November 2024

Acknowledgements

I would firstly like to thank my supervisor, Dr Cameron Pleydell-Pearce, for the support and guidance he offered me throughout the duration of my project. He gave insightful knowledge, comments and suggestions that allowed me to make important decisions and progress with my project in the best direction.

I am also very grateful to the Materials and Manufacturing Academy (M2A), Engineering and Physical Sciences Research Council (EPSRC) and Tata Steel for funding and sponsoring my project. I would like to give a special thanks to Chris Stevens and Dr Jinlong Du of Tata Steel for providing me with material, data, and knowledge. Without their assistance and support my studies would have been impossible to carry out.

I would like to express my thanks to the Advanced Imaging of Materials (AIM) facility in Swansea University. They provided me with training and the use of equipment for imaging and analysis techniques including scanning electron microscopy (SEM), energy dispersive spectroscopy (EDS) and electron backscatter diffraction (EBSD). I wish to say a big thank you to Peter Davies for providing me with much of the training, as well as offering me constant support throughout my use of the facilities.

I would also like to thank the Steel and Metals Institute (SaMI) for providing me with the use of their Charpy impact testing equipment.

Lastly, I want to thank my friends and family for their encouragement and support throughout my project.

Declarations

This work has not previously been accepted in substance for any degree and is not being concurrently submitted in candidature for any degree.

Signed.....[redacted]...

Date.......11/11/2024...

This thesis is the result of my own investigations, except where otherwise stated. Other sources are acknowledged by footnotes giving explicit references. A bibliography is appended.

Signed......[redacted]...

Date.......11/11/2024...

I hereby give consent for my thesis, if accepted, to be available for electronic sharing.

Signed.....[redacted]...

Date.......11/11/2024...

The University's ethical procedures have been followed and, where appropriate, that ethical approval has been granted.

Signed.....[redacted]...

Date.......11/11/2024...

Abstract

The growth of the gas and oil industry into cold regions has driven the demand for high frequency induction welded pipes that are resistant to sour service. However, the toughness of the weld line can deteriorate in cold and harsh environments and producing a weld line that is resistant to these conditions is challenging since it is already difficult to guarantee acceptable weld line toughness with a sufficiently high level of confidence.

Previous research has investigated the factors causing poor toughness. Nonetheless, the research was somewhat limited due to several reasons. The literature has also suggested that a more uniform temperature distribution during welding can improve the weld quality. However, justifications to why have not been determined.

This researched aimed to develop a deeper understanding of the factors influencing the toughness of the weld line on a 16 mm thick X60 high frequency induction welded pipe, so subsequent rational could then be developed to establish why a more uniform temperature distribution during welding could improve the weld line toughness. If successful, this knowledge could then be used to develop a method to improve the temperature distribution, and thus enhance the weld line toughness.

Characterisation and impact testing established the main factors influencing the toughness of the weld line. It was also discovered that the microstructure varied through the depth of the weld line, where the parts which experienced the greatest heating displayed the most undesirable features for satisfactory toughness. Therefore, it was concluded that by reducing the high temperatures in these regions, the overall microstructure could be improved, subsequently enhancing the toughness of the weld line. With this new knowledge, computational modelling was implemented to explore a method to improve the temperature distribution during welding. This was successful, and achieved by altering the geometry of the strip edges.

Table of contents

1 Introduction

High Frequency Induction (HFI) welding has been a common technique used for the production of steel pipes since the 1960's. These pipes are used in a variety of different applications, where they are widely used in the energy field for the transportation of hydrocarbons. The growth of the gas and oil industry in cold regions has increased the demand for pipes that are resistant to sour service conditions. Although, a major challenge with the use of HFI welded pipes is that the toughness of the weld line can deteriorate in cold and harsh environments.

The input material to manufacture HFI welded pipes comes in the form of a steel strip. To produce the pipe the steel strip is progressively formed into a pipe shape by forming rolls where the faying strip edges are brought together into a vee shape. Next the faying strip edges are heated to welding temperature by the induction coil under skin and proximity effects of high frequency current. The molten strips edges are then fused together via pressure from the weld rolls, creating a forged weld with a very narrow heat affected zone (HAZ) [1]. However, the toughness of the weld line is typically very low. Therefore, a Post Weld Heat-Treatment (PWHT) commonly follows welding to improve the toughness of the weld line. Nevertheless, the toughness can often remain poor, and consequently a satisfactory weld quality cannot always be guaranteed. This is especially problematic when trying to ensure acceptable weld toughness in cold and harsh environments. This uncertainty of guaranteeing adequate weld line toughness can be damaging to customer confidence.

Research has already been conducted investigating the weld line toughness of X65 HFI welded pipes. Initial work concluded that the cause of poor toughness was a large grain size produced at the weld line that remained even after a PWHT [2]. However, this work overlooked other factors influencing toughness such as the constituents present at the weld line. Further studies proposed that the reason for low toughness at the weld line was a high fraction of grains orientated for easy fracture [3–5]. This was considered to be when grains were orientated with their {100} plane aligned parallel to the weld plane. However, the {110} plane has also been shown to influence the toughness of a material [6–8], and the role of this plane was not considered in any of the previous studies. There was also a lack of fracture surface analysis in the previous research. Therefore, a well-developed understanding of how fracture initiated and propagated through the weld line had not been established. This consequently raised questions about how strong the previous relationships made between the weld line microstructure and its toughness actually were.

It is well known that the heating distribution during welding is not uniform through the depth of the weld. Therefore, it is probable that the microstructure, and consequently the toughness varies through the depth of the weld. Yet, so far only localised zones of the weld have been analysed. As a result, there is no knowledge of whether the toughness may potentially change through the depth of the weld, and that certain locations within the weld line may present themselves as greater sources of poor toughness than others. Although, it has been suggested that improving the uniformity of the heating during welding could improve the toughness of the weld. Numerous computational models have been built to find a method to improve the uniformity of the temperature distribution during welding, though this had only been achieved on thin-walled pipe [9–11]. It is well known that thick-walled pipes are more susceptible to poor weld quality due to the large temperature differences across the strip faces during welding [12]. Therefore, a method needs to be explored with the aim of achieving a uniform heating when producing thick-walled pipe. Nevertheless, justifications to why a more uniform heating would improve the weld line toughness have yet to be determined.

The initial aim of the project was to develop a deeper understanding of the factors influencing the toughness of the weld line of a 16 mm thick X60 HFI welded pipe. This was necessary since the previous research has been somewhat limited. To achieve this, microstructural analysis was to be conducted where the variation in microstructure through the depth of the weld would also be investigated. This was to be accompanied with Charpy impact testing and an in-depth fracture surface analysis so that strong relationships between the weld line toughness and the microstructure could be established. With a deeper understanding, the next objective was to determine justifications to why the literature had suggested that a more uniform temperature distribution through the depth of the strip edges during welding would result in toughness improvements. With this knowledge a method could then be developed to explore whether the temperature distribution could be made more uniform when producing thick-walled HFI welded pipe. It was hypothesised that reducing the high temperatures at the strip edge corners would create microstructures in these locations that would have a more favourable toughness than previous. Consequently, improving the overall toughness of the weld line and gaining customer confidence in the use of HFI welded pipes for the transportation of hydrocarbons in harsh and cold environments.

2 Literature review

2.2 HFI welded pipe manufacturing process and principles

2.2.1 HFI welded pipe manufacturing process

The HFI welded pipe manufacturing process involves several stages. A schematic of the process is displayed on Figure 2.1. At the first stage the steel strip is uncoiled and fed through the leveller. The purpose of the leveller is to improve the flatness of the steel strip and remove any shape defects [13]. Next the strip is edge milled, where the edges are prepared for welding. This is a very important stage since incorrectly milled edges can result in defects. Also, any rust left on the strip edges will affect the weld quality by lowering the viscosity of the molten material, making it more difficult for oxide inclusions to be expelled from the bond plane [14]. Following edge milling, the steel strip is then passed through the roll forming mill where it is progressively formed into a pipe shape and the strip edges are brought together in the shape of a vee. The forming stage needs to guarantee the shape of the pipe is as circular as possible so that the strip edges meet parallel to ensure that good welding quality is achieved [15].

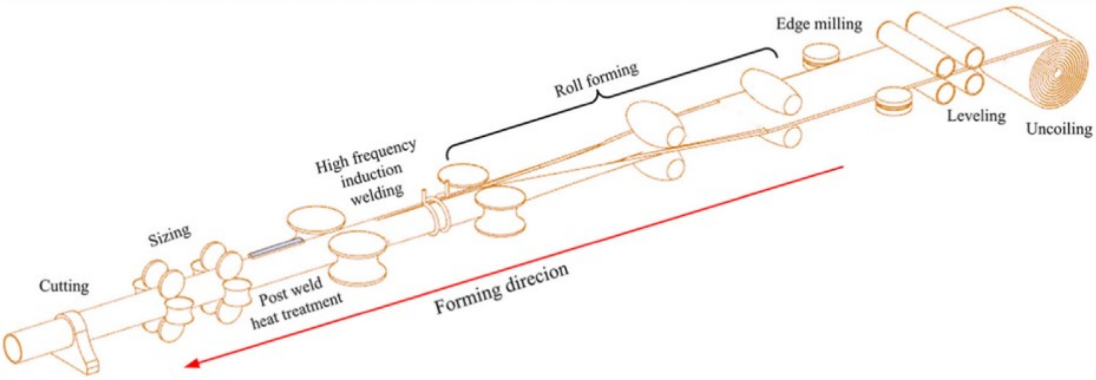

Figure 2.1. Schematic of HFI welded pipe manufacturing process [1].

After form rolling the strip edges are heated by the induction coil via high frequency electromagnetic induction. The induced high frequency alternating current concentrates at the strip edges due to skin and proximity effects and heats the strip edges to welding temperature via joule heating effect. Pressure from the weld rolls then squeeze the molten strip edges together to create a forged weld. When the strip edges are pressed together it gives rise to metal flow, which expels undesirable oxides from the weld and metallurgically bonds the two strip edges together by breaking the two interfaces between the strip edges [1]. Welding is then immediately followed by the inside and outside weld beads being trimmed off before the weld cools down. The weld then undergoes a Post Weld Heat-Treatment (PWHT), where it is induction annealed to replace the undesirable microstructure that was created during welding. Finally, the pipe is sized to ensure it is the correct dimensions before being cut to the required length [16].

2.2.2 HFI welded pipe heating process principles

High frequency alternating current flowing through the induction coil causes a magnetic field to develop around the induction coil which then intersects with the open pipe. This induces a high frequency electric field on the pipe surface, creating a voltage difference between the faying strip edges. The high frequencies associated with HFI welding cause the current to flow in a certain way around the open pipe due to skin and proximity effects [17]. The path of the induced current flow on the pipe can be seen on Figure 2.2, where the current flows circumferentially around the pipe and in opposite directions at the faying strip edges.

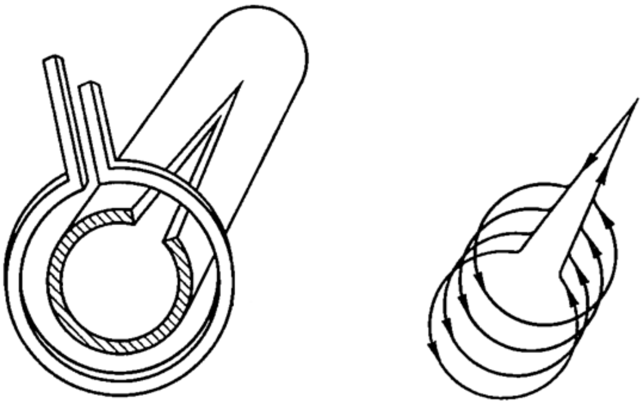

Figure 2.2. Path of current around pipe [18].

The skin effect is the tendency of high frequency alternating current to become distributed such that the current density is greatest at the outer surface of the conductor. Here the current essentially flows at a thin layer at the surface of the conductor, where the depth of this layer is dependent on the frequency and the material properties. The material properties include conductivity and magnetic permeability [19]. The thickness of this layer can be expressed by equation (2.1).

$$\delta = \sqrt{\frac{2}{\omega\mu\sigma}} \tag{2.1}$$

Where ω is angular frequency, μ is magnetic permeability and σ is conductivity [20]. Figure 2.3 illustrates how skin depth changes as a function of frequency for several different metals, where it can be seen that it decreases as the frequency is increased. When alternating current flows through a conductor it induces changing magnetic fields within the conductor. The magnetic fields then generate eddy currents which oppose current flow at the centre of the conductor and assist with current flow near the surface. It is these eddy currents that redistribute the current flow so that the current density is greatest near the surface of the conductor [21].

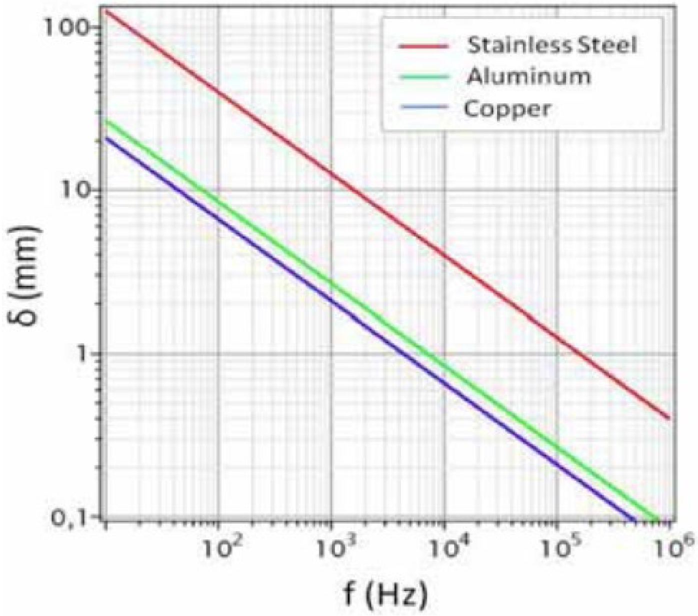

Figure 2.3. Skin depth as a function of frequency for different metals [22].

The proximity effect is an inductive mechanism caused by magnetic fields and it operates similarly to the skin effect where eddy currents cause the current to flow in a certain way. However, in the case of the proximity effect, magnetic fields from one conductor induce eddy currents on a second conductor which then redistributes the current flow. The current will still flow at a thin layer at the surface of the conductor due to its own skin effect, however the proximity effect will redistribute the current around the perimeter of the conductor. When the two currents are flowing in opposite directions, the proximity effect causes the currents to be mutually attracted to each other, and vice versa [21]. Since the current flow along each of the faying strip edges are in opposite directions during HFI welded pipe production, they are mutually attracted to each other. Consequently, the combination of the skin and proximity effects redistribute the current so that the current density is the greatest at the faying strip edges. The high current density then heats the faying strip edges to welding temperature by the means of Joule heating [23].

2.2.3 Process parameters and components

There are many important components and parameters that need to be setup correctly in order to achieve high efficiency as well as high weld quality. A schematic of the weld setup displaying some of these parameters is shown on Figure 2.4, where A is the pipe outside diameter, B is the vee length, C is the weld roll diameter, D is the coil length, E is the fin pass to coil centre, F is the ferrite ahead of the coil centre, and G is the coil inside diameter.

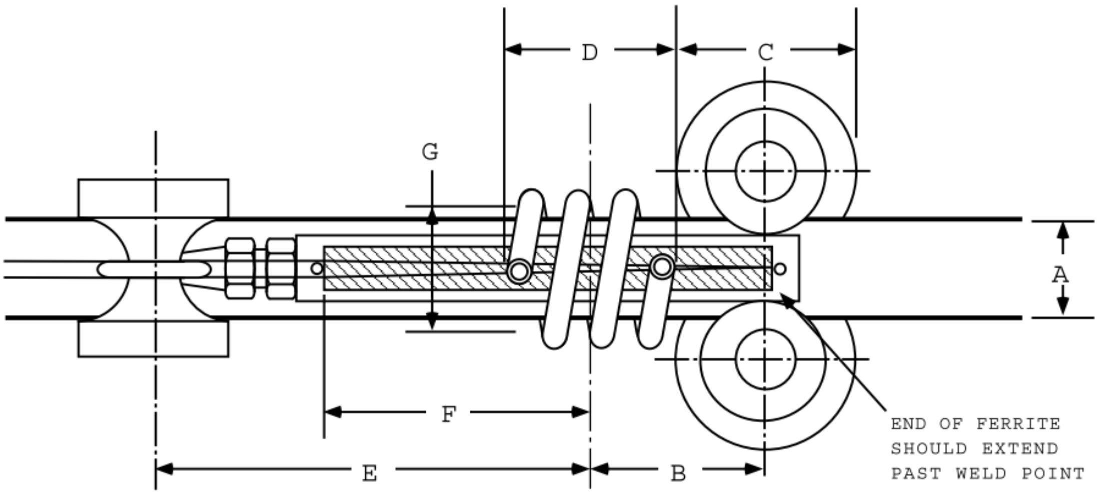

Figure 2.4. Welding setup and dimensions [17].

The vee length is defined as the distance from the vee convergence point to the centre of the induction coil. The greater the vee length the lower the efficiency is since there is more time for heat to be conducted away from the strip edges. Also, a longer vee length can put more stress on the impeder [24]. From an efficiency standpoint the vee length should be kept as short as possible to avoid conduction losses [25]. However, there are factors that determine the minimum vee length that can be used. For instance, if the vee length is too short it can cause an uneven temperature distribution through the strip edges where the temperature will be greater at the strip edge corners. This will lead to either incomplete welding at the centre of the weld or overheating of the strip edge corners [26]. The size of the weld rolls will also be a determining factor in the minimum vee length, because if the induction coil is too close to the weld rolls it will induction heat them [25].

The induction coil only heats the strip edges to welding temperature. Welding actually occurs when the weld rolls squeeze the molten strip edges together. The design and setup of the weld rolls is critical to achieve proper welding, where they need to provide a high degree of precision as well as withstanding large forces and thermal shock [17]. As previously discussed, they also have to be kept small so that they are not induction heated by the induction coil. It is paramount that the weld rolls apply the correct squeeze force to ensure that any undesirable oxides formed during the heating of the strip edges are expelled from the weld [27]. It has been reported that an increase in weld roll squeeze force can improve the efficiency of the welding process. It was found than an increase in weld squeeze from 1.85 to 2.35 mm could reduce the power requirements by 4.3 % [28]. The weld rolls don't just have to precisely apply the correct squeeze force, they also have to ensure that the strip edges meet each other parallel or otherwise the mismatch defect can occur. When the mismatch defect arises the skin and proximity effects do not work as desired. This can potentially lead to the cold weld defect forming, where the strip edges will be insufficiently bonded [29]. Figure 2.5 displays how misalignment of the strip edges affects the current distribution.

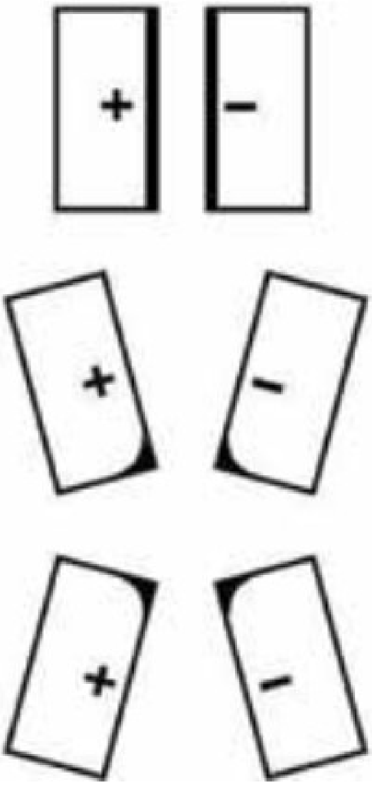

Figure 2.5. How misalignment of strip edges can cause an undesired current distribution [29].

The heating process is most efficient when a short coil length is used. When using a longer coil length, the coil starts to heat the strip edges further way from the welding point, so consequently energy is lost via thermal conduction. A shorter coil increases the impedance of the pipe and increases the current flow in the vee, reducing the power input requirements [25]. However, if the coil is too short it will raise its inductance to a point where it cannot be matched by the welder, limiting the maximum power that the welder can deliver to the coil [17].

The vee angle is the angle at which the faying strip edges meet each other. The efficiency is best when a small vee angle is used since the proximity effect will be larger. This increases current density at the faying strip edges causing greater joule heating [27]. However, there is a limit on the minimum vee angle that can be used. This is because if the vee angle is too small pre-arcing can occur. This is when the current jumps between the faying strip edges ahead of the vee convergence point, momentarily robbing the strip edges of heat. Consequently, the vee angle is a limited to around 2° to 3° for carbon steel, and 5° to 8° for stainless steel and other non-ferrous metals [25]. It has been reported that increasing the vee angle results in a wider and more pronounced Heat Affected Zone (HAZ), and in response of this the frequency should be increased. [30].

The frequency is a significant parameter in the HFI welded pipe manufacturing process since it is high frequency that confines the current to the strip edges which heats them to welding temperature. The frequencies applied are generally in the range of 100 to 800 kHz and are chosen in relation to the size of the pipe. Large heavy-walled pipes will use lower frequencies and small thin-walled pipes will use higher ones [31]. Thick-walled pipes use the lower end of the range because if the frequency is too high it will produce a highly non-uniform temperature distribution through the thickness of the strip edges. In this scenario the corners are heated to a much greater extent than the centre, which will be detrimental to the quality of the weld [12]. It has been demonstrated using computational modelling that welding temperature increases rapidly as a function of frequency, indicating that using a higher frequency can improve the efficiency of the process [32]. This is because less magnetic flux is required to heat the strip edges, and in turn allows for the induction coil to be kept small [25]. However, there are problems that arise when the frequency is too high.

These include pre-arcing and uneven heating through the thickness of the strip edges, which can lead to the cold weld defect occurring.

The impeder is a critical component in the HFI welded pipe manufacturing process. It is essentially a bar of ferromagnetic material that is placed inside the pipe by the weld area. The main role of the impeder is to increase the impedance of the current path around the inside of the pipe, consequently directing more energy to the faying strip edges. The impeder also draws magnetic flux into the pipe, resulting in a greater amount of energy induced into the pipe. The position of the impeder within the pipe is important for weld quality and efficiency. If the impeder is incorrectly placed the temperature in the vee can drop by up to a few hundred degrees, which can result in cold welds and other weld defects forming [27]. Since magnetic flux can only enter the impeder between the faying strip edges, the impeder is most effective when it is placed close to them. However, the impeder is susceptible to damage here [25]. The length and position of the ferrite within the impeder is also important for efficiency. The ferrite should extend from the centre of the induction coil to just past the vee convergence point and a similar distance in the opposite direction. If the ferrite is short of the vee convergence point by 25 mm it can increase the power requirement by up to 25 % [17]. The most important part of the impeder is the material it is made from. Traditionally impeders have been made from ferrites that have low saturation flux densities. When welding heavy-walled tubes at lower frequencies they can easily become saturated causing inefficient heating, which can potentially reduce the quality of the weld. It has been proposed that using a soft magnetic composite material called Fluxtrol A can improve welding efficiency. This was because it has a greater saturation flux density than traditional ferrite and can maintain better efficiency and weld quality during HFI welded pipe production. Large efficiency improvements have been observed when using Fluxtrol A, where the power requirement can be reduced by approximately 25 % [33,34].

2.3 Factors influencing toughness

2.3.1 Grain size

It has been well reported that grain refinement reduces the Ductile to Brittle Transition Temperature (DBTT) of steel. This has been displayed in a number of different steels including ultra fine-grained steels, soft magnetic steels, and dual phase steels [35–37].

The influence of grain size on the DBTT can be expressed in the Hall-Petch form, given by equation (2.2).

$$DBTT = T_0 - K_B d^{-1/2} \tag{2.2}$$

Where T_0 is dependent on the tensile properties of the material, K_B is the fit parameter and d is the grain size [38]. Brittle fracture arises when the yield stress, σ_y, near the crack tip exceeds the brittle fracture stress, σ_F [39]. σ_y increases at low temperatures, and the σ_F is independent of temperature. Therefore, as temperature decreases, the σ_y at the crack tip approaches the σ_F, where the material will eventually transition from a ductile to a brittle fracture as the σ_y exceeds the σ_F. The σ_y and σ_F both increase with relation to $d^{-1/2}$. However, the increase in σ_F is much greater than that of σ_y, meaning that the DBTT becomes lower with grain refinement [40].

Although there is a well-established relationship between the DBTT and grain size, the relationship between grain size and Upper Shelf Energy (USE) is not as clear. In a ferritic steel, as well as a dual phase steel, it has been reported that USE increased with decreasing grain size [35,41]. It was also found there was an increase in Lower Shelf Energy (LSE) for the dual phase steel. On the contrary, in an ultra-fine-grained steel, the USE started to decrease with decreasing grain size for grain sizes of 5 µm and lower [37]. However, these studies only took grain size into account and ignored other influencing factors such as crystallographic texture, potentially leading to a false assessment of the material. For example, it has been found that an increase in {100} planes parallel to the fracture plane will decrease the USE due to delamination on the {100} planes [7].

When investigating the toughness of steel, it has become common to examine the effective grain size of the material**.** The effective grain size considers high angle grain boundaries which are typically 15 ° or higher. An increase in the number of high angle grain boundaries results in a reduction of the effective grain size [42]. Grain boundary angles are taken into account because they play an important role in cleavage crack propagation, where it has been shown that high angle grain boundaries offer resistance to cleavage crack propagation [43,44]. When a cleavage crack propagates from one grain to another, the crack must change its surface from the cleavage plane of the first grain to that of the second. When the misorientation angle between the two grains is small, the crack will cross the grain boundary and propagate continuously into the next grain. If the misorientation angle is large, then the crack is forced to propagate discontinuously, where a new crack is started in the second grain. In both scenarios there will be a change in energy absorption as the crack crosses the grain boundary, although it is much greater for the second [45,46]. The effective grain size plays an important role in crack propagation. It has been reported that the crack propagation absorbed energy increases with decreasing effective grain size, which is also accompanied by a decrease in brittle crack propagation speeds [47]. The relationship between DBTT and the effective grain size can also be expressed by equation (2.2), where d is the effective grain size [47].

2.3.2 Crystallographic Texture

Crystallographic texture plays a very significant role in the in the fracture toughness of steels. A number of studies have investigated the influence of crystallographic texture on impact toughness, where the $\{100\}$ and $\{110\}$ planes were of interest. The $\{100\}$ plane is considered the cleavage plane of BCC steel and has a negative influence on the toughness since it has a low surface energy [48]. An increase in the fraction of $\{100\}$ planes parallel to the fracture surface leads to brittle behaviour. It has been reported that an increase in $\{100\}$ planes parallel to the fracture surface reduces the USE due to delamination related to the separation in the $\{100\}$ cleavage planes [49]. In a variety of different steels, it has been consistently found that increasing the fraction of $\{100\}$ planes parallel to the fracture surface increased the DBTT and helped to promote cleavage fracture propagation. It has also been established that with a higher fraction of $\{100\}$ planes parallel to the fracture surface it is less probable for crack arrest to occur [6–8].

Theoretically the $\{110\}$ plane should be the preferred cleavage plane since it has a lower surface energy than the $\{100\}$ plane. However, $\{110\}$ crack propagation is associated with large crack tip plasticity due to twinning events and crack tip dislocation emission. Therefore, promoting cracking along $\{110\}$ planes can improve the intrinsic brittle crack resistance by frequent blunting of the crack tip [48]. Relationships between the fraction of $\{110\}$ planes parallel to the fracture surface and impact toughness have been established, where an increase in the fraction results in an increase in the USE [6–8]. In an X65 pipeline steel, where Charpy impact specimens were machined from different orientations, an increase in fraction of $\{110\}$ planes parallel to the fracture surface from approximately 0.5 % to 7.0 % resulted in a large increase in USE. The increase was roughly double, where it increased from approximately 200 to 400 J. The fraction of {100} planes parallel to the fracture surface was consistent for both orientations [50].

When a material directionally solidifies, a given crystallographic texture in relation to the solidification direction can be produced. This has become an area of interest for electrical steels and nickel based super alloys where there is a preferential texture. In grain oriented electrical steels, the preferred texture is where the <100> direction is parallel to the rolling direction since this texture has the lowest energy losses as it is the easiest direction for magnetisation. In a cold-rolled 3.04%-Si steel sheet, a laser was used to melt a spot and the texture with respect to the solidification direction was analysed. It was observed that a strong <100> texture was produced. In an air atmosphere and an argon atmosphere, the area fraction of grains orientated with their <100> directions parallel to the solidification direction were 23.4 % and 26.3 % respectively. It was suggested that the <100> direction was the preferred direction since it is the most loosely packed direction [51]. A study was conducted to find the optimal solidification rate to produce the sharpest <100> texture in a Fe-6.5 wt.% Si steel with the aim to improve its magnetic properties. It was uncovered that for different solidification rates a different texture would be produced. The crystallographic textures produced were <130>, <100> and <142> for solidification rates of 0.5 mm/min, 1 mm/min and 4 mm/min respectively, demonstrating that different solidification rates produced different textures. When the solidification rate was 1 mm/min the volume fraction of grains with their <100> direction orientated to the solidification direction was 100 % [52]. Texture caused by directional solidification has also been extensively studied in Nickel based alloys. It has been shown in a SRR99 Nickel based super alloy, that a sharper <100> texture would be produced when the solidification rate was increased [53]. In two different studies investigating texture development during directional solidification in a CMSX4 and a CM186LC Nickel based superalloy, again it was displayed that a sharper <100> texture was produced with faster solidification rates. However, it was also discovered that the chemistry of the material played a role. When both alloys were solidified under identical conditions, a sharper texture was developed in the CM186LC alloy [54,55].

Even after heat-treatment, when a material has undergone the ferrite → austenite → ferrite transformation, the original ferrite crystallographic texture can be recovered and remain in the final microstructure. This is understood to be caused by a texture memory effect and has been observed in a number of different materials. It has been found that both the chemistry and the heat-treatment have an influence on the intensity of the effect. A study was conducted to investigate how the addition of Mn to an interstitial free steel impacted the texture memory effect. The results showed that it was enhanced by the addition of Mn, although when a sufficiently fast cooling rate was applied the effect also occurred in the steel when Mn wasn't present. It was observed that when the austenite → ferrite transformation was lower than 800 °C the texture memory effect always occurred regardless of the chemical composition. However, the memory effect could be supressed when holding the material at a higher soak temperature for a longer time [56]. The influence of peak temperature on the texture memory effect was also investigated in a cold rolled Zr alloy, where it was found the greater the peak temperature the lesser the effect. It was also observed that incomplete transformations resulted in perfect texture memory [57]. The effect of Mn in two ultra-low carbon steels containing 0.08 and 0.98 Mn was investigated where it was again found that Mn addition enhanced the memory effect. It was suggested that the effect was caused by a variant selection mechanism, either controlled by the surface energy or as a result from the release of transformation stresses [58]. It has been speculated that the residual stresses introduced during the ferrite → austenite transformation contributes to the variant selection during the austenite → ferrite transformation. Therefore, the original texture of the ferrite is inherited after the ferrite → austenite → ferrite transformation since the expansion axis in the ferrite → austenite transformation matches with the compression axis of the austenite → ferrite transformation. This infers that the variant selection is controlled by residual stresses created during phase transformation [59].

2.3.3 Constituents

The constituents that form in a weld have an influence on its mechanical properties. The main constituents that form are allotriomorphic ferrite, Widmanstätten ferrite, acicular ferrite and Martensite-Austenite (M-A) [60].

Allotriomorphic ferrite is the first phase to form when the austenite grains cool to a temperature below Ar_3. It nucleates at the prior austenite grain boundaries since they are easy diffusion paths. The austenite grain boundaries become decorated with thin and continuous layers of ferrite which thicken at a rate which is controlled by the diffusion of carbon in the austenite ahead of the transformation interface. Assuming isothermal conditions, the thickness of the ferrite changes parabolically with time. This can be expressed by equation (2.3).

$$z = \alpha_1 t^{1/2} \tag{2.3}$$

Where z is the ferrite thickness, α_1 is the parabolic rate constant, and t is time [60]. It is difficult to determine how the volume fraction of allotriomorphic ferrite affects the toughness of steel. This is because the grain size and number of high angle grain boundaries between allotriomorphic ferrite grains can significantly influence the toughness [61]. It has been shown that increasing the number of high angle grain boundaries between allotriomorphic grains in a weld metal increases the materials resistance to cleavage crack propagation, resulting in a higher toughness [62].

Widmanstätten ferrite starts to form when the weld has cooled to a temperature lower than approximately 600 °C and the diffusional growth of ferrite has slowed so much that the allotriomorphic ferrite has reached a limiting thickness [60]. It nucleates at the ferrite-austenite grain boundaries and grows as a displacive mechanism in the form of thin wedge-shaped plates at a rate which is controlled by the diffusion of carbon in the austenite ahead of the plate tip. The growth happens at a constant rate since the carbon is partitioned to the sides of the plate and the tip can therefore grow into the fresh austenite [63]. Since it grows in parallel plates with similar crystallographic textures, it has very little resistance to cleavage crack propagation which is detrimental to the toughness [64].

In a high strength steel metal cored arc welded joint it was found that the welded joint had a much lower toughness than that of the base metal. The reduction in toughness was attributed to a large grain size and the presence of Widmanstätten ferrite, where the reduction in toughness at ambient temperature was approximately 32 %. However, at temperatures of -80 °C and lower, the toughness of the base metal became very similar to that of the welded joint as the LSE region was reached [65].

A study was conducted to investigate the influence of the amount of TiO_2 nanoparticles in three different fluxes on a weld. It was found that with the changing number of nanoparticles different microstructures were formed. Impact testing revealed that as the volume fraction of Widmanstätten ferrite increased the toughness decreased, where the lowest toughness was 43 J, and the highest was 72 J. Although, when the Widmanstätten ferrite volume fraction decreased the acicular ferrite volume fraction increased [66]. This aspect was significant since toughness increases with the increase in volume fraction of acicular ferrite [67]. Therefore, the changes in toughness could not be attributed to the different volume fractions of Widmanstätten ferrite alone. This was also found in a submerged arc welded carbon steel, where three welding rods containing different amounts of Cr were used. Again, the toughness decreased with increasing Widmanstätten ferrite content, but was also accompanied by a decreasing volume fraction of acicular ferrite [68].

Acicular ferrite nucleates at inclusions and its morphology is often referred to as the basket weave structure due to its interlocking structure [69]. During transformation the ferrite grains spread in numerous directions resulting in a chaotic formation of crystallographically disorientated plates, giving it an interlocking and fine-grained structure. This structure makes it very difficult for cleavage cracks to propagate, meaning acicular ferrite formation results in a significant increase in toughness [70]. The formation of Widmanstätten ferrite and acicular ferrite is competitive. This is because the Widmanstätten ferrite plates growing from the austenite grain boundaries interfere with the acicular plates that nucleate at inclusions located throughout the material. If the number density of inclusion nucleation sites is increased relatively to the number of austenite grain boundary nucleation sites, then the formation of acicular ferrite will be favoured at the expense of the Widmanstätten ferrite [60].

Research work has been carried out comparing the toughness of an acicular ferrite and a bainitic microstructure in an ultra-low carbon steel. It was shown that the fully acicular microstructure had a much greater toughness than the bainitic one where the toughness's were 163 J and 64 J respectively. The reason for the greater toughness of the acicular ferrite was because the cleavage crack was deflected more often when compared to that of the bainitic microstructure [71].

M-A constituent forms when the weld has cooled to a temperature below 500 °C, where it transforms from the small amount of remaining austenite. In welding terminology, it is referred to as a microphase since it has a small volume fraction [60]. Numerous Gleeble thermal simulations have been conducted to investigate the influence of M-A constituent on toughness. Samples from an X100 pipeline steel were heat-treated using a Gleeble thermal simulator to investigate how M-A constituents that formed at different intercritical annealing temperatures affected the toughness. It was found that the size and dispersion of the M-A constituents had the greatest impact on the toughness. The lowest toughness occurred when the M-A constituents were large and near-connected to each other along prior austenite grain boundaries. For these the average size was 2.4 μm and produced an impact toughness of 43 J. It was established that large near-connected M-A constituents were detrimental to the toughness and extremely brittle fractures occurred regardless of whether high angle grain boundaries existed. When the M-A constituents remained coarse but had larger interspacing, the toughness increased to 83 J. However, the scatter of the results became much greater. The highest toughness was achieved when the M-A constituents were fine and were well dispersed. In this scenario the toughness became more stable, and the average toughness was 105 J [72]. In a micro-alloyed pipeline steel, Gleeble thermal simulations displayed that the prior austenite grain size influenced the size and distribution of the M-A constituent, consequently affecting the toughness. When the prior austenite grain size was larger the M-A constituent was coarser resulting in a reduction in toughness [73].

As well as the size and distribution, the morphology of M-A constituent has been observed to influence the toughness. In a high strength low alloy steel, three different heat inputs achieved via Gleeble simulations, were used to create varying M-A morphologies. When the heat input was low the M-A constituents were small and round. These were found to have no influence on the toughness, and the impact toughness was 75 J. As the heat input increased the size of the M-A constituents increased. For the medium heat input, an elongated morphology was produced and had the lowest toughness of 15 J. This was because this M-A constituent contained almost 100 % martensite. The high heat input produced the coarsest M-A constituent but had a better toughness than the medium heat input. The high heat input impact toughness was 21 J. The increase in toughness was because the M-A constituent had a shell structure, where martensite formed the shell and austenite formed the core [74].

The influence of M-A constituent on toughness has also been studied in a submerged arc welded joint of a carbon bainitic steel. This study had an advantage over Gleeble simulation studies since the microstructure was produced from cooling molten metal which cannot be achieved via Gleeble thermal simulations. When the M-A constituent was less than 1 μm and had a low volume fraction, it did not influence the toughness. However, as the size of the M-A constituents increased the crack initiation energy decreased and cleavage fracture was found to be initiating at M-A constituent [75].

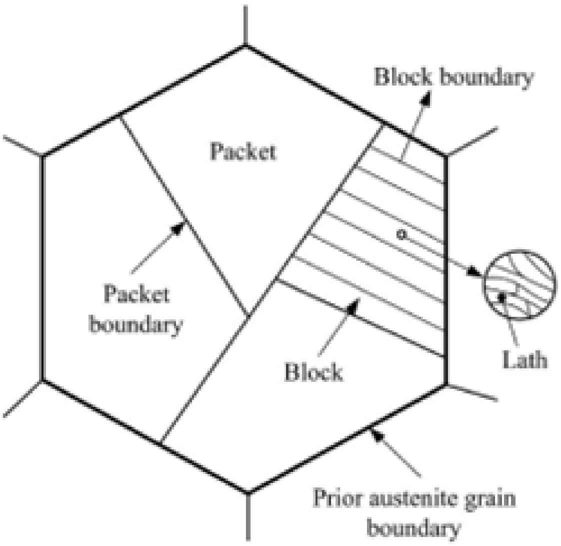

Figure 2.6. Schematic of structure of lath martensite [76].

Lath martensite is a typical structure that forms in quenched low carbon steels [77]. It consists of prior austenite grain boundaries, packets, blocks, and laths as presented on Figure 2.6. Its formation is a diffusionless phase transformation where martensite forms from austenite upon rapid quenching below the martensite start (M_s) temperature. Here the carbon in solid solution in the austenite remains in the solid solution in the martensite [78].

Martensite is typically considered a hard and brittle microstructure. However, this is typical of high carbon plate martensite, whereas lath martensite has shown good toughness properties in the as-quenched state without the need for any tempering heat-treatment. The high dislocation density and the narrow lath width is considered the source of its good toughness, where the reduction in lath length can improve the toughness [79]. Grain refinement has been shown to be an effective way to improve the resistance to cleavage crack propagation of lath martensite in a 0.1C 1.1Si 1.7Mn steel. This was because it introduced barriers to the cleavage crack propagation, where the packet and block boundaries were able to impede the crack propagation. It was found that the block width was essentially the effective grain size that determined the toughness of the material [76]. A study investigating the effect of lath martensite morphology and its volume fraction in a dual-phase steel found that the impact toughness of the lath martensite was superior to that of the ferrite. It was established that refining the martensite block size improved the toughness of the martensite, consequently lowering the DBTT of the dual phase steel. However, when martensite twins formed the toughness of the martensite was significantly reduced [80].

2.3.4 Inclusions and defects

Inclusions can have a detrimental influence on the toughness of a material where both the USE and DBTT can be affected. It has been shown that the size, occurrence and type of inclusions play an important role. The impact of inclusions in micro-alloyed steels, Additive Manufactured (AM) steels, Gas Metal Arc (GMA) welds, as well as other steels on toughness has been well investigated.

A study was performed which examined the influence of TiN inclusions on the toughness of micro-alloyed steel plate. Three steel plates, which all had the same microstructure containing granular bainite, that consisted of different levels of TiN inclusions were examined. It was found that as the volume fraction of TiN inclusions increased so did the DBTT, where cleavage fracture was initiating at coarse inclusions. The DBTT increased because the TiN inclusions had a thermal expansion coefficient that was smaller than that of the matrix. Therefore, when the temperature decreased, residual stresses were generated at the interface between the inclusions and the steel due to the different thermal contractions. This led to a reduction of the energy required to initiate cleavage fracture [81]. This has also been observed for silicate, aluminate and oxide inclusions, where the greater the inclusion size the more detrimental it was to the toughness [82]. In an AM 316L stainless steel, Si and Mn rich oxide inclusions were found to be detrimental to the toughness since they served as initiation sites for microvoid formation. As the volume of oxide inclusions increased the impact toughness also decreased [83].

Inclusions don’t always influence the USE and/or the DBTT. In a low carbon micro-alloyed steel [84] and in an ultra-high strength medium carbon steel [85], it was shown that only the USE deteriorated as the MnS inclusion volume fraction increased. For both steels there was minimal change in the DBTT and the LSE. In the low carbon micro-alloyed steel, the USE decreased from 110 J to 75 J with an increase in sulphur content from 0.002 wt.% to 0.022 wt.%. The reduction in USE occurred since it was easy for the MnS inclusions to debond from the steel matrix as they had low interfacial strength. During fracture, the MnS inclusions were responsible for the nucleation of microvoids and cleavage facets because they acted as large stress concentrators. Although it was found that the fracture initiated at the inclusions, they played no role in the growth of microvoids or cleavage crack propagation, which instead was dependant on the effective grain size and the strength of the ferrite matrix [84].

The shape of the inclusion also affects the toughness. Three Cr-Mo-V type steels, consisting of a microstructure of tempered martensite, had different cleanliness levels resulting in different volumes and types of inclusions forming. It was found that the volume, size, distribution and shape of the inclusions had an influence on the toughness. When only small and spherical inclusions were present the percentage of ductile fracture was much greater. As the inclusions became larger and elongated in shape the toughness was reduced [86].

Non-metallic inclusions do not always have an impact on the toughness of a material. In a duplex steel it was found that small and spherical inclusions less than 1 μm in size had no influence on the toughness. However, when inclusions greater than 1 μm were found, the toughness of the steel decreased. Microcracks linking with the initial fracture were observed [87]. A "cut-off" size, where only inclusions over a minimum size are active in the fracture process was also observed in GMA welds. This study investigated how shielding gases with different levels of oxygen content affected inclusion formation and the toughness of the weld. It was discovered that the weld produced using the shielding gas with the greatest oxygen content produced the greatest number of inclusions and had the lowest toughness. This was because the weld melt pool had the greatest amount of oxygen, so consequently had the highest driving force for inclusion nucleation. Therefore, nucleation was able to start earlier resulting in larger inclusions [88]. The complex formation of an inclusion can be described by equation (2.4).

$$xM + yN + zO = M_xN_yO_z \tag{2.4}$$

Where M, Z and O are solute elements [89]. The thermodynamic driving force, ΔG, for the inclusion formation is given by equation (2.5).

$$\Delta G = \Delta G^O + RT\ln\frac{[M_xN_yO_z]}{[M]^x[N]^y[O]^z} = RT\ln\frac{Q}{K_{eq}} \tag{2.5}$$

Where K_{eq} is the thermodynamic equilibrium constant for the formation of the oxide inclusion, Q is the activity quotient, $[M]$, $[N]$ and $[O]$ are the activities of the reacting species, and $\left[M_xN_yO_z\right]$ is the activity of the resulting oxide. The ratio of Q/K_{eq} is the supersaturation of the system, and when Q/K_{eq} is < 1 there is a thermodynamic driving force for inclusion nucleation [89].

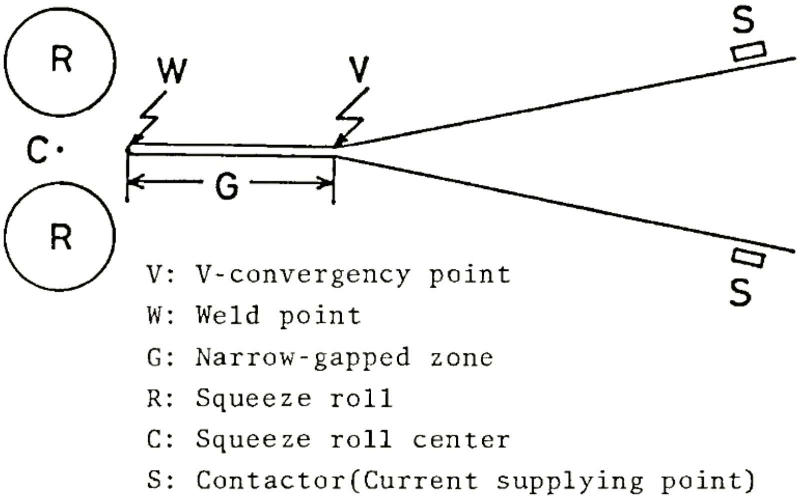

Figure 2.7. Schematic of narrow gap [90].

In HFI welded pipe production, oxides inclusions can form and get trapped within the bond plane. These inclusions are referred to as either the penetrator or cold weld defect and their formation is linked to the heating and squeezing together of the strip edges. Therefore, the type of welding phenomena determines which inclusion defect occurs.

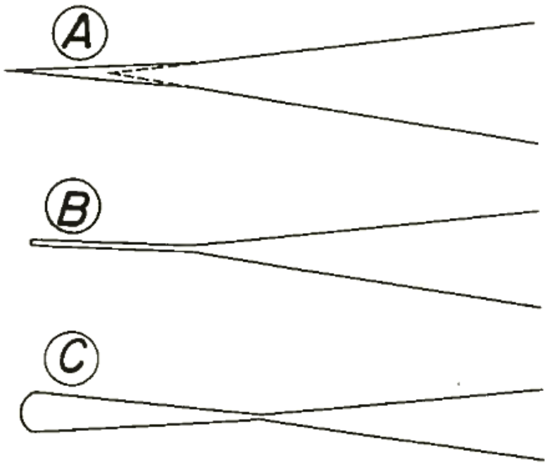

Figure 2.8. Schematic of narrow gaps formed during for each phenomenon. (A) Low heat input, (B) optimum input and (C) high heat input [90].

Observations of the HFI welded pipe manufacturing process have shown that the strip edges are not always welded together at the vee convergence point, and that a narrow gap develops as shown on Figure 2.7. The shape and size of the narrow gap is dependent on the type of welding phenomena. There are three phenomena types called the 1st, 2nd and 3rd, which are low heat input, optimum heat input and high heat input respectively [90]. The three different gap shapes are displayed on Figure 2.8.

The cold weld defect is an oxide inclusion that is in the form of a film that occurs continuously and is produced when the heat input is too low resulting in insufficient melting of the strip edges. Consequently, when the strip edges are squeezed together by the weld rolls, there is not enough material flow to eject the oxide inclusions from the bond plane [91]. Therefore, the cold weld is associated with the 1st phenomena.

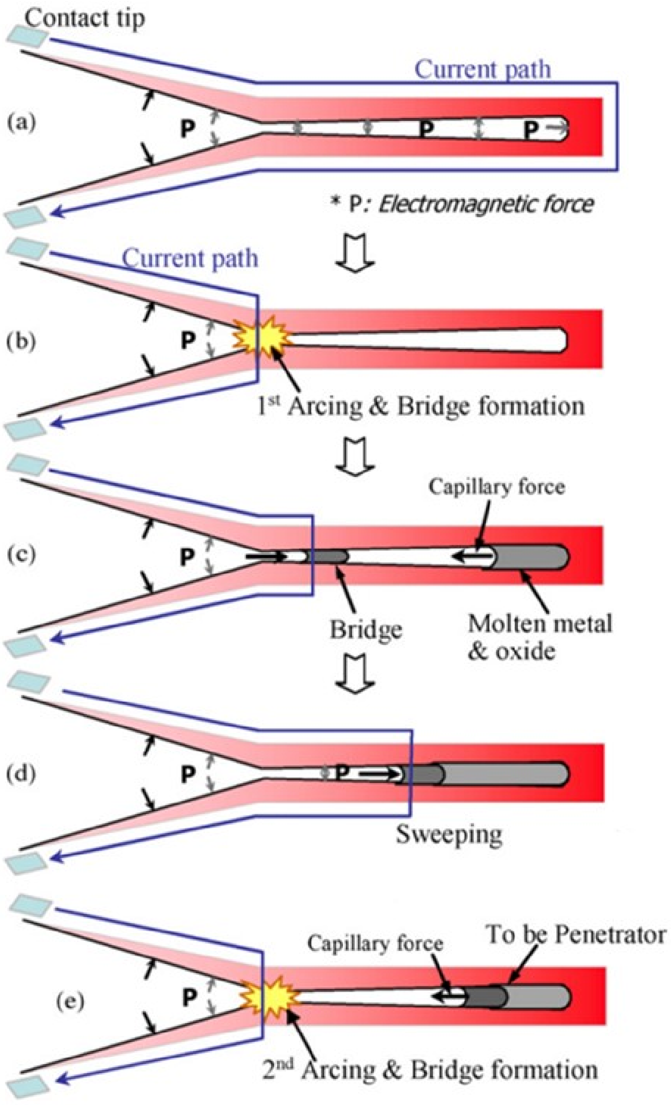

Figure 2.9. Schematic of penetrator formation [92].

The penetrator defect is associated with the 3rd phenomena when the heat input is too high. It has a pancake morphology and occurs intermittently [91]. When the heat input is too high the small gap becomes a comet shape as displayed on Figure 2.8C. This is because there is much greater melting at the welding point due to higher current densities. The current density along the narrow gap affects the Lorentz force, denoted by P on Figure 2.9a, which pushes on the molten strip edges. The Lorentz force at the welding point is greatest; therefore, a larger amount of material is expelled from the gap here, resulting in a comet shape. Following the formation of the comet shaped gap, arcing and bridge formation occurs at the apex, Figure 2.9b. The current path then goes through the bridge and the capillary force becomes dominant at the welding point, drawing discharged molten metal and oxides into the narrow gap. Electromagnetic forces then push the bridge towards the welding point, Figure 2.9c. The molten metal, containing oxides, and bridge then meet each other at the centre of the narrow gap, Figure 2.9d. At high temperatures, second arcing occurs creating a second bridge. The molten metal and oxides are drawn towards the second bridge by the capillary force, Figure 2.9e. The narrow gap containing molten metal and oxides then passes through the welding point and if not sufficiently squeezed out remain as penetrators in the bond plane [92].

Although cold welds and penetrators are associated with the 1st and 3rd phenomena respectively, it has been shown than they can occur during the 2nd. The cold weld can occur during the 2nd when there is insufficient squeeze out of the molten material. When the penetrator defect occurs during the 2nd phenomena, the size and the frequency of the inclusions is less than that of when they form during the 3rd [93].

A study was conducted investigating the formation of the penetrator defect and how the chemical composition of the steel influenced the formation. To ensure penetrator defect formation, the study used non-optimal welding conditions to produce the pipe. The difference in chemistry between the samples was the Mn/Si ratio. The penetrator defects produced typically consisted of Mn and Si, although some inclusions consisting of Al were also formed. It was discovered that with lower ratios of Mn/Si it was more likely that penetrator defect would form, and that the Mn/Si ratio should be kept greater than 8 to reduce the probability of oxide formation [94].

2.3.5 Alloying elements

Alloying elements are added to steels to achieve desired mechanical properties. Carbon is the most important alloying element in steel since it raises properties such as strength, hardness and resistance to wear. However, as the carbon content of steel increases the weldability is lowered [95]. The weldability of a steel can be determined by the carbon equivalent which is a measure of the effect of carbon and other alloying elements on hardenability. It essentially determines how readily martensitic structures are able to form [96]. There is a large variety of different equations that have been used to describe the carbon equivalent where many have been designed for specific steel types [97]. For welding, BS EN 1011-2 recommends using equation (2.6) to calculate the carbon equivalent [98].

$$CE = C + \frac{Mn}{6} + \frac{Cu + Ni}{15} + \frac{Cr + Mo + V}{5} \tag{2.6}$$

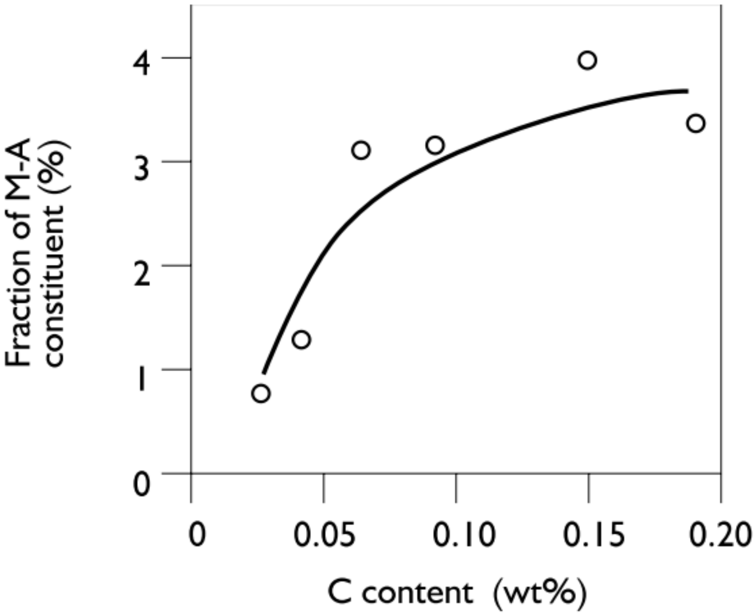

Figure 2.10. Effect of carbon content on volume fraction of M-A constituent [99].

Numerous studies have been conducted to determine how carbon equivalent influences a steels toughness. In a high strength bainitic steel it was found that when increasing the carbon equivalent, a greater volume fraction of martensite formed during cooling. This resulted in a decrease of the USE and an increase in the DBTT. The study also investigated how the cooling rate affected the toughness properties of steel, where it was found that an increase in cooling rate was detrimental to both the USE and DBTT.

However, these properties were more sensitive to carbon equivalent than the change in cooling rate [100]. Bending tests have been performed on the weld of high strength low alloy steels plates with varying carbon equivalents. It was observed that as the carbon equivalent increased there was an increase in crack length, indicating that the materials ability to arrest cracks was reduced [101]. In a micro-alloyed steel, it was found that the volume fraction of M-A constituent increased with carbon content. This relationship is displayed on Figure 2.10. With the increase in M-A constituent volume fraction there was also an increase in the fracture facet size observed [99]. As previously discussed, M-A constituent can be detrimental to the toughness of steel since it can promote brittle fracture initiation [75].

To achieve good weldability, microalloying elements are added to steel so that the carbon content of the steel can be reduced without deteriorating the mechanical properties. Niobium is an important microalloying element that is used to achieve this via grain refinement during thermomechanically controlled processing [102]. It is well known that niobium is added to these steels for three main reasons. These are: to refine the austenite grain size during hot rolling, which then assists with refining the ferrite grain size; to lower the austenite to ferrite transformation temperature, consequently refining the ferrite grain size and increasing dislocation density; and to impart precipitation hardening [103,104].

The thermomechanically controlled processing of micro-alloyed steel involves the reheating of a cast slab followed by defined number of hot rolling passes above, and then subsequently below the non-recrystallisation temperature (T_{nr}). Hot working below the T_{nr} creates pancaked austenite grains and deformation bands. This is accompanied with an increase in stored deformation energy, prior to the transformation to ferrite, in terms of greater dislocation density. This results in a large amount of nucleation sites for austenite to ferrite transformation [103]. During the hot working, niobium carbide (NbC) precipitates form on the deformation structures of the austenite. This suppresses sub grain migrations and thus inhibits the recrystallisation of the austenite, resulting in a fine final microstructure [105].

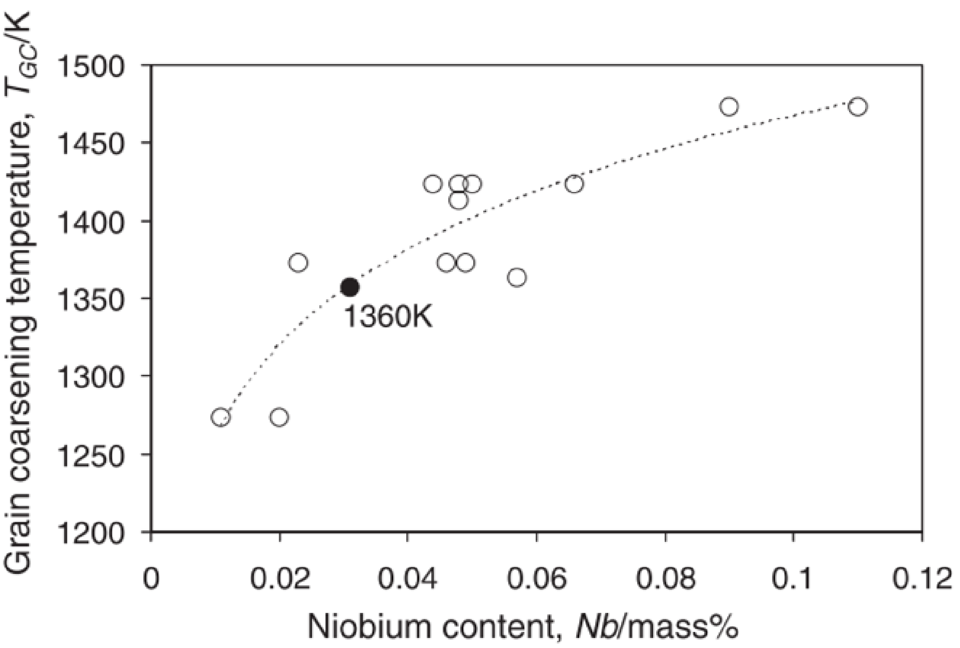

Figure 2.11. Grain coarsening temperature as a function of niobium content [106].

In plain carbon steels austenite grain growth is exponential as a function of temperature, however in micro-alloyed steels a two-stage grain growth occurs. In numerous micro-alloyed steels, it has been observed that austenite grain growth in the initial stages of heating was extremely slow due to the existence of precipitates inhibiting the movement of grain boundaries. Once the temperature increased and the precipitates were dissolved the austenite grains were free to grow [106–108]. The temperature which separates these two stages of austenite grain growth is referred to as the grain coarsening temperature (T_{GC}), although the limits between both stages cannot be clearly divorced. It has been shown that the type, size and concentration of the micro-alloying elements affects the T_{GC} [107]. Figure 2.11 displays the influence of niobium content on the T_{GC} where it can clearly be seen how T_{GC} increases with increasing niobium content. The heating rate has also been found to have an influence on the T_{GC} where the faster the heating rate the higher the T_{GC}. It has been shown that when increasing the heating rate from 0.5 Ks^{-1} to 5 Ks^{-1} the T_{GC} can be raised by approximately 30 K. It was also observed that the T_{GC} was roughly 40 K to 70 K below the temperature at which the precipitates were fully dissolved [106]. In the coarse-grained zone, where the NbC precipitates have been dissolved and the austenite is free to grow, the hardenability increases since it becomes easier for phases such as martensite to form during cooling which can lead to a reduction in toughness [60].

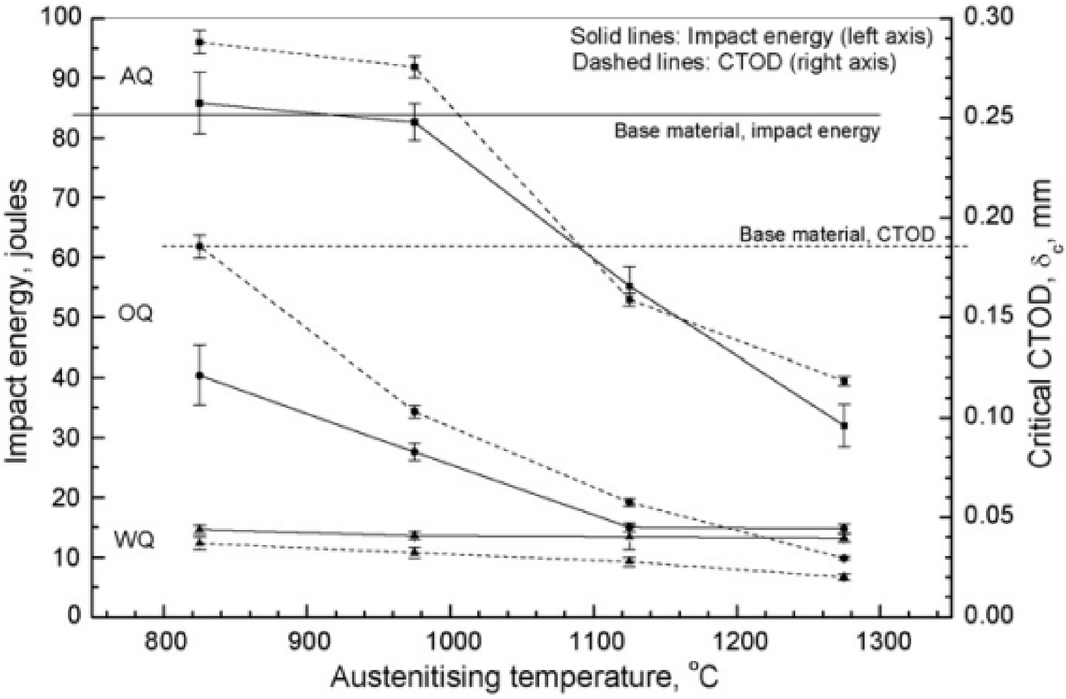

Figure 2.12. Influence of austenitising temperature on impact toughness [109].

A study was conducted to investigate the effects of austenitising temperature and quenching media on the toughness of a micro-alloyed niobium steel. It was found that when the temperature was above 1000 °C the austenite grains became very coarse due to the dissolution of NbC precipitates. The increase in prior austenitising temperature was accompanied with a decrease in toughness as displayed on Figure 2.12. The severity of the quench media also affected the toughness where water quenching resulted in the lowest toughness and air quenching the highest. It was observed that a larger prior austenite grain size led to an increased number of martensitic structures forming, accompanied with an increase in the final grain size. This resulted in a decrease in toughness [109]. The effect of prior austenite grain size was also studied in a 0.1 C – 5 Mn martensitic steel. It was discovered that with increasing austenitising temperature there was an increase in the M_s temperature. The higher M_s temperature meant martensite transformation was more likely to occur. It was also observed that there was a decrease in both the toughness and the percentage of high angle grain boundaries [110]. The reduction in high angle grain boundaries with increasing prior austenite grain size was also observed in an ultra-high strength low alloy steel. Like before this was accompanied with a decrease in toughness [111]. As well as increasing the volume fraction of martensite, the volume fraction of Widmanstätten ferrite has been shown to increase with increasing prior austenite grain size, where it was also found that with increasing niobium content more Widmanstätten ferrite was able to form [112].

The effect of niobium content on the microstructure and toughness of the HAZ coarse-grained zone of a weld has been investigated using Gleeble simulations. One study found that the addition of niobium degraded the toughness of the steel, where fracture was initiating at large M-A islands [113]. This was also observed in a variety of hot rolled steels with differing alloying elements. The reduction in toughness was attributed to the presence of Widmanstätten ferrite as well as M-A constituent. The formation of these phases was believed to be due to the fact that niobium lowered the Ar_3 temperature, encouraging martensitic transformation and making the steel more hardenable [114]. However, not all studies agreed with the previous. It has been observed that for low heat inputs that an increasing niobium content increased the toughness due to the greater amount of acicular ferrite formation. Although, for higher heat inputs, there was only a very small increase in toughness with niobium content due to the formation of Widmanstätten ferrite. Nevertheless, the niobium content did not degrade the toughness of the steel at higher heat inputs in this study [115].

In numerous materials complete precipitate dissolution has been observed during welding. This was observed in a micro-alloyed ultra-high strength steel gas metal arc multi-pass weld. In the original weld no precipitates were found. However, precipitates did form during reheating caused by subsequent welding passes [116]. Similar was observed in a friction stir welded aluminium alloy plate, where the dissolved precipitates were not able to reprecipitate due to the fast-cooling rates. Although, they were able to form via heat-treatment, even if they were much coarser than that of the base metal [117]. The type of heat-treatment will affect the precipitates that form. In an ultra-high strength steel, complete precipitate dissolution happened during welding and no significant precipitation occurred on cooling. Precipitation occurred during heat-treatment where the temperature affected the size of the precipitates. A heat-treatment at 550 °C for 30 minutes produced extremely fine precipitates, whereas a similar heat-treatment at 660 °C resulted with ones that were coarser [118]. It has been found that it is possible for re-precipitation during the cooling of a weld. This was observed in a laser welded micro-alloyed C-Mn steel, where large niobium titanium carbonitrides, 100 to 350 nm in size, were found [119]. It has been found that whether or not re-precipitation occurs is dependent on the cooling rate. In a gas tungsten arc welded HSLA steel, re-precipitation of TiC particles only occurred when there was a slow cooling rate [120].

2.4 HFI welded pipe welds

2.4.1 HFI welded pipe weld macrostructure

The classical weld profile produced during HFI welded pipe manufacturing has an hourglass shape which is created due to the greater heating at the strip edge corners during welding. This profile is always observed in the as-welded (AW) condition regardless of the steel grade used to produce the pipe. The AW condition refers to the weld directly following welding, so it therefore has not experienced any type of PWHT. This typical weld profile is displayed on Figure 2.13 and can be split into four zones which are the base metal, thermomechanically affect zone (TMAZ), HAZ, and the weld line. These are labelled 1, 2, 3 and 4 respectively.

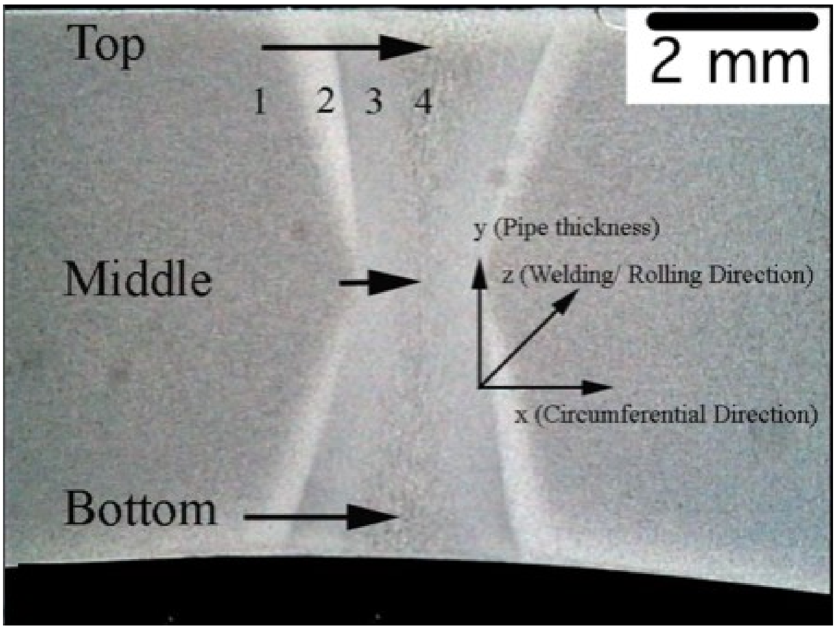

Figure 2.13. Zones of AW HFI welded pipe weld [2].

The TMAZ is formed when the weld rolls squeeze the molten strip edges together. It is therefore created by the deformation and heat associated with the welding process. The microstructure of the TMAZ will be similar to that of the base metal, however the shape of the grains will be anisotropic, since they have been deformed [3]. The HAZ is then created by the heat associated with welding. The temperature in this zone will exceed Ac_3 but will not be hot enough to melt the material. Therefore, this zone transforms to austenite during heating and then a new microstructure is formed on subsequent cooling, altering its mechanical properties. The weld line is then formed when the material that was melted during heating solidifies [60].

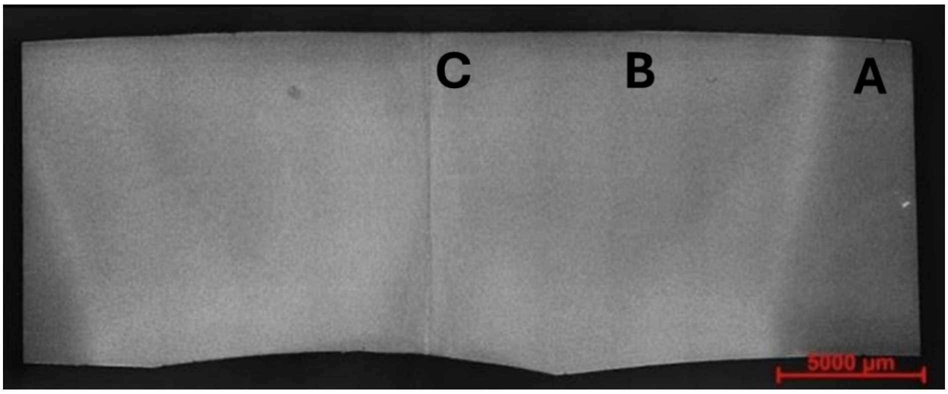

Figure 2.14. Zones of PWHT HFI welded pipe weld [121].

If a PWHT follows welding the previous hourglass shape weld profile and its associated zones are replaced. The resulting macrostructure consists of the base metal, affected zone (AZ) and the weld line. These are labelled A, B and C on Figure 2.14 respectively. This is the typical macrostructure observed after a PWHT. The aim of the PWHT is to replace the undesirable microstructure produced during welding with one consisting of better mechanical properties.

2.4.2 Weld line toughness and microstructure relationships

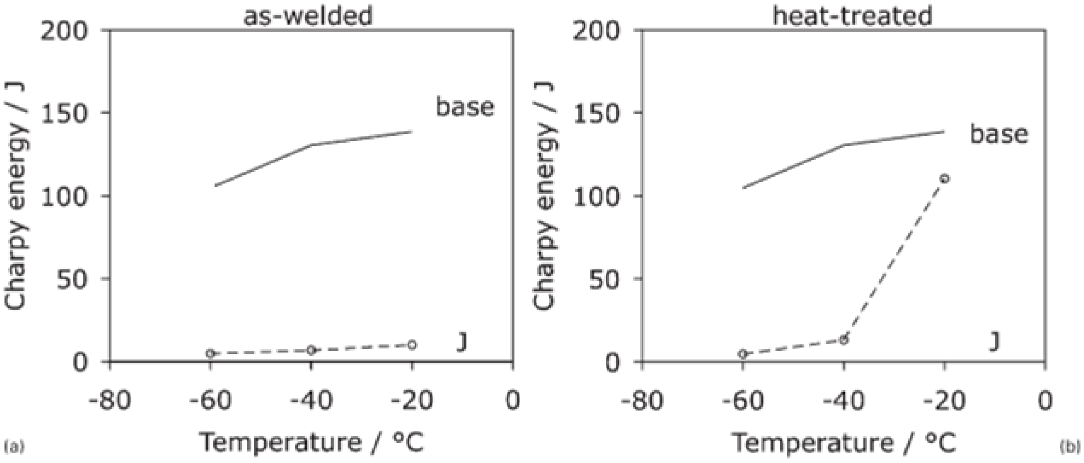

Figure 2.15. Charpy impact test results. (a) As-welded and (b) heat-treated [2].

Charpy impact testing was conducted in a study investigating the weld line toughness of a HFI welded pipe that was produced using a micro-alloyed pipeline steel containing niobium and vanadium. The testing was performed on the base metal, and the weld line in the AW condition and following a PWHT. The Charpy impact test results are displayed on Figure 2.15, where the lines labelled base and J refer to the base metal and the weld line respectively. It was found that the AW weld line had an inferior toughness when compared to that of the base metal. The weld line toughness was improved by the PWHT at -20 °C. However, it was less than that of the base metal and was still extremely poor at lower temperatures. It was concluded that the poor toughness of the weld line was due to the large crystallographic grain size created during welding, that still remained even following a PWHT [2]. However, this was not the only obvious factor contributing to the reduction in toughness. The microstructural analysis found that Widmanstätten ferrite was produced at the weld line and that traces of the original weld line microstructure still remained following the PWHT. Widmanstätten ferrite is detrimental to toughness because it grows in parallel plates that offer little resistance to cleavage crack propagation [64]. Therefore, the presence of Widmanstätten ferrite at the weld line was overlooked since it would have also influenced the toughness of the weld line.

Numerous studies have been conducted to investigate factors causing poor weld line toughness of X65 HFI welded pipes. One study found that the AW weld line produced fully brittle fractures across the entire test temperature range of -5 °C to -60 °C. In the AW condition the poor toughness was somewhat attributed to the large grain size and the presence of M-A islands at the weld line. However, it was also revealed that there was a large fraction of grains orientated for easy fracture at the weld line, which was considered to be when the {100} plane was aligned within 10° parallel to the bond plane. This was determined to be the primary factor negatively influencing the toughness of the weld line. The PWHT was able to improve the toughness at -5 °C, yet it was still much lower than that of the base metal, and at temperatures lower than -30 °C the fractures were still fully brittle. The PWHT was able to reduce the intensity of the reduce the intensity of grains orientated for easy fracture, which was thought to be the reason for the improvement in toughness [3]. However, this study did not quantify the intensity of the crystallographic textures. There was also a lack of fracture surface analysis conducted. Therefore, strong relationships between the microstructure and the toughness could not be well established. For instance M-A islands were assumed to be detrimental to the toughness of the weld line as they have been shown to trigger cleavage fracture initiation [73]. Though, it has also been shown that M-A can be present and play no role in influencing cleavage fracture initiation [75].

Therefore, without any fracture analysis, the factors believed to be impacting the toughness were educated assumptions.

Another X65 study also determined that grains orientated for easy fracture was the reason for the poor toughness at the weld line. Again, the crystallographic texture was only analysed qualitatively, although the distribution of the grains was considered. It was observed that grains orientated for easy fracture were present in clusters or strings, concluding that there were easy paths for cleavage crack propagation through the weld line [4]. This was because the misorientation angles between the grains orientated for easy fracture were small, resulting in a low resistance to cleavage crack propagation since there would be very small energy absorption as the cleavage crack propagated from the cleavage plane of one grain onto the cleavage plane of the next [45,46].

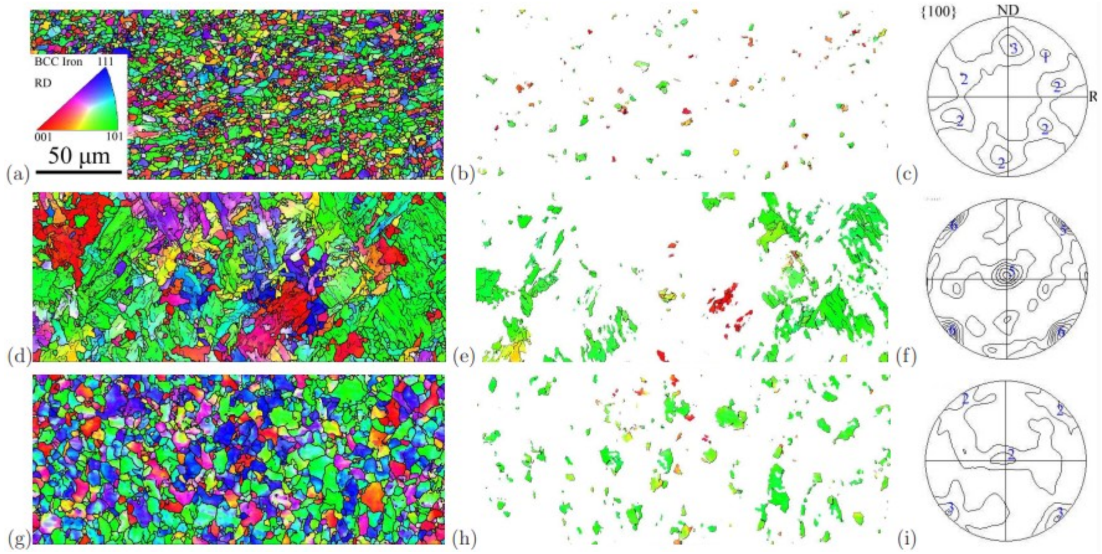

Figure 2.16. Orientation images of base metal (a)-(c), AW weld line (d)-(e), and weld line following a PWHT(g)-(i) [5].

Manganese silicate inclusions have been shown to be detrimental to the toughness of an X65 HFI welded pipe weld line. They were formed during heating of the strip edges and were then not squeezed out when the faying strip edges were joined together. However, whether these inclusions were present or not, the weld line toughness was still poor when compared to the base metal. The poor toughness in the AW condition was attributed to the formation of Widmanstätten ferrite and M-A islands, the large grain size, and a high density of grains orientated for easy fracture. However, this study only used fracture analysis to determine whether inclusions were present or not on the fracture surface. Therefore, an in-depth fracture analysis was not performed which could have created stronger relationships between the microstructure and the toughness of the weld line. Unlike the previous studies, this time the intensity of the {100} planes parallel to the bond plane was quantified. EBSD analysis revealed that a 3 % fraction of grains in the base metal were orientated for easy fracture, whereas in the AW condition it was 19 %. Figure 2.16 displays orientation maps from the study. The microstructure at the weld line following a PWHT consisted of a ferrite matrix with a small amount of pearlite, hence the constituents detrimental to toughness were removed. However, the fraction of grains orientated for easy fracture was only reduced to 10 %. This was still much greater than that of the base metal and was concluded to be the main reason why the improvement in toughness following a PWHT was only small [5].

A strong intensity of {100} planes parallel to the bond plane has been attributed as a major factor causing poor toughness in the previously discussed studies [3–5]. However, the literature has shown that the {110} plane also plays an important role in crack propagation. It has been found that {110} crack propagation is associated with large crack tip plasticity which improves the intrinsic brittle crack resistance by frequent blunting of the crack tip [48]. Therefore, the role of the {110} plane needs to be considered when investigating the toughness of a HFI welded pipe weld line. The toughness has also only ever been analysed using the standard Charpy impact test which measures the absorbed energy associated with the whole fracture alone. When analysing the total absorbed energy alone, many important characteristics can be overlooked which can lead to a false assessment of the material [122–124]. Charpy impact testing with an instrumented head can give a better evaluation of the material since it can provide absorbed energies associated with specific facture events. Due to the way that the high frequency current flows along the faying edges the heating is greatest at the strip edge corners during welding [12]. Consequently, different thermal cycles would be experienced through the depth of the weld. This would most likely result in the microstructure changing as a function of depth through the weld line, and subsequently the toughness also changing. Current research has generally only analysed the microstructure at localised locations in the weld line. Therefore, overlooking that the toughness potentially may significantly vary through the depth of the weld line.

2.4.3 Computational modelling of HFI welded pipe heating process

Computational modelling has been employed as a technique to understand and optimise the HFI welded pipe manufacturing process. It has been used to see how frequency, mill speed, vee angle, ferrite position and other variables can influence factors such as power requirements and the current distribution [125,126]. However, building the models can be complicated because they have to use a coupled electromagnetic and thermal field solution. They also need to consider the movement of the pipe in a 3D geometry, which is generally achieved by translational motion of the temperature field [127]. Figure 2.17 displays the algorithm that is generally used to achieve the solution. It is also important that temperature dependant properties are correctly defined, since specific heat, thermal, conductivity, electrical conductivity and magnetic permeability do not change linearly as a function of temperature [128,129].

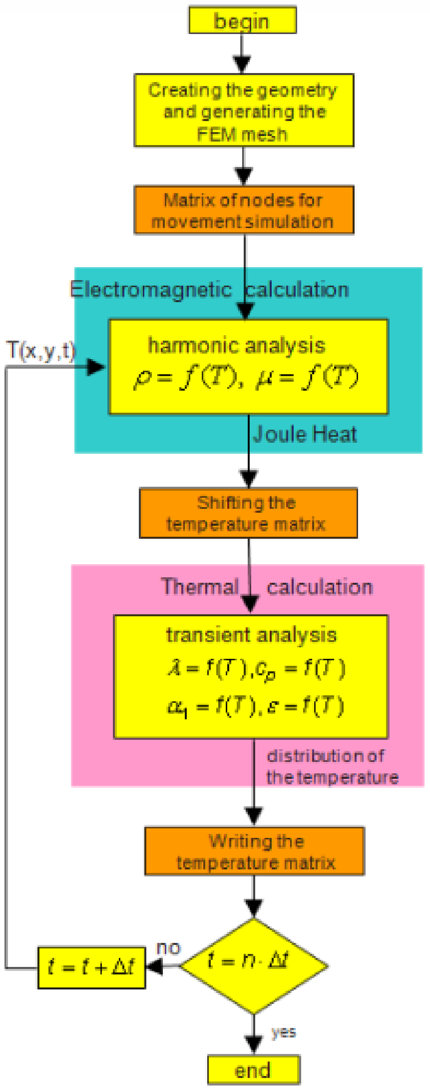

Figure 2.17. Algorithm of transient coupled electric thermal analysis [129].

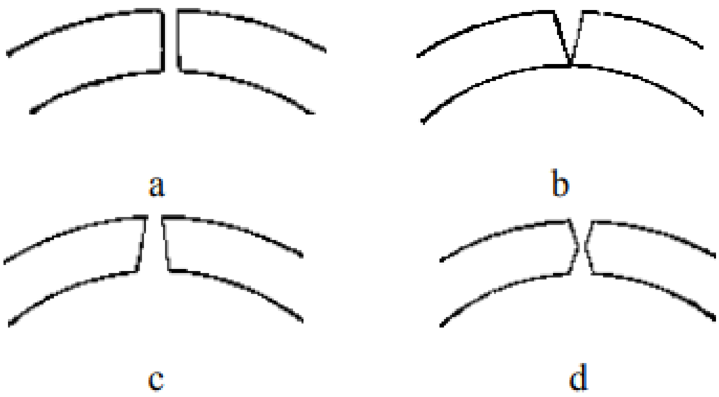

Figure 2.18 Shape of strip edges in study [9].

It is well known that it is difficult to achieve a uniform temperature distribution through the depth of the strip edges during welding since the strip edge corners experience greater heating than at the strip edge centres. Therefore, research has been undertaken investigating how the geometry of the strip edges affects the temperature distribution. A study was conducted to explore how the strip edge geometry affected the temperature distribution through the thickness of the strip edges of a pipe produced using an 8.94 mm thick strip. Four different geometries were simulated and are displayed on Figure 2.18. It was found that geometries b and c produced the largest temperature gradients through the depth of the strip edges, where the greatest temperatures were at the corners in the closest proximity to each other. Geometry a had the classic hourglass shaped profile and produced the most uniform temperature distribution, where the difference between the maximum and minimum temperature was 190 °C. The temperature difference for shape d was 255 °C, since there was a high temperature produced at the tips at the centre of the strip edges [9].

A further study was then performed that investigated how different dimensions for geometry d affected the temperature distribution. Again, an 8.94 mm thick strip was used for the study. It was found that by adjusting the angles of the geometry, a much more uniform temperature distribution could be achieved. The optimum geometry had a difference of approximately 50 °C between the maximum and minimum temperatures, indicating that the strip edge geometry could be altered to improve the temperature profile through the depth of the strip edges [10].

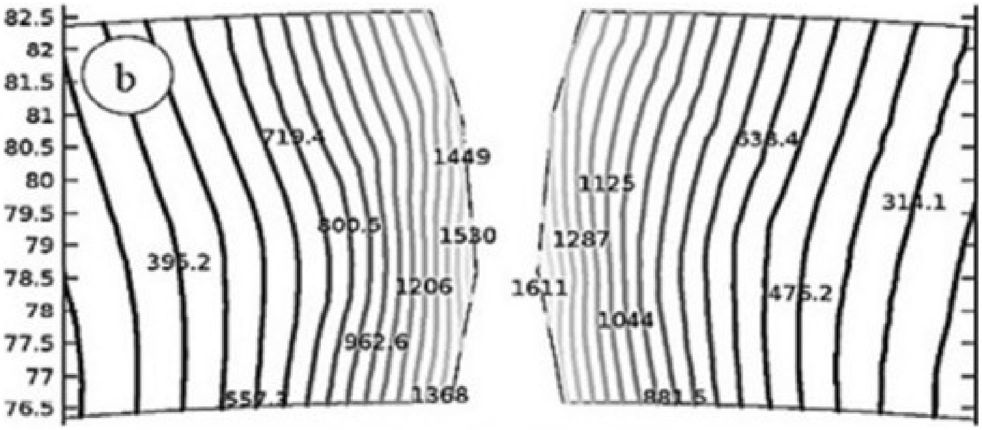

Figure 2.19. Final geometry with chamfers [11].

It has also been demonstrated that the temperature distribution can be improved by altering the edge geometry on a HFI welded pipe produced using a 5 mm thick strip. Although, this time the shape of the edge geometry was different to that of the studies previously discussed. For this study the geometry involved adding a chamfer to each of the strip edge corners, such that there was no point at the centre of the strip edges like that of geometry d on Figure 2.18. The angle and depth of the chamfers were altered in order to find the optimum edge profile, where the final geometry is displayed on Figure 2.19. The thermal contour lines display how the temperature had become more uniform where the high temperatures at the corners were removed. When the above geometry was compared to the standard square edge, it was found that the temperature gradient was reduced by approximately 600 °C. However, the model only used temperature dependant properties for specific heat capacity and thermal conductivity. Therefore, there are questions over the accuracy of the results since electrical conductivity and magnetic permeability were not included [11].

Computational modelling has shown that for HFI welded pipes produced from steel strips approximately 9 mm and thinner, the temperature profile at the strip edges can be made more uniform by altering the geometry of the strip edges. It has been suggested that this could improve weld quality by reducing the high temperatures at the strip corners. Nevertheless, it has not been shown if producing a more uniform temperature distribution is achievable for thick-walled pipes. Thick-walled pipes are more susceptible to poor weld quality due to large temperature differences across the strip edges during welding [12]. Therefore, an improvement in the uniformity of the temperature distribution would most likely be extremely beneficial to the weld quality of thick-walled HFI welded pipes. However, none of the computational modelling studies provided reasoning to why a more uniform temperature distribution during welding would potentially improve the toughness of the weld.

2.5 Knowledge gaps

The toughness of HFI welded pipe welds have currently only been evaluated using the standard Charpy impact test. Since this only measures the absorbed energy associated with the whole fracture it can lead to a false assessment of the toughness [122–124]. Hence, the current analysis is limited. Charpy impact testing with an instrumented head gives the absorbed energy at specific fracture events, allowing for a more accurate evaluation to be made. Therefore, properties such as the weld lines resistance to fracture initiation and crack propagation can be determined, allowing for a greater understanding of the toughness of the weld line.

Fracture surface analysis following Charpy impact testing has been very limited, where it has only been used to determine whether or not inclusions were present on the fracture surface. Therefore, strong relationships between the weld line microstructure and its toughness have not been well established. Fracture analysis performed to a greater extent would give a better understanding of how fracture is initiating and propagating through the weld line, allowing for stronger relationships to be made.

A strong intensity of {100} planes has been attributed as a major factor causing poor toughness [3–5]. However, the literature has shown that the {110} plane also plays an important role in crack propagation since it can inhibit brittle crack propagation by frequent blunting of the crack tip [48]. Therefore, the role of the {110} plane needs to be considered when evaluating the influence of the crystallographic texture on the toughness of a HFI welded pipe weld line.

It is well known that during welding, heating is greatest at the strip edge corners due to the way the high frequency current flows along the faying edges. Accordingly, different thermal cycles are experienced through the depth of the weld. Therefore, it is highly probable the microstructure and toughness vary through the depth of the weld line. Current research has generally only analysed the microstructure at localised locations within the weld line. Consequently, overlooking that the toughness may change significantly through the depth of the weld. Therefore, microstructural analysis evaluating whether there is a large change in microstructure through the depth of the weld line needs to be conducted.

Computational modelling studies have suggested that producing a more even temperature distribution through the strip edges during welding could improve the quality of the weld. The modelling studies have shown that a more uniform temperature distribution at the strip edges can be achieved by altering the geometry of the strip edges. Although this has only accomplished on strip thicknesses below 9 mm and not on thick-walled pipe. Reasoning to why a more uniform temperature distribution could improve weld toughness has yet to be considered. However, investigating the microstructure through the depth of the weld may possibly help to explain why.

3 Aims and objectives

3.1 Project aims

The aim of the project was to develop a better understanding of the microstructure of an X60 HFI welded pipe weld and how it influenced the toughness of the weld line. With a deeper understanding justification to why a more uniform temperature distribution through the depth of the strip edges during welding would improve weld line toughness could be determined. It is envisaged that reducing the high temperatures at the strip edge corners would create microstructures in these locations that would have a more favourable toughness than typically produced. Consequently, improving the overall toughness of the weld line. A method to achieve uniform heating when producing thick-walled pipe could then be developed. If successful there would be a rational method available to improve the weld line toughness, with the potential ability to increase customer confidence in the use of HFI welded pipes for the transportation of hydrocarbons in harsh and cold environments.

3.2 Project objectives

- Perform an extensive analysis of the HFI welded pipe microstructure, where different locations through the depth of the weld line are analysed and multiple crystallographic textures are considered.
- Perform Charpy impact testing with an instrumented head so a more reliable assessment of the toughness of the weld line can be achieved.
- Conduct an in-depth fracture analysis of the fracture surfaces resulting from the Charpy impact testing in order to understand what factors may be initiating brittle fracture and/or influencing crack propagation, allowing for stronger relationships to be built between the weld line microstructure and its toughness.
- Develop a computational model to determine whether a more uniform temperature profile can be achieved for a thick gauge pipe by altering the geometry of the strip edges.
- Compare relationships between the microstructural analysis and the computational model to determine why a more uniform temperature profile could potentially improve the toughness of the weld line.

4 Materials and methods

4.1 Materials

The material for this work came in the form of three pipe segments, each cut from a different 16 mm thick X60 HFI welded pipe. All the pipe segments differed to each other and were in the following conditions: Base Metal (BM), As-Welded (AW) and Heat-Treated (HT). The chemical compositions for the material are on Table 4.1.

Table 4.1. Chemical compositions of material (wt.%).

	BM	AW	HT
C	0.066	0.070	0.060
Si	0.200	0.180	0.174
Mn	1.29	1.28	1.27
P	0.016	0.018	0.012
S	0.003	0.002	0.002
Cr	0.035	0.024	0.022
Mo	0.004	0.002	0.002
Ni	0.032	0.021	0.014
Al	0.042	0.033	0.034
B	0.0002	0.0002	0.0001
Cu	0.025	0.018	0.018
Nb	0.041	0.042	0.041
Sn	0.013	0.009	0.011
Ti	0.016	0.016	0.016
V	0.003	0.004	0.003
N2	0.0057	0.0055	0.0041
Ca	0.002	0.003	0.001

The AW segment was cut from the pipe immediately following welding and included the weld line. It had experienced no heat-treatment. The BM and HT segments were cut from pipes that had been fully processed. These pipes had experienced a weld line Post Weld Heat-Treatment (PWHT), which occurred directly after welding, and a full body heat-treatment. The weld line PWHT involved induction annealing the weld line, where the induction annealers A, B, C and D were set to 900 °C, 1020 °C, 1020 °C and 1020 °C respectively. This was closely followed by air quenching the weld line to a temperature below 300 °C. The mill speed during this process was 55 m/min. The pipes were then tempered in a furnace at 670 °C for an aim time of 41 minutes. The HT segment included the weld line, and the BM segment was taken from part of the pipe that did not.

4.2 Charpy impact testing

4.2.1 Charpy impact specimen preparation

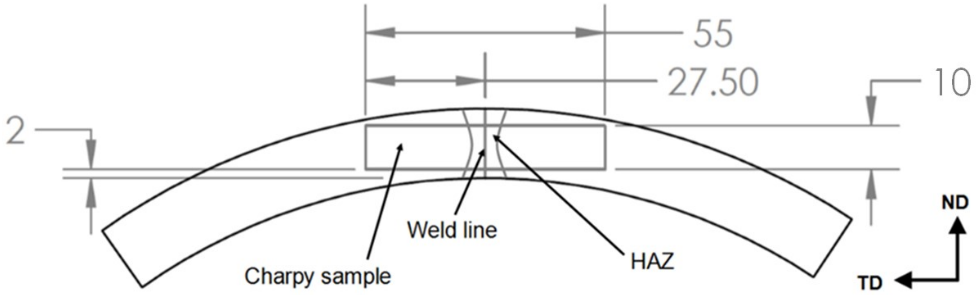

Figure 4.1. Location that Charpy impact specimens were machined from pipe segments (dimensions in mm).

Full size Charpy test specimens were machined from the pipe segments to dimensions in accordance with ISO 148-1:2016, where the notch geometry was the v-notch [130]. The dimensions of the specimens were 55 mm x 10 mm x 10 mm. The specimens were taken from each of the pipe segments in the location shown on Figure 4.1. It is important to note that no weld line was present on the BM material. The v-notch was machined along the normal direction (ND), as displayed on Figure 4.2. It was ensured that the weld line on the AW and HT specimens was located within the radius of the v-notch. A total of 34, 13 and 30 Charpy specimens were taken from the BM, AW, and HT pipe segments respectively.

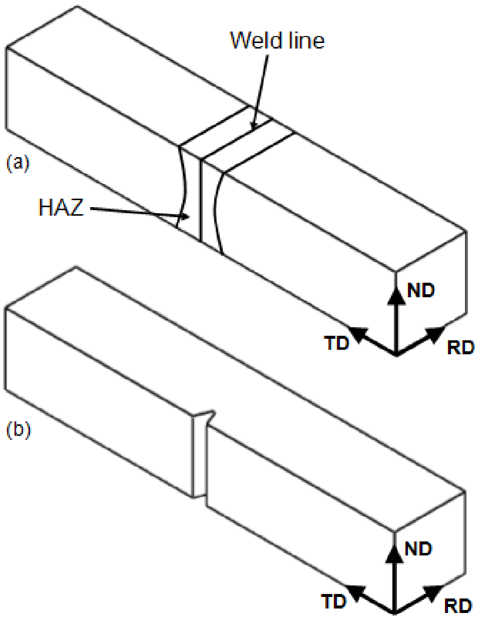

Figure 4.2. Weld line and v-notch orientation.

4.2.2 Charpy impact testing method

Charpy impact testing was conducted in accordance with ISO 148-1:2016 [130]. A Zwick pendulum Charpy impact test machine with instrumented head was used to perform the testing over a variety of temperatures. The test temperatures ranged from ambient to -60 °C, where an interval of 20 °C was implemented where possible. A liquid nitrogen chiller unit was used to cool the test specimens to the desired temperatures.

Table 4.2. Number of repeats.

	BM	AW	HT
Ambient	6	4	6
0 °C	5	-	6
-20 °C	7	5	6
-40 °C	7	-	6
-60 °C	6	4	5

The number of repeats at each temperature is displayed on Table 4.2. Two repeats performed at 0 °C and a single repeat at -60 °C for the BM specimens were disregarded. The repeats at 0 °C were omitted because the specimens were not machined to within tolerance. The specimen tested at -60 °C was disregarded since it was dropped during transportation from the chiller unit to the Charpy impact test machine and may have been tested at an incorrect temperature. The AW specimens were only tested at ambient, -20 °C and -60 °C due to the limited number of specimens available. A single HT repeat at -60 °C was disregarded since it displayed a Charpy impact energy considerably larger than any other test specimens tested at the same temperature, and therefore may have been incorrectly tested.

4.2.3 Instrumented head data analysis

During Charpy impact testing, the instrumented head recorded force and work done data with respect to time. This allowed for a more accurate analysis of the toughness of the material since traditional Charpy impact testing only measures the absorbed energy associated with the whole fracture. When analysing the total absorbed energy alone, many important characteristics can be overlooked which can lead to a false assessment of the material [122–124]. Charpy impact testing with an instrumented head directly provided information such as the maximum force, yield point and the absorbed energy up until identifiable fracture events [131,132] Therefore, it has been made possible for the full fracture process to be divided into different parts. Dependent on the nature of the fracture, these could include the stable propagation phase, crack instability propagation phase and crack arrest [133].

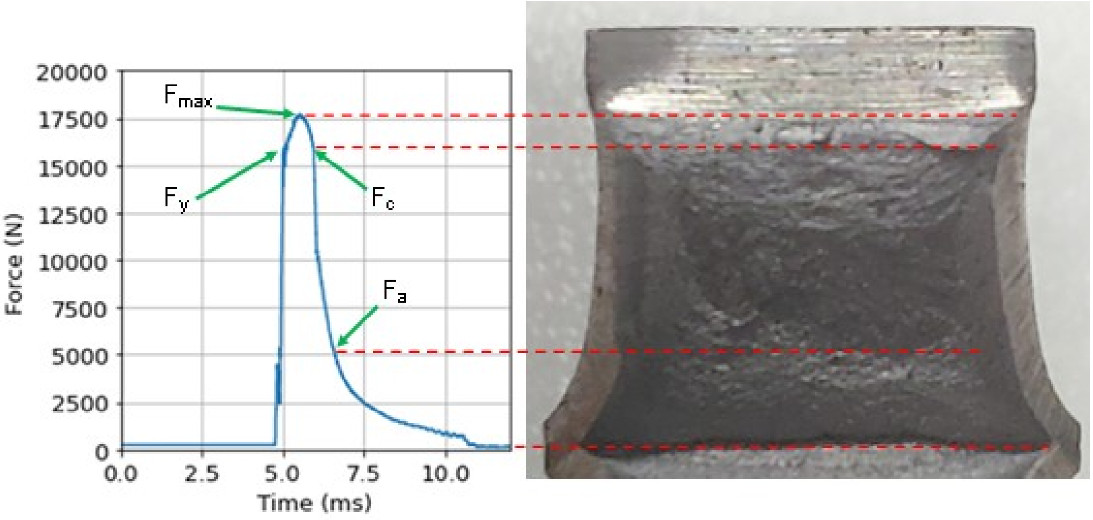

Figure 4.3 Correlation between force-time plot and fracture surface.

A force-time plot of a Charpy specimen which experienced a mixture of ductile and brittle fracture is displayed on Figure 4.3, where the different fracture events have been labelled. From the shape of the curve, the nature of the fracture and the different fracture events could be determined. At point F_y, general yielding of the material started which was then followed by crack initiation at point F_{max}. From F_{max} to F_c, the fracture went through the stable crack propagation phase, which was ductile. However, if this was a fully brittle fracture then this phase would not exist and there would be an abrupt drop in force from F_{max}. In this scenario F_{max} and F_c would be the same. At point F_c cleavage fracture initiation occurred, and as previously discussed this event is followed by an abrupt drop in force. From point F_c to F_a, the fracture went through the crack instability phase. If the fracture was completely ductile then this phase would not exist and the decrease in force would not be sharp. Crack arrest then came about at point F_a where the rest of the following fracture was ductile. Since the instrumented head also recorded the work done with respect to time, the absorbed energy at each of the events could be identified.

Relationships between force-time plots and the fracture surface have also been established [134]. These relationships are displayed on Figure 4.3 where it can clearly be seen how the fracture events on force-time plot align with the corresponding fracture surface.

The area under the curve gives either the total absorbed energy or the impulse depending on whether it is a force-displacement or a force-time plot respectively. Since the instrumented head generated force-time curves, the area under the curves gave the impulse, which is defined as the change in momentum [135]. Although the area under a force-time curve gives the impulse, it can be directly related to the total absorbed energy. The absorbed energy is the same as work done. This is because work done is defined as the amount of energy transferred from one object to another, and the Charpy impact test measures the amount of energy transferred from the hammer to the test specimen. The definitions of impulse and work done are given by equations (4.1) and (4.2).

$$\Delta p = F\Delta t \tag{4.1}$$

$$W = Fd \tag{4.2}$$

Where Δp is the impulse, F is force, Δt is the change in time, W is work done, and d is distance [136]. By rearranging equation (4.2) to make F the subject, and then substituting into equation (4.1) gave equation (4.3), where the relationship between impulse and work done can be defined.

$$\Delta p = \frac{W\Delta t}{d} \tag{4.3}$$

Equation (4.3) displays that work done increases proportionally as the impulse increases.

4.3 Fracture analysis

Due to the high number of Charpy specimens, only specifically selected specimens were chosen for fracture analysis under SEM. If specimens displayed low toughness, they were analysed to determine what may have caused the poor toughness. Specimens which produced greater toughness were also analysed. This was done to try to distinguish the differences between the fracture surfaces of the specimens. The methods used for the analysis are discussed in section 4.4.3. The brittle fracture percentage of all the Charpy specimens was also calculated. They were estimated by measuring the width and height of the cleavage fracture area as well as using a fracture appearance chart in accordance with ISO 14556:2015 [137].

4.4 Metallography

4.4.1 Sample preparation

Samples were hot mounted in conductive resin using a hot mounting press and were mounted in the ND-TD plane. Once mounted, the samples were consecutively ground with 120, 400, 600 and 1200 grit silicon carbide grinding papers, followed by polishing using 6 µm, 3 µm and 1 µm diamond suspension polycrystalline polish with the relevant polishing cloths. Samples used for Optical Microscope (OM) and Scanning Electron Microscope (SEM) imaging were then etched with 3 % nital etching solution. The etched samples were also used to take microhardness measurements from. Samples prepared for Electron Backscatter Diffraction (EBSD) were polished with colloidal silica (50 nm).

4.4.2 Optical microscope

OM images were taken using a Zeiss Primostar upright compound microscope, where etched samples of the AW and HT welds were imaged.

4.4.3 Scanning electron microscope

A Zeiss Evo SEM was used to conduct a variety of analysis techniques, which included ordinary imaging, energy dispersive spectroscopy (EDS) and EBSD. EDS and EBSD analysis were able to be conducted since the SEM contained an EDS system and was also fitted with an Oxford Instruments EBSD detector. Ordinary imaging was used for the analysis of etched samples and the Charpy impact specimen fracture surfaces. The etched samples that were analysed included the AW and HT welds. The Charpy specimen fracture surfaces were cleaned from any debris using an air duster before being inserted into the SEM. EDS analysis was used during fracture surface analysis to identify the chemical composition of any inclusions or defects found on the fracture surfaces. The crystallographic texture of the BM, AW and HT samples was studied using EBSD.

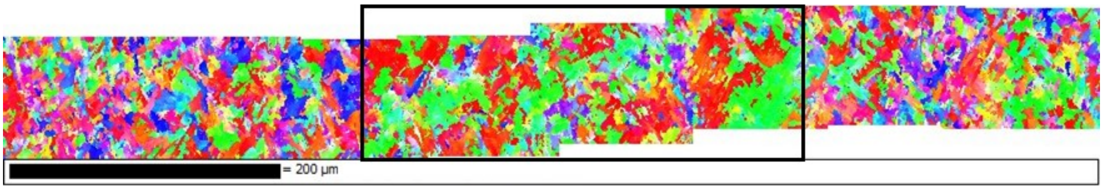

Figure 4.4. Cross-weld scan of AW weld line near inner pipe surface, with weld line highlighted at the centre of the scan.

For the AW and HT samples, large cross-weld maps were generated to ensure the weld line was captured. An Inverse Pole Figure (IPF) map of a cross-weld scan is displayed on Figure 4.4. The IPF colouring on the map was then used to locate the weld line, which is highlighted by the black box. On the IPF map it can be seen that the colouring and grain size of the weld line was distinctly different to that of the HAZ.

The EBSD maps were processed using Oxford Instruments – HKL Channel 5 software, where IPF and texture component maps were produced. The data was analysed with respect to the RD-ND plane since it was parallel to the weld plane. The texture component maps displayed grains which had a specified crystal plane aligned within 10° to the RD-ND plane. The EBSD data was also used to determine the distribution of grain boundary angles.

4.5 Grain size analysis

Average grain size measurements were calculated using images produced using either OM or SEM imaging. The intercept method was used to estimate the average grain size in accordance with ASTM-E112-13 [138]. ImageJ software was used to calculate the average grain size measurements.

4.6 Microhardness measurements

Microhardness measurements were taken using an Innovatest Vickers hardness test machine. The measurements were taken in the ND-TD plane of etched samples which were prepared as explained in section 4.4.1. A load of 300 gf, dwell time of 10 seconds and an indent spacing of 0.2 mm was used unless stated otherwise. The indent spacing was chosen in accordance with ISO 6507-1:2018 to ensure it was kept small for good resolution without distorting the results [139].

4.7 Computational modelling

4.7.1 Purpose of computational modelling

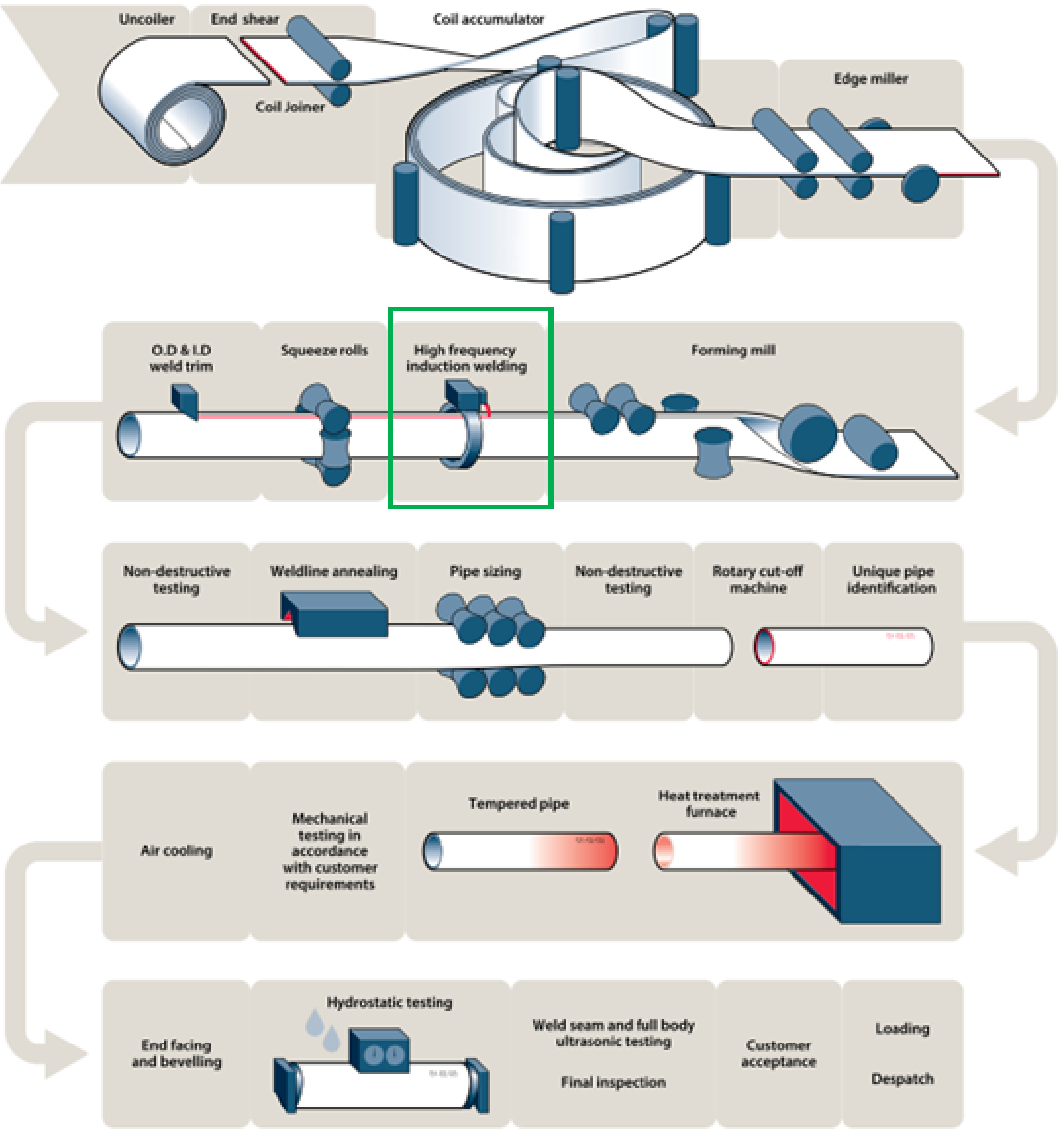

Figure 4.5. HFI welded pipe manufacturing process [140].

A computational model was built to simulate the induction heating stage of the HFI welded pipe manufacturing process. This stage has been highlighted by the green box on Figure 4.5. The model was used to compute the thermal cycles and temperature distributions at the faying strip edges during welding, for the purpose of assisting with the microstructural analysis. Studies to explore a method to produce a more uniform temperature distribution through the depth of the strip edges during welding were also conducted using the computational model.

4.7.2 Description of the computational model

COMSOL Multiphysics software was used to create and run the simulation. Also, SolidWorks CAD software was used to generate some of the more complicated geometries, which were then imported into the COMSOL software.

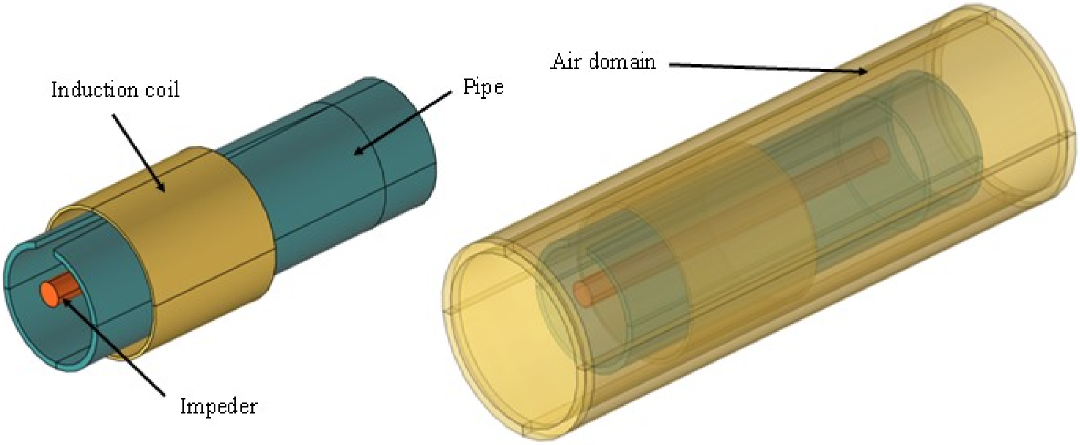

Figure 4.6. Model components. Induction coil, pipe, and impeder (left), and air domain (right).

The model comprised of a coupled electromagnetic field and temperature field solution, where the fields were distributed in time as well as in space. It consisted of four main components: the pipe, induction coil, impeder, and air domain. The set-up of these components is displayed on Figure 4.6, where the pipe, induction coil and impeder were located centrally within the air domain. The components and assembly were created in 3D due to the complex way the high frequency current flowed around the pipe. The induction coil was built as a tube around the pipe, since the COMSOL software was able to convert it into a coil when the computational analysis was run.

The heating of the strip edges in the model worked in the same way as the real HFI welded pipe manufacturing process. The induction coil in the model generated a high frequency electromagnetic field, which was then able to interact with the pipe and impeder via the air domain. The air domain included an outer layer called an infinite element domain which stretched the magnetic fields to improve the accuracy of the model. The high frequency electromagnetic field then induced a high frequency current on the pipe, where the current concentrated at the strip edges due to skin and proximity effects. The high current densities at the strip edges then heated the strip edges to welding temperature. A translational motion was added into the heat transfer node of the model to simulate the movement of the pipe.

4.7.3 Governing equations

When using COMSOL Multiphysics software, the mathematical model used to simulate the HFI welded pipe process was a coupled electromagnetic field and transient temperature field solution. Therefore, the governing equations used in the model were as follows. The electromagnetic field was given by the governing equations (4.4) – (4.7).

$$\nabla \times \vec{H} = \vec{J} \tag{4.4}$$

$$\vec{B} = \nabla \times \vec{A} \tag{4.5}$$

$$\vec{J} = \sigma \vec{E} + j\omega \vec{D} + \overrightarrow{J_e} \tag{4.6}$$

$$\vec{E} = -j\omega \vec{A} \tag{4.7}$$

Where $\vec{H}$ was the magnetic field intensity, $\vec{J}$ was the current density, $\vec{B}$ was the magnetic flux density, $\vec{A}$ was the magnetic vector potential, σ was the electrical conductivity, $\vec{E}$ was the electric field intensity, $\vec{D}$ was the electric flux density and $\overrightarrow{J_e}$ was the externally generated current density. The temperature field was given by the governing equations (4.8) and (4.9).

$$\rho C_p \frac{\partial T}{\partial t} + \rho C_p u \cdot \nabla T + \nabla \cdot q = Q + Q_{ted} \tag{4.8}$$

$$q = -k \nabla \mathrm{T} \tag{4.9}$$

Where ρ was density, C_p was specific heat capacity, T was temperature, u was the velocity field, q was conductive heat flux, k was thermal conductivity, Q was heat source density and Q_{ted} was thermoelastic damping. The component $\rho C_p u \cdot \nabla T$, provided movement by translation in the model.

4.7.4 Temperature dependant thermo-physical properties of steel

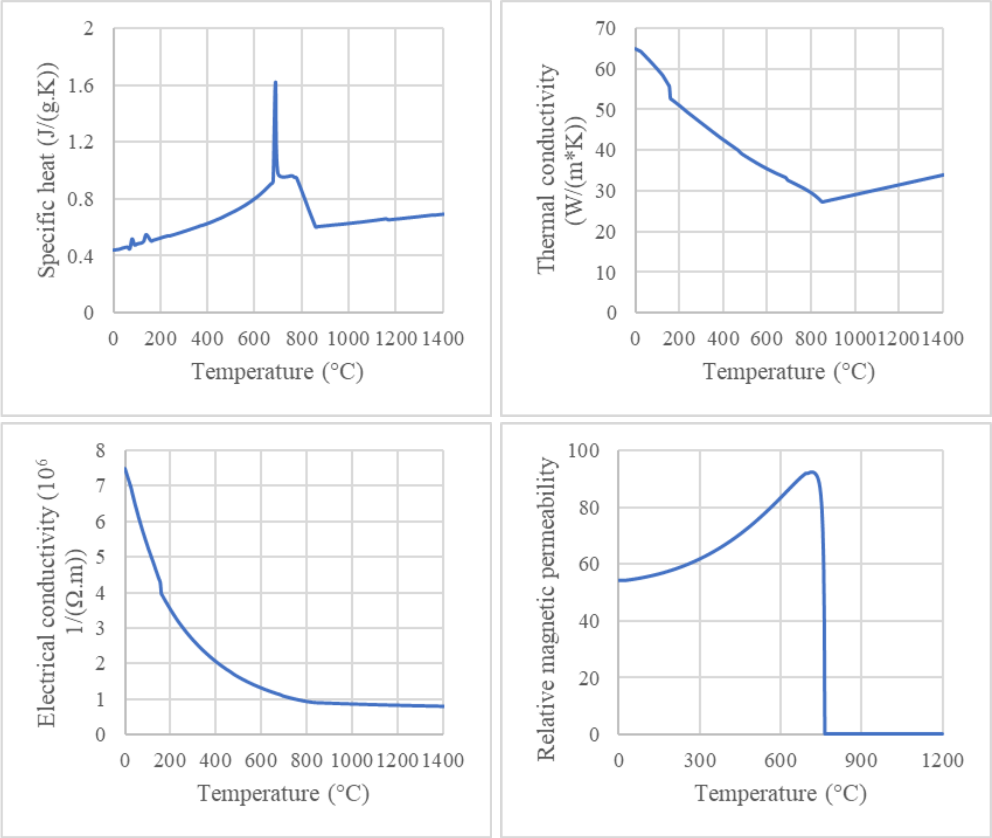

Figure 4.7. Temperature dependant thermo-physical properties of steel.

Steel has properties which change non-linearly as a function of temperature [141]. Thermal conductivity, specific heat capacity, electrical conductivity and magnetic permeability were properties that needed to be defined as a function of temperature in order to build the most accurate model possible. Since they changed non-linearly with temperature, and there were no function equations to accurately express them, tables defining these properties were built into the model. JMatPro simulation software was used to predict the necessary properties with respect to temperature, where the chemistry of an X60 pipeline steel was entered into the software. The chemistry used for the calculation was the AW composition in Table 4.1. Figure 4.7 displays plots showing a graphical representation of the temperature dependant property tables. These tables could be altered to model different steel grades or chemistries. However, there were limitations to these properties. This was because specific heat was not properly characterised past 1400 °C. Consequently, temperatures above approximately 1500 °C in the model results were most likely lower than observed.

4.7.5 Model geometry

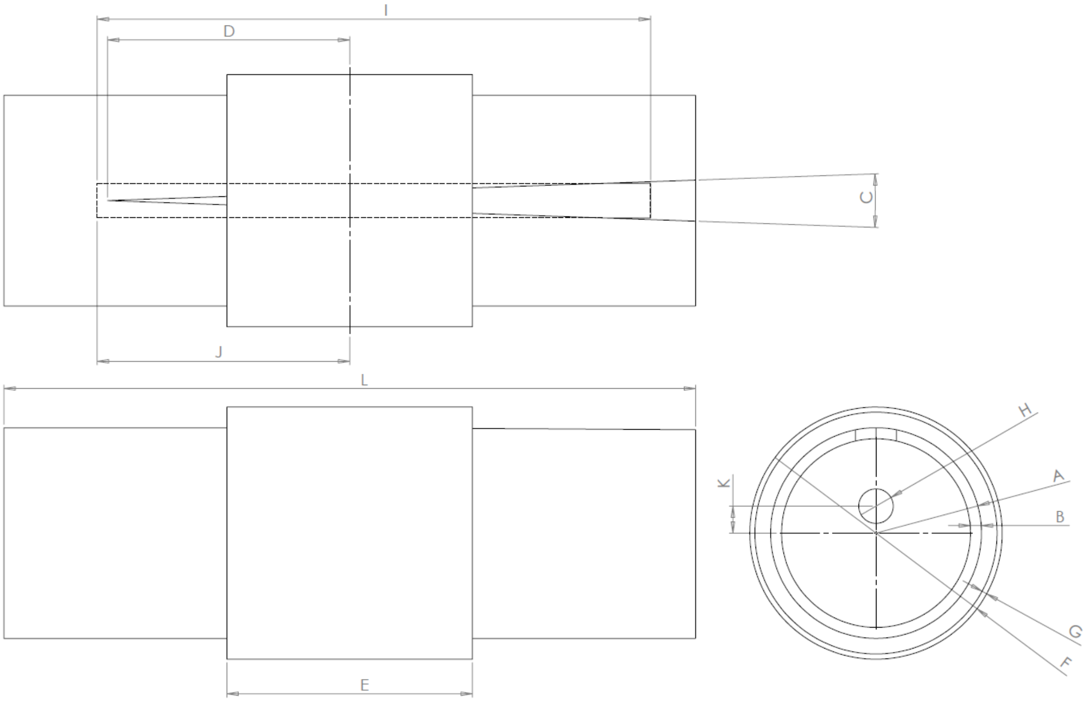

Figure 4.8. Model geometry.

Figure 4.8 shows a diagram of the model geometry, where the dimensions have been labelled. A description and unit for each of the dimensions can be seen in Table 4.3. All the labelled dimensions could be changed within the model, allowing for a variety of different component geometries and setup configurations to be modelled.

Table 4.3. Descriptions of model geometry dimensions.

Label	Description	Unit
A	Pipe outside radius	mm
B	Pipe thickness	mm
C	Vee angle	°
D	Vee length	mm
E	Coil length	mm
F	Coil outside diameter	mm
G	Coil thickness	mm
H	Impeder diameter	mm
I	Impeder length	mm
J	Impeder ahead of coil centre distance	mm
K	Impeder offset	mm
L	Pipe length	mm

4.7.6 Motion of the pipe

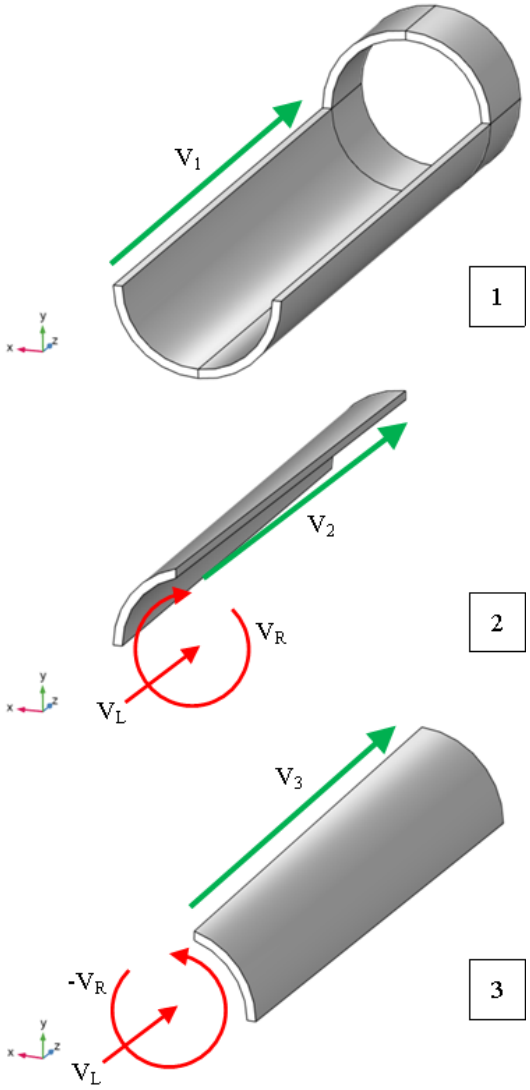

Figure 4.9. Motion of domains of pipe.

For the heat to be able to travel along the length of the pipe a translational motion was built into the heat transfer node of the model. To achieve this the pipe was split into three domains. These domains can be seen on Figure 4.9 and are labelled 1, 2 and 3. Domain 1 consisted of the bottom half of the pipe, up until the vee convergence point, and then all of the pipe from the vee convergence point onwards. Domains 2 and 3 were the upper left and upper right of the pipe before the vee convergence point respectively. Three translational motion sub nodes within the heat transfer node were then created, one for each domain. The translational motion sub nodes provided movement by translation, where the temperature was moved through each of the domains at a specified velocity. When these sub nodes were created, the component

$\rho C_p u \cdot \nabla T$ was added into equation (4.8), where u was the velocity field with the SI unit m/s. The velocity field was then defined in each of the sub nodes to give each of the domains the correct motion.

The velocity field for domain 1 was very simple to define. This was because it only had motion in the z-direction, where the z-direction was parallel to the mill direction. Therefore, it was defined with a linear velocity in the z-direction that was equal to the mill speed. This velocity is represented by the green arrow labelled V_1 on Figure 4.9. The motion for domains 2 and 3 was more complex. This was because the translational motion had to travel in the mill direction but also along the faying strip edges. To accomplish this, the velocity field included a linear velocity coupled with a rotational velocity. For both of the domains, the linear velocity was in the z-direction and was equal to the mill speed. The rotational velocity rotated around the z-axis for domains 2 and 3. They both had the same magnitude but rotated in opposite directions, where domain 2 rotated clockwise and domain 3 rotated anti-clockwise. The components for the coupled velocities are illustrated by the red arrows labelled V_L and V_R/-V_R on Figure 4.9, which are the linear velocity and rotational velocities respectively. The coupled rotational and linear velocities then produced the appropriate velocity fields to describe the translational motions of domains 2 and 3. These velocity fields are labelled V_2 and V_3 on Figure 4.9. When inputting the rotational velocity for domains 2 and 3, it was of high importance that they were correctly coupled with the velocity in the z-direction and the vee angle. If the rotational velocities did not precisely match the vee angle and the z-direction velocity, then the translational movement would be incorrect, and the model would yield inaccurate results.

4.7.7 Mesh sensitivity study

A mesh sensitivity study was carried out to find optimum the mesh to be used for the computational analysis. This was because the accuracy of the results and the computing time for the analysis were determined by the mesh element size. Models with very fine mesh element sizes can produce highly accurate results but will have long computing times, whereas models with large mesh element sizes will have short computing times but yield less accurate results [142]. The aim of the mesh sensitivity study was to find a mesh where the results started to become mesh independent. This occurs when on further increasing the number of mesh elements the results of the model do not change. Therefore, the point at which the results become mesh independent, the most accurate results with the shortest computing time can be achieved. Table 4.4 displays the model dimensions and inputs for the mesh sensitivity study.

Table 4.4. Geometries and inputs for mesh sensitivity study.

Description	Value	Unit
Pipe outside diameter	300	mm
Pipe length	850	mm
Pipe thickness	16	mm
Vee angle	4	°
Coil length	300	mm
Coil outside diameter	325	mm
Coil thickness	7.5	mm
Vee length	300	mm
Impeder length	620	mm
Impeder diameter	75	mm
Impeder ahead of coil centre distance	310	mm
Impeder offset	75	mm
Frequency	170	kHz
Current	2750	A
Velocity	0.254	m/s

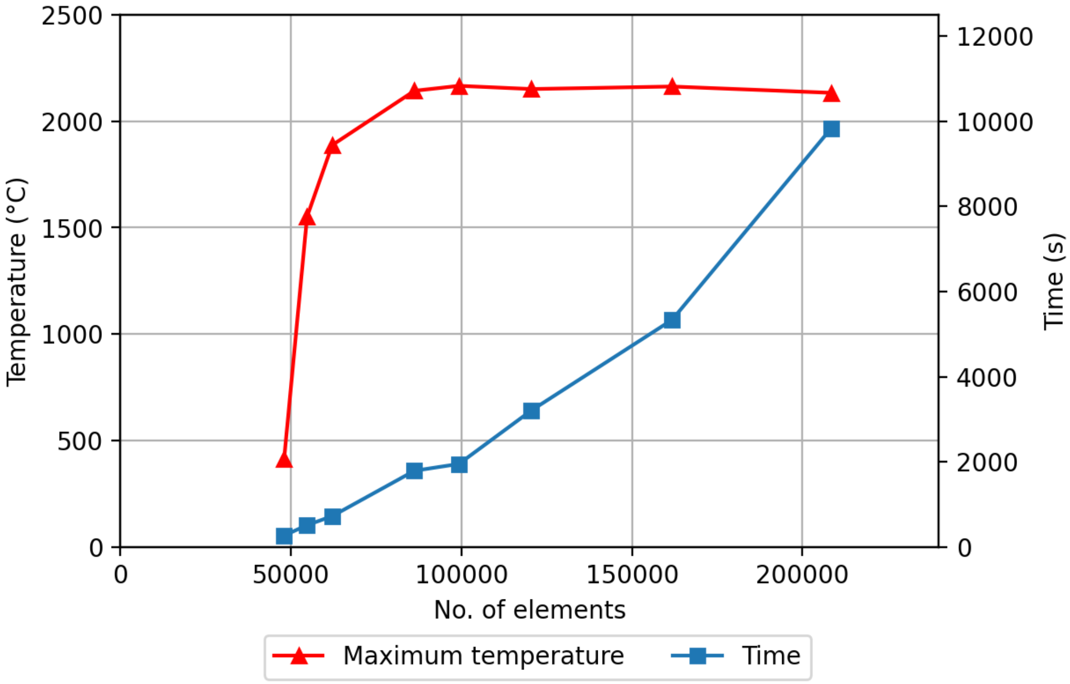

Figure 4.10. Mesh sensitivity study results.

The mesh sensitivity study was carried out by initially applying a coarse mesh to the model, running the simulation, and then recording the maximum temperature and the computational time. This was repeated, where each time the simulation was run using a finer mesh. As the mesh was made finer, the mesh size at the strip edges was decreased the most when compared to the rest of the model. This was because the temperature at the strip edges was the main area of interest when exploring the welding thermal cycles and heat distributions at the strip edges.

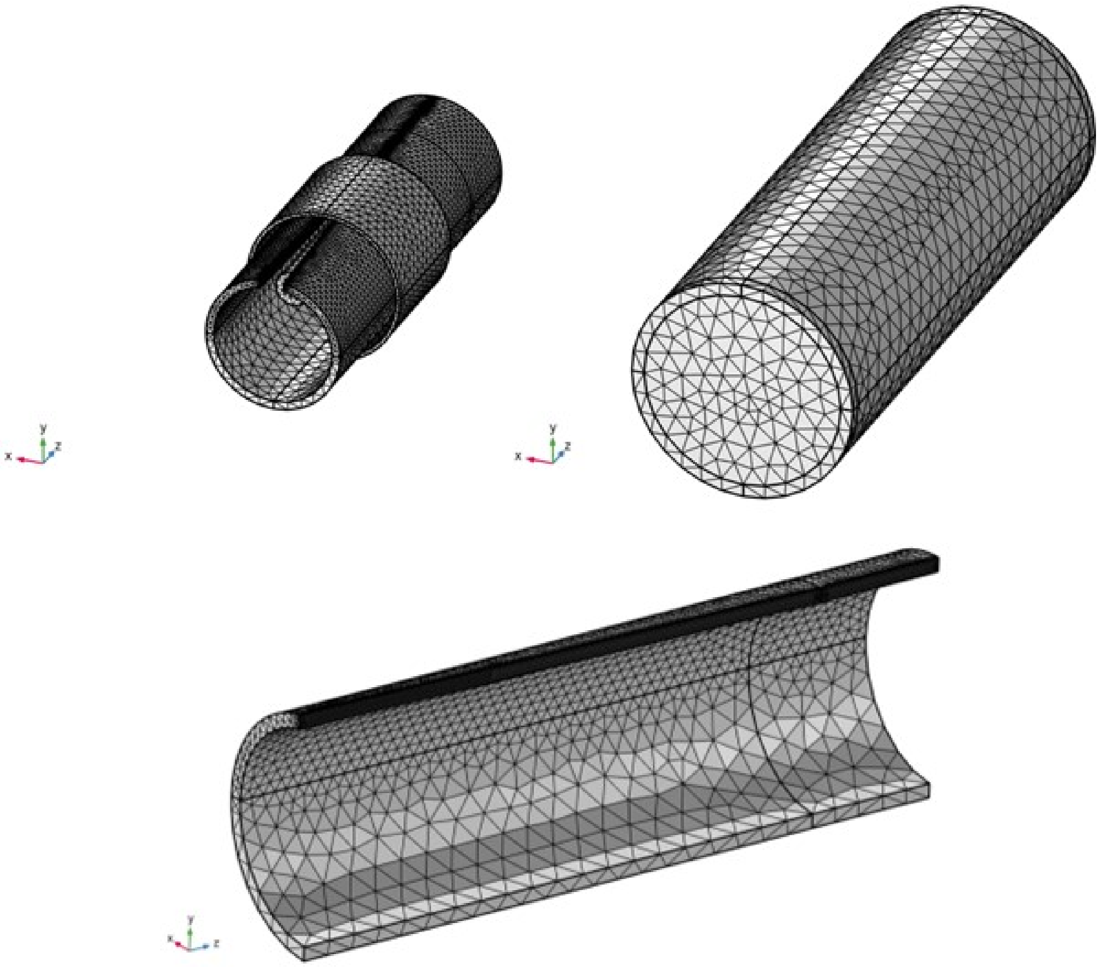

Figure 4.11. Final mesh. Pipe, impeder, and coil (top left), air domain (top right), and cross-section of pipe (bottom).

The maximum temperatures and computational times were plotted as a function of the number of mesh elements, where the results are displayed on Figure 4.10. The first simulation was run using the default normal mesh size that was built into the COMSOL Multiphysics software. This mesh produced a computational time and maximum temperature of 271 s and 414 °C respectively. As the mesh was initially made finer, both the maximum temperature and the computational time increased. As the number of mesh elements approached 100,000 the maximum temperature had almost fully converged. When increasing the number of elements above 100,000 the maximum temperature stayed greatly consistent, demonstrating that the model had become mesh independent. However, the computational time kept increasing when increasing the number of mesh elements passed 100,000. When comparing the mesh with 99,000 elements to the mesh with 208,000, there was approximately a 1 % difference between the maximum temperatures. However, the computational time for the finer mesh was five times greater. Since there were extremely small accuracy benefits when using a mesh with a number of elements greater than 100,000, the mesh with 99,000 elements was chosen to be developed to produce a final mesh for the model.

The final mesh is displayed on Figure 4.11. The mesh was finest at the strip edges since this was the main area of interest. As the distance from the strip edges increased, so did the mesh size, where the mesh size was coarsest at the air domain. It was also ensured that the mesh was fine at the weld following the vee convergence point. When modelling other pipe geometries, the mesh element size was made finer at the strip edges when the pipe wall thickness was reduced below 16 mm. For pipe wall thicknesses above 16 mm the mesh size was kept the same as the final mesh.

4.7.8 Extracting thermal cycles from computational model

Table 4.5. Geometries and inputs for heating and cooling rate simulation.

Description	Value	Unit
Pipe outside diameter	300	mm
Pipe length	2500	mm
Pipe thickness	16	mm
Vee angle	4	°
Coil length	300	mm
Coil outside diameter	325	mm
Coil thickness	7.5	mm
Vee length	300	mm
Impeder length	620	mm
Impeder diameter	70	mm
Impeder ahead of coil centre distance	310	mm
Impeder offset	75	mm
Frequency	170	kHz
Current	2750	A
Velocity	0.254	m/s

The computational model was used to determine thermal cycles at given locations across the weld to assist with understanding and explaining why the microstructures formed at those locations. Since the model did not include the induction annealing and quenching stage, it could only be used to assist with the analysis of the AW weld. The model used geometries and inputs that matched that of the production of the AW pipe and are displayed in Table 4.5. It was important to acknowledge that the model did not simulate the squeeze out of the molten material, which occurred when the weld rolls squeezed the molten strip edges together to create a forged weld. This was not included in the model due to the increased complexity that would have been added.

In order to be able to gather the appropriate cooling data, the length of the pipe was extended to 2500 mm. This allowed the weld to cool to a temperature below 500 °C. This was of importance because when studying the HAZ it has become standard practice to report on the time taken for the material to cool through the critical temperature range from 800 °C to 500 °C [143].

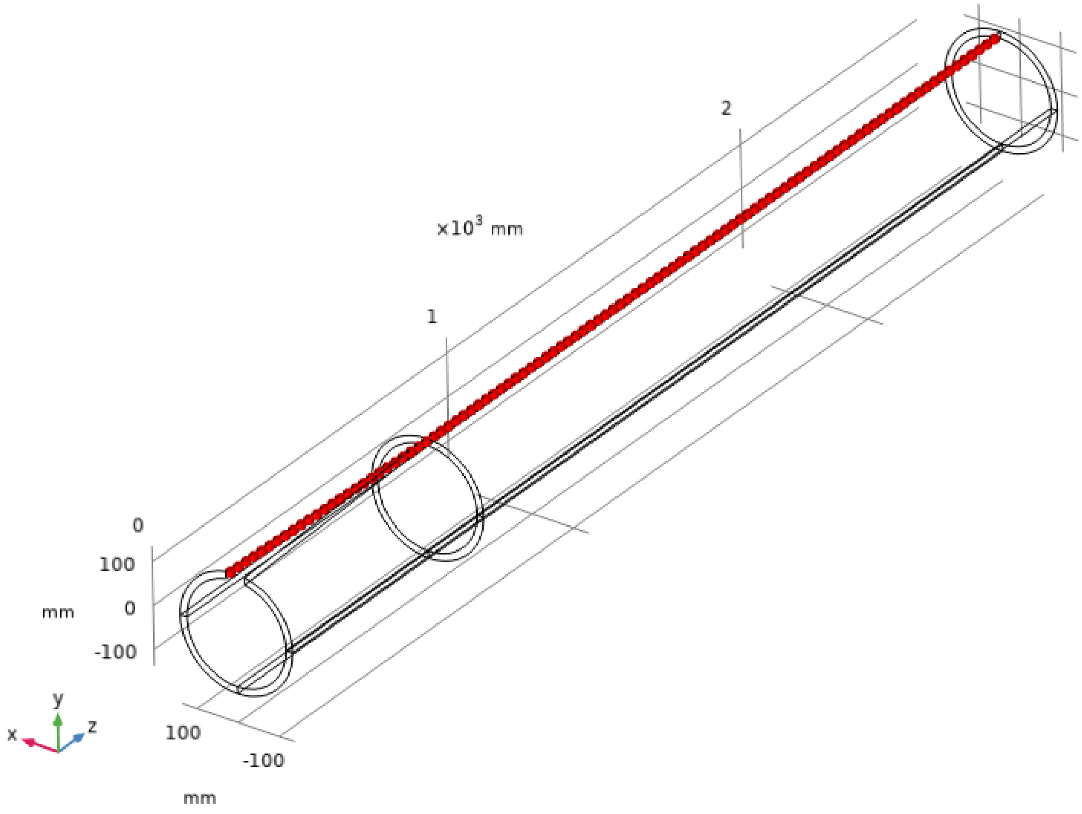

Figure 4.12. Position of nodes along pipe.

To obtain a thermal cycle at a given location in the weld, nodes were added along the length of the pipe where they were placed in relation to the chosen location on the weld. Figure 4.12 displays an example where the nodes were placed along the centre of the face of the strip edge across the whole length of the pipe.

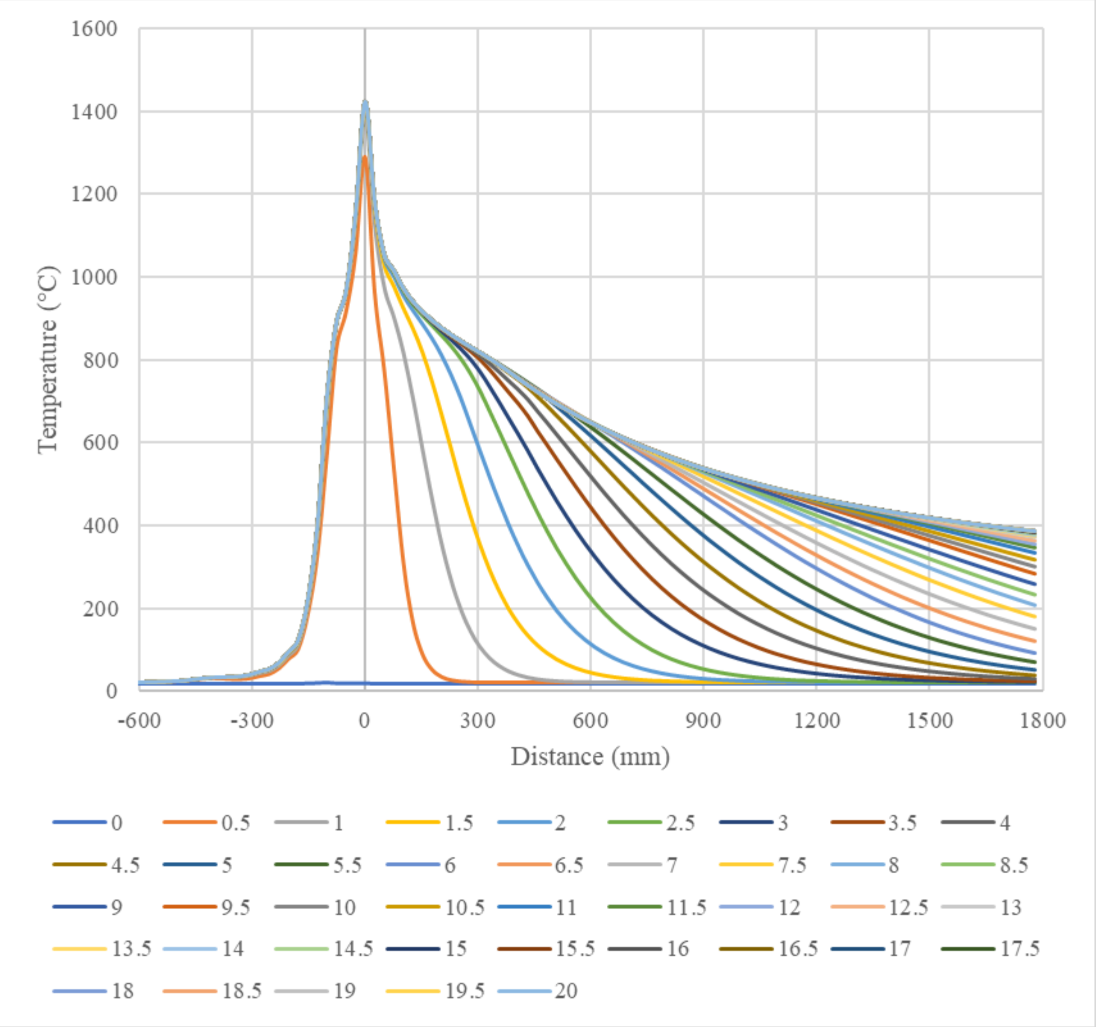

Figure 4.13. Temperature profile along length of pipe at specified times.

The simulation was run to calculate solutions up until 20 s. This was done to ensure that the temperature profile had become stable across the whole length of the pipe. Figure 4.13 shows the temperature as a function of distance along the length of the pipe from 0 to 20 s at 0.5 s intervals. For the simulation the nodes were located at the centre of the strip edge. The vee convergence point was located at 0 mm on the plot. At a time of approximately 16 s the temperature across the length of the pipe had become stable since the temperature profiles for times of 16 s and greater overlapped each other. Therefore, when calculating the heating and cooling rates associated with welding, they were taken at a time greater than 16 s because this was when the simulation had reached steady state.

Since the velocity of the pipe was constant, the heating and cooling rates could be calculated from the temperatures recorded at each of the nodes. In the z direction, the nodes were placed at intervals of 0.0254 m. Since the pipe travelled in the z direction at 0.254 m/s the time it took for the pipe to travel from one node to the next could be calculated using equation (4.10).

$$v = \frac{d}{t} \tag{4.10}$$

Where v is velocity, d is distance and t is time. Rearranging the equation to make time the subject and substituting in the known distance and velocity gave the following result.

$$\frac{0.0254\ m}{0.254\ m/s} = 0.1\ s$$

Therefore, the time for the pipe to travel from one node to the next was calculated to be 0.1 s. This value would have to be recalculated if a different mill speed was used or if the distance between the nodes was changed.

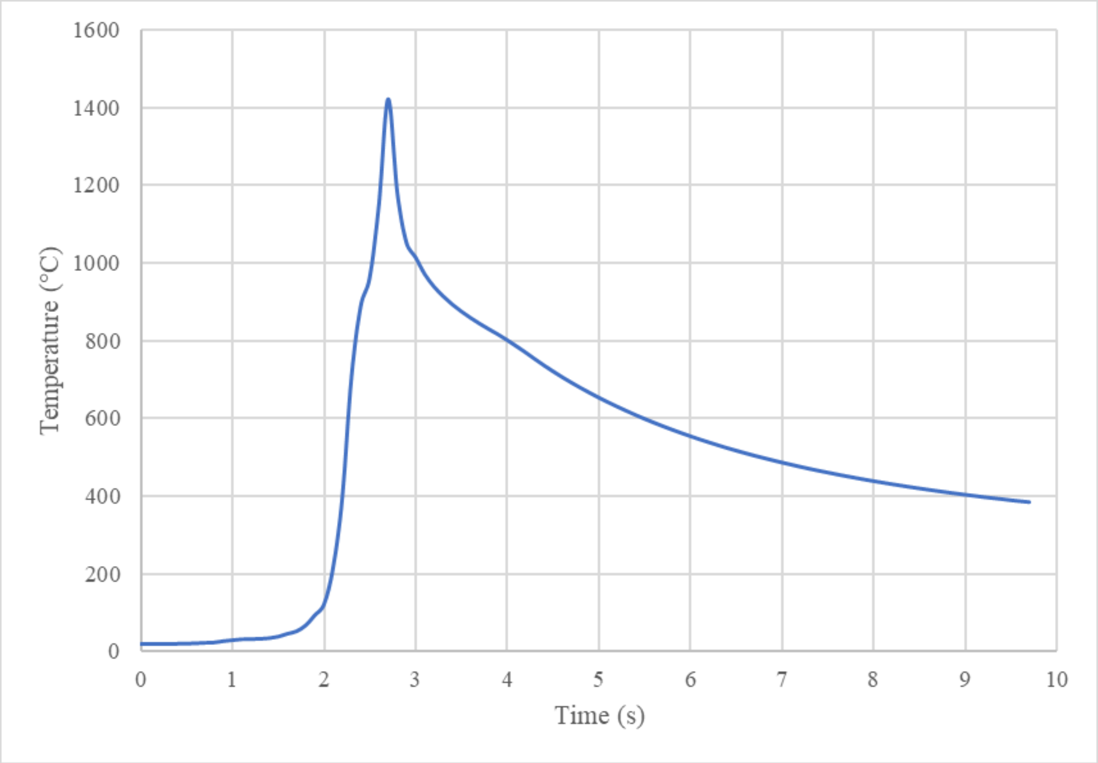

Figure 4.14. Heating and cooling thermal profile at centre of strip edge.

The temperature as a function of time could then be plotted as shown on Figure 4.14. Heating and cooling rates could be determined by calculating the gradient at the curve.

4.7.9 Effect of frequency on temperature distribution

A study was carried out to understand how frequency affected the temperature distribution through the strip edges of a thick walled HFI welded pipe, where the strip thickness was 16 mm. The frequencies in the study ranged from 25 kHz to 250 kHz, at an interval of 25 kHz. For each of the frequencies, the input current was adjusted to ensure a temperature of 1500 ± 10 °C was reached at the strip centre at the vee convergence point. The fixed inputs and geometries for study can be seen in Table 4.6.

Table 4.6. Fixed geometries and inputs for frequency study.

Description	Value	Unit
Pipe diameter	300	mm
Pipe length	800	mm
Strip thickness	16	mm
Vee angle	4	°
Coil length	300	mm
Coil outside diameter	325	mm
Coil thickness	7.5	mm
Vee length	300	mm
Impeder length	620	mm
Impeder diameter	70	mm
Impeder ahead of coil centre distance	310	mm
Impeder offset	75	Mm
Velocity	0.254	m/s

4.7.10 Effect of strip thickness on temperature distribution

A study was carried out to help understand how the thickness of the steel strip affected the heat distribution through the strip edges, where a fixed frequency of 170 kHz was used. This was because it was a frequency that would be typically used when producing a 16 mm thick HFI welded pipe. The strip thicknesses used in the study ranged from 5 mm to 20 mm with an interval of 2.5 mm. Other than the strip thickness, the only input variable that was changed for each of the thicknesses was the input current. This was to ensure that the centre of the strip face had reached a welding temperature of 1500 ± 10 °C, where the temperature at the centre of the strip face was measured at the vee convergence point. The fixed inputs and geometries for all the analysis can be seen in Table 4.7.

Table 4.7. Fixed model geometries and inputs for thickness study.

Description	Value	Unit
Pipe diameter	300	mm
Pipe length	800	mm
Vee angle	4	°
Coil length	300	mm
Coil outside diameter	325	mm
Coil thickness	7.5	mm
Vee length	300	mm
Impeder length	620	mm
Impeder diameter	70	mm
Impeder ahead of coil centre distance	310	mm
Impeder offset	75	mm
Frequency	170	kHz
Velocity	0.254	m/s

4.7.11 Effect of edge geometry on temperature distribution

The computational model was used to investigate whether altering the strip edge geometry could create a more uniform temperature distribution at the faying strip edges when producing a HFI welded pipe manufactured using 16 mm thick steel strip.

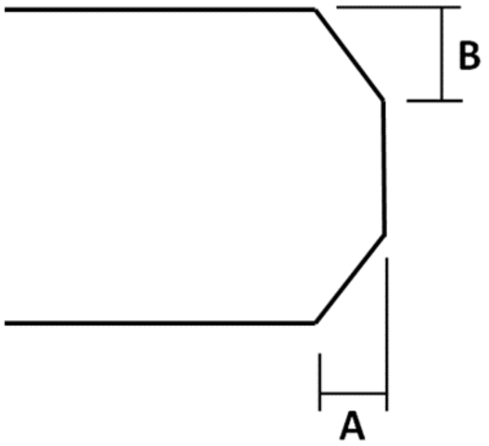

Figure 4.15. Critical dimensions of edge geometry study.

The edge geometry was altered by adding a chamfer to each of the strip corners. This was done to keep the geometry of the strip edges simple to ensure that the strip edges could be milled into the desired shape during the HFI welded pipe manufacturing process, where it would be most likely to be milled during the edge milling stage. This is the stage where the strip edges are prepared for welding. For the study, dimensions A and B on Figure 4.15, were changed. For the initial study, 1 mm and 2 mm were the chosen dimensions for A, and 4 mm, 6mm and 8 mm were the chosen dimensions for B. These dimensions were chosen by measuring the width of the HAZ at given depths through the thickness of the weld and then predicting what dimensions may help produce a more even temperature profile. The geometry which provided the most uniform temperature distribution was then chosen for further development, where a number of new geometries were subsequently simulated. The fixed geometries and inputs for the study can be seen in Table 4.8.

Table 4.8. Fixed model geometries and inputs for edge geometry study.

Description	Value	Unit
Pipe outside diameter	300	mm
Pipe length	800	mm
Pipe thickness	16	mm
Vee angle	4	°
Coil length	300	mm
Coil outside diameter	325	mm
Coil thickness	7.5	mm
Vee length	300	mm
Impeder length	620	mm
Impeder diameter	70	mm
Impeder ahead of coil centre distance	310	mm
Impeder offset	75	mm
Velocity	0.254	m/s
Frequency	170	kHz
Current	2750	A

4.8 ThermoCalc Prisma

ThermoCalc Prisma software was used to investigate how the volume fraction of niobium carbide (NbC) precipitates changed during the welding thermal cycles. Thermal cycles from the computational model were inputted into the Thermo-Calc Prisma software to make the predictions. For the simulations, the pre-existing average precipitate size and volume fraction were chosen to be 10 nm and 0.0007 respectively. These were chosen based on literature of HSLA steels produced by hot rolling with similar chemistries [144,145].

5 Results

5.1 Microstructural analysis

5.1.1 As-welded microstructure

Figure 5.1 displays an etched cross-section of the weld from a 16 mm thick X60 HFI welded pipe, where the weld was in the as-welded (AW) condition. This sample was cut from the AW material as described in Section 4.1 of this document, so had therefore not experienced any sort of heat-treatment following welding. At the bottom of the sample, it can be seen that the inside weld bead was present since it had not been trimmed off following welding.

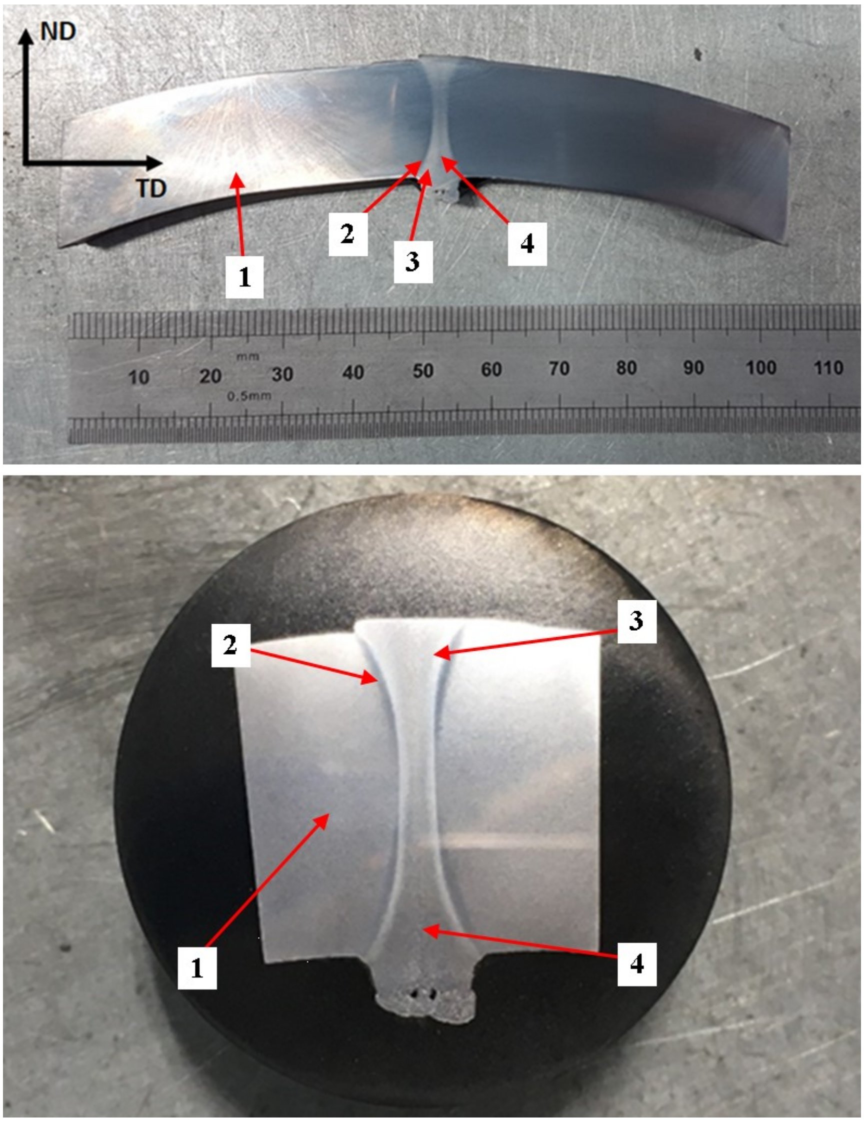

Figure 5.1. Macrostructure of 16 mm thick AW X60 HFI welded pipe weld. (1) Base metal, (2) TMAZ, (3) HAZ and (4) weld line.

The weld could be split into four distinct zones, which were the base metal, Thermomechanically Affected Zone (TMAZ), Heat Affected Zone (HAZ) and weld line. These are labelled 1, 2, 3 and 4 on Figure 5.1 respectively. The profile of the weld had the classical hourglass shape associated with HFI welded pipes. This shape was produced as direct result of the high frequencies used during welding, which caused the current density to be greater at the strip edge corners when compared to the strip edge centres during welding. This led to greater joule heating at the strip edge corners, consequently producing an hourglass shaped weld. The width of the weld at the inner and outer surfaces of the pipe was approximately 6 mm – 7 mm, whereas the width at the mid-thickness was approximately 2 mm – 2.5 mm.

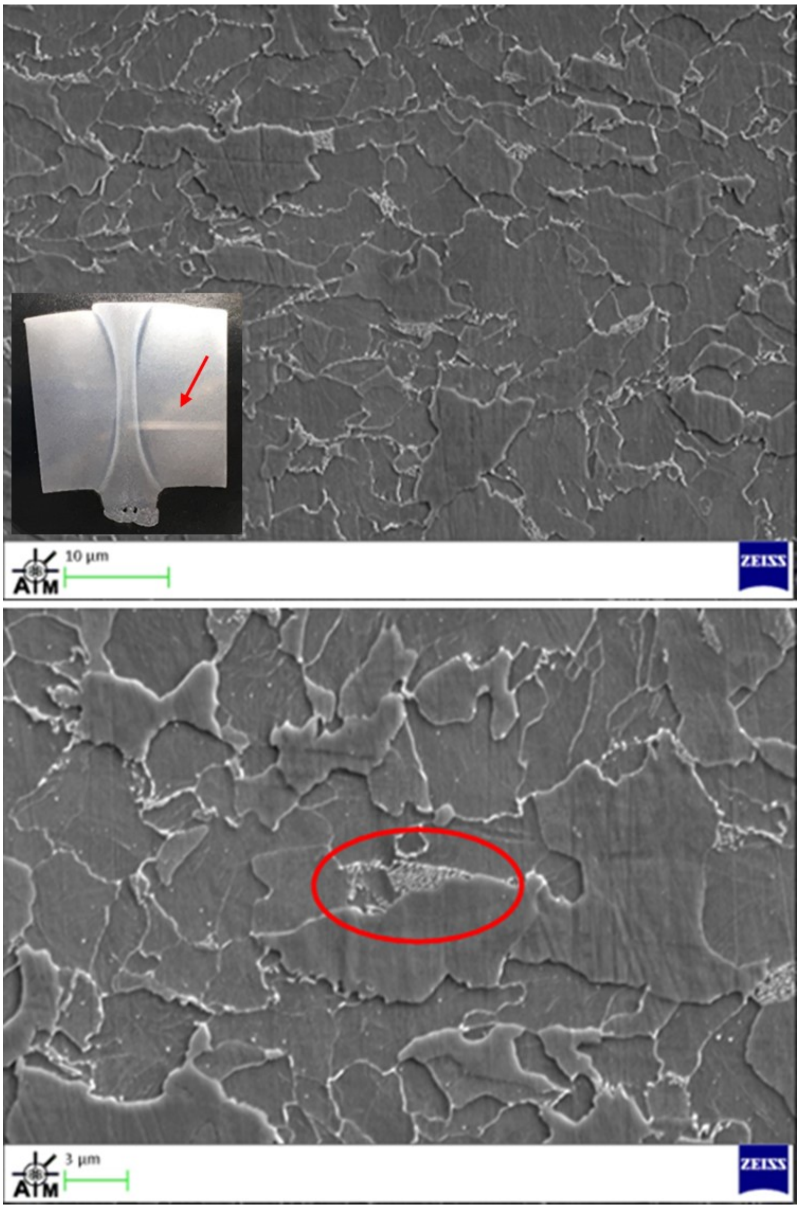

Figure 5.2. SEM images of the base metal.

The base metal was the zone that had not been affected by welding. However, it would have experienced cold forming as the steel strip was progressively formed into a pipe shape by the forming rolls. The microstructure of the base metal consisted of an allotriomorphic ferrite matrix containing a small amount of pearlite. The allotriomorphic ferrite would have been the first phase to form during the hot rolling process to produce the steel strip, where it nucleated at the prior austenite grain boundaries. Following the allotriomorphic ferrite formation, the small amount of remaining austenite was then enriched in carbon and transformed into pearlite [60]. The steel was micro-alloyed with niobium. Therefore, during the hot working niobium carbide (NbC) precipitates formed on the deformation structures of the austenite. Here they were able to offer grain boundary pinning and inhibit the recrystallisation of austenite which helped produce a fine final microstructure [102,104].

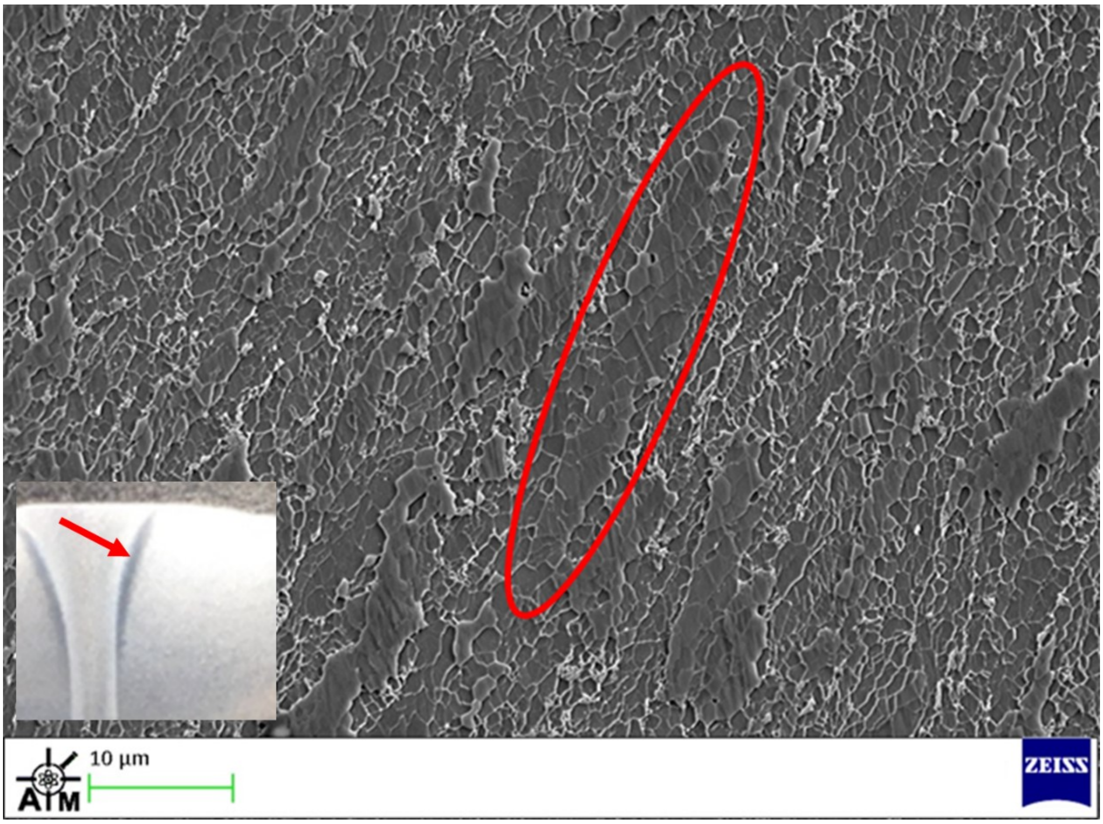

Figure 5.3. SEM image of TMAZ next to HAZ.

This microstructure of the base metal is displayed on Figure 5.2. An example of the pearlite has been highlighted by the red circle, where it can be seen that it had a lamellar structure consisting of cementite and ferrite layers. The average size of the ferrite grains was estimated to be 5.2 ± 0.7 µm. The ferrite grains in the base metal were relatively equiaxed but did have a small amount of elongation and anisotropy. This would have most likely been created during the hot rolling to produce the steel strip, and the cold forming which occurred when the strip was progressively formed into a pipe shape by the forming rolls.

The TMAZ was located between the HAZ and the base metal, although it was not present at the mid-thickness of the weld. This can clearly be seen on Figure 5.1. The TMAZ was created as a result of the heat and plastic deformation associated with the welding process. This zone was formed when the weld rolls squeezed the molten strip edges together to produce a forged weld. An SEM image of the TMAZ next to the HAZ is displayed on Figure 5.3. The microstructure of this zone was very similar to that of the base metal; however, the ferrite grains had become elongated and anisotropic due to deformation at high temperatures during the welding process. Since this part of the weld contained deformed original ferrite grains, the temperatures in this zone were lower than Ac_1.

The ferrite grains in the TMAZ next to the HAZ were highly deformed, where they contained newly formed sub-grains and grain structures that were typical features induced by plastic deformation [146]. A highly deformed elongated grain containing these substructures has been highlighted by the red circle on Figure 5.3. These substructures were produced during plastic deformation where dislocations occurred to accommodate plastic strains. The dislocations then led to the formation of dense dislocation walls that formed within the original grains which created dislocation cells that were confined by low angle grains boundaries that were less than 1°. Once a specific strain level had been reached, the dense dislocation walls transformed into sub-grain boundaries. Here the misorientations between each of the sub-grains were small but were greater than that of the dense dislocation walls. As straining increased further, the sub-grain boundaries evolved into highly misoriented grain boundaries, which generated new grains within the original grains [147].

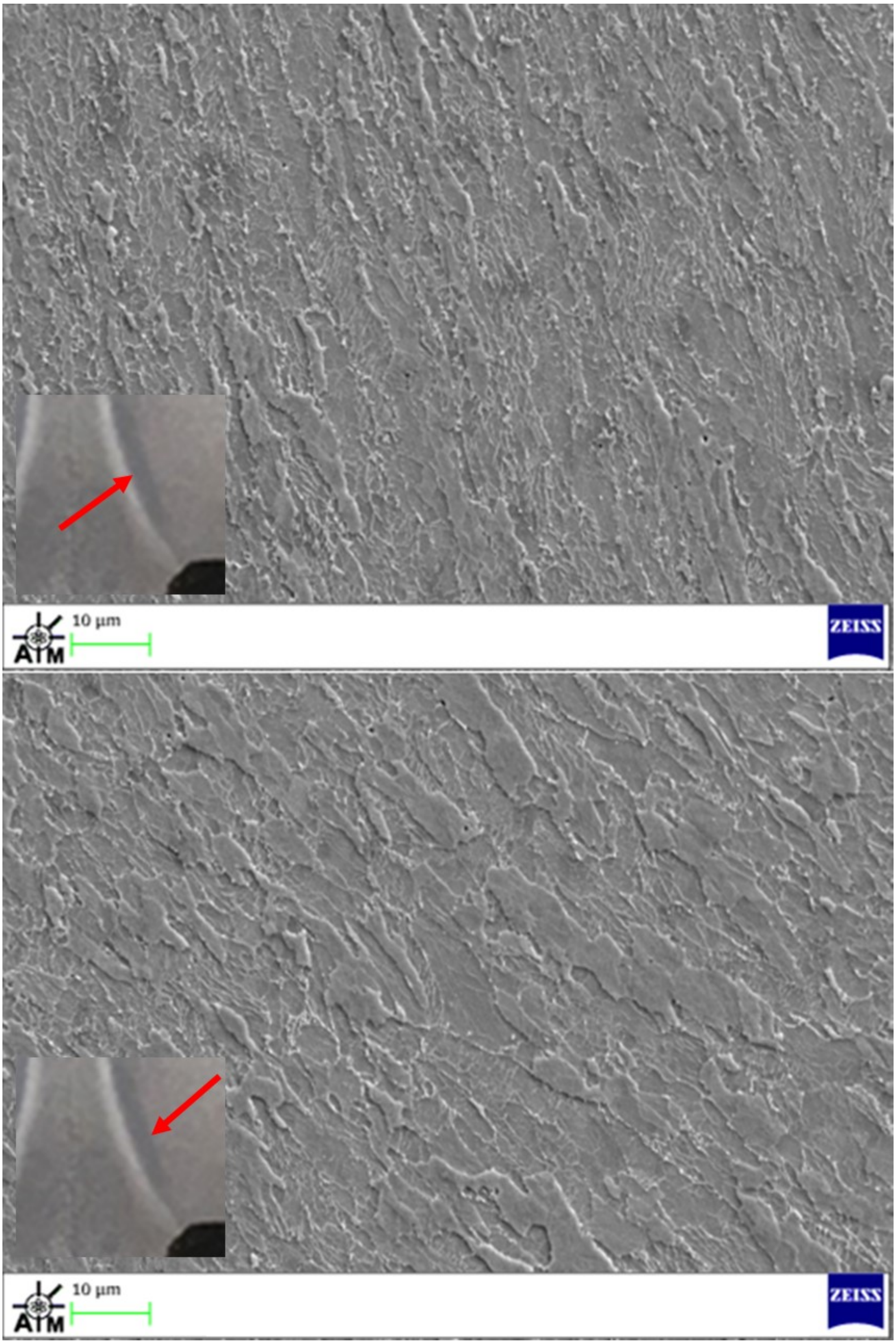

Figure 5.4. TMAZ near HAZ (top) and near base metal (bottom).

Although the TMAZ was very narrow, there was an obvious change in the level of deformation across its width. It was observed that the amount of deformation decreased as a function of distance from the HAZ. SEM images of the TMAZ next to the HAZ and the base metal are displayed on Figure 5.4. It can clearly be seen that the amount of deformation was much greater the next to the HAZ. This was a direct result of the temperature gradient present across the TMAZ during welding. Here the hotter parts of the TMAZ were able to deform more easily because the hardness of steel decreases with increasing temperature [148].

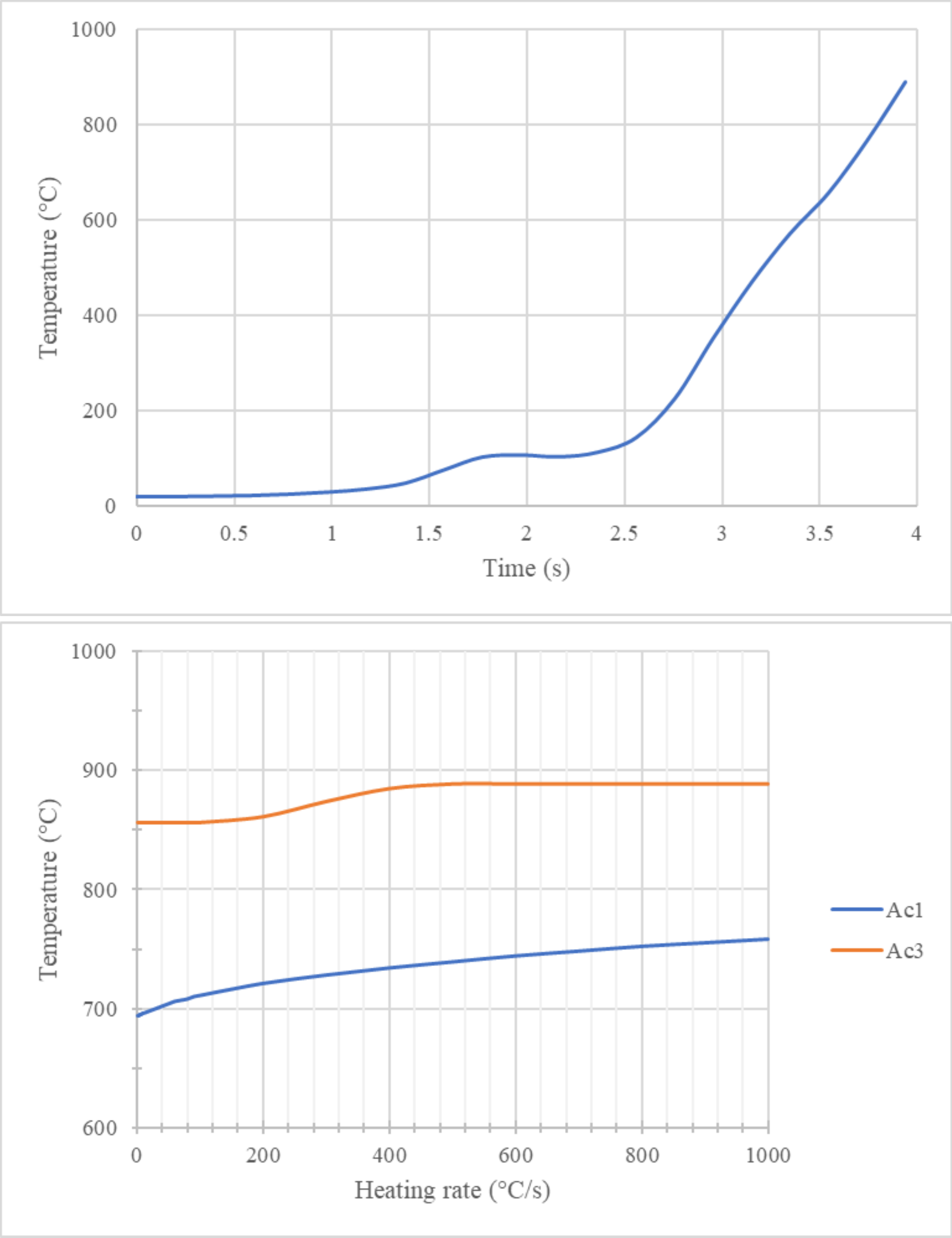

Figure 5.5. Heating curve for part of TMAZ with highest peak temperature located at 3 mm below pipe outer surface (top) and TTA diagram for X60 steel (bottom).

The TMAZ presented itself as a source of poor toughness. This was because severe plastic deformation reduces the toughness steel. In a commercial structural steel, it was found that the toughness decreased as the amount of plastic deformation increased. The plastic deformation led to the embrittlement of the steel and the DBTT was found to increase [149]. Similar was observed in ship plate steels where plastic deformation deteriorated the toughness by increasing the DBTT and reducing the materials resistance to ductile tearing [150]. Since the TMAZ had an anisotropic microstructure, it would have an anisotropic fracture behaviour. It has been shown that the fracture resistance is extremely low when the crack propagates parallel to the alignment of the microstructure, and that the highest fracture toughness occurred when the crack was perpendicular to the alignment of the microstructure [151]. Since the ferrite grains in the TMAZ were aligned with the HAZ it may be possible for cleavage cracks to propagate through the TMAZ in the direction of lowest fracture resistance, which consequently would be highly detrimental to the toughness.

The HAZ was the part of the material that had not been melted during welding, but had its mechanical properties and microstructure altered as a result of the heat associated with welding. In this region the original microstructure was completely transformed to austenite and replaced with a new microstructure during cooling. For this zone to be fully transformed to austenite the peak temperatures across the zone were greater than Ac_3. The computational modelling displayed that the heating rates across the HAZ were in excess of 500 °C/s. JMatPro simulation software was used to produce a Time-Temperature Austenitisation (TTA) diagram using the chemical composition of the AW material as described in Section 4.1. The TTA diagram is presented on Figure 5.5 and is accompanied with the thermal cycle at the edge of the TMAZ next to the HAZ. It shows that for heating rates greater than 500 °C/s, the Ac_3 temperature is 889 °C.

Due to the temperature difference across the HAZ, the side of the HAZ next to the TMAZ would have been at Ac_3 and the HAZ next to the weld line would have been peritectic. These temperatures were approximately 889 °C and 1450 °C respectively. Therefore, a large temperature range across a narrow distance was created, where an obvious gradient in microstructure across the width of the HAZ was produced.

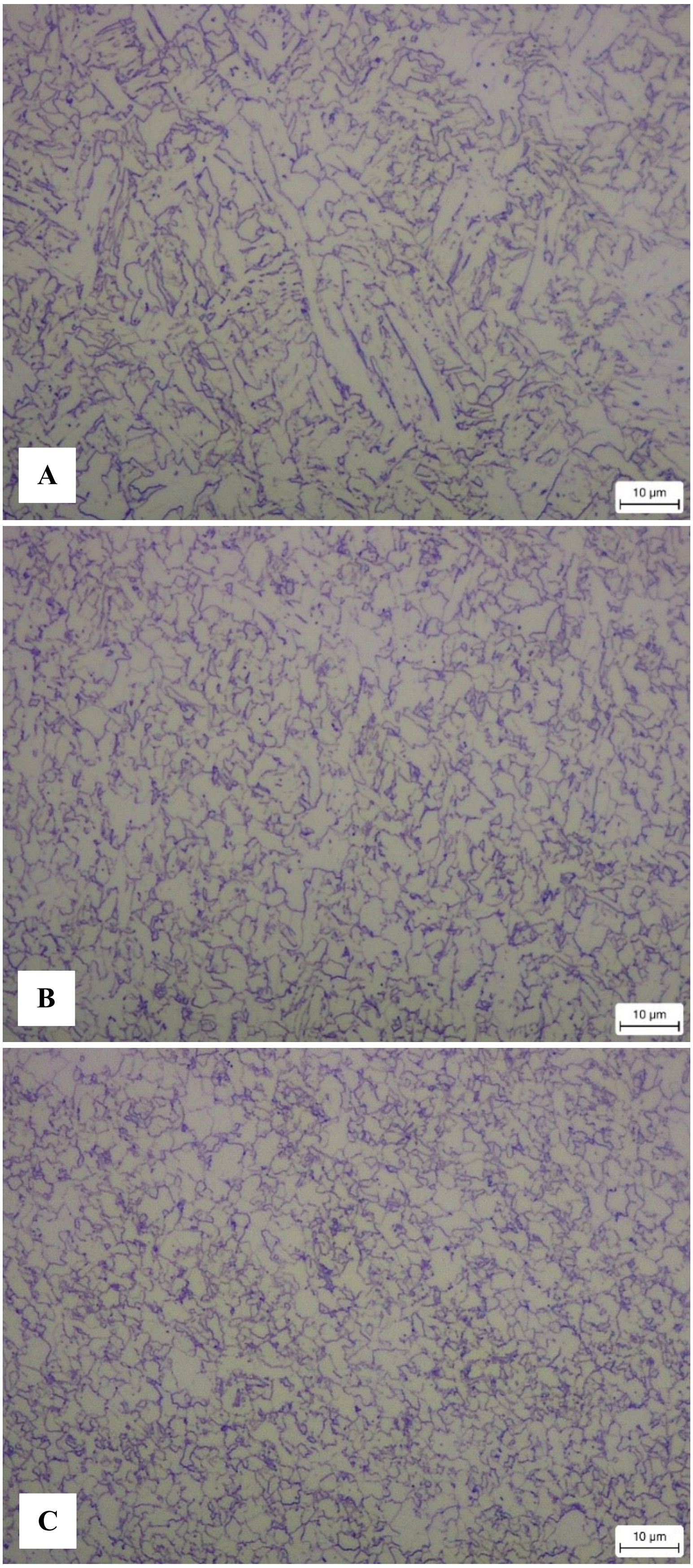

Figure 5.6. Optical micrographs of HAZ approximately 3 mm above inner pipe surface. Next to the weld line (A), centre of the HAZ (B), and next to the TMAZ (C).

The microstructure of the HAZ was very similar to that of a classical fusion weld, where it consisted of a fine-grained zone and a coarse-grained zone [60]. These were located next to the TMAZ and weld line respectively. Optical micrographs of the HAZ next to the weld line, at the centre of the HAZ, and next to the TMAZ are displayed on Figure 5.6, where an obvious change in microstructure can be seen.

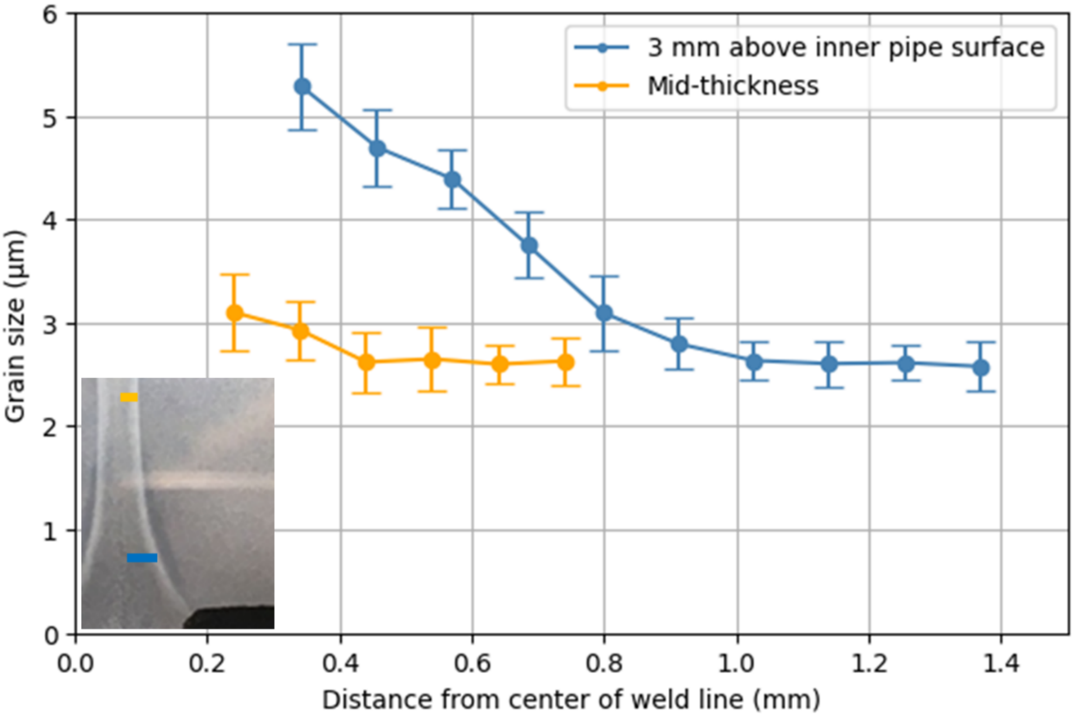

Figure 5.7. Grain size as a function of distance from weld line approximately 3 mm above the inner pipe surface and at the mid-thickness.

The fine-grained zone consisted of an equiaxed allotriomorphic ferrite matrix containing M-A islands. The ferrite grains had an approximate size of 2.6 ± 0.2 µm, which was much finer than that of the base metal. Meta-dynamic recrystallisation may have possibly been the reason for the finer grain size there. Meta-dynamic recrystallisation occurs when dynamic recrystallization begins during deformation, and recrystallisation continues to happen once the deformation has stopped. Finer grains are produced by meta-dynamic recrystallisation than by static recrystallization alone [107]. The meta-dynamic recrystallisation could have potentially started when the weld rolls squeezed the molten strip edges together, deforming the austenite grains. The fine grain size in this zone would be beneficial to the low temperature toughness since a finer grain size results in a reduction of the DBTT [35–37].

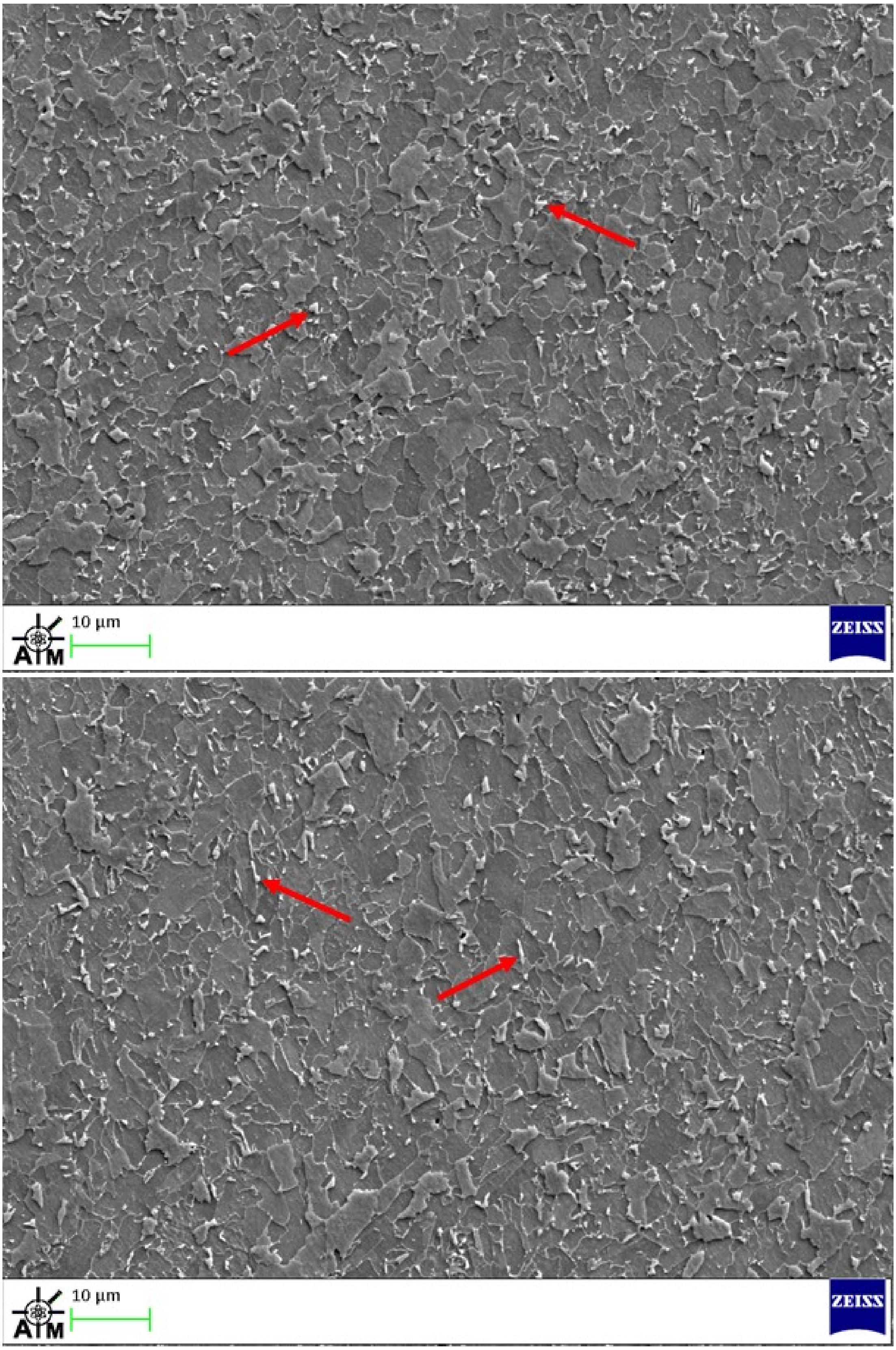

Figure 5.8. SEM images of M-A islands in the HAZ. Next to the TMAZ (top) and near the centre of the HAZ (bottom).

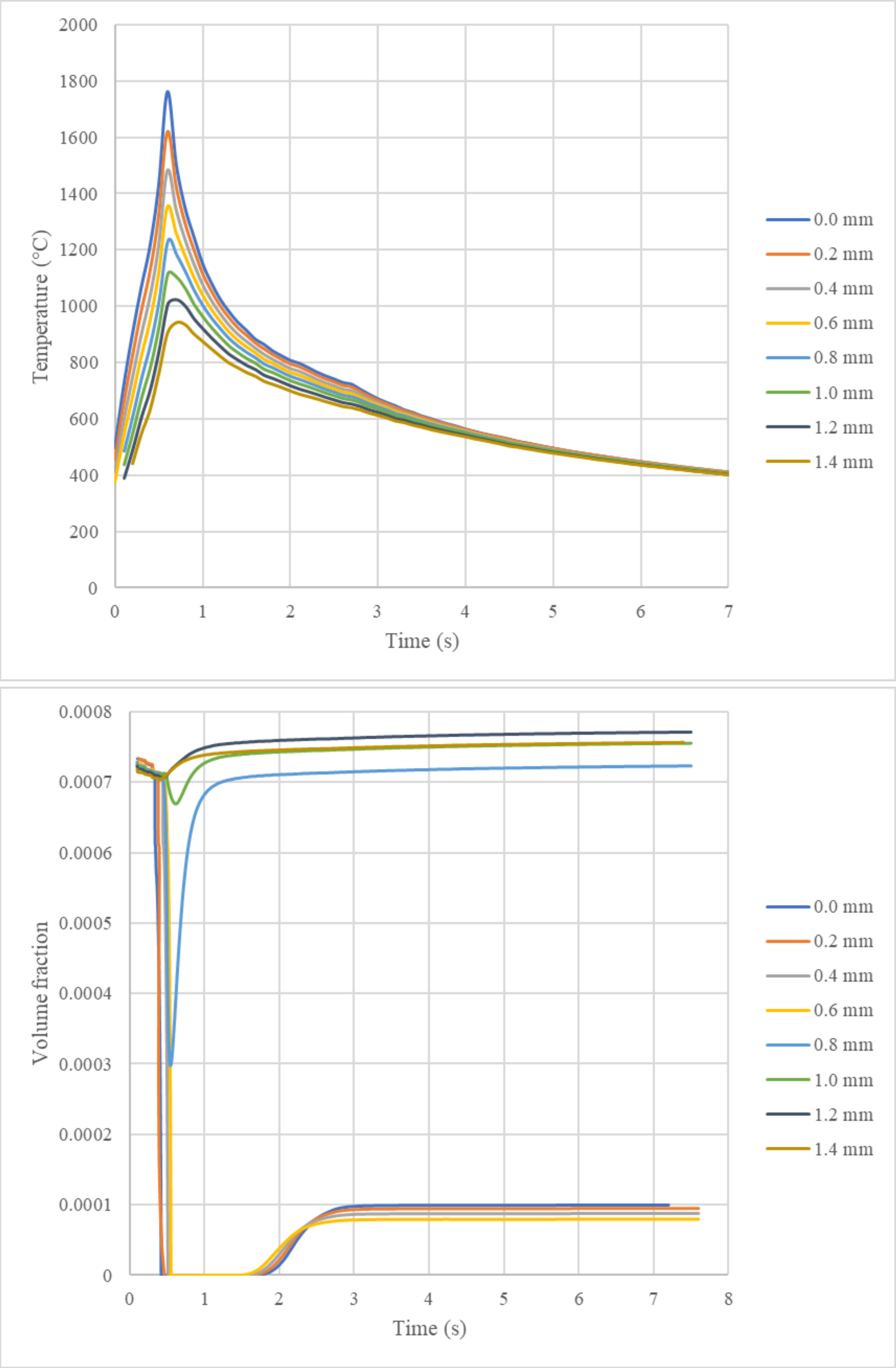

Figure 5.9. Welding thermal cycles (top) and volume fraction of NbC precipitates during welding thermal cycles (bottom) at 3mm below pipe outer surface.

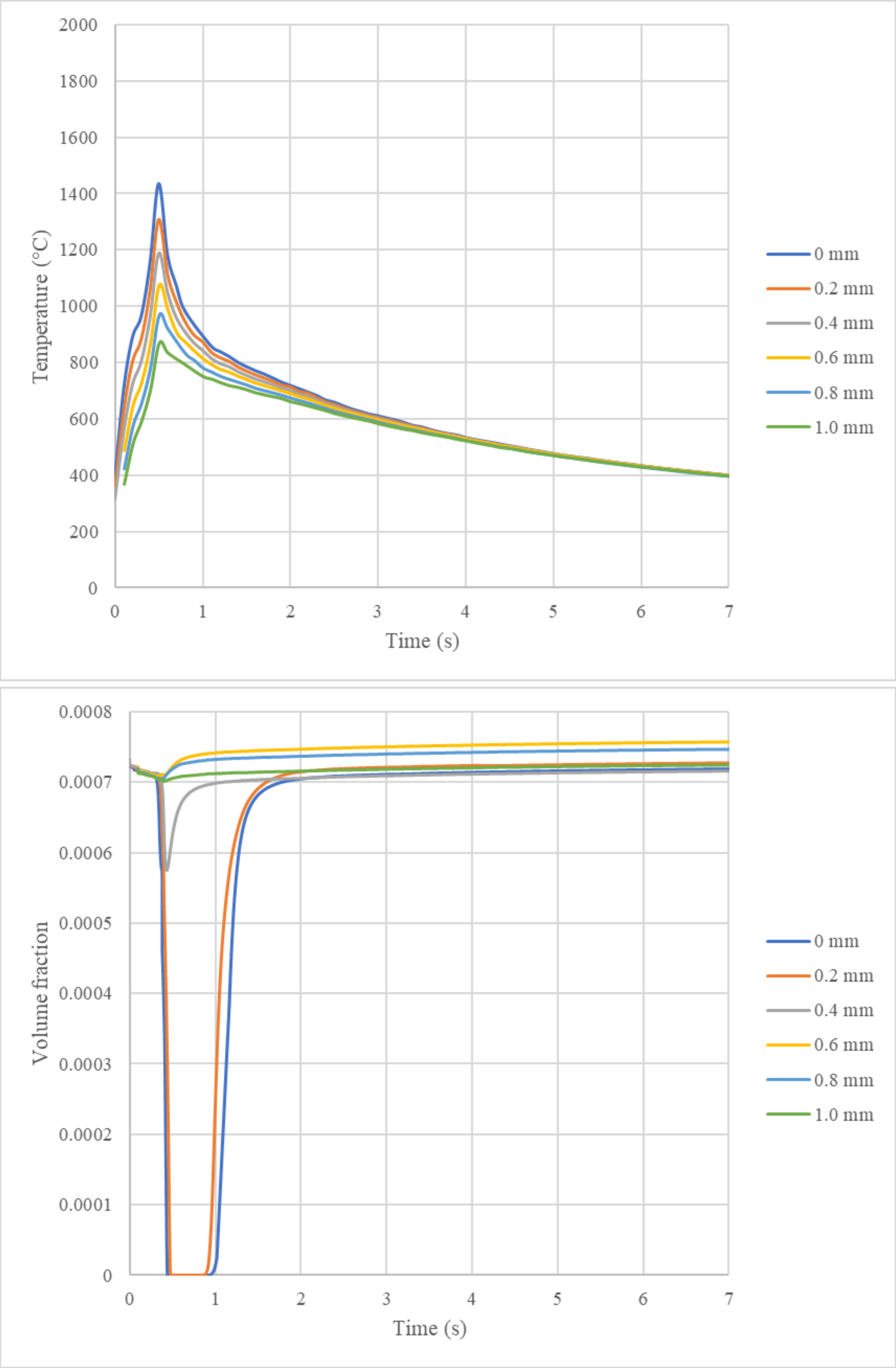

Figure 5.10. Welding thermal cycles (top) and volume fraction of NbC precipitates during welding thermal cycles (bottom) at mid-thickness.

M-A constituent is considered a brittle microphase which can trigger cleavage fracture initiation [75]. Therefore, the presence of this phase in the fine-grained zone could potentially have had a negative influence on the toughness. The morphology of the allotriomorphic ferrite grains was relatively consistent across the whole of the fine-grained zone, although this could not be said about the M-A constituent. Figure 5.8 displays SEM images of the fine-grained zone located next to the TMAZ and the coarse-grained zone. Next to the TMAZ the M-A islands had an equiaxed morphology, whereas the M-A islands next to the coarse-grained zone had an elongated rod shape morphology. The change in morphology was a result of the different cooling rates across the width of the fine-grained zone, where shorter cooling times produced an elongated rod morphology, and longer times produced an equiaxed morphology. The morphology of this phase also plays an important role in toughness. It has been shown that an elongated morphology is more detrimental to the toughness [74]. Consequently, it may have been more likely for brittle fracture to initiate at the M-A constituent in the part of the HAZ closest to the weld line.

There was a two-stage grain growth observed across the width of the HAZ, which is typical of micro-alloyed steels [106–108]. In the fine-grained zone the ferrite grain size was consistent with an approximate size of 2.6 ± 0.2 μm, which is displayed on Figure 5.7. In this zone it was extremely likely that the NbC precipitates that were formed during the thermomechanically controlled processing to produce the steel strip would have inhibited the movement of the austenite grain boundaries, consequently retarding the austenite grain growth. The precipitates inhibiting grain growth may have also been another reason, along with the meta-dynamic recrystallisation, why the grain size of the fine-grained zone was smaller than that of the base metal. It was observed that the ferrite grain size and the width of the fine-grained zone was very consistent through the depth of the weld as well as the breadth, where the width of the fine-grained zone was approximately 0.3 to 0.4 mm. The only considerable difference in the fine-grained zone at different locations of the weld was its proximity to the weld line which was a direct result of the hourglass shaped thermal profile during welding.

Figure 5.9 and Figure 5.10 display the welding thermal cycles and the NbC precipitate volume fraction during welding as a function of distance from the weld line at 3 mm below pipe outer surface and the mid-thickness of the weld respectively. It can be observed that the NbC precipitates were not dissolved at distances greater than approximately 0.5 and 1 mm from the weld line at the mid-thickness and 3 mm below pipe outer surface respectively. Therefore, NbC precipitates were present to retard austenite grain growth here. This agreed with the consistent grain size through the fine-grained zone displayed on Figure 5.7. From the plots it could be estimated that the T_{GC} was approximately 1100 °C to 1200 °C, which was similar to that as observed in previous research [106].

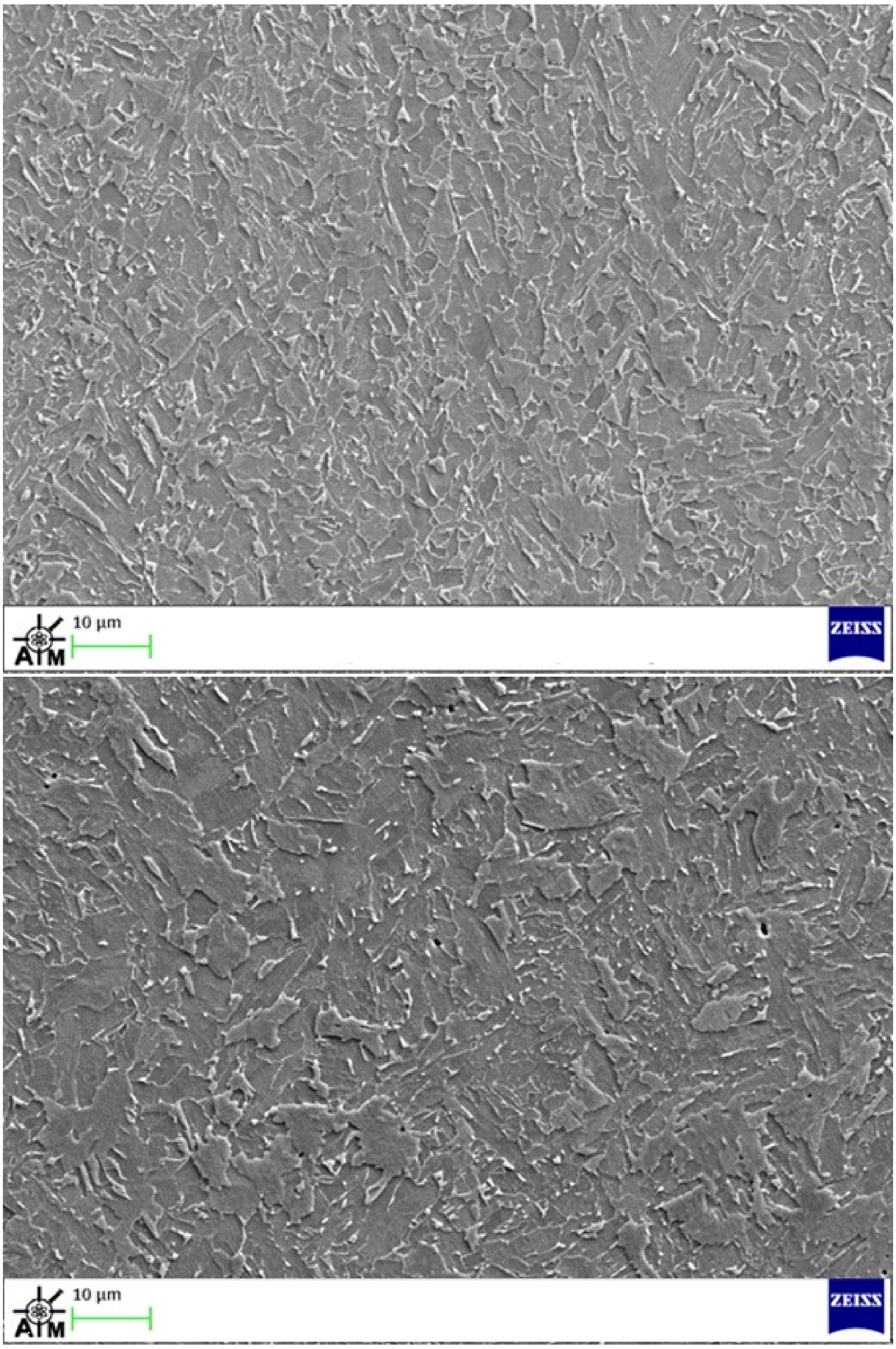

Figure 5.11. HAZ next to weld line at mid-thickness (top) and 3 mm above inner pipe surface (bottom).

Due to the steep thermal gradient across the HAZ, once the T_{GC} had been exceeded it was highly probable that the NbC precipitates were dissolved extremely fast. This would have allowed the austenite grains to grow freely as a function of temperature. On Figure 5.7, there was an increase in grain size across the coarse-grained zone. It is important to note that grain size measurements were only taken to roughly 0.3 mm away from the centre of the weld line due to the difficulty of obtaining measurements once the grains had become coarse and columnar.

With the increase in grain size the microstructure across the HAZ developed. The ferrite transformed from equiaxed allotriomorphic ferrite to a mixture of allotriomorphic ferrite and Widmanstätten ferrite. The formation of Widmanstätten ferrite was caused by the increasing peak temperature, where the prior austenite grain size increased with peak temperature. This happened because the volume fraction of Widmanstätten ferrite increases with prior austenite grain size [112]. The presence of Widmanstätten ferrite would have been detrimental to the toughness of the HAZ since it grows in parallel plates which offer very little resistance to cleavage crack propagation [64]. As well as Widmanstätten ferrite, there was M-A constituent present in the HAZ next to the weld line. It had an elongated morphology which has been shown to be the most effective shape for promoting cleavage fracture initiation [74]. The constituents present in the HAZ near the weld line presented themselves as sources of poor toughness, therefore it was highly probable that the toughness in this zone was inferior to that of the base metal. There was also the possibility of a reduction of High Angle Grain Boundaries (HAGBs) in this zone since it has been observed in numerous steels that it can be reduced by a larger prior austenite grain size [110,111]. This would further reduce the materials resistance to cleavage crack propagation. Therefore, the HAZ next to the weld line most probably had a poor toughness due to its constituents and the strong possibility of containing a low volume of HAGBs.

The HAZ at the mid-thickness and 3 mm above the inner pipe surface had similar microstructures, however the grain size was visually much finer at the mid-thickness, as seen on Figure 5.11. The coarse microstructure near the outer pipe surfaces was a result of greater heating at the strip edge corners during welding. Since a finer grain size is beneficial to toughness [35–37], the HAZ next to the weld line at the mid-thickness would highly likely have better toughness properties than nearer to the outer pipe surfaces. Literature has suggested that improving the uniformity of the heating through the depth of the weld by reducing the high temperatures at the strip edge corners can improve weld quality [11]. Reducing the temperature at the strip edge corners, would result in a reduction in the grain size of the HAZ next to the weld line near the outer pipe surfaces. This would improve the toughness in these areas, subsequently improving the overall toughness of the coarse-grained zone.

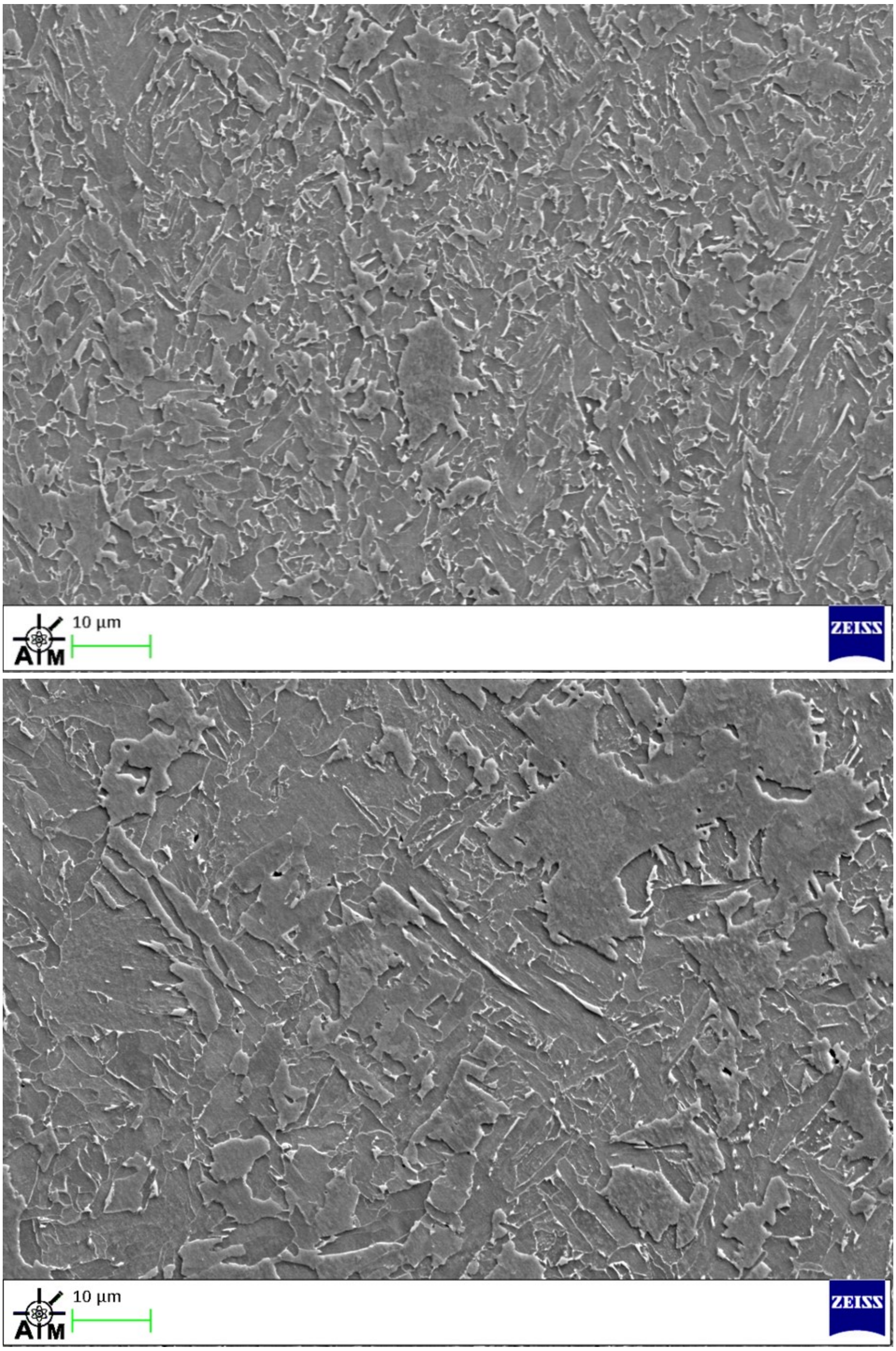

Figure 5.12. Weld line at mid-thickness (top) and near inner pipe surface (bottom).

The microstructure of the weld line consisted of a mixture of allotriomorphic ferrite, Widmanstätten ferrite and elongated M-A constituent. SEM images of the weld line at the mid-thickness and near the inner pipe surface are displayed on Figure 5.12. The allotriomorphic ferrite would have been the first phase to form once the weld line cooled to a temperature below Ar_3. On further cooling the next phase to form was Widmanstätten ferrite because the diffusional growth of the ferrite became so slow that the allotriomorphic ferrite reached a limiting thickness. Its growth was also promoted by the fast-cooling rates associated with welding. Once the weld line had cooled to approximately 500 °C, the small amount of remaining austenite transformed into M-A constituent [60].

The presence of Widmanstätten ferrite and elongated M-A constituent at the weld line presented itself as a source of poor toughness. Consequently, the toughness of the weld line would be expected to be much less than that of the base metal. At the weld line there were numerous large grains present, which were much larger than their surrounding grains. For example, on the bottom SEM image on Figure 5.12, there is a large grain approximately 40 µm in size present in the top right corner. These large grains can act as local stress raisers, reducing the local toughness associated with it, in turn causing the grain to become a fracture origin site [152]. The size of these large grains was greater near the outer pipe surfaces when compared to the mid-thickness of the weld line. Elongated M-A constituent was present through the whole depth of the weld line. However, the length of some of this constituent was much greater near the outer pipe surfaces, where some of this constituent was approximately 10 µm in length. Consequently, this would have reduced the energy required for cleavage fracture initiation in these areas, since large and elongated M-A constituent promotes cleavage fracture initiation [72].

Like in the HAZ, the grain size of the weld line at the mid-thickness was visually finer than that near the inner pipe surface. This again was a result of the greater heating at the strip edge corners during welding. The dissolution and reprecipitation of NbC precipitates may have potentially contributed to the difference in grain size as well. Figure 5.9 and Figure 5.10 display that the NbC precipitates were fully dissolved during welding, although they were able to fully reprecipitate at the mid-thickness. It was possible that the precipitates that did form during cooling at the mid-thickness may have been able to pin austenite grain boundaries and offer grain refinement.

Nevertheless, it was likely that the precipitates following welding were larger and less well dispersed than before since there were no dislocation cores for them to nucleate at. Therefore, the grain refinement effect would have been much lesser than during the thermomechanically controlled process to produce the steel strip.

The microstructure of the weld line near the inner pipe surface presented itself as a much greater source of poor toughness when compared to the mid-thickness since it contained a coarser grain size, bigger singular grains acting as stress raisers, and larger elongated M-A constituent. This was a result of the greater heating at the strip edge corners during welding. As previously discussed, literature has suggested the weld quality can be improved by making the heating more uniform through the depth of the weld, by reducing the high temperatures at the strip edge corner [11]. Lowering the temperatures at the strip edge corners could potentially improve the toughness of the weld line near the outer pipe surfaces by refining the grain size and reducing the size of the M-A constituent. Thus, improving the overall toughness of the weld line.

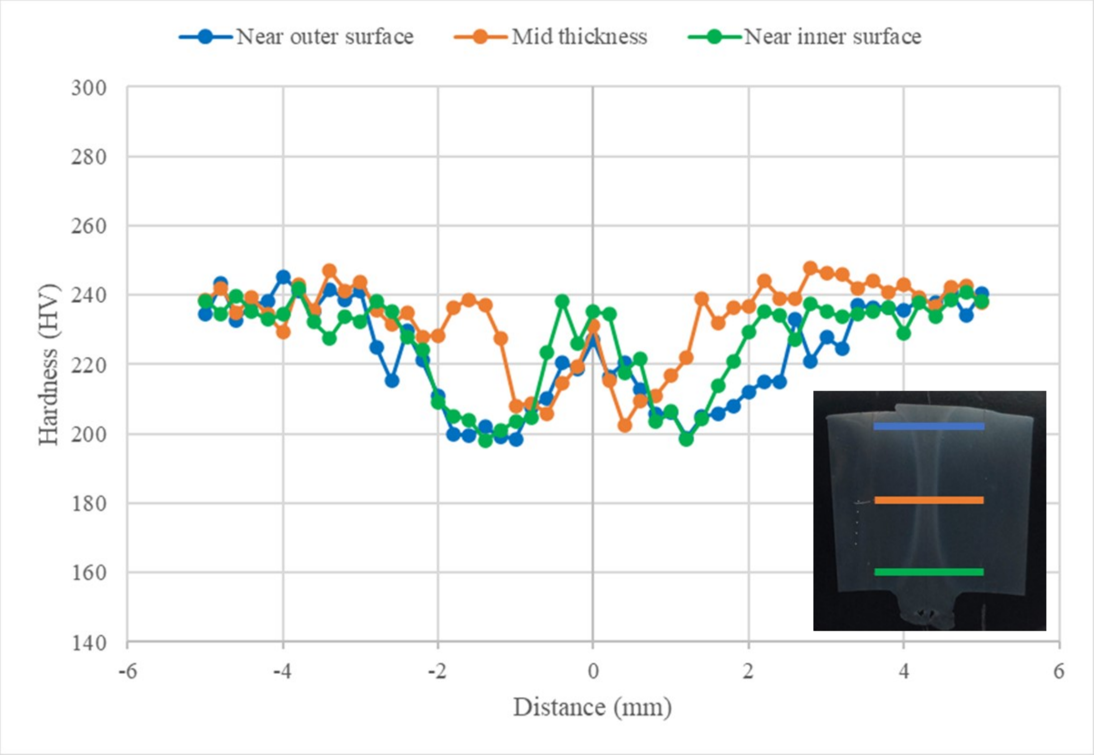

Figure 5.13. Cross-weld microhardness measurements of AW weld.

Cross-weld hardness measurements of the AW weld are presented on Figure 5.13, where the weld line is located at 0 mm. The difference in hardness across the width of the weld displayed that there was a sharp variation in microstructure across the width of the weld, which agreed with the microstructural analysis. The base metal had an average hardness of 235 HV, which then dropped to 200 HV at the fine-grained zone of the HAZ. Typically hardness increases with a decreasing grain size [38]. Therefore, it would be expected for the fine grained-zone to have a greater hardness than the base metal. However, the hardness of steel increases with cold working [153]. Hence, the base metal most likely had a higher hardness due to the cold working it experienced when the forming rolls progressively formed the steel strip into a pipe shape. The hardness then increased again through the coarse-grained zone. This was due to the increasing volume fraction of Widmanstätten ferrite, which was caused by the increasing prior austenite grain size as the peak temperatures increased. The increase in hardness was observed because hardness increases with Widmanstätten ferrite content [112]. The hardness then increased to approximately 235 HV at the weld line.

5.1.2 Microstructure following a PWHT

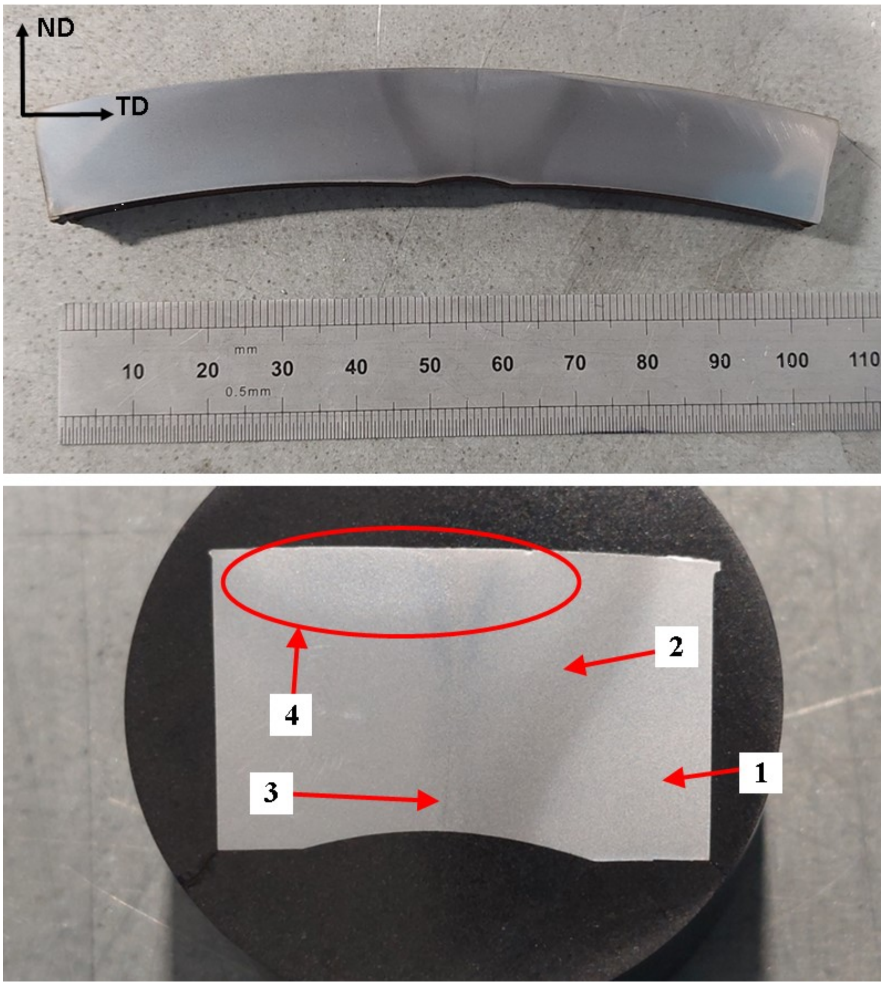

Figure 5.14. Zones of 16 mm thick heat treated X60 HFI welded pipe weld. Base metal (1), affected zone (2), weld line (3) and thumbnail (4).

An etched sample of the cross-section from a 16 mm thick X60 HFI welded pipe weld following a PWHT is displayed on Figure 5.14. The sample was cut from the HT material as described in Section 4.1 of this document. The heat-treated weld had 3 main zones. These were the base metal, AZ and weld line and are labelled 1, 2 and 3 on Figure 5.14 respectively. Even following a PWHT, a remanence of the hourglass shaped weld was still visible on the etched cross-section. At the top of the weld, a light-coloured zone similar to the shape of a thumbnail was present. Hence it was referred to as the thumbnail and is labelled 4 on Figure 5.14. This zone was an undesirable microstructure that was created during the induction annealing and quenching PWHT.

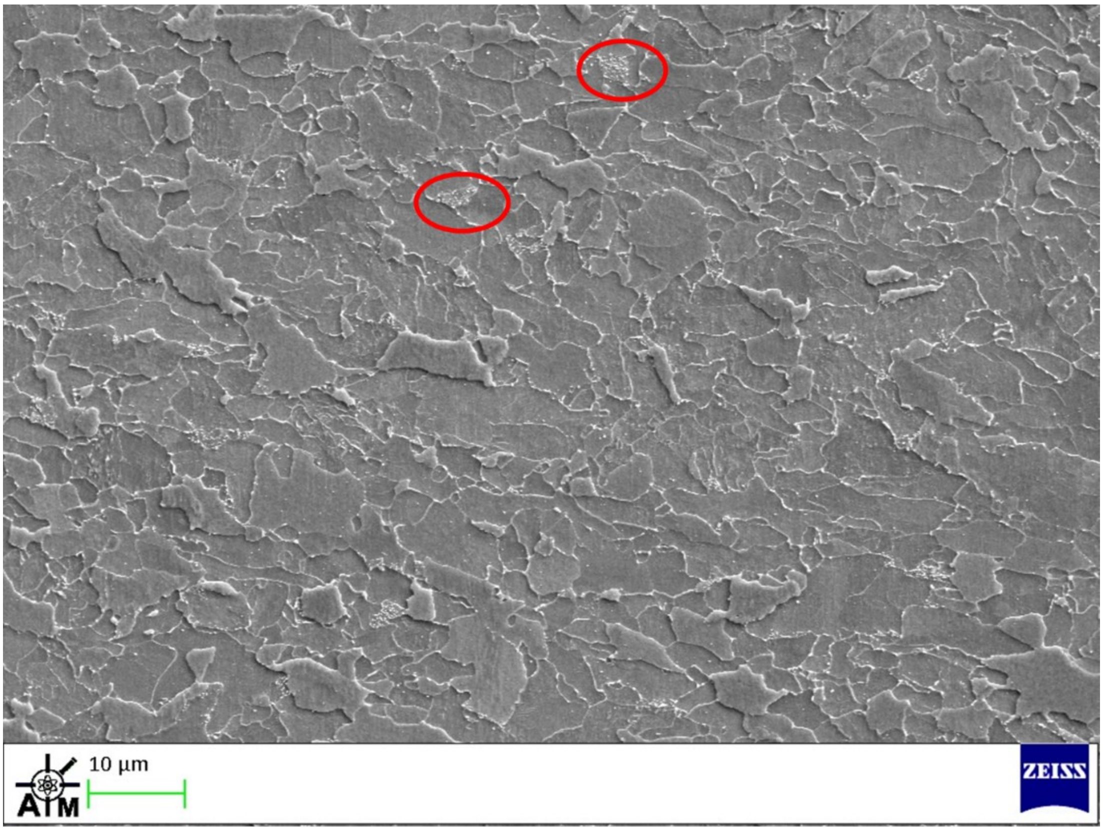

Figure 5.15. SEM image of base metal.

The base metal in the heat-treated weld was the part of the weld that had not been affected by the induction annealing and quenching process. Therefore, this part of the material had only experienced the full pipe body tempering heat-treatment following welding. Details of this treatment are included in Section 4.1. Its microstructure was very similar to that of the AW weld. It consisted of an allotriomorphic ferrite matrix containing a small amount of pearlite and had a grain size of 5.1 ± 0.3 µm. The ferrite grains were relatively equiaxed. However, they had a very small amount of elongation and anisotropy, which would have been caused by the hot rolling when producing the steel strip and the cold forming that occurred during the form rolling stage of the HFI welded pipe manufacturing process. This was consistent with the AW base metal. The main difference between the microstructures was the pearlite. In the AW base metal, the pearlite had a well-defined lamellar structure, which can be seen on Figure 5.2. The pearlite in the heat-treated base metal had become spherodised. Examples of the spherodised pearlite are highlighted by the red circles on Figure 5.15. The tempering process of the full body heat-treatment caused this, where the pearlite colonies disintegrated, transforming the lamellar cementite into spherical carbides [154,155].

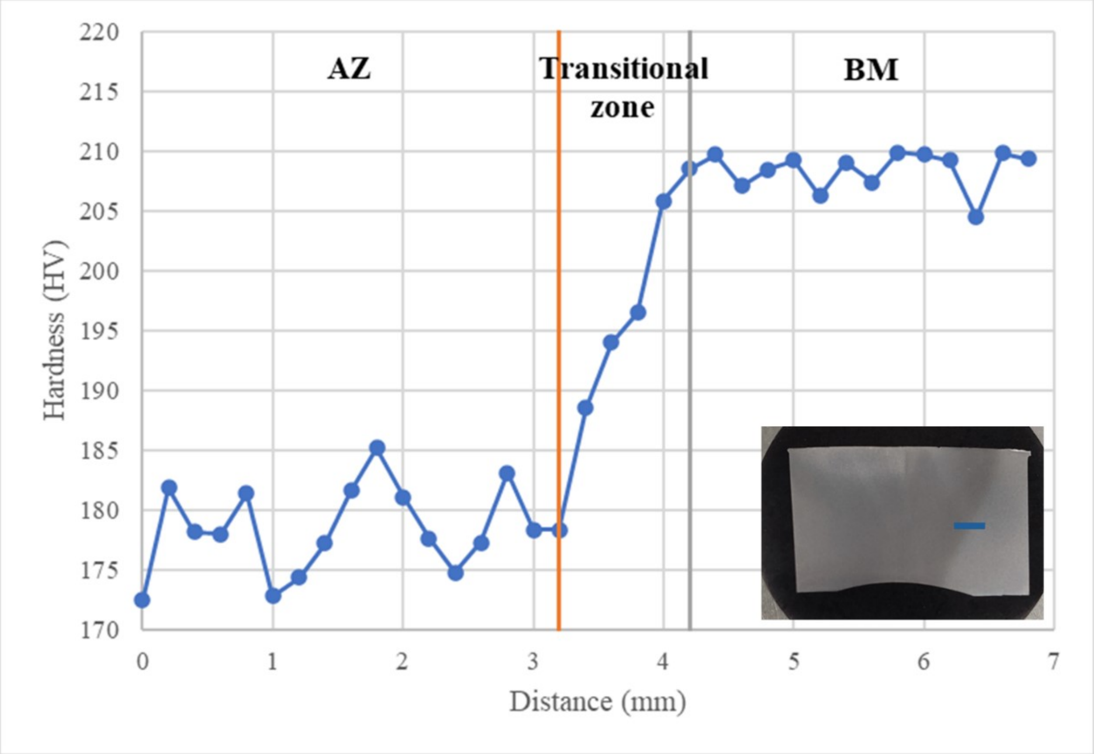

Figure 5.16. Microhardness measurements from AZ into base metal of HT specimen at mid-thickness of the weld.

The hardness of the base metal in the heat-treated weld was lower than that of the AW weld, where it was approximately 209 HV. This was a decrease of around 25 HV and was a result of the full body tempering heat-treatment. Here the heat-treatment would have softened the base metal by reducing the dislocation density that was created during the roll forming stage of the production process. During the tempering the pearlite also became spherodised resulting in a further reduction in toughness [156].

The AZ was the area that had its microstructure altered by the induction annealing and quenching process and had a distinct trapezium shape as shown on Figure 5.14. The full body tempering heat-treatment would have also affected this zone. The weld line and the thumbnail were both located within the AZ but were analysed separately. Therefore, the microstructural analysis of the AZ evaluated how effective the PWHT was at the removal and the replacement of the microstructures of the TMAZ and HAZ.

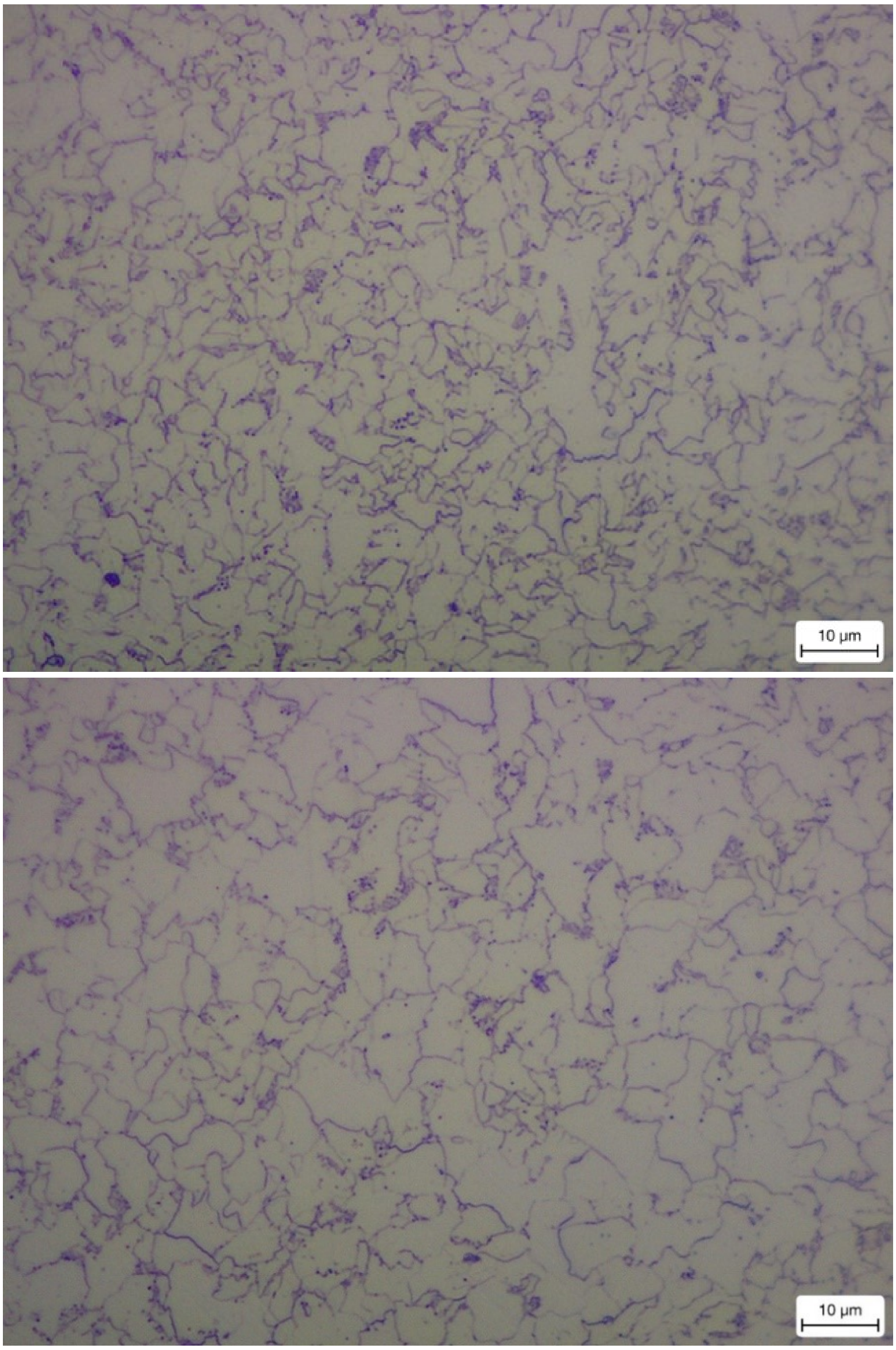

Figure 5.17. Optical micrographs of AZ taken at the mid-thickness (top) and near the inner pipe surface (bottom).

Although there were remanences of the original hourglass shaped weld profile still visible on the etched cross section of the weld, the previous microstructures were found to have been completely removed when analysed under SEM. The coarse ferrite grains, Widmanstätten ferrite and the M-A constituents in the HAZ were removed along with the deformation structures associated with the TMAZ. The microstructure produced in the AZ following heat-treatment consisted of an equiaxed ferrite matrix with a small amount of pearlite. Optical micrographs of the AZ are displayed on Figure 5.17. An increase in toughness would be expected to be seen with the vast improvement in microstructure.

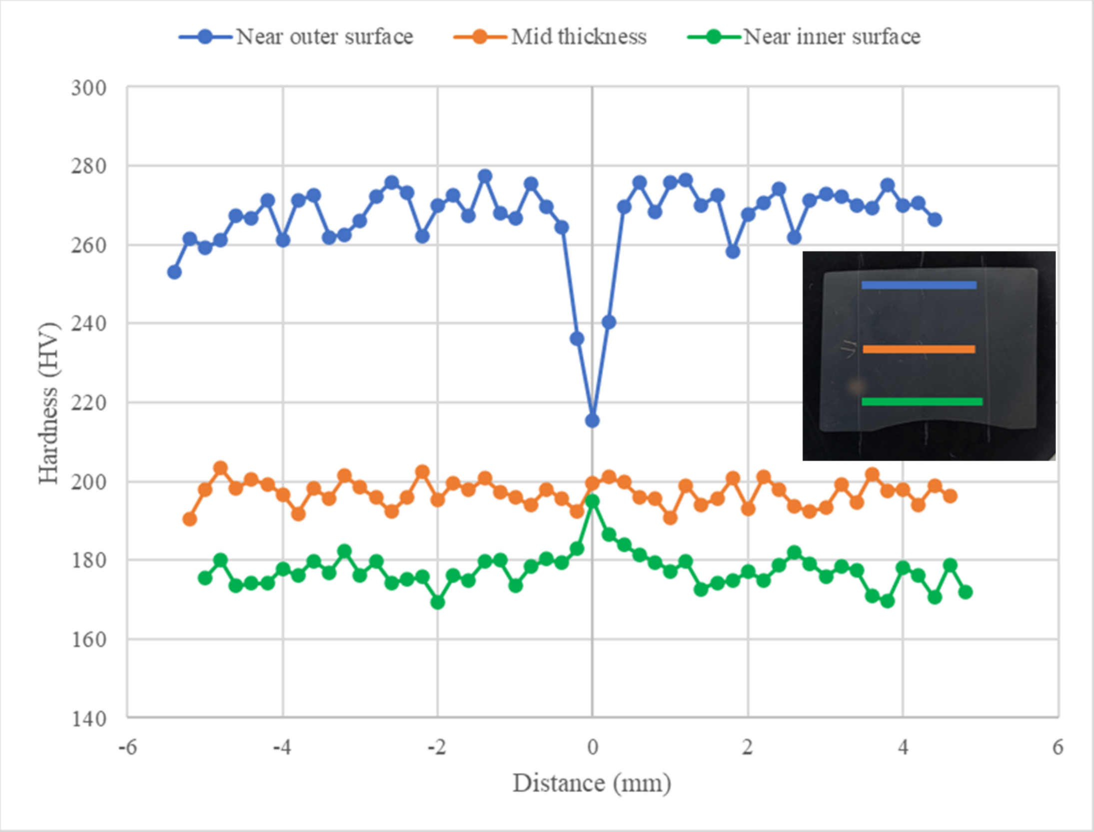

Figure 5.18. Cross-weld microhardness measurements of heat-treated weld.

The annealing and quenching heat-treatment used a rapid austenitising thermal cycle to produce the microstructure observed in the AZ. This involved rapidly heating the AZ to a temperature above Ac_3, and as soon as it was completely transformed to austenite it was air quenched. Rapid austenitising was used because it ensures a fine prior austenite grain size is achieved because the material is quenched before the austenite grains have time to grow, resulting in a fine final microstructure [157]. This would result in a microstructure with a good DBTT [35–37].

Figure 5.18 displays cross-weld microhardness measurements of the heat-treated weld where the weld line is located at 0 mm. Measurements taken near the inner pipe surface and at the mid-thickness clearly show that the hardness was uniform across the width of the weld, which would suggest that the microstructure was uniform in this direction. However, there was a difference in hardness through the depth of the weld, where the hardness at the mid-thickness was approximately 20 HV greater than near the inner pipe surface. The optical micrographs on Figure 5.17 clearly show that the grain size was finer at the mid-thickness when compared to the inner pipe surface.

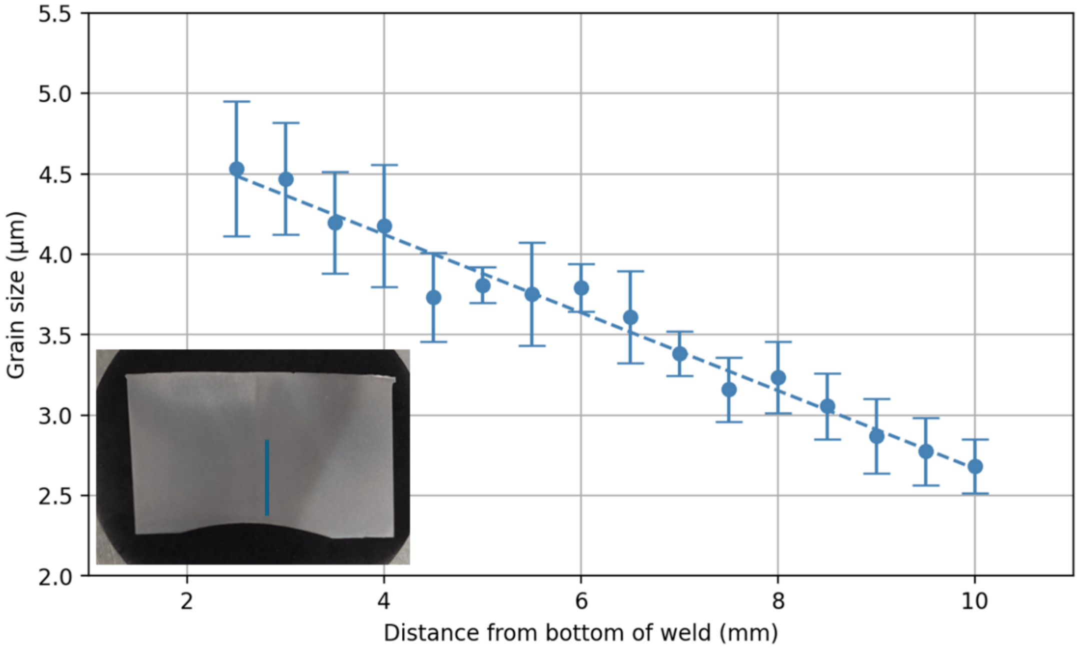

Figure 5.19. Grain size measurements through the depth of the AZ.

The grains size as function of distance from the inside surface of the pipe is displayed on Figure 5.19. The measurements were taken at 0.5 mm intervals and were not taken through the full depth of the weld due to the presence of the thumbnail. It can be seen that the grain size decreased linearly as a function of distance. The gradient in grain size was a direct result of the different thermal cycles that occurred through the depth of the AZ during the induction annealing and quenching heat-treatment. This happened because the induction annealer and quencher contacted the outside surface of the pipe, therefore higher peak temperatures and faster cooling rates were experienced here. Faster cooling rates lead to greater grain refinement [158,159]. Therefore, the parts of the AZ closer to the quencher were able to cool faster resulting in a finer final grain size.

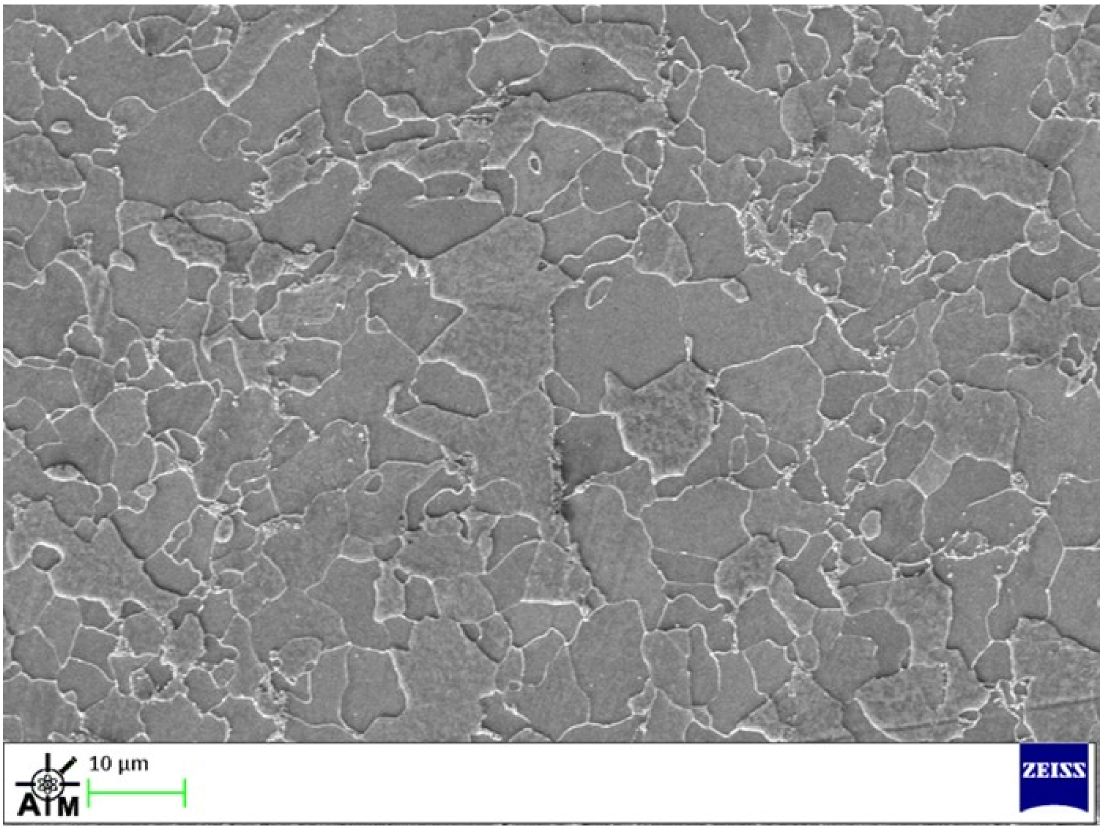

Figure 5.20. SEM image of heat-treated weld line 3 mm above the inner pipe surface.

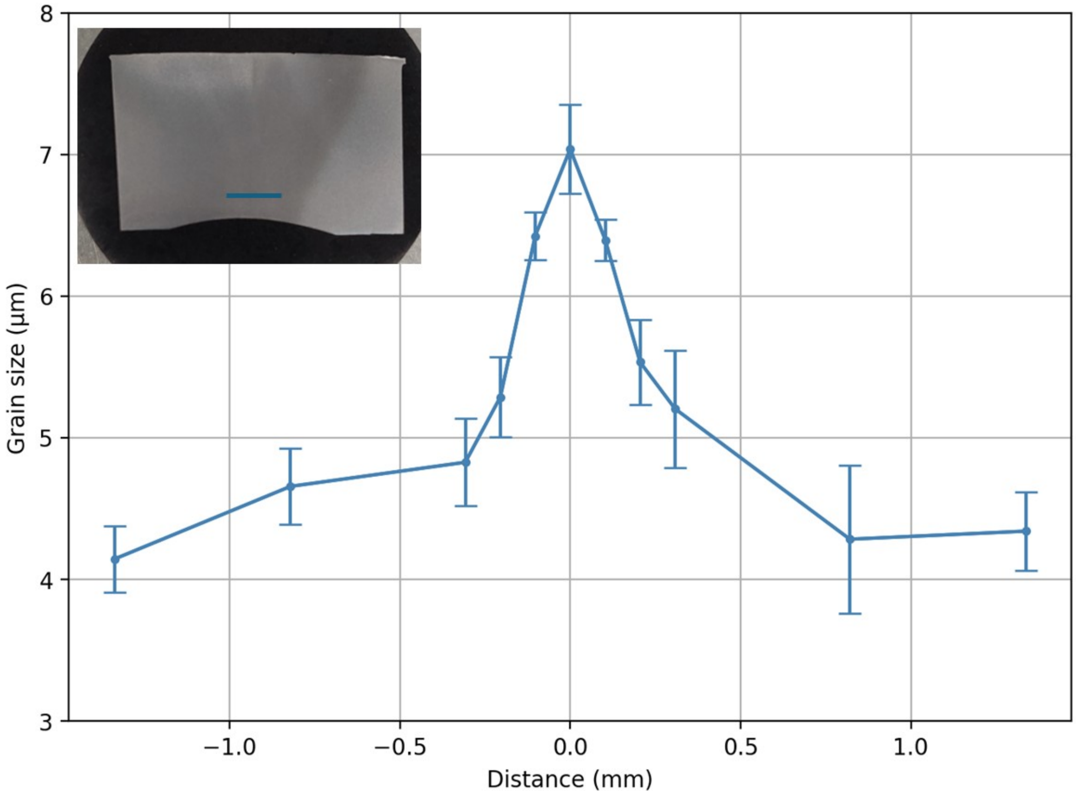

Figure 5.21. Grain size across weld line 3 mm above inner pipe surface.

The induction annealing and quenching heat-treatment greatly improved the microstructure of the weld line. The microstructure containing constituents including Widmanstätten ferrite and elongated M-A constituent were removed and replaced with a microstructure consisting of equiaxed allotriomorphic ferrite. The microstructure of the weld line 3 mm above the inner pipe surface is displayed on Figure 5.20. Although a vast improvement of the microstructure was observed, there was still a large grain size present at the weld line.

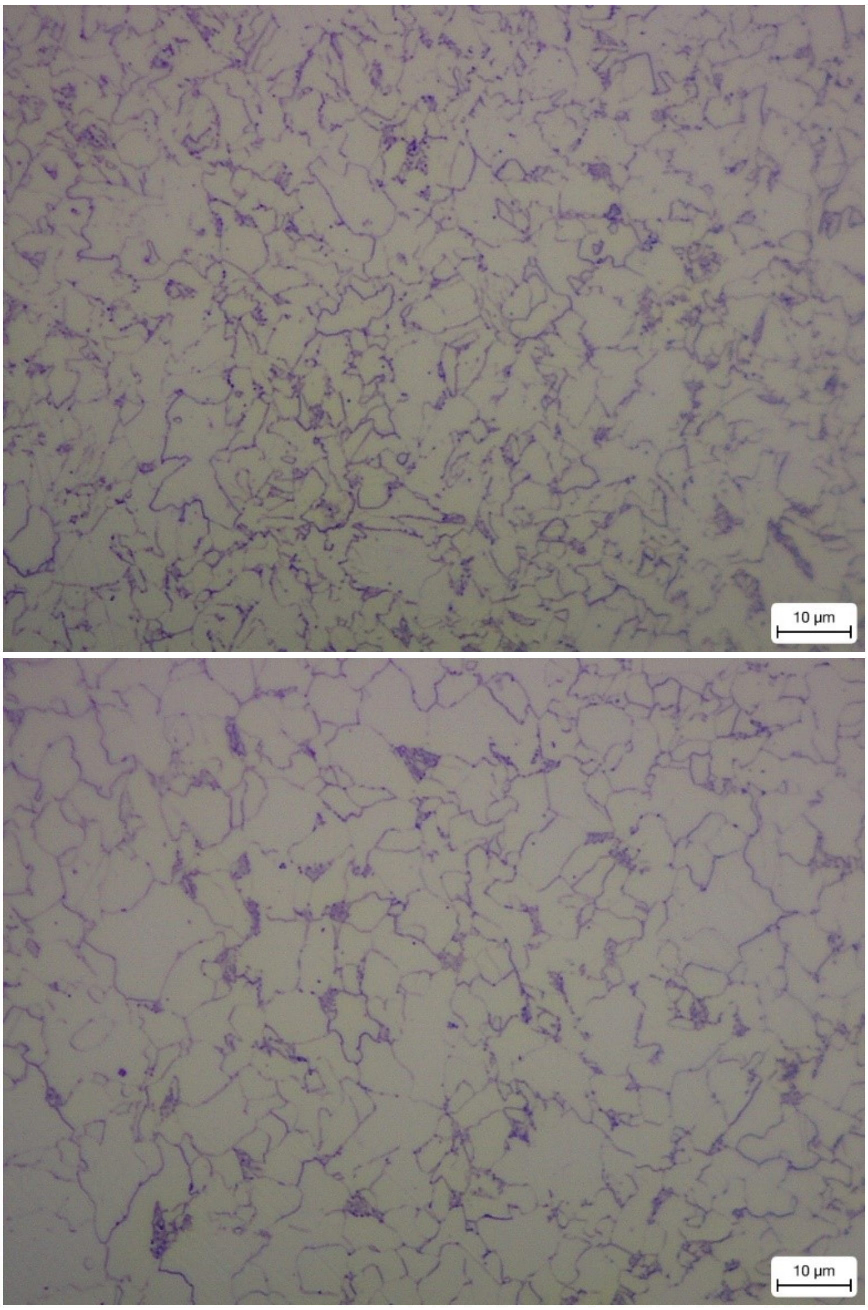

Figure 5.22. Optical micrographs of weld line. Taken at the mid-thickness (top) and near the pipe inner surface (bottom).

The grain size of the weld line was greater than that of the adjacent AZ. Figure 5.21 displays the grain size across the width of the weld approximately 3 mm above the inner pipe surface. The centre of the weld line is located at 0 mm on the plot. It can be seen that the grain size at the weld line was approximately 7 μm, whereas the grain size of the adjacent AZ was approximately 4 μm. The large grain size at the weld line presented itself as a source of poor low temperature toughness since the DBTT increases with grain size [35–37]. The persistent coarse grain size at the weld line may have been a result of structural heredity. This is when the original grain size is recovered after a heat-treatment, and is most likely to occur when a rapid thermal cycles are used [160]. Since the annealing and quenching heat-treatment used a rapid austenitising thermal cycle it was probable that the continual coarse grain size was a result of structural heredity.

Just like the AZ there was a gradient in grain size at the weld line through the depth of the weld, where the grain size was larger near the inner pipe surface. Figure 5.22 displays optical micrographs of the weld line near the inner pipe surface and at the mid-thickness, where the grain size was visibly smaller at the mid-thickness. Again, this was most likely a result of the different thermal cycles experienced through the depth of the weld during the induction annealing and quenching process. Here the parts of the weld closer to the quencher experienced the fastest cooling rates leading to greater grain refinement.

The thumbnail was formed at the top of the AZ during the induction annealing and quenching heat-treatment and it is highlighted by the red circle on Figure 5.14. It was lighter in colour than the rest of the AZ and was referred to as the thumbnail due to its visual resemblance to one. The cross-weld hardness measurements on Figure 5.18 displayed that the thumbnail was much harder than the rest of the AZ. The average hardness of the thumbnail was approximately 270 HV, which was roughly 70 HV greater than that of the AZ at the mid-thickness of the weld. However, the part of the weld line that was located within the thumbnail had a much lower hardness than the adjacent thumbnail, displaying that the microstructure here was likely to be much different to that of the thumbnail.

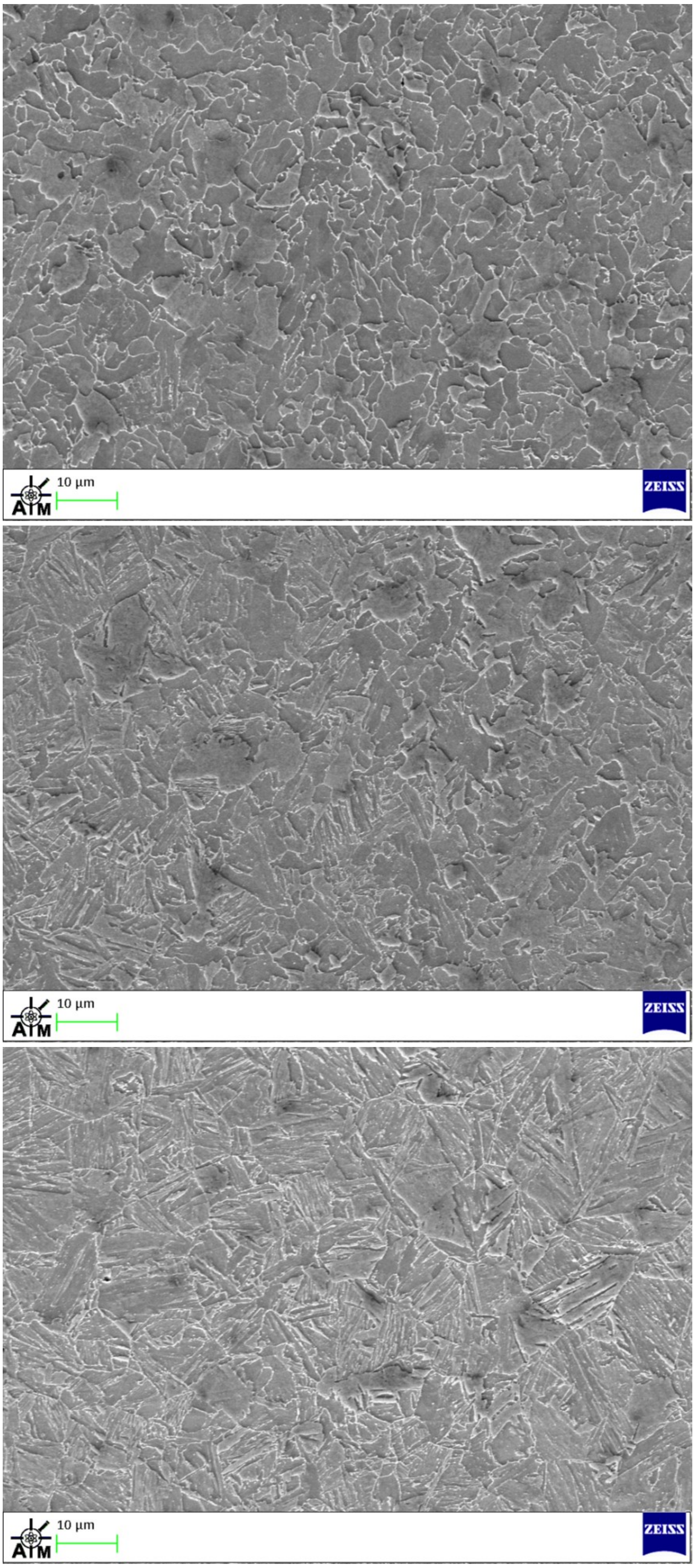

Figure 5.23. SEM images of thumbnail. Weld line in thumbnail (top), transitional zone between weld line and thumbnail (middle), and thumbnail (bottom).

SEM images of different location across the width of the thumbnail are displayed on Figure 5.23. The thumbnail consisted of lath martensite, which is a hierarchical structure made up of prior austenite grains, packets, blocks and laths [76]. These components are visible on the bottom image of Figure 5.23. Since lath martensite has a high dislocation density it explained why the hardness of the thumbnail was so much greater than the rest of the AZ [161].

Lath martensite is a microstructure that forms in quenched low carbon steels [77]. Therefore, the thumbnail was created when the weld was quenched, which occurred directly after induction annealing when the AZ was transformed to austenite. Since the quencher was located at the outside of the pipe, the material at the top of the weld would have experienced the fastest cooling rates. The rapid cooling rates here caused the diffusionless transformation of the austenite to lath martensite, where the carbon in the austenite solid solution remained in the martensite solid solution [78]. Although martensite is typically considered a hard and brittle constituent, lath martensite has been shown to have good toughness properties, where it has been observed to have a better toughness and a lower DBTT than ferrite [80]. Therefore, the thumbnail may not have had a detrimental effect on the toughness of the weld.

The thumbnail consisted of lath martensite, however the weld line within the thumbnail did not. An SEM image of the weld line is displayed on the top image of Figure 5.23. The weld line mainly consisted of allotriomorphic ferrite with a small amount of Widmanstätten ferrite, where the grains had a mixture of equiaxed and columnar morphology. The formation of Widmanstätten would have been detrimental to the toughness of the weld line here since it grows in parallel plates with similar orientations that offer little resistance to cleavage crack propagation [64]. The different microstructure present at the weld line may potentially have been due to residual heat from the welding process. The gradient in microstructure between the weld line and the adjacent thumbnail was extremely sharp. An SEM image of this transitional zone is displayed on middle image of Figure 5.23. The thumbnail and the weld line are located on the left-hand side and right-hand side of the image respectively, where a sharp transition in microstructure can be observed. An extremely fast change in hardness from the weld line to the thumbnail was also observed during the cross-weld microhardness, as shown on Figure 5.18.

5.1.3 EBSD analysis

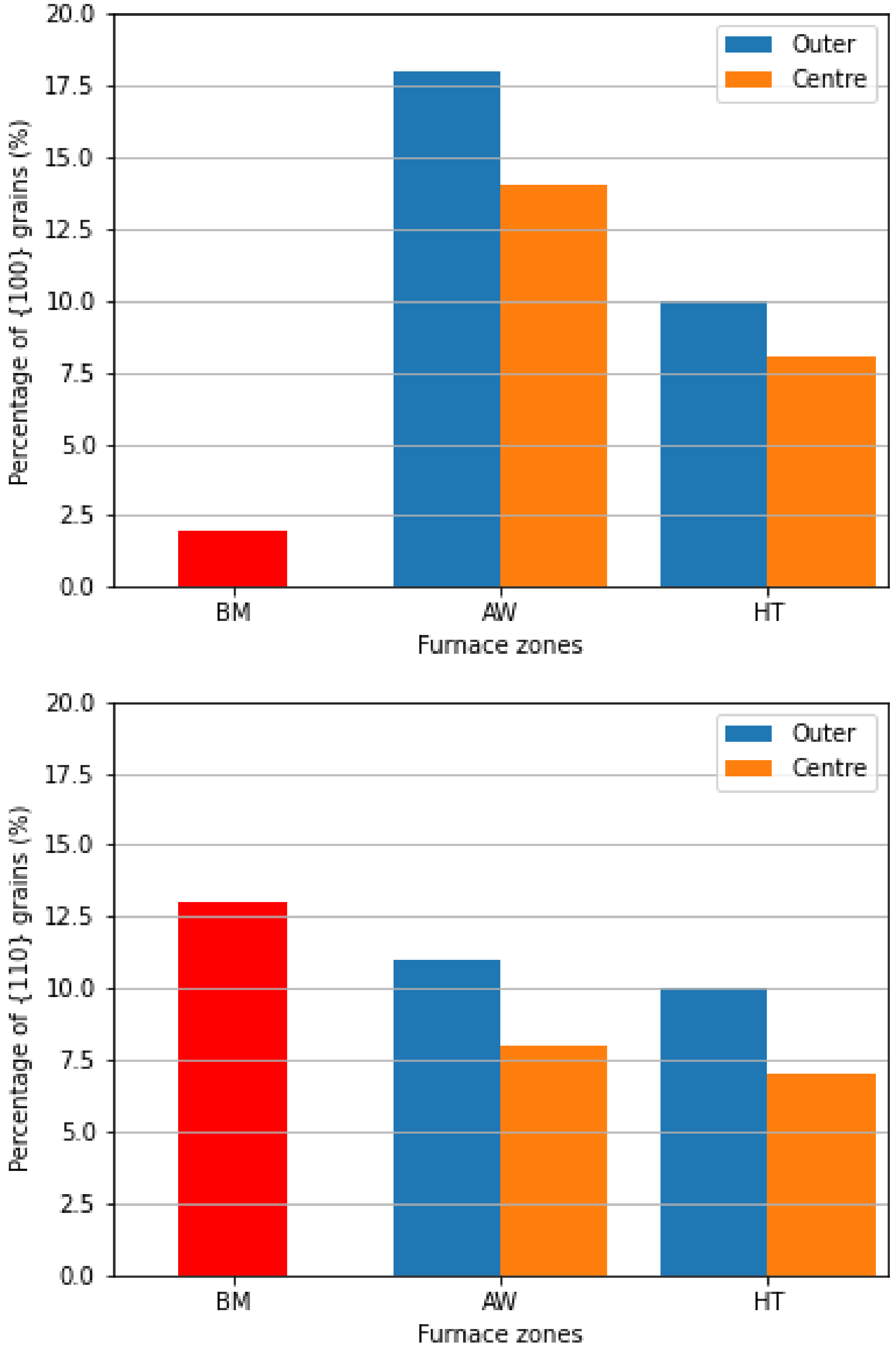

Figure 5.24. Area percentage of {100} (top) and {110} (bottom) planes orientated within 10 ° of the weld plane.

Figure 5.24 displays bar charts of the area percentage of {100} and {110} planes orientated within 10° of the weld plane. Grains orientated with their {100} plane aligned within 10 ° of the weld plane were considered to be orientated for easy fracture. This was because an increase in the fraction of {100} planes aligned parallel to the fracture surface increases the DBTT and helps to promote cleavage fracture propagation [6–8]. The percentage of grains orientated for easy fracture in the base metal was approximately 2 %. Following welding this percentage increased dramatically. In the AW weld line, it was 18 % and 14 % near the inner pipe surface and at the mid-thickness respectively. Consequently, the weld line towards the inner pipe surface presented itself with a lower toughness than at the mid-thickness. Therefore, the toughness of the weld line could potentially be improved by making the heating more uniform through the depth of the weld by reducing the high heating at the strip corners. This could possibly reduce the intensity of the {100} texture towards the outer pipe surfaces, leading to an overall improvement of the weld line toughness.

The PWHT was able to somewhat reduce the fraction of grains orientated for easy fracture. However, it was still much greater than that of the base metal, where the percentage of grains orientated for easy fracture near the inner pipe surface and at the mid-thickness were reduced to 10 % and 8 % respectively. Since this was still much greater than the base metal, it was expected that the weld line’s ability to resist crack propagation would still be poor. The undesirable texture remaining at the weld line was likely caused by a texture memory effect. This is when a material has undergone the ferrite → austenite → ferrite transformation and the original ferrite crystallographic texture is recovered and remains in the final microstructure [56].

Grains with their {110} plane orientated within 10° of the weld plane were considered good for toughness. This was because {110} crack propagation is associated with large crack tip plasticity due to twinning events and crack tip dislocation emission which can improve brittle crack resistance by frequent blunting of the crack tip [48]. The base metal had a percentage of grains with this orientation of approximately 13 %. In the AW weld line this was reduced to 11 % and 8 % near the inner pipe surface and at the mid-thickness respectively. This would have been detrimental to the toughness, however the change in this texture was not as significant as the {100} previously discussed. Following the PWHT the percentage of grains with their {110} planes orientated within 10°C was decreased further to 10 % and 7 % near the inner pipe surface and at the mid-thickness respectively. However, this decrease was small and still very similar to the AW weld line. Again, the persisting texture was most likely due to a texture memory effect.

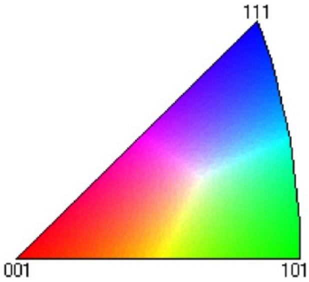

Figure 5.25. IPF map legend.

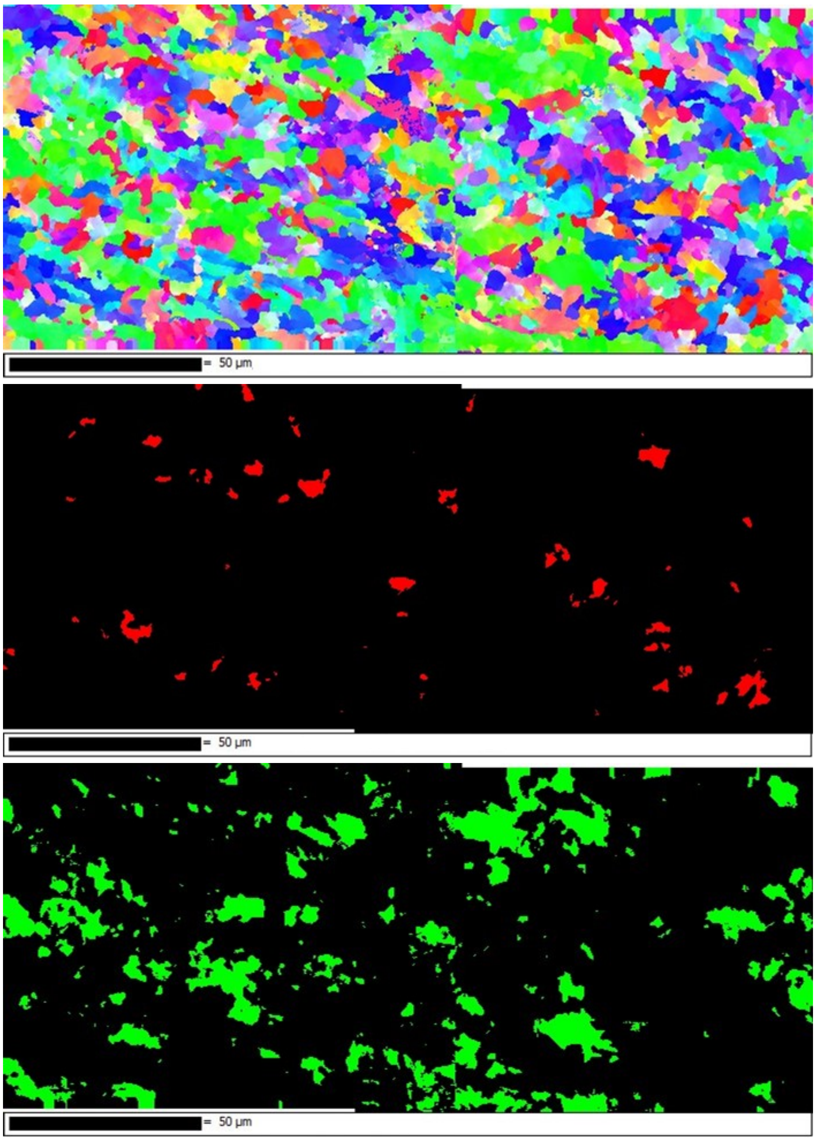

Figure 5.26. BM EBSD maps. IPF (top), {100} texture component map (centre), and {110} texture component map (bottom).

The reduction in {110} planes and increase in {100} planes, aligned within 10° to the weld plane, would have been detrimental to the toughness since the weld lines resistance to cleavage crack propagation would have been largely decreased. Even following a PWHT it was expected that the weld line would be susceptible to cleavage fracture propagation due to the persistent undesirable texture.

Figure 5.25 displays the Inverse Pole Figure (IPF) legend for the following IPF maps. The reference direction was the TD direction as this direction was perpendicular to the weld plane. On the following texture component maps, grains with their <110> direction and <100> direction aligned within 10° to the TD direction are lime green and red respectively.

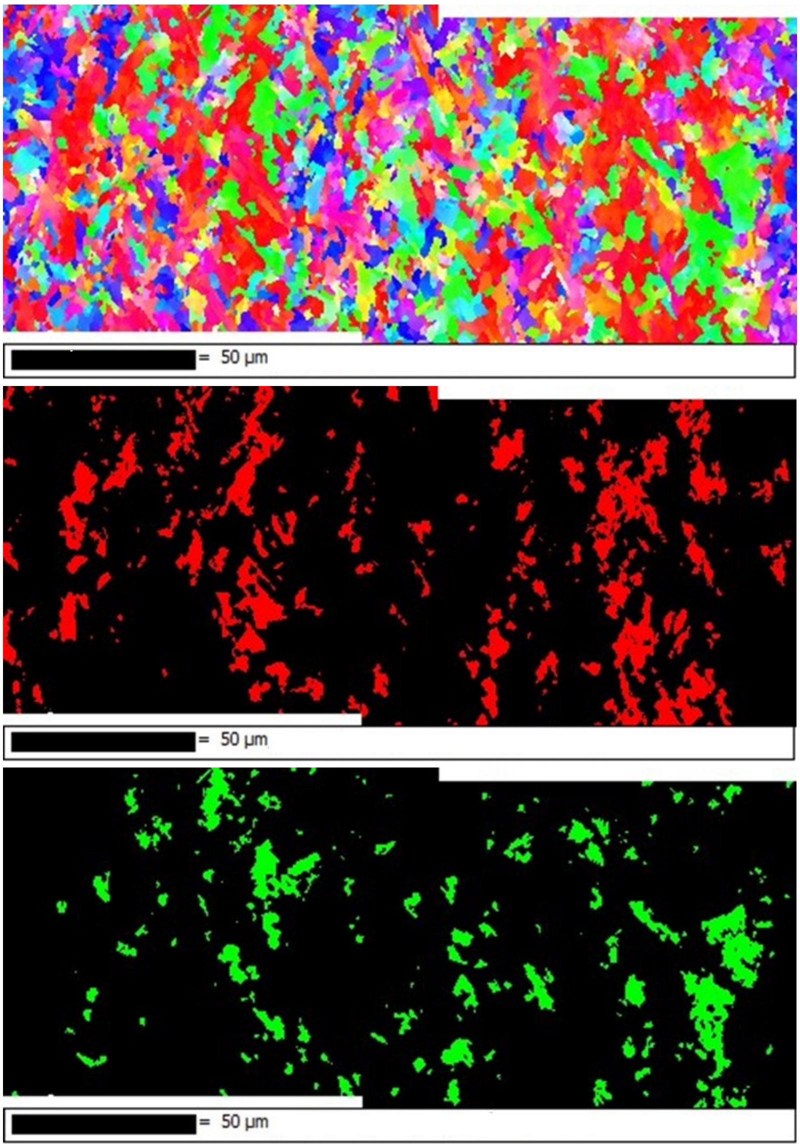

Figure 5.27. AW weld line at mid-thickness EBSD maps. IPF (top), {100} texture component map (centre), and {110} texture component map (bottom).

The IPF and texture component maps for the base metal are displayed on Figure 5.26. It can be observed that the grains orientated for easy fracture were small and well dispersed. This would provide the material with good toughness since there were no easy cleavage crack propagation paths. However, this was not observed for the AW weld line.

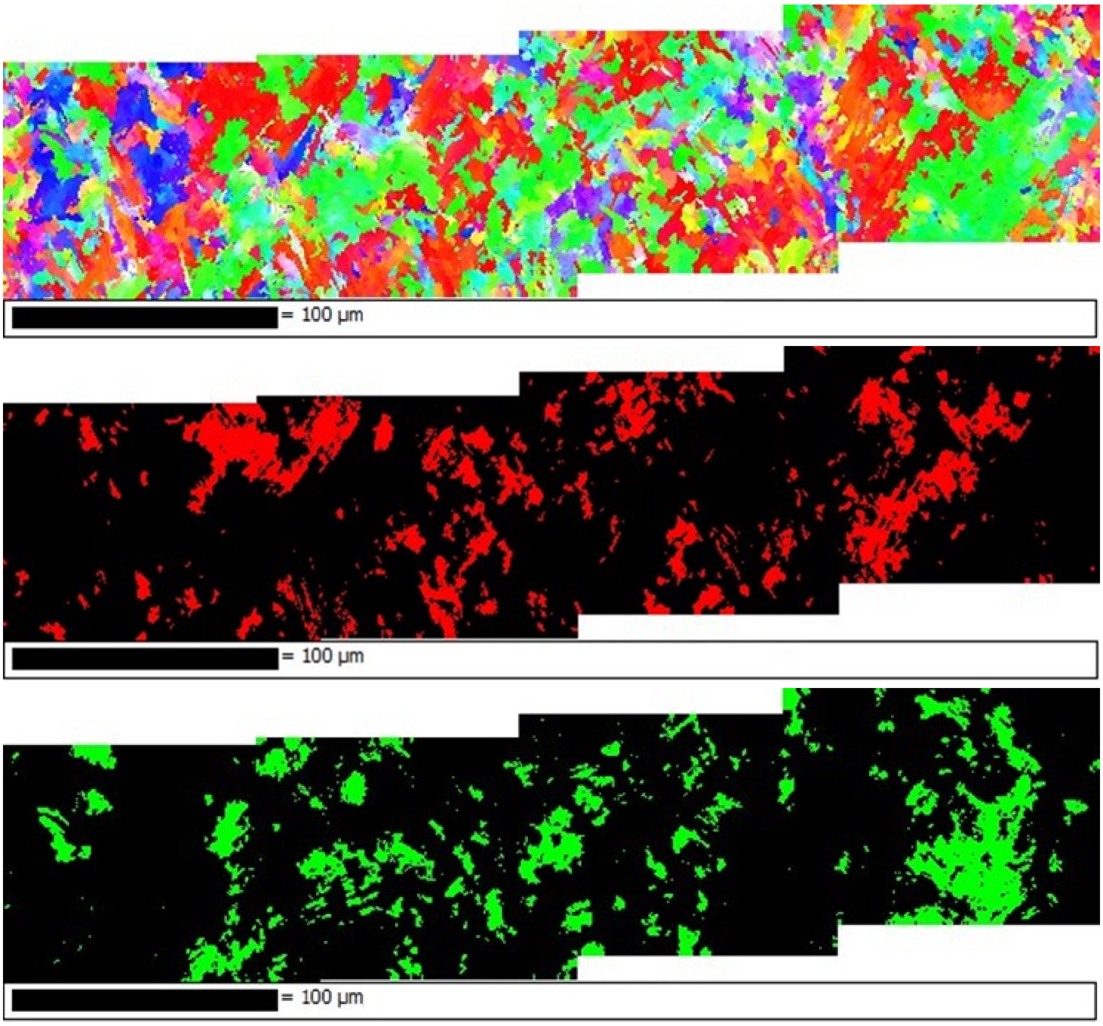

Figure 5.28. AW weld line near inner pipe surface EBSD maps. IPF (top), {100} texture component map (centre), and {110} texture component map (bottom).

The EBSD maps for the AW weld line at the mid-thickness and near the inner pipe surface are displayed on Figure 5.27 and Figure 5.28 respectively. At both the mid-thickness and near the inner pipe surface the grains orientated for easy fracture were large and very near connected. This meant that the weld line would offer extremely poor resistance to cleavage crack propagation, since the crack would be able to propagate easily from one grain to the next. There were some differences between the two locations of the weld line analysed. The width of the weld line was approximately

150 µm and 300 µm at the mid-thickness and near the inner pipe surface respectively. This was a direct result of the greater heating towards the strip edge corners as more material was melted there. The grain structures on the EBSD maps were also visually different. Near the inner pipe surface the grains were visually larger and somewhat more clustered, displaying that the weld lines resistance to cleavage crack propagation was worse towards the outer surfaces of the pipe.

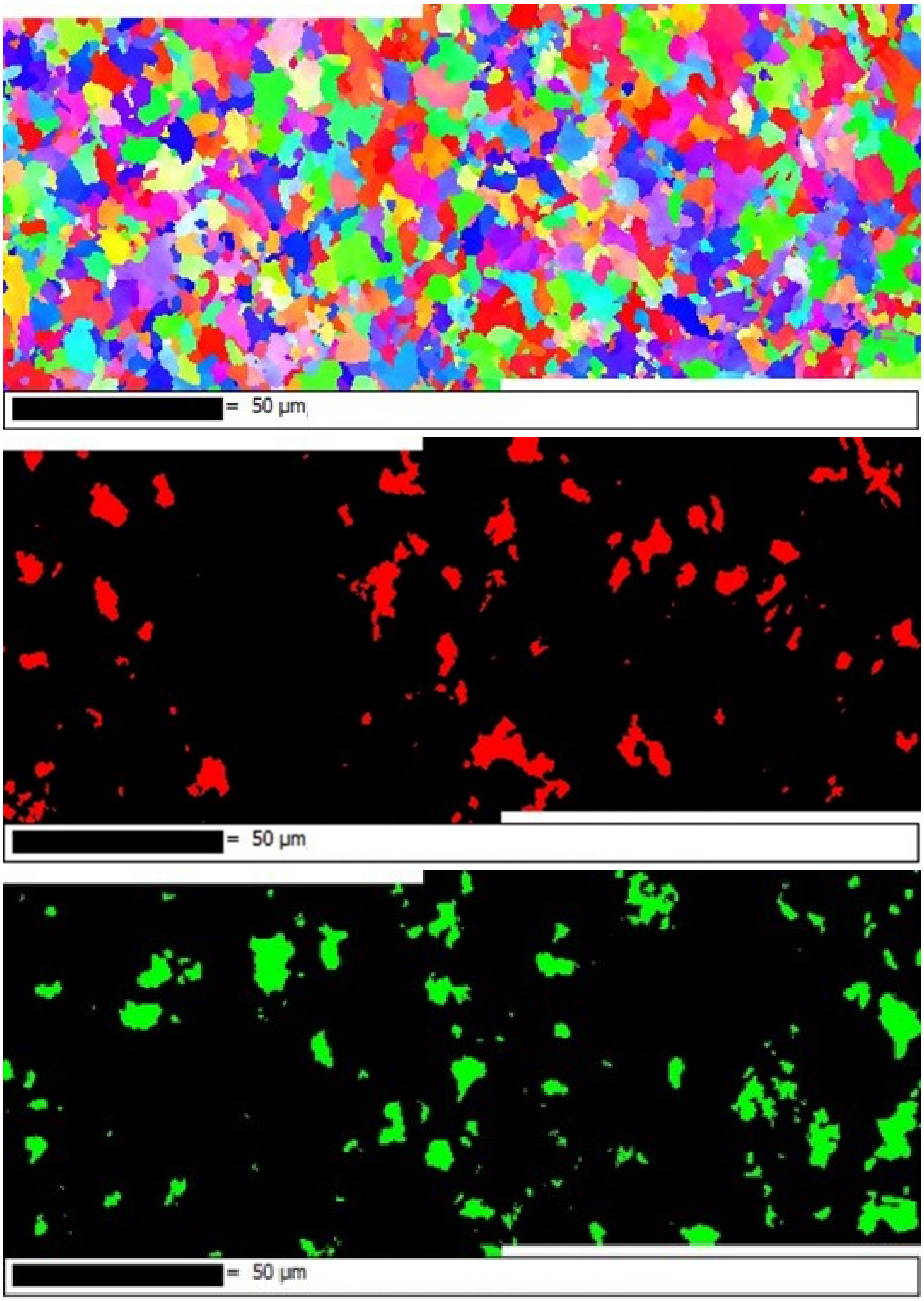

Figure 5.29. HT weld line at mid-thickness EBSD maps. IPF (top), {100} texture component map (centre), and {110} texture component map (bottom).

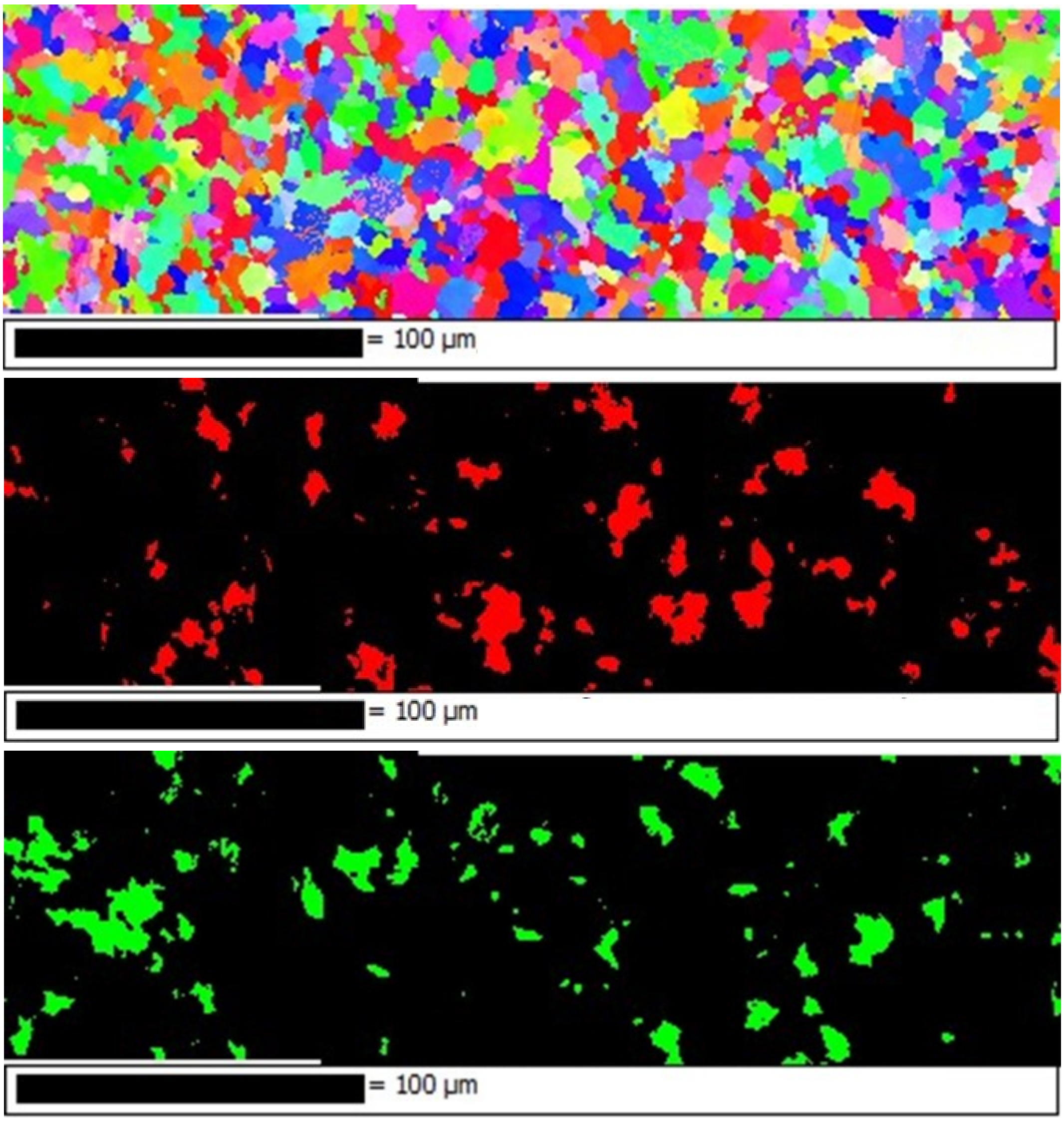

Figure 5.30. HT weld line near inner pipe surface EBSD maps. IPF (top), {100} texture component map (centre), and {110} texture component map (bottom).

Following the PWHT, the EBSD maps on Figure 5.29 and Figure 5.30 visually displayed that the grains orientated for easy fracture at the weld line were still large. However, they were no longer clustered together. This would have been beneficial to the toughness of the weld line since there were no easy propagation paths, meaning that there would be more energy absorption as the crack propagated through the weld line. However, the fraction of grains orientated for easy fracture was still large, as well as the grains themselves. Therefore, it would be expected that the toughness improvements would not be substantial here.

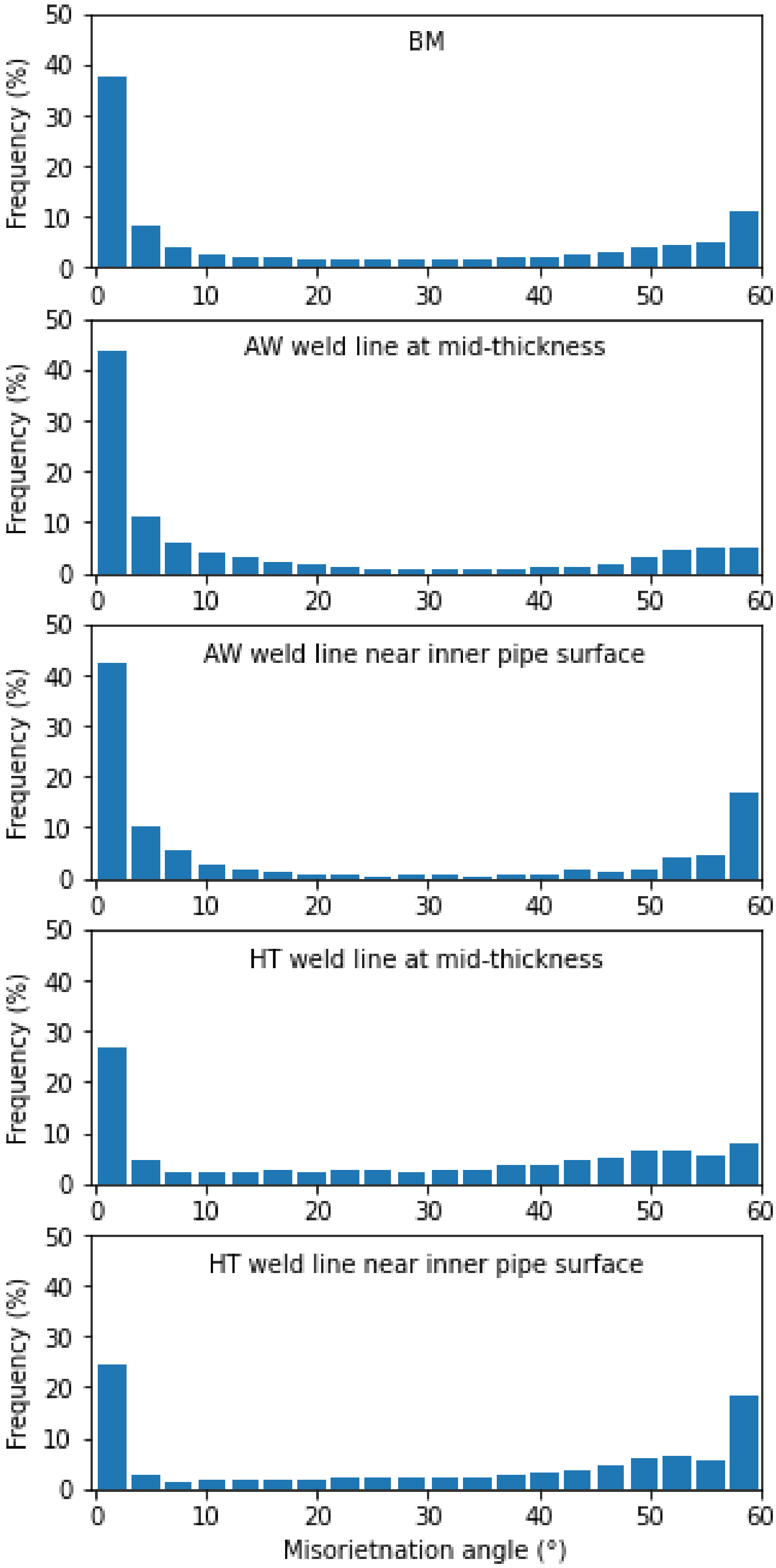

Figure 5.31. Grain boundary misorientation distributions.

Figure 5.31 displays the grain boundary misorientation distributions for the base metal and the different locations within the AW and HT weld line. When comparing the base metal with the AW weld line it was observed that the percentage of grain boundaries with misorientation angles lower than 15° was increased. These were considered as Low Angle Grain Boundaries (LAGBs). This would have been detrimental to the toughness since HAGBs play an important role in toughness as they offer resistance to cleavage crack propagation [43,44]. The increase in percentage of LAGBs was expected to be seen since when analysing the EBSD maps the grains orientated for easy fracture were clustered together.

The percentage of LAGBs was reduced by the PWHT, where they were reduced to a percentage that was lower than that of the base metal. This would be beneficial to the toughness as more energy would be absorbed during cleavage crack propagation through the weld line. The EBSD maps displayed that both the {110} and {100} planes orientated within 10° to the weld plane were both more dispersed following the PWHT. However, it was important to remember that the crystallographic texture of the HT weld line was still extremely poor when compared to that of the base metal. Consequently, the increase in percentage of HAGBs would not be able to negate the poor texture and a poor resistance to cleavage crack propagation was still expected to be seen.

5.1.4 Summary

- The TMAZ and HAZ presented themselves as poor sources of toughness, however they were completely removed by the PWHT. Therefore, it was extremely unlikely that they would play a role in negatively affecting the toughness of the weld.
- The microstructure at the AW weld line contained features that are associated with poor toughness. These included a large grain size, Widmanstätten ferrite and M-A islands. These features would have promoted cleavage fracture initiation as well as offering very little resistance to cleavage crack propagation. There was a change in microstructure observed through the depth of the weld line where the grain size was largest near the outer pipe surfaces and the M-A constituent was large with an elongated morphology here. This suggest that by reducing the high temperatures at the strip edge corners the

overall toughness of the weld line could be increased by improving the microstructure towards the top and bottom of the weld.

- The PWHT removed the undesirable microstructure produced at the weld line and replaced it with one consisting of equiaxed allotriomorphic ferrite. This microstructure was very similar in appearance to that of the base metal. However, a large grain size still remained at the weld line which can negatively influence the toughness. The persisting large grain size was most likely caused by structural heredity or the dissolution of NbC precipitates.
- A poor crystallographic texture was produced at the AW weld line. There was a large percentage of grains orientated for easy fracture which were near connected, making it easy for cleavage cracks to propagate. There was also a reduction in {110} planes which further reduced the material’s resistance to cleavage fracture propagation.
- Even following a PWHT the poor crystallographic texture remained at the weld line, where a large percentage of grains were still orientated for easy fracture. Furthermore, the percentage of {110} grains orientated within 10° of the weld plane was further reduced. Therefore, a large improvement in toughness of the weld line following a PWHT was not expected to be seen. The continuing crystallographic texture was most likely caused by a texture memory effect.
- In the AW weld line, there was a reduction in the number of HAGBs when compared to the base metal, which was expected to be seen due to the clustering of grains orientated for easy fracture. However, following the PWHT the number of HAGBs was increased to a higher percentage than that of the base metal.

5.2 Charpy impact testing

5.2.1 Charpy impact testing data analysis

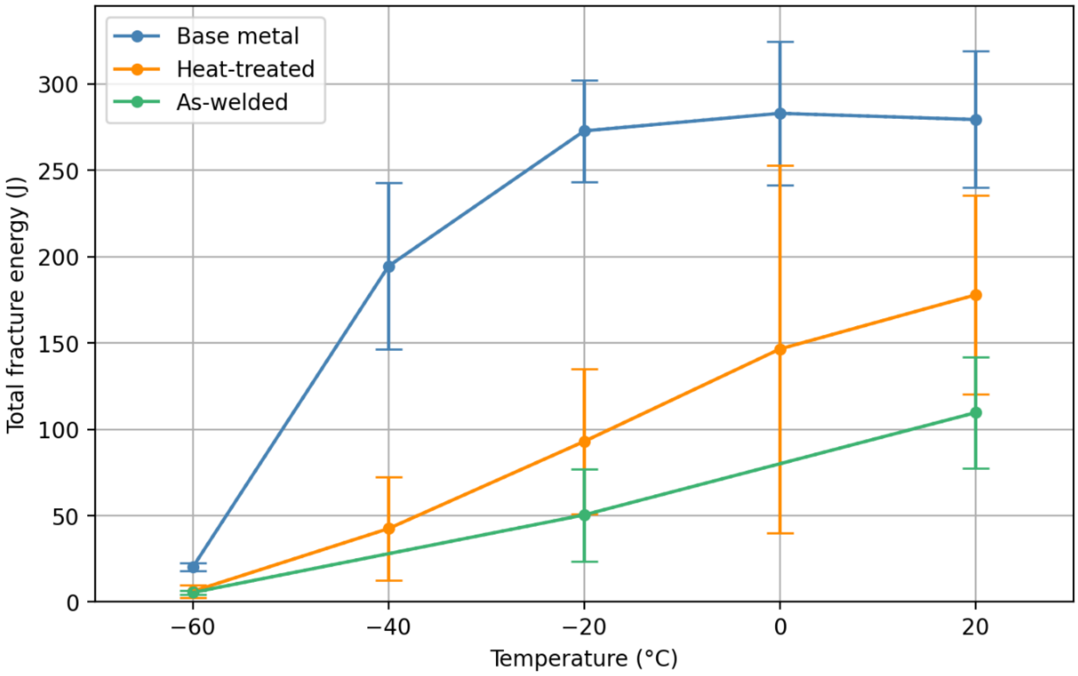

Figure 5.32. Charpy impact testing joule energy.

The Charpy impact energies associated with the whole fracture as a function of temperature are displayed on Figure 5.32. It was observed that the BM specimens possessed the greatest absorbed energies across the entirety of the test temperature range. They were 279 J, 283 J, 273 J, 195 and 20 J at ambient, 0 °C, -20°, -40 °C and -60 °C respectively. The BM material displayed an upper shelf region from ambient to -20 °C, where the USE was approximately 278 J. Therefore, the BM displayed good toughness at temperatures of -20 °C and higher. At -60 °C the absorbed energy was extremely low; hence it was likely that the lower shelf region was reached, and the material had become extremely brittle. The transition region approximately ranged from -20 °C to -60 °C since the upper shelf and lower shelf regions started at these temperatures respectively. Therefore, the DBTT was estimated to be -40 °C.

As expected, the AW specimens displayed the lowest total absorbed energies across the whole test temperature range. The results were 110 J, 50 J and 5 J at ambient, -20° and -60 °C respectively. At ambient and -20 °C, the results were considerably lower than that of the BM specimens. The reduction in toughness was expected to be seen due to the microstructure produced at the weld line which had a large grain size, poor crystallographic texture and constituents that offered little resistance to cleavage crack propagation. Unlike the BM, the AW results did not display an upper shelf region and consequently the DBTT could not be estimated. The absence of distinguishable regions is not unusual and has been observed in high carbon steels [162]. Also, the large intervals between test temperatures could possibly have been another reason why the different regions were not captured, if any were present.

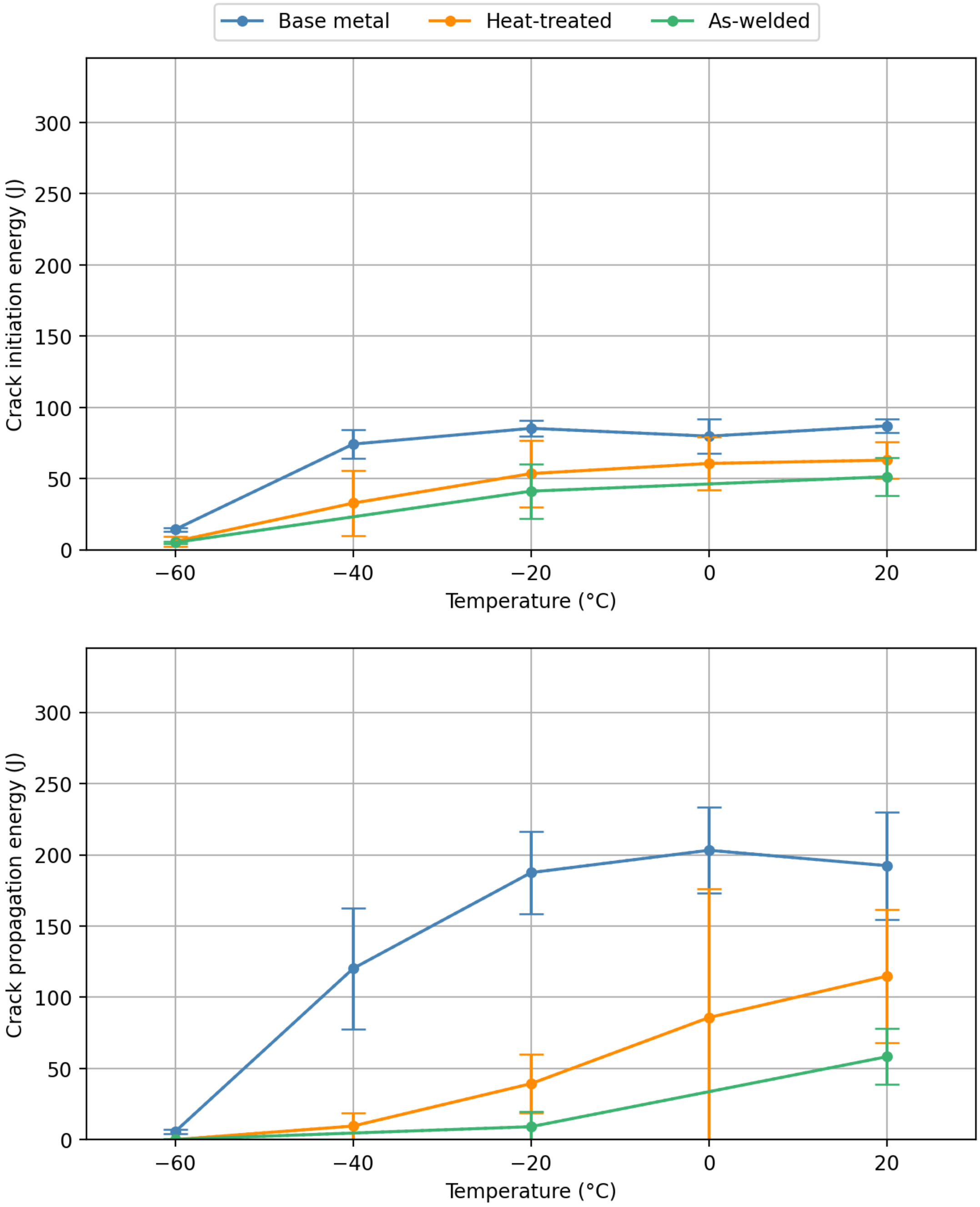

Figure 5.33. Charpy impact testing absorbed energy until fracture initiation (top) and absorbed energy during crack propagation (bottom).

The HT results were 178 J, 146 J, 93 J, 42 J and 6 J at ambient, 0 °C, -20°C, -40 °C and -60 °C respectively. This displayed that the PWHT improved the toughness of the weld line, however the absorbed energies were still much lower than that of the BM. The poor toughness at the weld line, relative to the toughness of the BM, was a result of the large grain size and poor crystallographic texture remaining even after following a PWHT. Just like the AW results there were no distinguishable regions. At 0 °C the standard deviation was large, displaying a wide scatter in the results which could have potentially been caused by several different factors. It is typical to see a large scatter in results between the upper and lower shelves. This occurs because small differences in microstructure between the specimens cause the material to become brittle at slightly lower or higher temperatures. These small changes in microstructure may have been intensified by the gradient of microstructure previously observed through the depth of the weld line. It would have also been impossible to machine the Charpy impact specimens from the exact same depth in the pipe segments, which also may have caused slight differences in microstructure. Although numerous test specimens were checked to ensure the weld line was located within the radius of the v-notch, on some specimens the location of the weld line may have not been optimal. This would be due to the difficulty of producing the test specimens, where a 150 µm wide weld line has to be positioned within a 0.25 mm radius. During welding, defects or inclusions can be produced on the bond plane which will reduce the toughness [92]. If these are only present in some specimens it will also cause a large scatter in results.

At -60 °C, all the specimens displayed very low Charpy impact joule energies, where the standard deviations were also small. At this temperature it was highly probable that the material as a whole had become very weak, where inclusions or defects would have had a minor influence on the overall toughness.

The instrumented head allowed absorbed energies at specific fracture events to be recorded. Figure 5.33 displays the absorbed energy up until fracture initiation and the absorbed energy during crack propagation, on the top and bottom plots respectively. The BM specimens possessed the greatest fracture initiation energy across the entirety of the test temperature range. The results were 87 J, 80 J, 85 J, 74 J and 14 J at ambient, 0 °C, -20 °C, -40 °C and -60 °C respectively. From ambient to -40 °C the fracture initiation energies were very similar, although there was a slight decrease at -40 °C. Therefore, the temperature did not greatly affect the fracture initiation energy over this temperature range. However, at -60 °C the fracture initiation energy had become extremely small. This indicated that the material's resistance to crack initiation had been deteriorated at this temperature. The fracture initiation energies were much lower than that of the total absorbed energies, although this was not the case at -60 °C. The fracture initiation energies as a percentage of the total absorbed energies were 31%, 28 %, 31 %, 38 % and 70 % at ambient, 0 °C, -20 °C, -40 °C and -60 °C respectively. Therefore, for temperatures below -20 °C the proportion of total absorbed energy associated with fracture initiation increased. The crack propagation energies for the BM specimens were 192 J, 203 J, 188 J, 120 J and 6 J at ambient, 0 °C, -20 °C, -40 °C and -60 °C respectively. In the upper shelf region, a large part of the total absorbed energy was associated with the crack propagation energy. The crack propagation energies as a percentage of the total absorbed energies were 69%, 72 %, 69 %, 62 % and 30 % at ambient, 0 °C, -20 °C, -40 °C and -60 °C respectively. This displayed that in the upper shelf temperature range the BM specimens were very resistant to crack propagation. Although below -20 °C the material's ability to inhibit crack propagation decreased with dropping temperature.

The fracture initiation energies for the HT specimens were lower than that of the BM specimens, nevertheless the difference wasn't as considerable as when comparing the total absorbed energies. 63 J, 61 J, 54 J, 33 J and 6 J were the fracture initiation energies for the HT specimens at ambient, 0 °C, -20 °C, -40 °C and -60 °C respectively. However, there was a much larger difference in crack propagation energies between the HT and BM specimens. The crack propagation energies for the HT specimens were 114 J, 86 J, 39 J, 10 J and 0 J at ambient, 0 °C, -20 °C, -40 °C and -60 °C respectively. The HT specimens having a much lower resistance to crack propagation was a result of the poor crystallographic texture present at the weld line. Here a high percentage of grains had their {100} plane aligned within 10° to the weld plane, which offered very little resistance to crack propagation [49].

The fracture initiation energies for AW specimens were 51 J, 41 J and 5 J at ambient, -20 °C and -60 °C respectively. These were not considerably lower than that of the HT specimens. The crack propagation energies for AW specimens were 58 J, 49 J and 0 J at ambient, -20 °C and -60 °C respectively. Therefore, the AW specimens displayed very similar fracture initiation and crack propagation energies. Again, the poor crack propagation resistance was a result of the poor crystallographic texture.

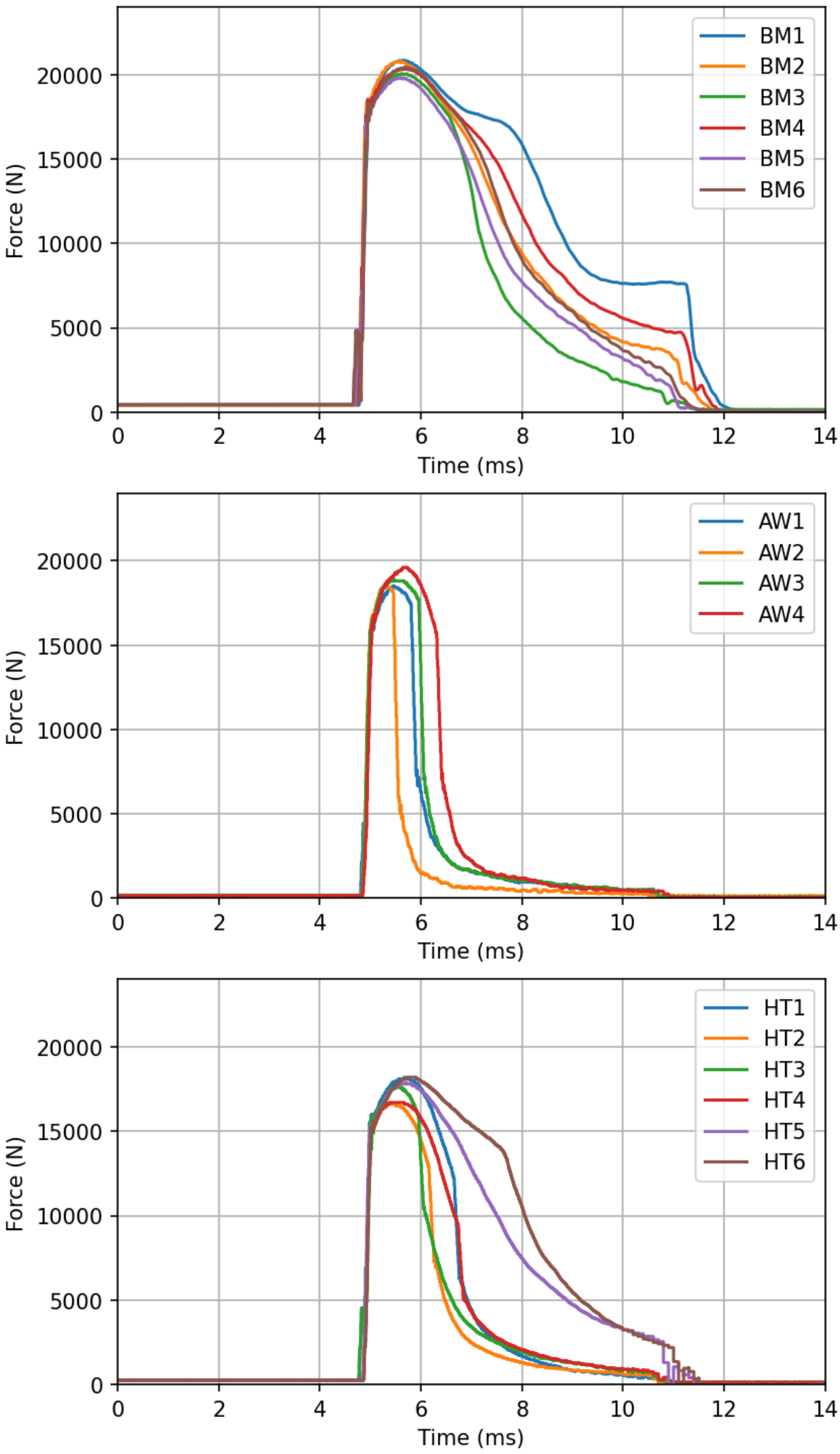

Figure 5.34. Ambient force-time plots. BM (top), AW (middle), and HT (bottom).

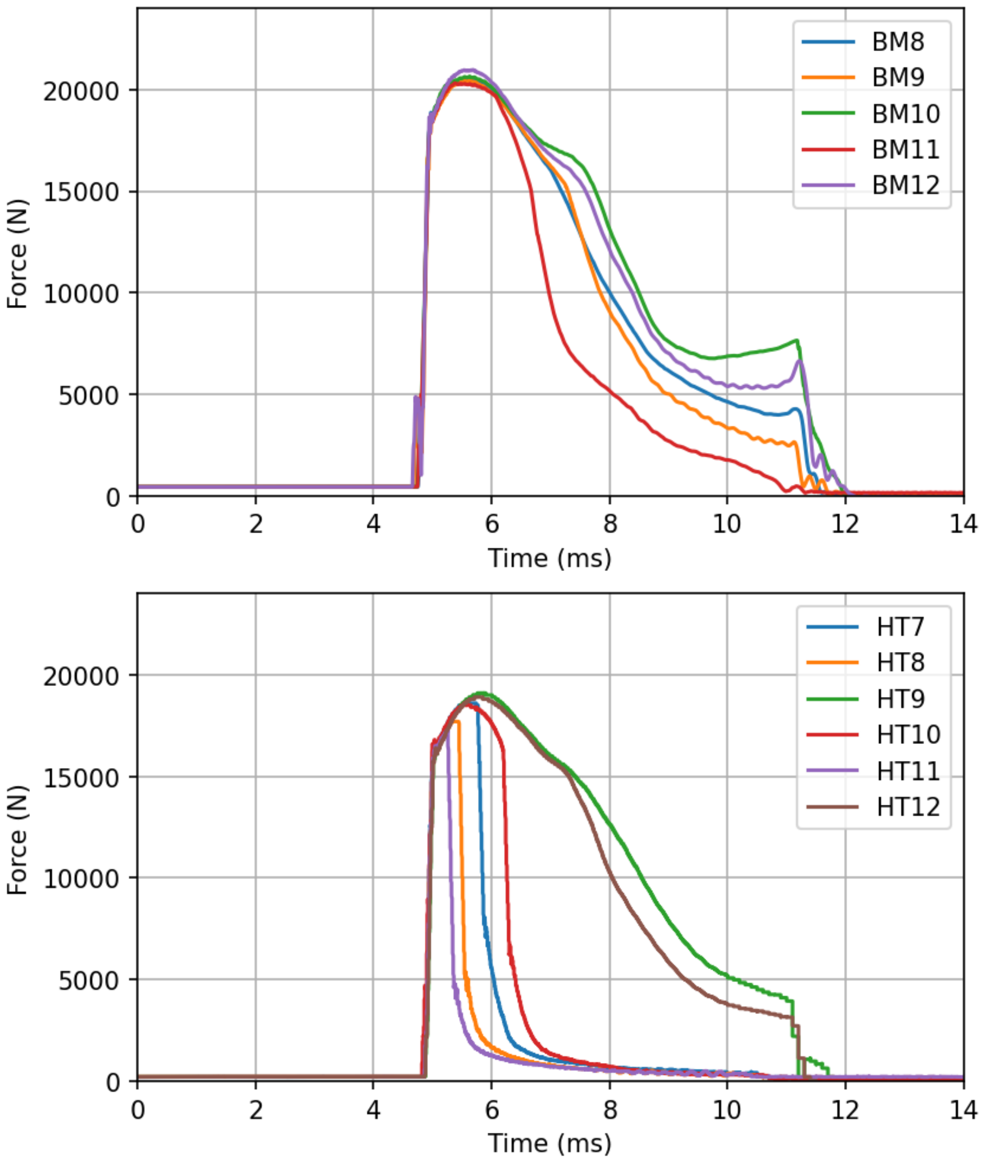

Figure 5.35. 0 °C force-time plots. BM (top) and HT (bottom).

At ambient temperature the shape of the curves on the force-time plots displayed that the BM specimens experienced fully ductile fractures and had high total absorbed energies. The force time-plots at ambient temperature are displayed on Figure 5.34. The BM specimens produced the greatest average yield and max forces, which were approximately 18,800 N and 20,400 N respectively. This was most likely due to the finer grain size of the BM specimens when compared to that of the HT and AW, since the strength of steel increases as the grain size is refined [38]. The shallow decrease in force demonstrated that the BM specimens were resistant to crack propagation, which could be attributed to the small percentage of grains with their {100} plane aligned parallel to the bond plane.

The force-time curves for the AW specimens displayed that the AW specimens had a much lower toughness than the BM specimens, due to the much smaller areas under the curves. The AW fractures experienced both ductile and brittle fracture even at ambient temperature. However, the fractures were dominated by brittle fracture shown by the large crack instability phase on each of the curves. The inferior toughness was a product of the undesirable microstructure produced at the weld line. All the AW specimens tested at ambient temperature displayed a crack stability phase before cleavage fracture initiation apart from AW2, where fracture initiation was directly followed by the crack instability phase. On this specimen there may have been a feature promoting cleavage fracture initiation.

At ambient temperature the majority of the HT specimens experienced a mixture of ductile and brittle fracture, however two specimens displayed fully ductile fractures. These were HT5 and HT6. The variation in fracture type explains the large standard deviation in total absorbed energy for the HT specimens. The greater area under the curves, when compared to the AW curves, displayed that the PWHT improved the toughness of the weld. The HT specimen’s fractures were also less brittle than the AW specimens since the crack instability phases were smaller. This showed that the HT specimens were more resistant to cleavage crack propagation than the AW specimens. The improvement in resistance to crack propagation was a result of the reduction in the percentage of grain orientated for easy fracture. Also, the grains orientated for easy fracture were not clustered together, meaning there were no easy paths for cleavage crack propagation. The AW specimens displayed a higher average max force at ambient temperature than the HT specimens. This was due to the presence of Widmanstätten ferrite in the AW weld line, since yield strength increases with its volume fraction [163].

Even at 0 °C, two of the HT specimens displayed fully ductile fractures. These are HT9 and HT12 shown on Figure 5.35, and had very similar curves to the fully ductile HT fractures experienced at higher temperatures. However, the specimens which produced a mixture of ductile and brittle fractures displayed worse toughness characteristics than at ambient temperature. This was shown by a reduction in the areas under the curves and the larger crack instability phases. HT8 and HT11 displayed extremely brittle fractures.

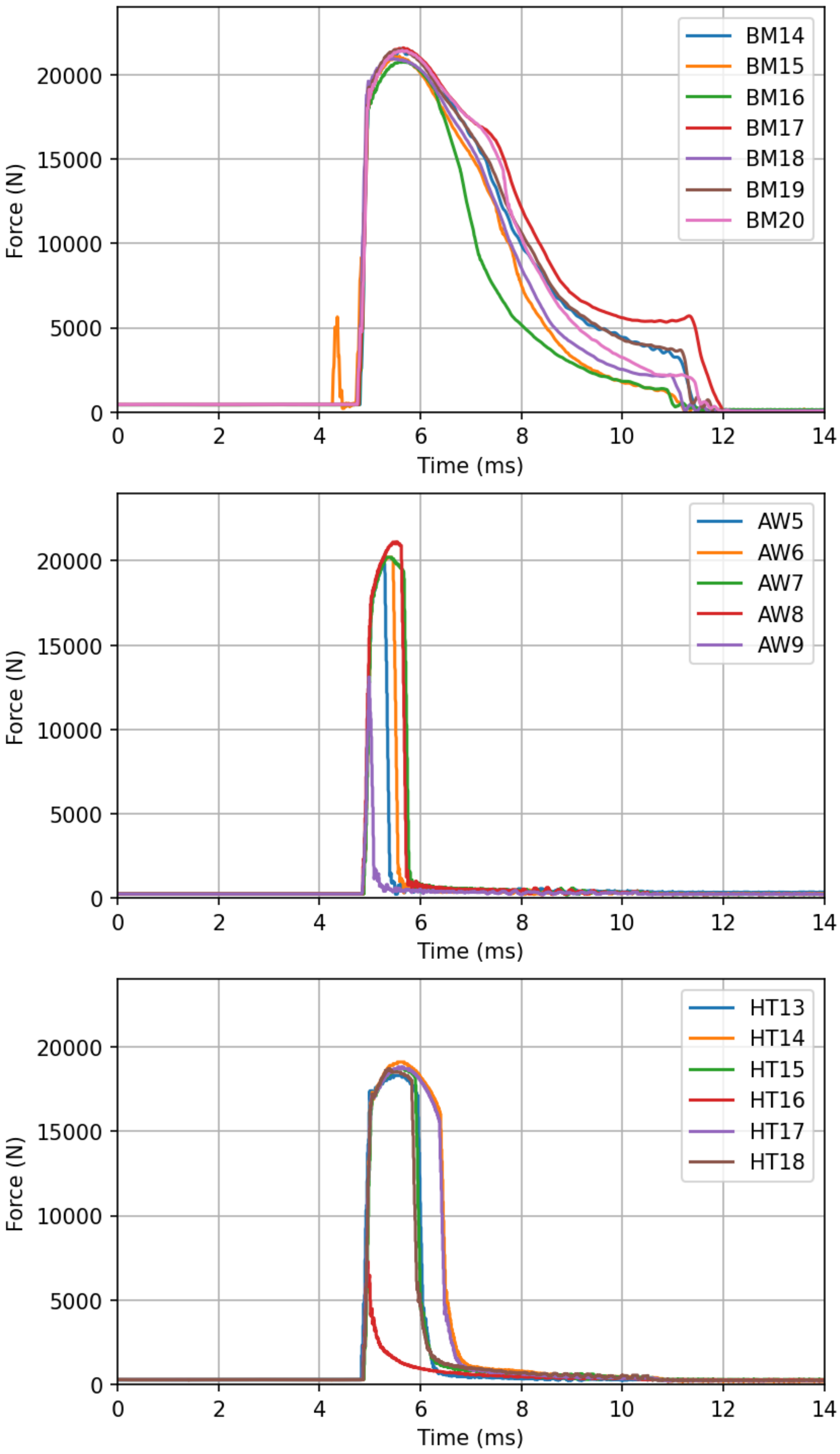

Figure 5.36. -20 °C force-time plots. BM (top), AW (middle), and HT (bottom).

The only noticeable change in the BM curves from ambient to -20 °C, was that there was an increase in the average max forces, where they were 20,400 N, 20,900 N and 21,300 N respectively. The increased happened because the UTS of steel increases as temperature decreases [164]. This occurs since dislocations have less mobility to move due to the lower thermal energies [165].

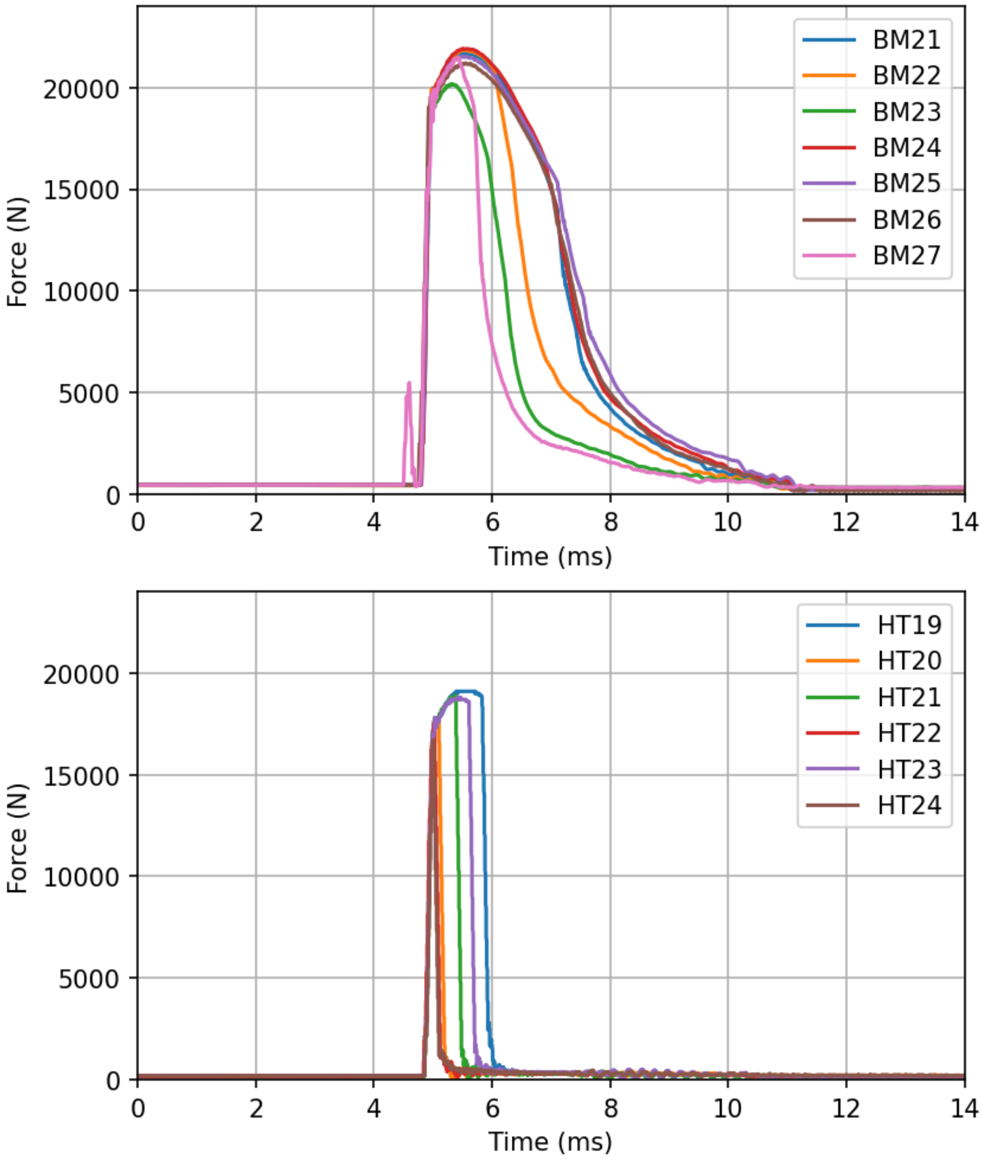

Figure 5.37. -40 °C force against time plots. BM (top) and HT (bottom).

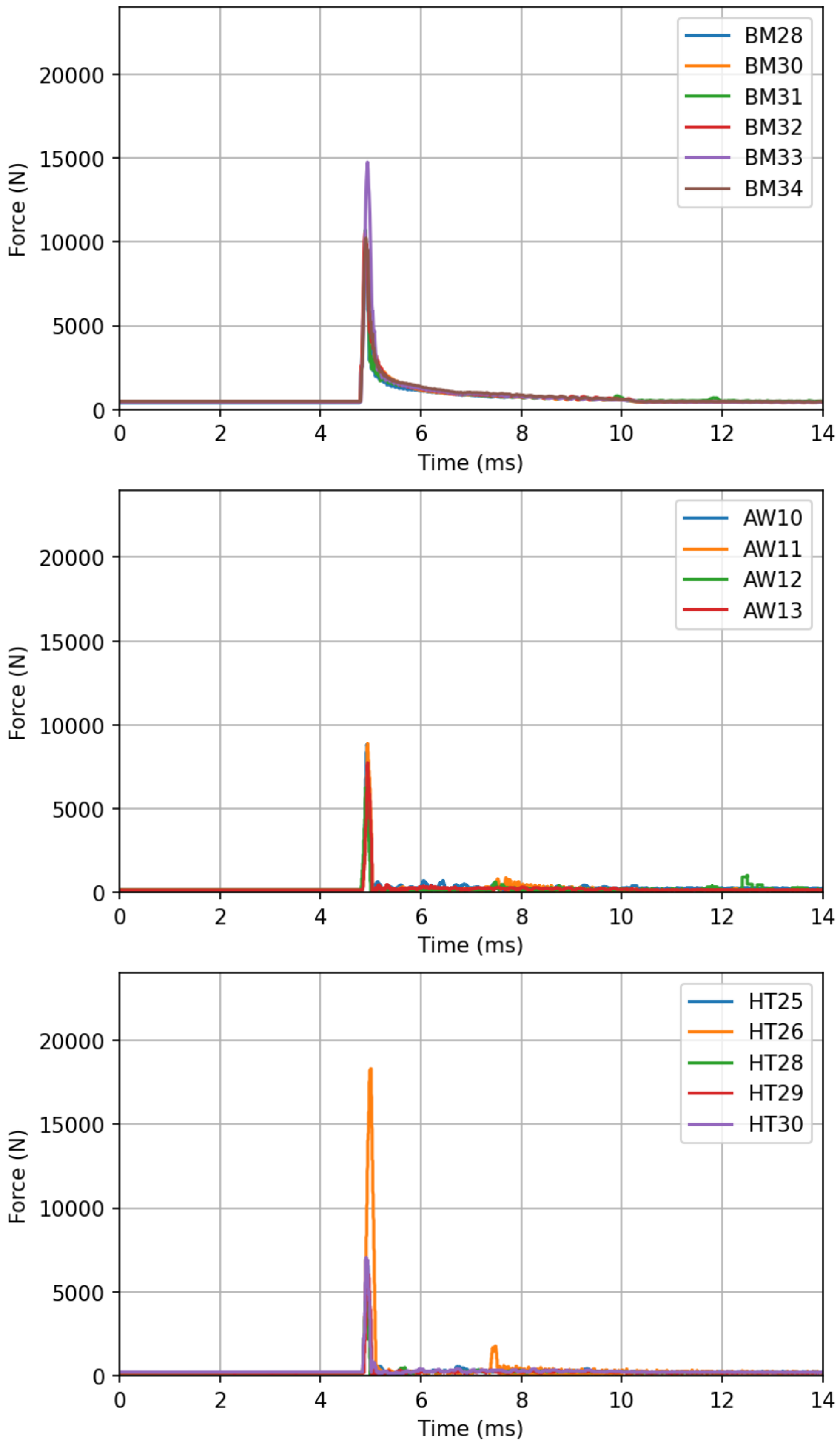

Figure 5.38. -60 °C force-time plots. BM (top), AW (middle), and HT (bottom).

Unlike the BM specimens, the AW and HT specimens had curves that displayed a deterioration in toughness with each drop in temperature from ambient to -20 °C. At a temperature of -20 °C all of the HT specimens displayed a mixture of ductile and brittle fracture where brittle fracture was extremely dominant. The crack instability phases were very large with only a small amount of crack arrest following. HT16 had an extremely brittle fracture since fracture initiation was directly followed by the crack instability phase. It was strongly probable that a specific feature was promoting cleavage fracture initiation. Similar was observed on the AW curves where the toughness was deteriorated with the decrease in temperature. However, the stable crack propagation phases were extremely minor in the AW specimens and crack arrest was also very small. All the AW curves were relatively consistent apart from AW9 which had an extremely brittle fracture with a low absorbed energy, where ductile fracture was only observed during crack arrest. Again, there may have been a feature promoting cleavage fracture initiation at the weld line.

The first considerable change in the shape of the BM curves was observed at -40 °C. The force time-plots at -40 °C are displayed on Figure 5.37. There was a significant reduction in the area under the curves demonstrating that the total absorbed energy had been reduced, meaning that the fractures were taking place within the transitional zone temperature range. Although the areas under the curves had been reduced, the curves showed that the fractures were still fully ductile. However, the rate in decrease of force through the crack stability phase was much faster. The steeper decrease in force meant that the crack propagation speed had increased, revealing that the materials resistance to crack propagation had fallen.

The biggest change in shape of the BM curves was observed at -60 °C. At this temperature the curves displayed highly brittle fractures. The force against time plots for -60 °C are displayed on Figure 5.38. At this temperature the area under the BM curves was extremely small, demonstrating that the toughness was greatly deteriorated. There was no stable crack propagation phase present before cleavage fracture onset. The curves were highly dominated by brittle fracture, however there was some ductile fracture since there was crack arrest present following the crack instability phase. Therefore, the BM specimens were able to offer a small amount of resistance to cleavage crack propagation. Although, the BM specimen's ability to resist crack propagation was much lower than at higher temperatures. The HT and AW specimens displayed very similar curves at -60 °C, where all the curves demonstrated fully brittle fractures. Since there was no crack arrest stage present the materials resistance to cleavage crack propagation was extremely poor and less than that of the BM specimens.

5.2.2 Fracture surface analysis

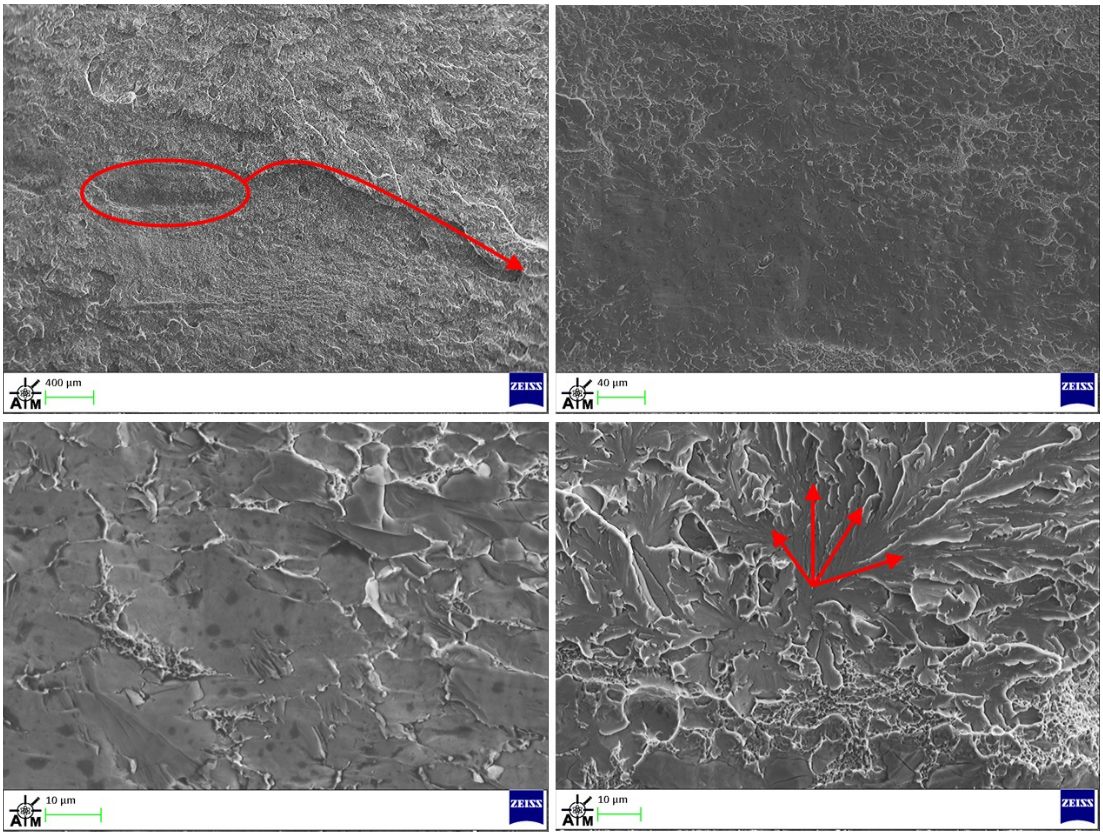

Figure 5.39. SEM images of defect on the fracture surface of the weakest AW specimen tested at ambient temperature. Defect and crack propagation path (top left), defect (top right), defect surface (bottom left) and crack initiation site propagating from edge of defect (bottom right).

When evaluating the fracture surfaces of the BM specimens, it was found that all the fractures were fully ductile from ambient to -40 °C and none of the specimens fully separated across this temperature range. Since all these fractures were fully ductile, they were not analysed under SEM. From ambient to -20 °C, the fractures were extremely similar, where there was a large amount of plastic deformation and necking present. Although the specimens tested at -40 °C experienced fully ductile fractures, the fracture was visually different to the specimens tested at higher temperatures, where the specimens tested at -40 °C displayed lower amounts of plastic deformation and necking. This was also observed on the force-time plots where the material's resistance to ductile crack propagation was reduced at -40 °C.

At ambient temperature all of the AW specimens experienced a mixture of ductile and brittle fracture, where none of the specimens were completely separated. The average percentage of ductile fracture was estimated to be 44 %. This was much lower than the BM which displayed 100 % ductile fracture. Therefore, the microstructure at the AW weld line was particularly brittle when compared to the BM at ambient temperature.

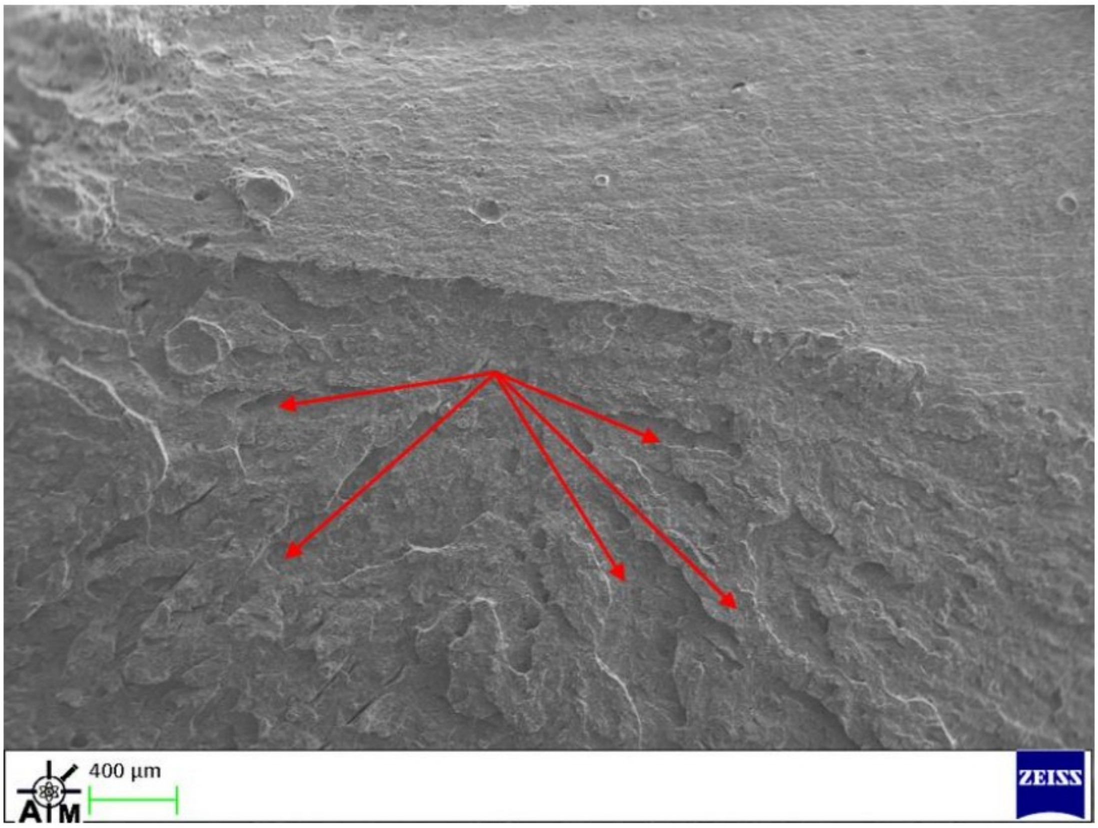

Figure 5.40. Cleavage fracture propagation paths on AW specimen with greatest Charpy impact toughness at ambient temperature.

AW2, on Figure 5.34, was chosen for fracture surface analysis because it was the specimen that produced the lowest total absorbed energy at ambient temperature which was considerably lower than the average of the AW specimens, where the absorbed energies were 67 J and 110 J respectively. The weakest specimen also had a lower percentage of ductile fracture, which was 33 %. Therefore, it displayed poor toughness characteristics when compared to the other AW specimens tested at ambient temperature.

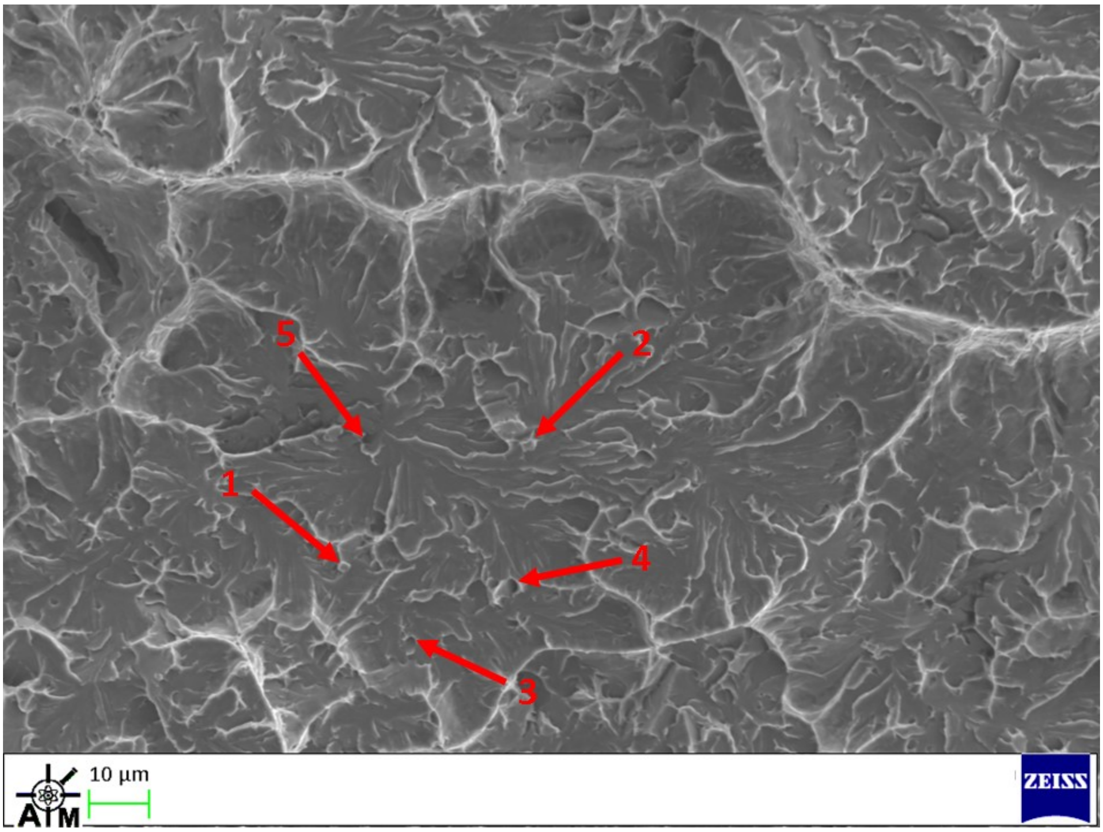

Figure 5.41. SEM image of fracture initiation site of AW specimen tested at ambient temperature with the highest toughness.

When inspecting the fracture surface of this specimen under a SEM, there were dark features visible at the centre of the brittle fracture zone that were relatively smooth and featureless. These features are displayed on Figure 5.39. EDS analysis revealed that these dark patches consisted of the same chemistry as the base metal. Consequently, it was concluded that these features were weld defects caused by lack of fusion. They were most likely caused by a pre-arc which would have occurred when the high frequency jumped between the strip edges, momentarily robbing the heat from the strip edges as the current was diverted [166]. On the top left image of Figure 5.39 the largest defect has been highlighted by the red circle and a cleavage crack propagation path can be seen initiating at the edge of the defect. The size of this defect was approximately 1150 µm long and 150 µm wide. The bottom right image shows the cleavage fracture initiation site at the edge of the defect. Cleavage fracture appeared to initiate at a large grain or grain boundary. The fracture did not initiate within the defect itself since it was a lack of fusion defect. The absorbed energy at fracture initiation for this specimen was 36 J, where the average for the AW specimens at ambient was 51 J. Therefore, it was concluded that brittle fracture was initiating at this defect and consequently deteriorating the toughness. Since the lack of fusion defect cannot be removed by a PWHT it is paramount that they are not formed during welding to ensure good weld quality.

AW4 was the AW specimen that produced the highest toughness at ambient temperature, so was therefore chosen for fracture analysis. When initially inspecting the fracture surface, cleavage crack propagation paths could be seen radiating from a fracture initiation site. This can be seen on Figure 5.40. The cleavage fracture initiation site was located at the edge of the brittle fracture zone that was closest to the notch. When following the cleavage fracture propagation paths to the cleavage fracture initiation site no inclusions were found. However, at the fracture initiation site smooth and blocky particles were found that had the typical appearance of M-A constituent. These have been labelled 1 and 2 on Figure 5.41. There were also small voids where particles would have previously been located but then pulled out during fracture. These are labelled 3, 4 and 5 on Figure 5.41. Therefore, it was concluded that cleavage fracture was initiated by M-A constituent. The cleavage fracture facet was also extremely large at the fracture initiation site where it was approximately 40 μm in size. Therefore, it was likely that fracture was initiating at clustered large grains with similar crystallographic orientations. This clustering was observed during the EBSD analysis.

The HT specimens with the highest Charpy impact joule energies, tested at ambient and 0 °C, were not analysed under an SEM because they both experienced fully ductile fractures. However, it was observed that both specimens experienced large amounts of plastic deformation and necking, where there were similar levels of plastic deformation on both specimens.

HT2 and HT11 were the HT specimens that produced the lowest toughness with ductile fracture percentages of 66 % and 23 % at ambient and 0 °C respectively. Their corresponding force-time curves are shown on Figure 5.34 and Figure 5.35. The reduction in ductile fracture percentage demonstrated that the weld line became increasingly brittle with the decrease in temperature, where greater amounts of necking and plastic deformation were clearly visible on the specimen tested at ambient temperature. On both specimens, no inclusions were found on either the cleavage fracture propagation paths or at the cleavage fracture initiation site. However, at the fracture initiation sites a large cleavage fracture facet was present on both specimens suggesting that cleavage fracture was initiating at a large grain. An example of cleavage fracture initiation triggered by a large grain is displayed on Figure 5.42. On each of the HT specimens the size of the facets were approximately 30 µm, which was smaller than observed on AW4.

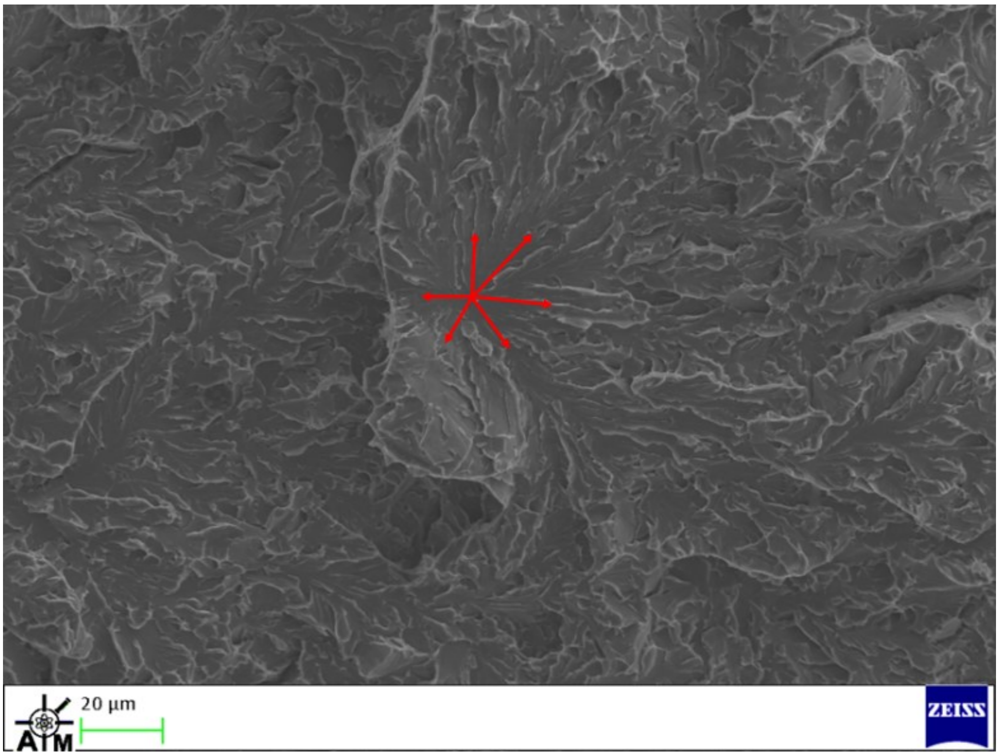

Figure 5.42. Example of cleavage fracture initiation site triggered by a large grain.

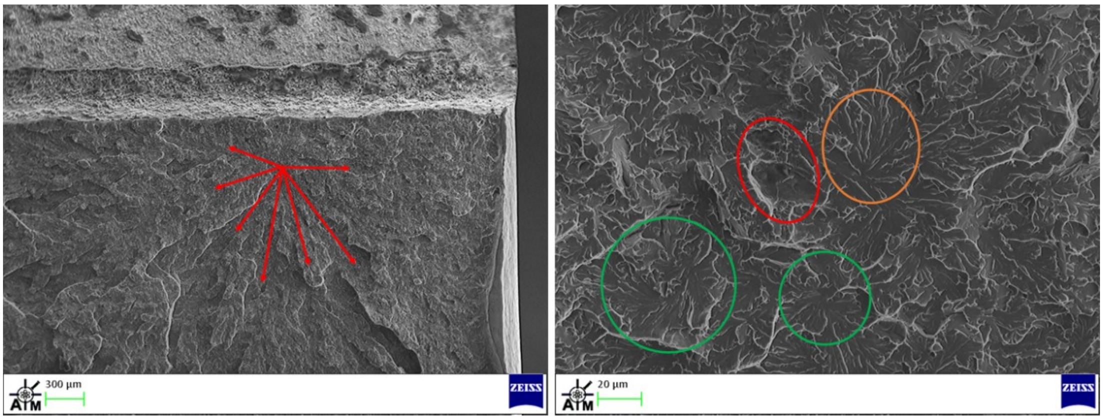

Figure 5.43. SEM image of weakest AW specimen at -20 °C. Crack propagation paths radiating from fracture site (left) and fracture initiation sites (right).

At -20 °C, the weakest AW specimen chosen for analysis had a much lower toughness and ductile fracture percentage than the other AW specimens tested at this temperature.

This was AW9 on Figure 5.36. The toughness and ductile fracture percentage of this specimen were 11 J and 11 % respectively. The average toughness and ductile fracture percentage for the AW specimens at -20 °C were 50 J and 20 % respectively. When initially inspecting the fracture surface there were clear cleavage crack propagation paths radiating from a fracture initiation site. This is displayed on the left image of Figure 5.43. The trigger of cleavage fracture initiation was found to be welding defects, which were large inclusions approximately 15 μm to 20 μm in size. These are highlighted by the red circle. The orange circle highlights cleavage fracture that can clearly be seen initiating and radiating from the edge of the inclusions. The green circles highlight potential cleavage fracture initiation sites that have been triggered by large grains. EDS analysis revealed that the inclusions consisted of aluminium and calcium. It was likely these inclusions were produced during welding and then not removed from the bond plane when the weld rolls squeezed the molten strip edges together. Since inclusions cannot be removed by a PWHT, it is of high importance to ensure sufficient squeeze out during welding to expel inclusions from the bond plane to achieve a good weld.

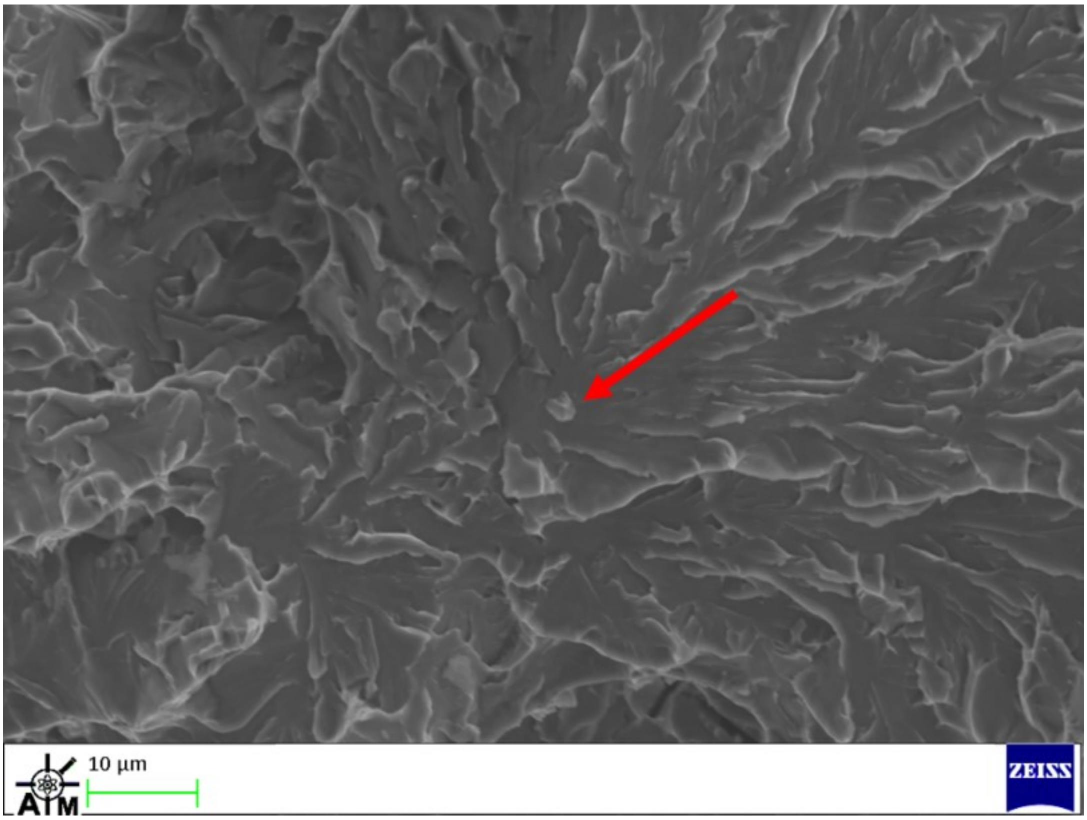

Figure 5.44. SEM image of fracture initiation site of the AW specimen with highest toughness at -20 °C.

Figure 5.44 displays an SEM image of the fracture initiation site of the AW specimen that had the greatest toughness at -20 °C. This was AW7 on Figure 5.36. At the centre of the cleavage fracture initiation site there was a smooth blocky particle present which had the appearance of M-A constituent. Therefore, it was concluded that this was the trigger of cleavage fracture initiation. This type of cleavage fracture initiation trigger was consistent with the toughest AW specimen tested at ambient temperature.

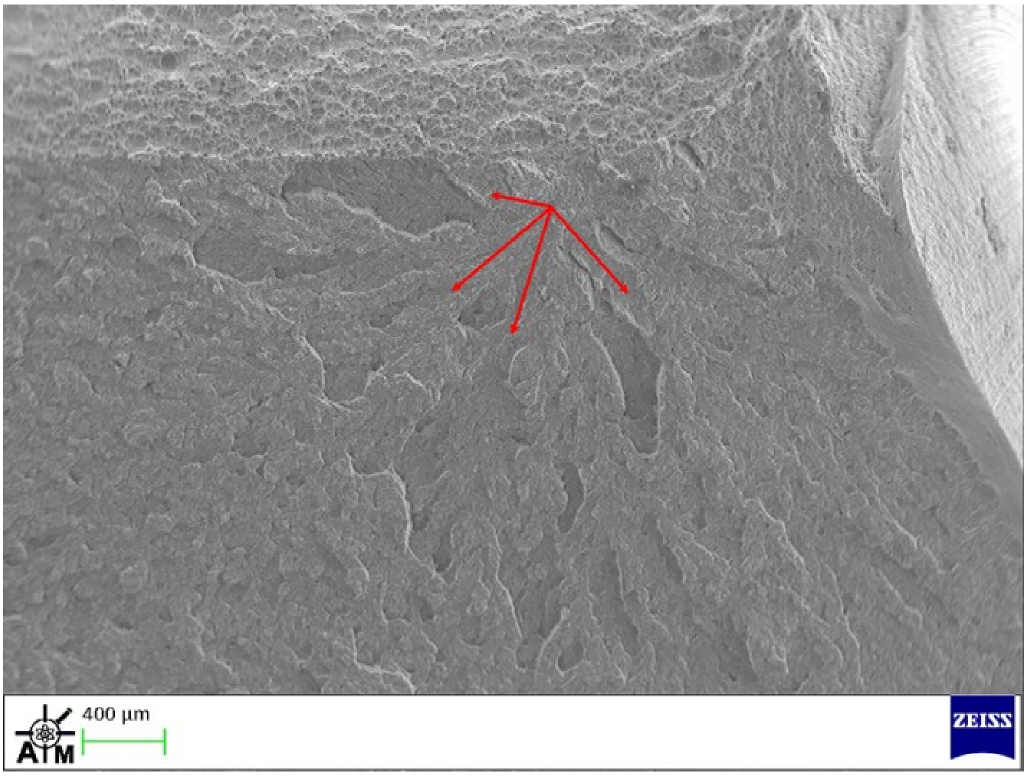

Figure 5.45. SEM image of crack propagation paths radiating from cleavage fracture initiation site of HT specimen at -20 °C with lowest Charpy impact toughness.

When initially evaluating the fracture surface of the HT specimen which produced the lowest toughness at -20 °C there were clear cleavage crack propagation paths radiating from a cleavage fracture initiation site. This can be seen on Figure 5.45. The toughness of this specimen was extremely low and had a highly brittle fracture as shown by HT16 on Figure 5.36. The Charpy impact toughness of this specimen was 16 J. When following the cleavage fracture initiation paths back the cleavage fracture initiation site no inclusions were found. Unfortunately, the trigger for cleavage fracture initiation could not be identified and the reason for the poor toughness could not be determined.

When inspecting the HT specimen with the highest toughness at -20 °C, like at higher temperatures, it was found that cleavage fracture initiation was triggered by large grains. The specimen chosen for analysis was HT14 which had a ductile fracture percentage of 41 %. The cleavage facet at the fracture initiation site was approximately 25 µm in size. This was also observed at -40 °C for the HT specimen with the greatest toughness, where the size of the facet at the cleavage fracture initiation site was also approximately 25 µm in size. However, with the reduction in temperature the ductile fracture percentage had reduced to 21 %.

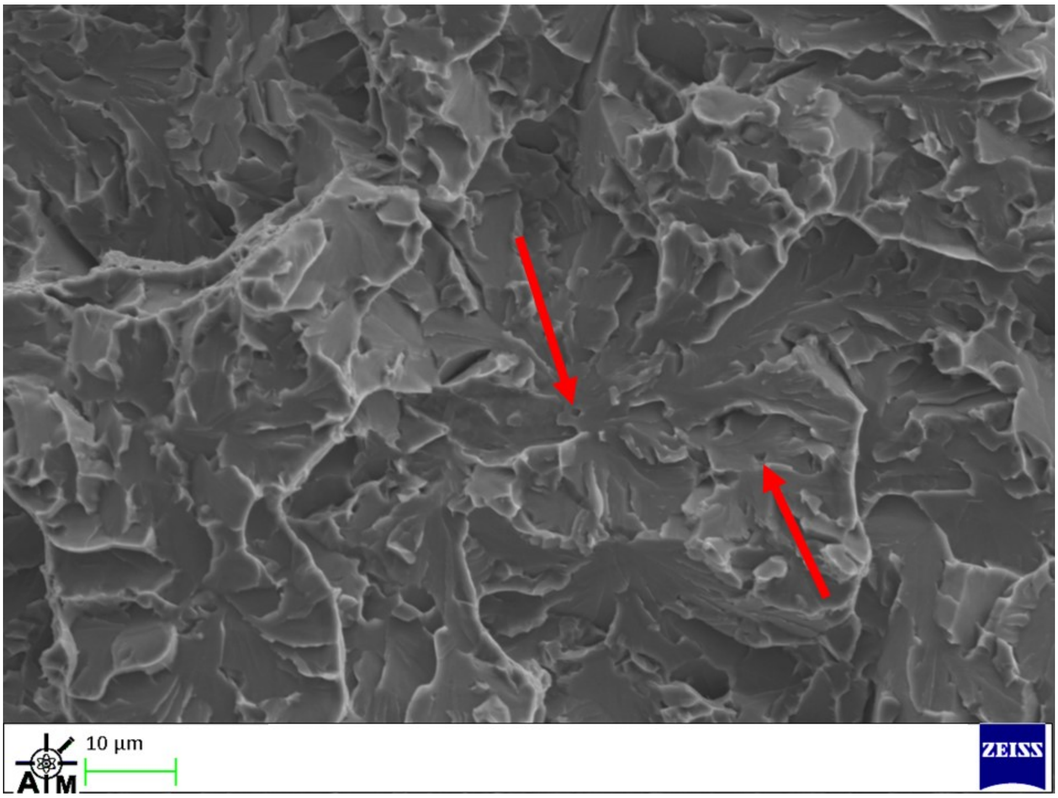

Figure 5.46. Fracture initiation site of HT specimen with lowest toughness at -40 °C.

The HT specimen with the lowest toughness at -40 °C had a highly brittle fracture, where ductile fracture was only present during crack arrest. The force-time curve for this specimen is labelled HT24 on Figure 5.37. The specimen had a ductile fracture percentage of 11 %. When inspecting the fracture initiation site, voids where particles were previously present were found. These particles would have been pulled out during fracture. It could not be determined what the particles previously occupying the voids consisted of, however it was concluded that these particles were triggering cleavage fracture initiation. The change in trigger of brittle fracture initiation was most likely because the particles had a different thermal expansion coefficient to that of the matrix. Therefore, as the temperature decreased, residual stresses were generated at the interface between the particles and the matrix due to the different thermal contractions. This would have resulted in a reduction of the energy required to initiate cleavage fracture at these particles [81].

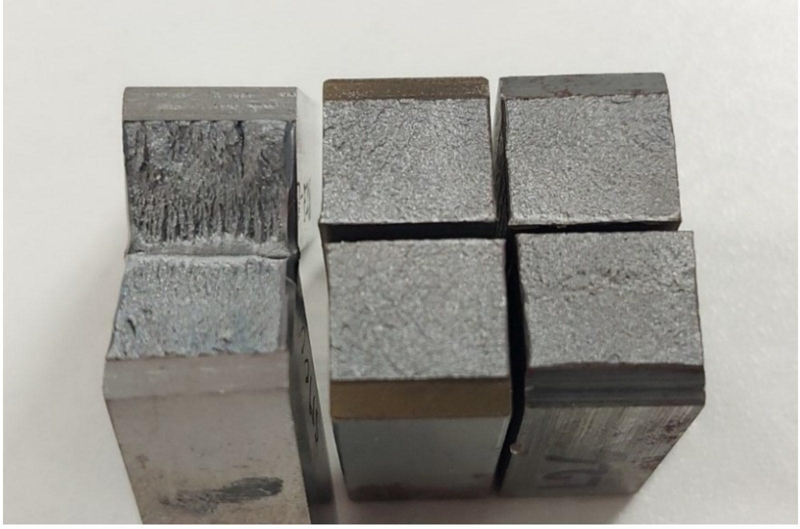

Figure 5.47. Fractured Charpy impact specimens at -60 °C. BM (left), AW (centre) and HT (right).

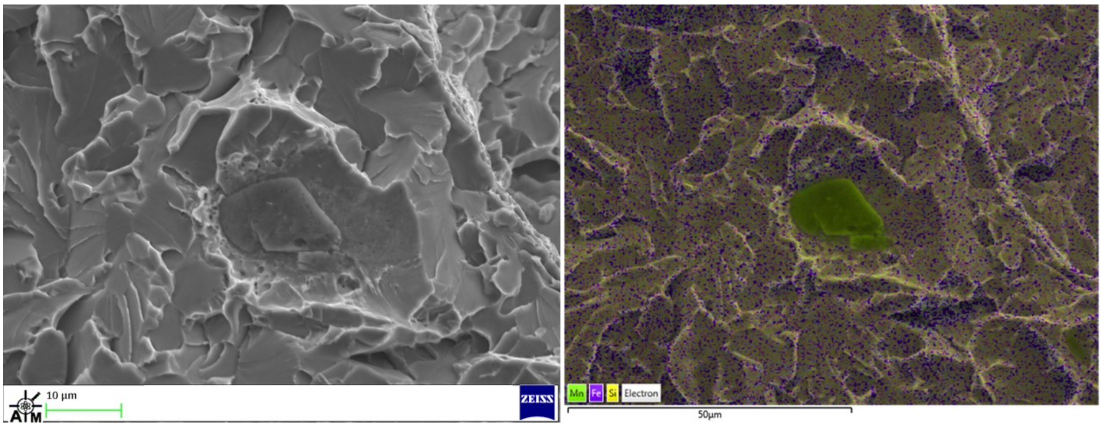

Figure 5.48. Manganese silicate inclusion located at cleavage crack propagation path on HT specimen with greatest Charpy impact toughness at -60 °C. SEM image (top) and EDS image (bottom).

The fracture surface analysis revealed that at -60 °C all the specimens experienced highly brittle fractures where the percentage of ductile fracture was calculated to be approximately 13 %, 0 % and 3 % for the BM, AW, and HT specimens respectively. The appearance of the fracture surface of the BM specimens was much different to that of the AW and HT specimens, where the fracture surfaces on the AW and HT specimens were significantly smoother. This can be seen on Figure 5.47. Also, none of the BM specimens were fully separated, where all of the AW and HT specimens were. The difference in appearance for the BM specimens was most likely due to its greater ability to resist cleavage crack propagation.

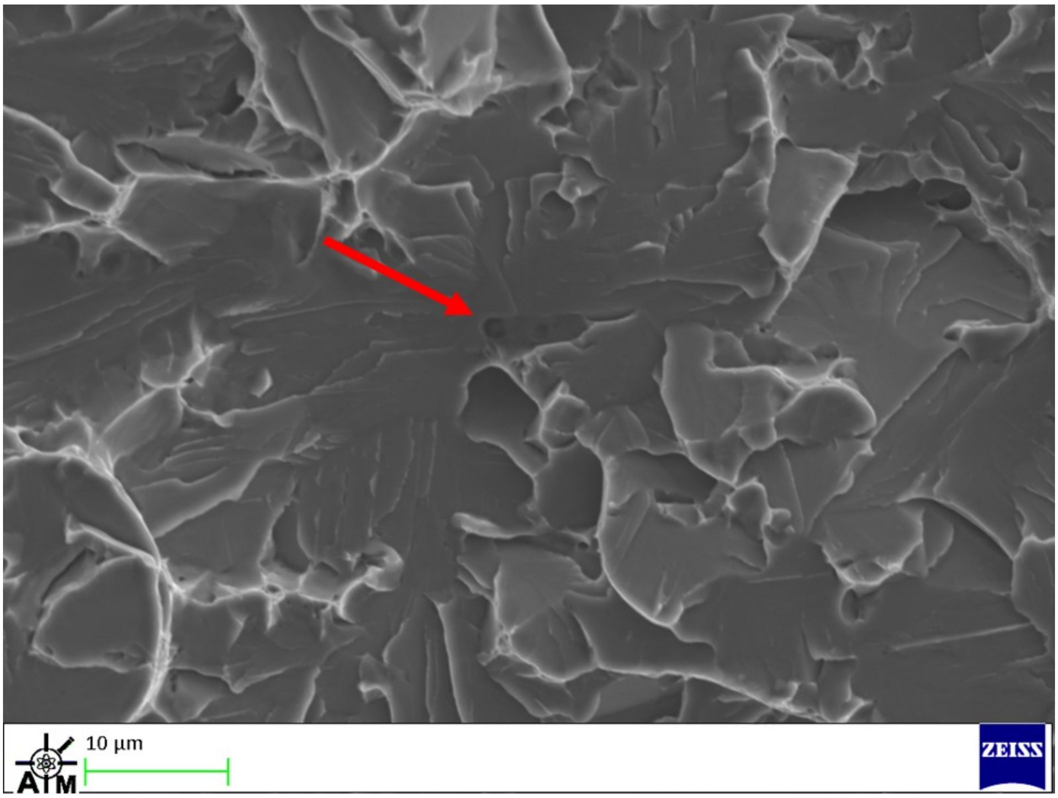

Figure 5.49. Particle at cleavage fracture initiation site on HT specimen with lowest Charpy impact joule energy at -60 °C.

On the HT specimen tested at -60 °C with the highest Charpy impact energy a large inclusion, approximately 15 µm in size, was found next to a cleavage crack propagation path. The inclusion was relatively close to the fracture initiation site which was located next to the notch at the top centre of the fracture surface. SEM and EDS images of the inclusion are displayed on Figure 5.48. EDS analysis revealed that the inclusion consisted of manganese and silicon. The inclusion would have formed when the strip edges were heated to welding temperature by the induction coil and then remained in the bond plane due to insufficient squeeze out by the weld rolls. Cleavage fracture was triggered by a large grain, where the size of the facet at the cleavage fracture initiation site was approximately 25 µm. Since the material as a whole had become highly brittle at -60 °C it could not be determined how much of an influence the inclusion had on the toughness of the HT weld line. However, it was likely that the inclusion would have been a detrimental influence since large silicate inclusions have been shown to reduce the toughness of a steel [82].

Cleavage fracture initiation on the HT specimen with the lowest Charpy impact toughness at -60 °C was triggered by a small particle. The particle was approximately 2 µm in size and can be seen on Figure 5.49. The chemistry of the particle was unable to be determined, however it was probable that it was either an inclusion or a coarse precipitate. It has previously been reported that coarse precipitates can reduce the toughness of a material [167]. Again, it was difficult to determine how detrimental the small particle was to the toughness since the material as a whole had become extremely brittle at -60 °C.

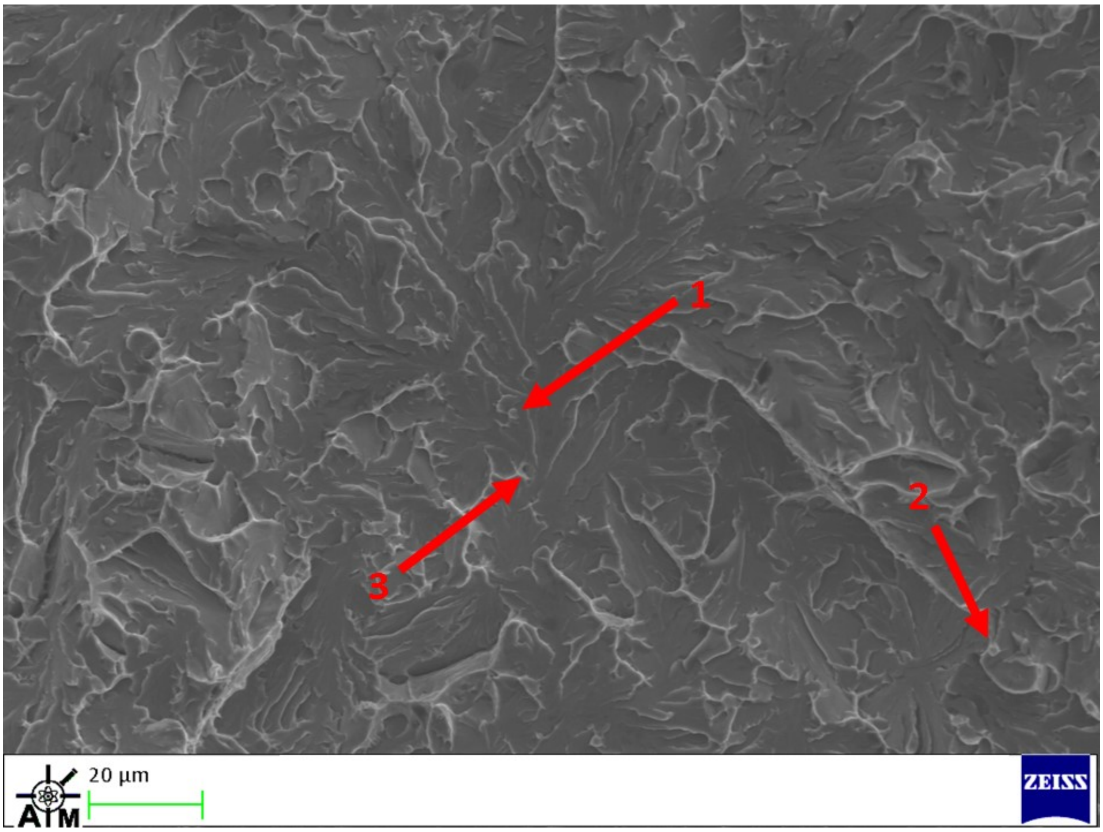

Figure 5.50. Cleavage fracture initiation site of AW specimen.

All the AW specimens tested at -60 °C displayed fully brittle force-time curves and fractures. Therefore, only one specimen was chosen for analysis. On inspection under SEM, it was found that the cleavage fracture initiation site was located next to the notch at the centre of the specimen where cleavage crack propagation paths could be clearly seen radiating from it. Just like at higher temperatures, it was found that cleavage fracture was initiating at M-A constituent, where large flat facets were also present suggesting that there was also a large grain size there as well. An SEM image of the fracture initiation site is displayed on Figure 5.50, where M-A constituent is labelled 1 and 2, and a void left by some M-A constituent since it was pulled out during fracture is labelled 3. Therefore, regardless of temperature cleavage fracture initiation in the AW specimens was typically triggered by M-A constituent.

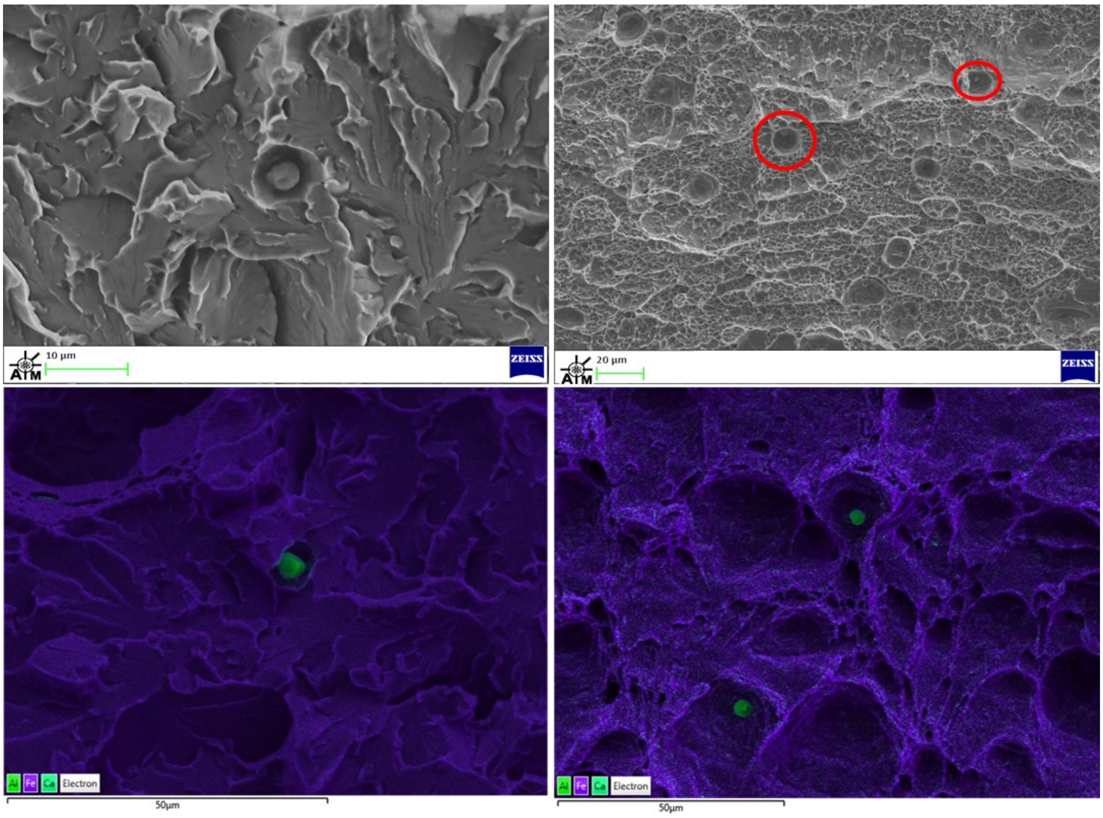

Figure 5.51. SEM images (top) and EDS images (bottom) of small and spherical inclusions consisting of aluminium and calcium located in both brittle (left) and ductile (right) fracture zones of weld.

Small and spherical inclusions with an approximate size of 2 to 5 μm were found on the brittle and ductile fracture surfaces of all the AW and HT specimens that were analysed under a SEM. EDS analysis revealed that the inclusions consisted of calcium and aluminium. Figure 5.51 displays SEM and EDS images of these inclusions in both ductile and brittle fracture zones. These inclusions were not found along any cleavage crack propagation paths or at any cleavage fracture initiation sites. Therefore, these inclusions played no role in initiating or promoting cleavage fracture. The inclusions found on the ductile fracture surfaces were located within the cup deformation structures. Therefore, the inclusions were acting as microvoid nucleation sites, potentially reducing the materials ability to resist ductile crack propagation.

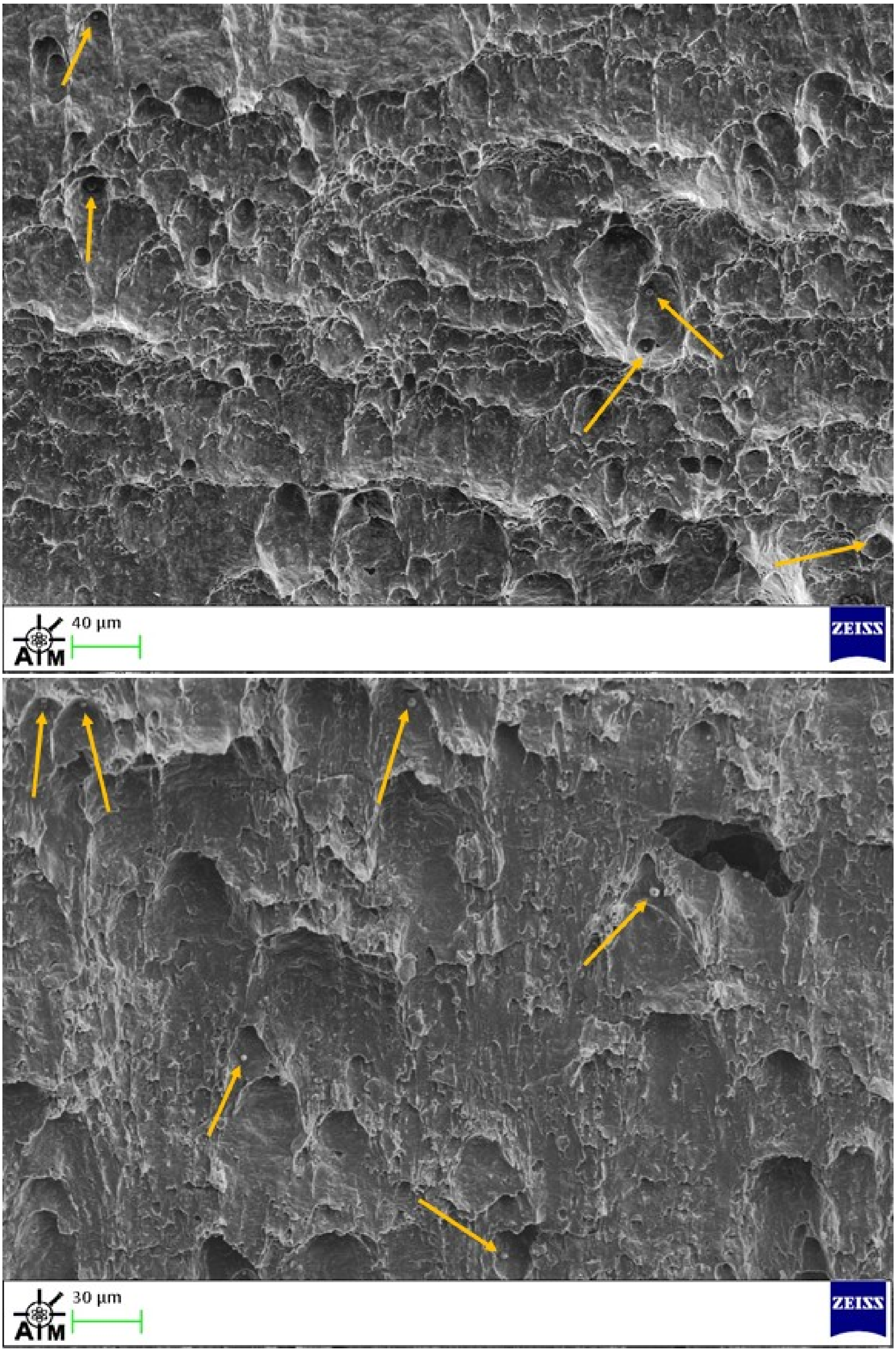

Figure 5.52. Inclusions consisting of aluminium and calcium on ductile fracture surface of AW specimen tested at ambient temperature (top) and BM specimen tested at -60 °C (bottom).

SEM analysis found small and spherical inclusions, approximately 2 to 5 µm in size on the ductile and brittle fracture surfaces of the BM specimens. They were identical in appearance to the small and spherical inclusions found on the AW and HT fracture surfaces, as shown on Figure 5.51. EDS analysis revealed that they consisted of calcium and aluminium. Figure 5.52 displays a section of a ductile fracture zone from a BM specimen tested at -60 °C and an AW specimen tested at ambient, where the small spherical inclusions have been highlighted by orange arrows. When comparing two images it could be seen that the size and dispersion of the inclusions were very similar on both of the fracture surfaces. Therefore, it was concluded that these inclusions were identical and were formed during the production of the steel strip. Since these inclusions were found on all the fracture surfaces, the lower toughness of the AW and HT specimens compared to that of the BM specimens, could not be attributed to the presence of these inclusions.

5.2.3 Summary

- The weld line in the AW condition produced a very low toughness across the entirety of the test temperature range. The PWHT was able to improve the toughness of the weld line, however the increase was not considerable and still much lower than that of the base metal. However, at -60 °C all the different conditions exhibited extremely low toughness.
- The instrumented head revealed that the fracture initiation energies for the BM specimens was not considerably larger than that of the AW and HT specimens. However, the BM specimens displayed superior crack propagation energies revealing that the BM had an extremely good resistance to crack propagation, where the HT and AW material did not.
- Fracture analysis revealed that large inclusions and defects produced during welding were highly detrimental to the toughness of the weld line. However, the weld line still produced a poor toughness even when they were not present.
- The AW specimens displayed highly brittle fractures across the entirety of the test temperature range where brittle fracture was initiating at M-A islands. The cleavage facet size at the cleavage fracture initiation sites was also very large, demonstrating there was a coarse grain size in these regions. With each reduction in temperature both the percentage of ductile fracture and toughness decreased.

- Like the AW specimens, the HT specimens also displayed brittle fracture across the whole test temperature range where there was again an increase in brittle fracture percentage with each reduction in temperature. However, the amount of brittle fracture was lower than that of the AW specimens, showing an improvement in toughness. At a temperature of -20 °C and higher, brittle fracture was initiating at large grains. However, this changed at temperatures of -20 °C and lower, where cleavage fracture started to initiate at small particles. The composition of these particles could not be concluded. Nevertheless, it was highly probable that they had a different thermal expansion coefficient to that of the steel matrix which was then generating residual stresses at the interface between them at lower temperatures. This resulted in a reduction of the energy required for cleavage fracture initiation at these particles.
- Small and spherical particles consisting of aluminium and calcium were found on all the fracture surfaces of each specimen analysed, where they were never found along any cleavage fracture propagation paths or at any cleavage fracture initiation sites. Therefore, they did not attribute to the reason why the toughness of the weld line was inferior to that of the base metal.
- At -60 °C all the different materials became highly brittle and produced poor toughness, regardless of whether inclusions, defects or brittle features were present.

5.3 Computational modelling studies

5.3.1 Effect of frequency on temperature distribution

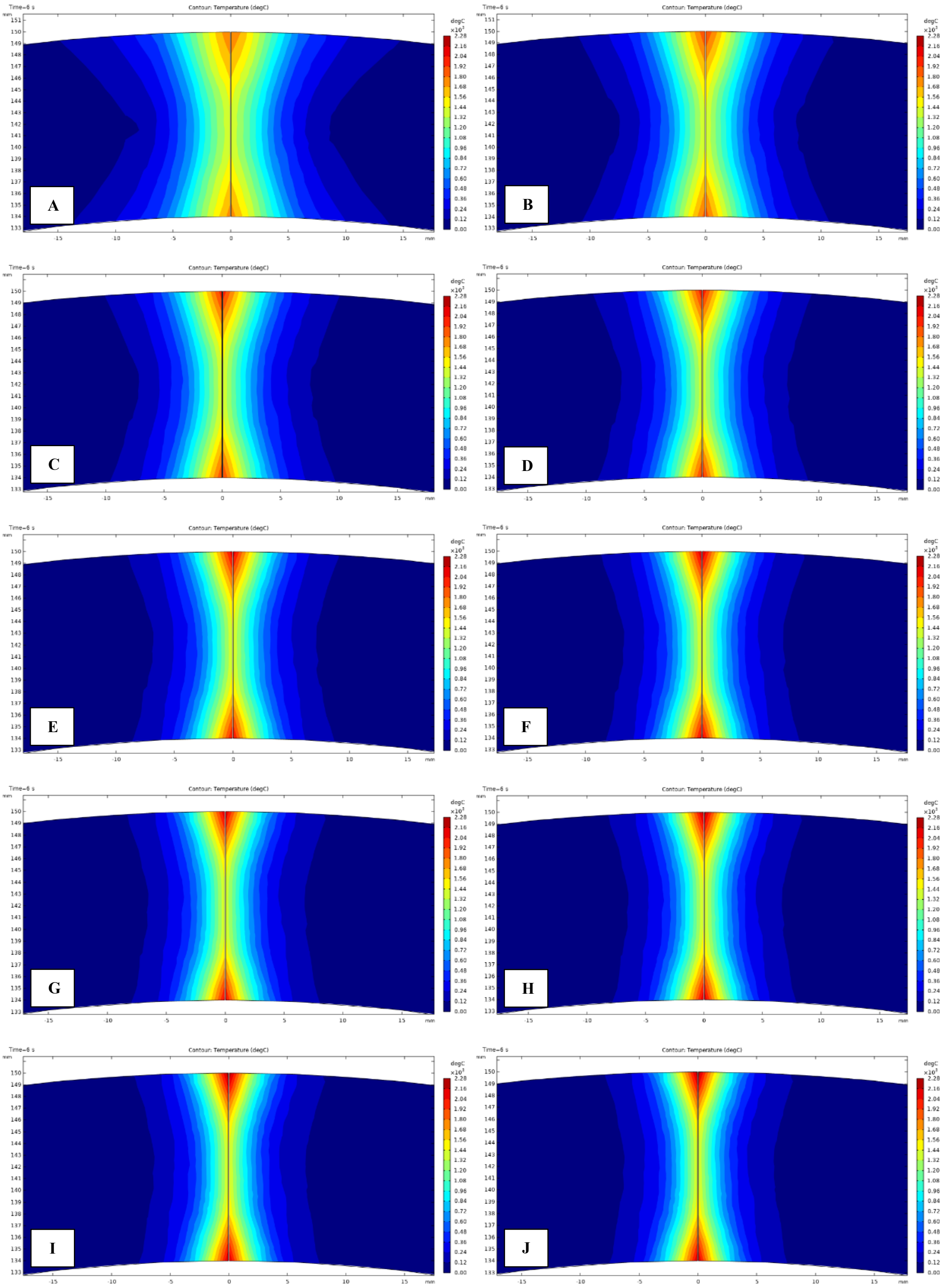

Figure 5.53. Temperature contour plots located 1 mm before the vee convergence point. (A) 25 kHz, (B) 50 kHz, (C) 75 kHz, (D) 100 kHz, (E) 125 kHz, (F) 150 kHz, (G) 175 kHz, (H) 200 kHz, (I) 225 kHz and (J) 250 kHz.

Temperature contour plots taken 1 mm before the vee convergence point for each of the different frequencies can be seen on Figure 5.53. For frequencies of 150 kHz and greater there was very little change in the width of the temperature profile, where the temperature profiles were all very similar visually. For frequencies below 150 kHz, the width of the temperature profile increased as frequency decreased, and all of the temperature profiles were visibly different. Even at the lower frequencies there was still an obvious hourglass shaped temperature profile produced. As the width of the temperature profile increased, a greater amount of material would have been heated in order for the strip edges to reach welding temperature. This would result in a greater amount of molten metal, a larger HAZ, and higher energy input requirements.

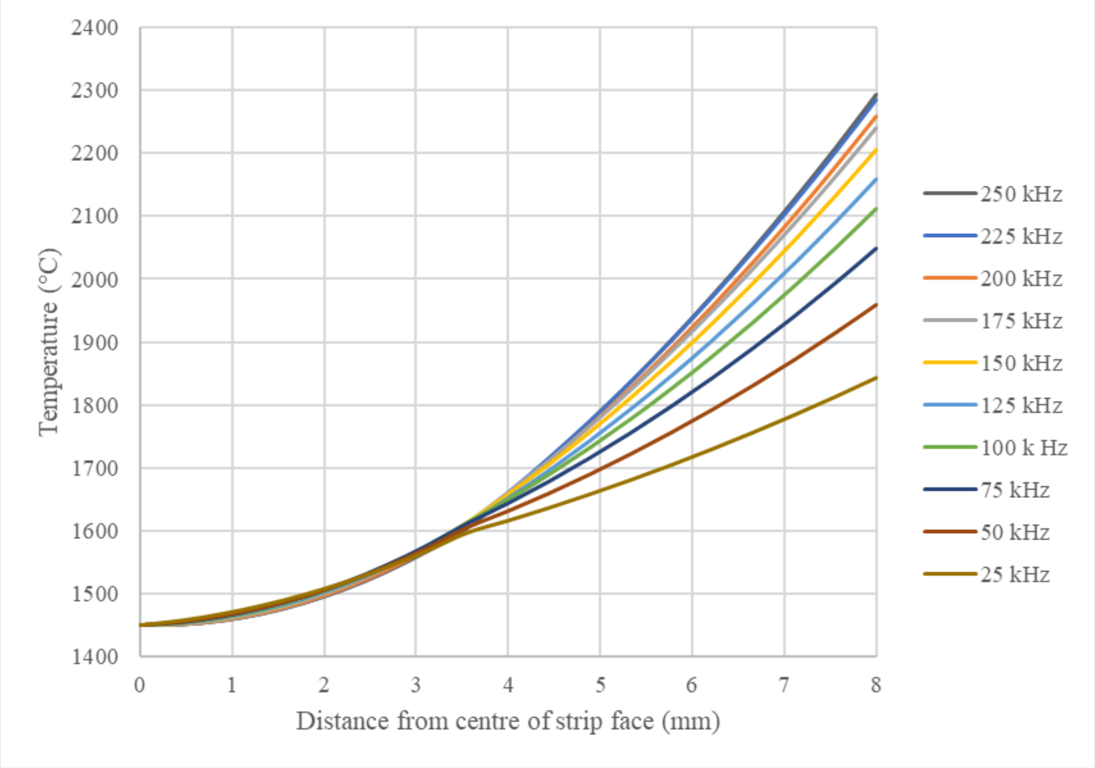

Figure 5.54. Temperature profile from centre of strip face to strip corner.

Figure 5.54 displays the temperature along the strip face from the centre of the strip to the top strip corner, where 0 mm on the plot represents the centre of the strip face. Like the temperature contour plots there was not a large amount of change in temperature when the frequency was increased above 150 kHz. However, for all frequencies greater than 150 kHz there was a very large difference in temperature between the centre of the strip and the strip corner. At frequencies below 150 kHz, the temperature at the strip edge corner did start to reduce, although there was still a large temperature difference between the strip edge corner and strip edge centre. It is important to note that specific heat was not accurately modelled above temperatures of 1400 °C. Therefore, the high temperatures at the strip edge corners were likely to be less than displayed. Nonetheless, the temperature differences were still highly likely to be large.

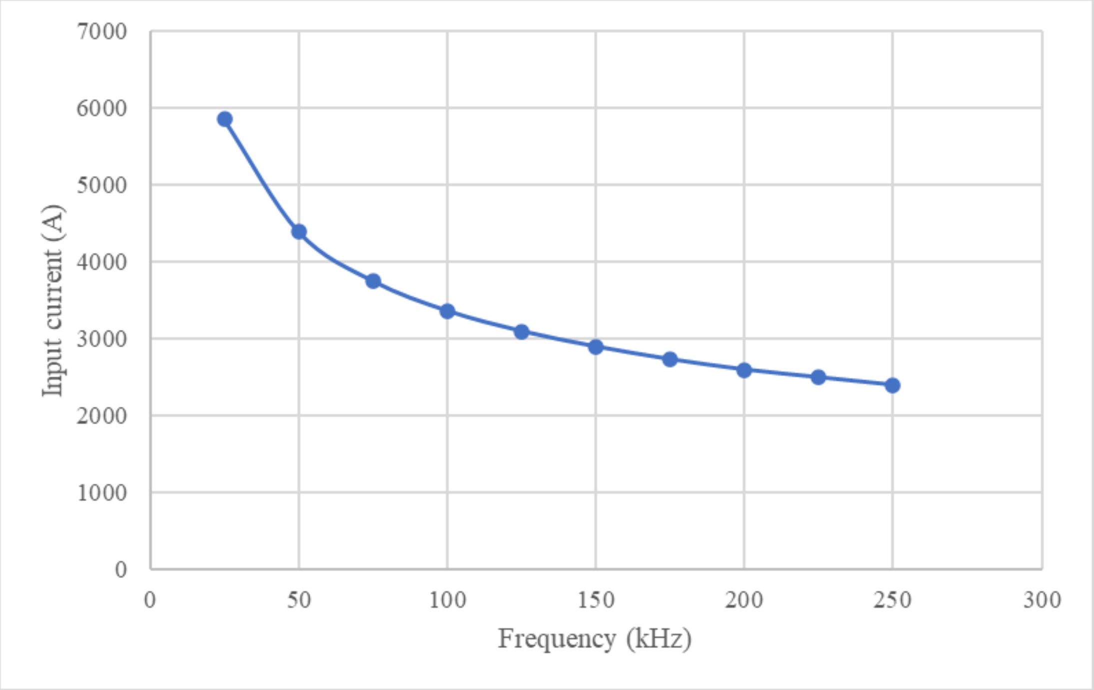

Figure 5.55. Required input current as a function of frequency.

The required input current as a function of frequency can be seen on Figure 5.55. As the frequency was increased the amount of input current needed to reach welding temperature reduced. This was because at higher frequencies the skin and proximity effects became greater leading to a smaller amount of material being heated [25]. The required input current decayed exponentially as the frequency was increased. This demonstrated that the lower frequencies needed a much greater input current to achieve welding temperature. For example, at 25 kHz the required input current was approximately double that of the current required at 150 kHz. Therefore, using lower frequencies would require greater energy inputs leading to a large increase in manufacturing costs. The higher frequencies improved the efficiency, however there is a limit on the maximum frequency that can be used. This is because using a frequency that is too high results in higher voltages across the induction coil and across the strip edges which can lead to arcing. Also higher frequency welders are more expensive to manufacture which will create an increase in manufacturing costs [17].

Therefore, using frequencies considerably greater than 150 kHz only offered a small benefit to improving welding efficiency.

The study demonstrated that by decreasing the input frequency the temperature difference across the strip edge faces became more uniform. However, when lower frequencies were used, an hourglass shape temperature profile was still produced, and the temperature difference between the strip centre and strip corner was still relatively large. This showed that on a thick walled HFI welded pipe the temperature distribution through the strip edges could not be made highly uniform by reducing the frequency alone. Even though the lower frequencies did lead to a more uniform temperature distribution, the efficiency of the process was reduced greatly. This was because at lower frequencies, more material was heated so higher current inputs were needed for the strip edges to reach welding temperature. The required energy increased greatly as the frequency decreased, which would result in extremely high production costs. It was concluded that improving the weld quality via reduced frequency to create a more uniform temperature distribution through the strip edges was not feasible. The study also demonstrated the difficulty of trying to achieve a uniform temperature distribution through the strip edges when producing thick wall HFI welded pipe.

5.3.2 Effect of strip thickness on heat distribution

In order to analyse the temperature profile through the strip edges, temperature contour plots 1 mm before the vee convergence point were produced and they can be seen on Figure 5.56. At a thickness of 5 mm the temperature distribution was rather uniform. This was because the temperature contour lines were relatively parallel to the weld line and there were no high temperatures at the strip edge corners. As the thickness was increased to 7.5 mm, an hourglass shaped temperature profile started to form, where the temperature at the strip corners increased. However, the intensity of the temperature at the strip corners was still relatively low. As the strip thickness increased further, the hourglass shaped temperature profile became more defined and the temperature at the strip corners became greater. This displayed that as the strip thickness was increased the temperature profile through the strip edges became less uniform. However, at a thickness of 15 mm and greater, there was only a small difference visually in the temperature profiles and a small increase in temperature at the strip corners. The temperature contour plots demonstrated that it was easier to achieve a uniform temperature distribution when producing HFI welded pipes using thin gauge steel strip, and that as the thickness of the steel strip increased the temperature distribution became more uneven, where an hourglass temperature profile was produced.

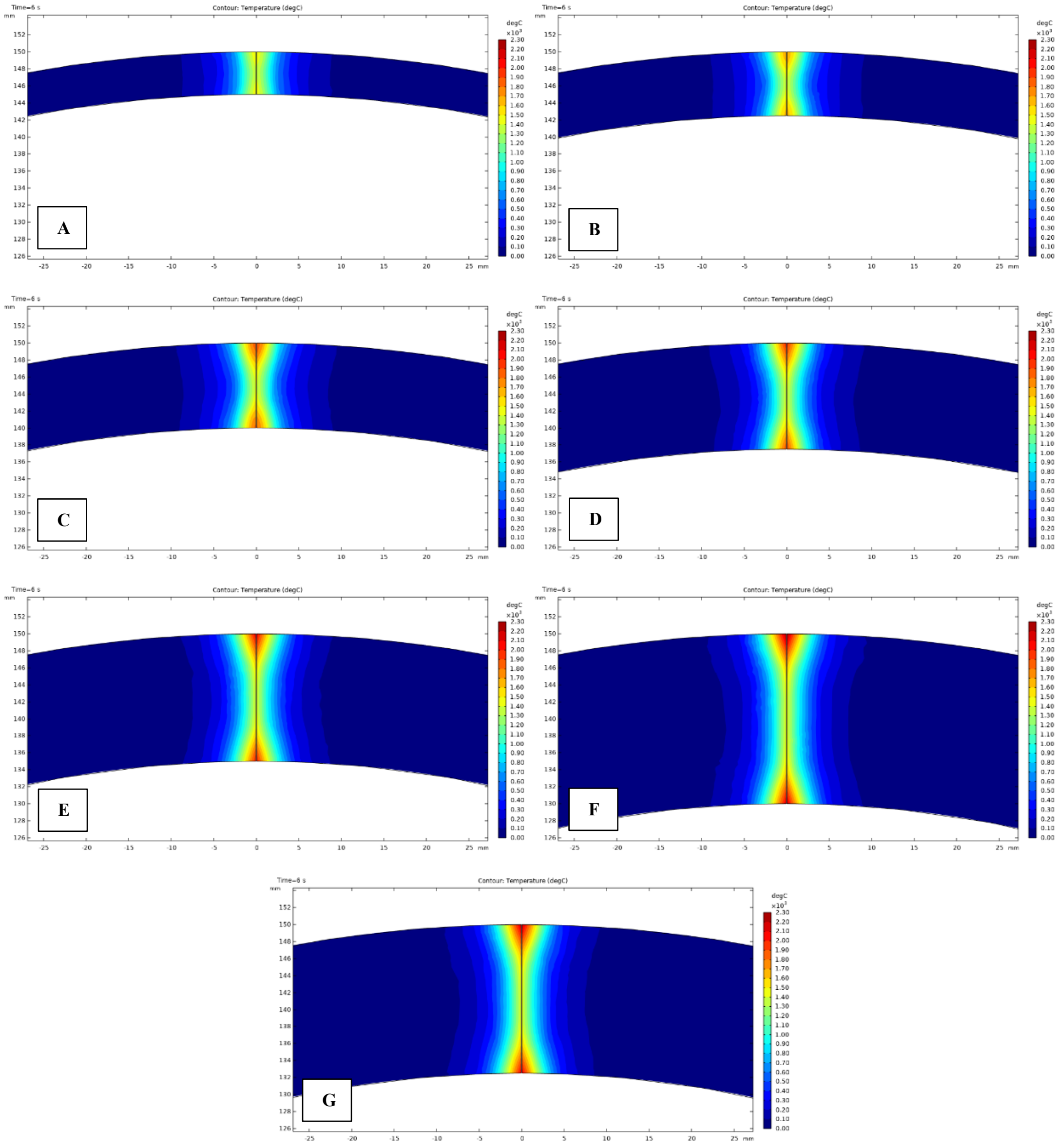

Figure 5.56. . Temperature contour plots located 1 mm before the vee convergence point. (A) 5 mm, (B) 7.5 mm, (C) 10 mm, (D) 12.5 mm, (E) 15 mm, (F) 17.5 mm and (G) 20 mm.

Figure 5.57 displays the temperature from the centre of the strip face to the strip corner for each of the different thicknesses. The distances from the centre of the strip faces to the strip corner have been normalised, therefore the strip face centre is located at 0 and the strip corner located at 1. The plot displayed that for a strip thickness of 5 mm the temperature profile along the strip face was relatively uniform where the difference in temperature between the strip face centre and the strip corner was small. As the thickness increased it could be seen that the temperature at the strip corners increased. With the initial increase in strip thickness, the increase in temperature at the strip corner was the greatest. When increasing the strip thickness above 15 mm the change in temperature at the strip corner became much smaller. This was also shown by the temperature contour plots where there was only a small increase in the intensity of the temperature at thicknesses of 15 mm and greater. The plots demonstrated that an even temperature distribution was much easier to achieve when producing HFI welded pipes using thinner gauge steel strips, and that the temperature distribution became quickly uneven as the strip thickness was increased. Again, it is important to note that specific heat was not accurately modelled above temperatures of 1400 °C. Therefore, the high temperatures at the strip edge corners were likely to be less than displayed.

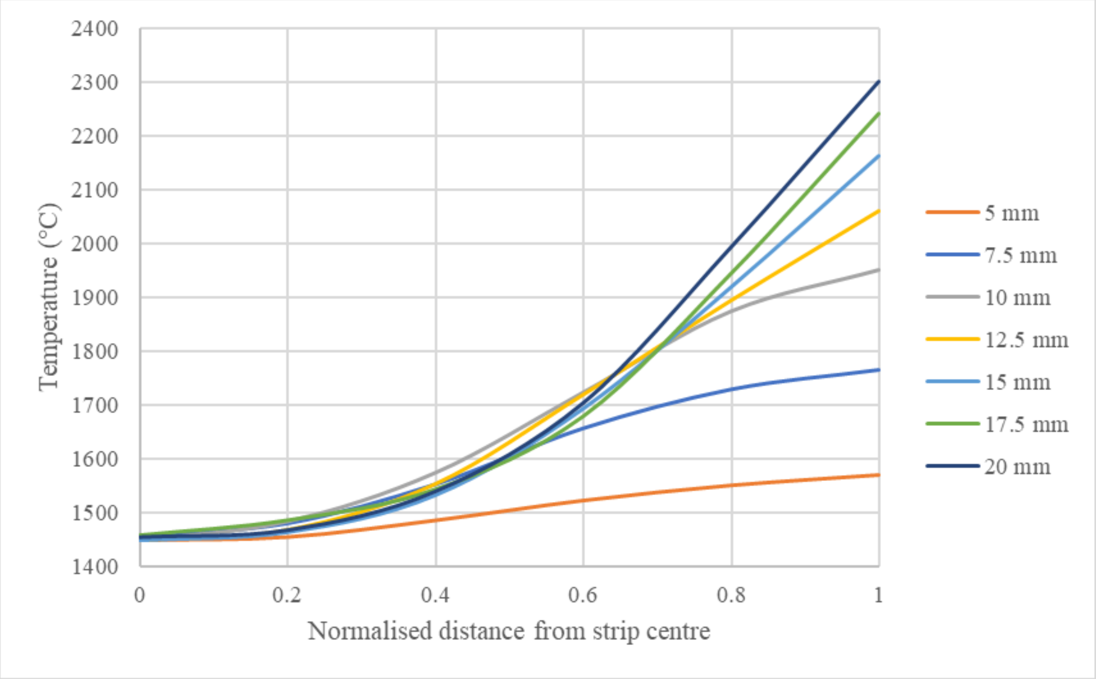

Figure 5.57. Temperature profile from centre of strip face to strip corner for different strip thicknesses.

In order to achieve welding temperature, the input current was increased as the strip thickness became greater. This was because as the strip thickness increased a greater amount of material needed to be heated, consequently leading to an increase in input current. The current as a function of the strip thickness can be seen on Figure 5.58. To achieve welding temperature, the input current increased linearly with the strip thickness. However, this study used a fixed frequency and typically with thinner gauge strips higher frequencies are used, which require a smaller input current.

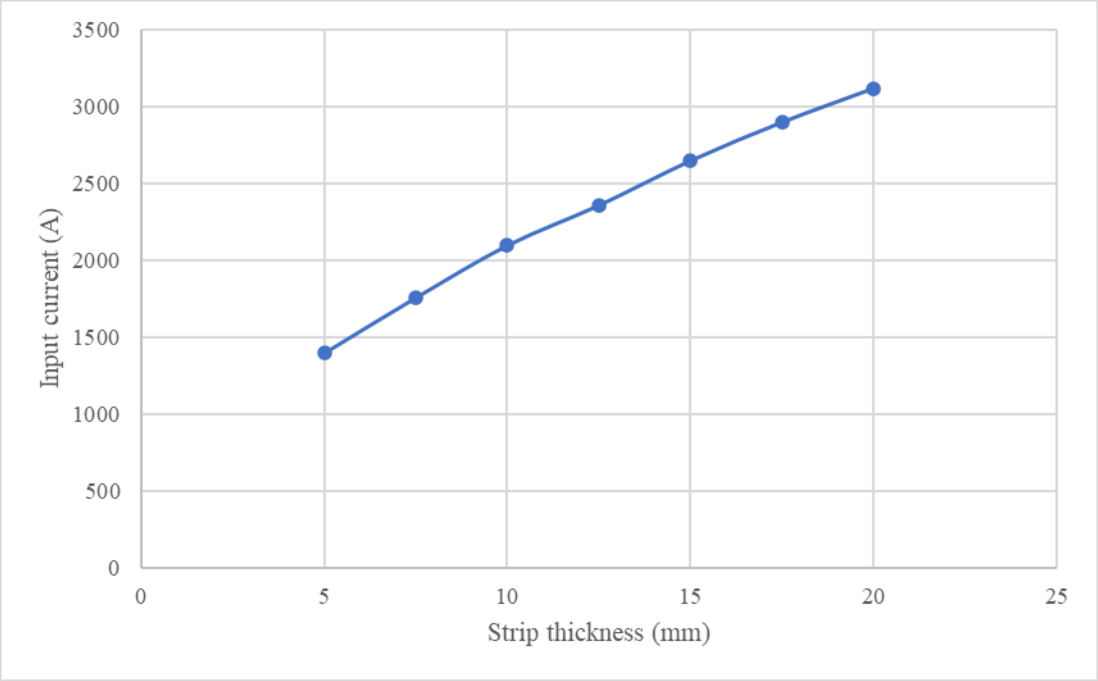

Figure 5.58. Input current as a function of strip thickness.

The study revealed that it was easier to achieve a more uniform temperature distribution when producing HFI welded pipe using thinner gauge steel strip. When increasing the strip thickness, the temperature profile through the strip edges became less uniform, displaying that an even temperature distribution became much harder to obtain when using thicker gauge strip. However, it is important to take into consideration that the study used a fixed frequency, whereas when producing HFI welded pipes different frequencies would be used with different thickness strips.

The results from the frequency study, coupled with the results from the thickness study, showed that it was extremely difficult to obtain a uniform temperature distribution through the strip edges when manufacturing HFI welded pipe using medium to thick gauge steel strips. This was because the thickness study displayed that the temperature distribution became less uniform when the strip edge thickness increased. The frequency study showed that as frequency was decreased the temperature profile did become more even. However, there was still an hourglass shaped temperature profile produced, with greater heating at the strip edge corners, and the energy requirements were increased significantly.

5.3.3 Effect of edge geometry on temperature distribution

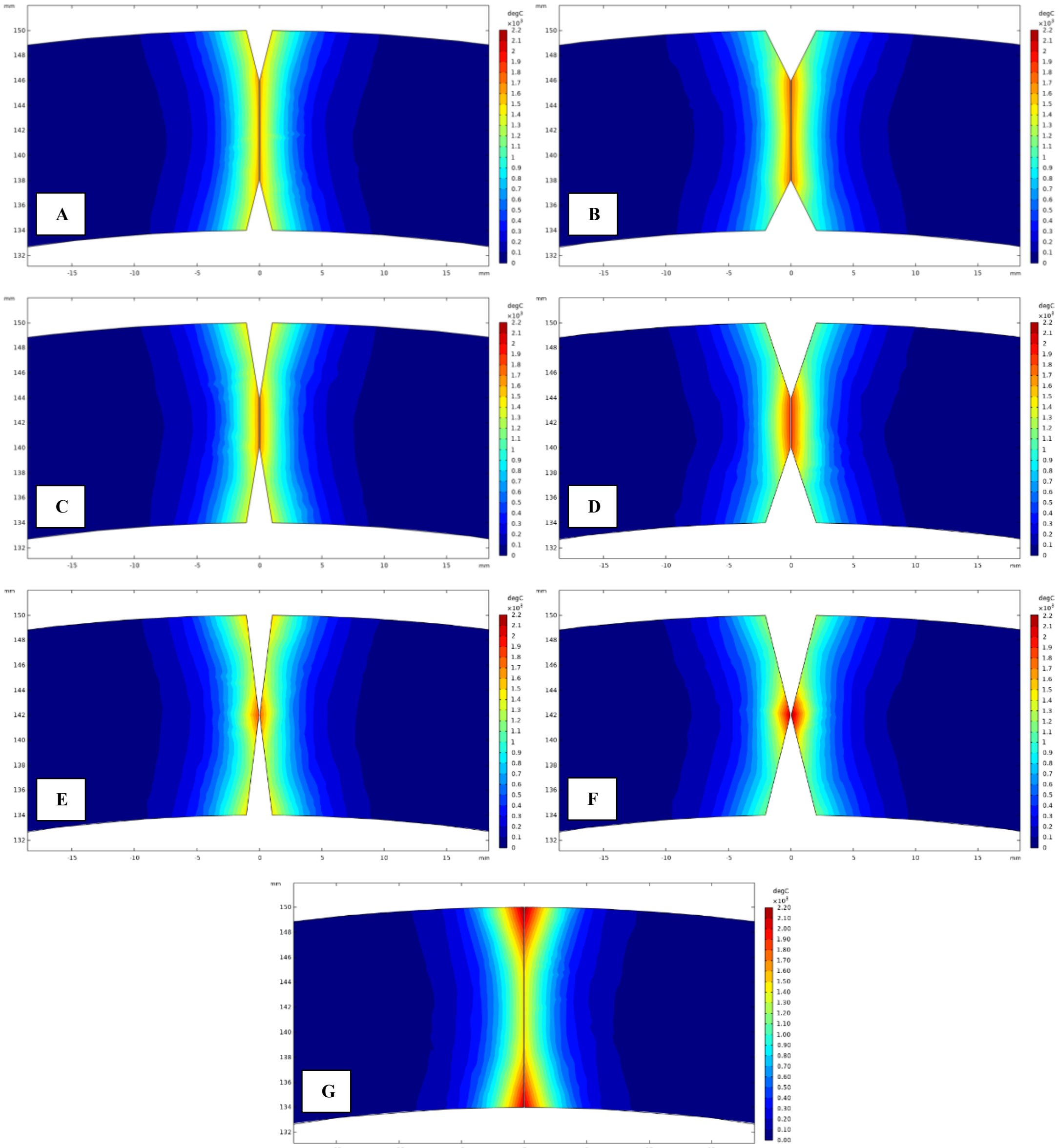

Figure 5.59. Temperature contour plots located 1 mm before vee convergence point. (A) A=1 B=4, (B) A=2 B=4, (C) A=1 B=6, (D) A=2 B=6, (E) A=1 B=8, (F) A=2 B=8, and (G) square.

Temperature contour plots, for each of the different modified edge geometries and the square edge geometry, at 1 mm before the vee convergence point are displayed on Figure 5.59. As previously observed the square edge geometry had much greater heating at the strip edge corners when compared to the strip edge centre. The chamfers on all the different geometries greatly reduced the high temperatures that were previously present at the strip edge corners. But just because the high temperatures at the corners were reduced it did not mean a more uniform temperature profile had been achieved. Contour plots B, D and F on Figure 6.22 display the results for A = 2 mm, where the B dimensions were 4 mm, 6mm and 8 mm respectively. On these plots it could clearly be seen that the temperature at the strip corners had been reduced, however there was a large increase in temperature at the strip edge centres, which increased as the B dimension increased. Figure 5.60 displays the temperature across the strip edge face from the strip edge centre to the strip edge corner at the vee convergence point for each of the different edge geometries and the square edge geometry. 0 mm on the plot denotes the strip edge centre. The plot clearly dipslayed that there was a large temperature difference across the strip edge when A = 2 mm.

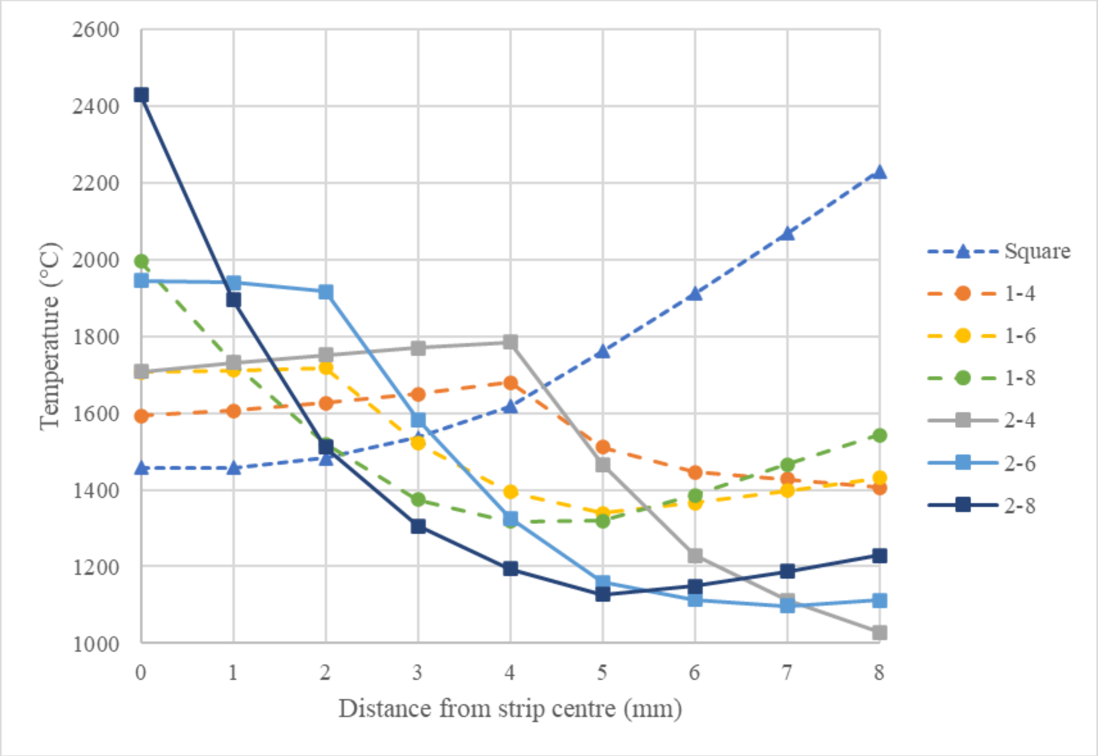

Figure 5.60. Temperature from strip edge corner to strip edge centre.

When the chamfer dimension was A = 1 mm, there was an improvement in the uniformity of the temperature distribution through the strip edges. However, this was not the case when B = 8 mm. Contour plots A, C and E on Figure 5.59 display the results for A = 1 mm, where the B dimensions were 4 mm, 6mm and 8 mm respectively. The temperature at the strip corners was reduced when A = 1 mm, although the reduction was not as large as when A = 2 mm. There was also a slight increase in temperature at the strip centres when compared to that of the square edge geometry, though it was not as large as the increase when A = 2 mm. On Figure 5.60 it could be seen that when A = 1 mm the most uniform temperature distributions were delivered, where the chamfer dimensions which produced the most uniform temperature distribution was when A = 1 mm and B = 4 mm. However, there was still some variation in the temperature across the strip edge face, although the differences between the minimum and maximum temperature was much less than that of the square edge geometry. The difference between the minimum and maximum temperatures when A = 1 mm and B = 4 mm, and the square strip edge geometry were 274 °C and 773 °C respectively. This was approximately a 500 °C decrease in temperature difference or a reduction of 65 %. However, this reduction was likely to be smaller since the specific heat was not accurately modelled at temperatures greater than 1400 °C.

The initial study showed that the uniformity of the temperature distribution through the strip edges during welding could be vastly improved by altering the geometry of the strip edges. The geometry that produced the best temperature distribution across the strip edge was when A = 1 mm and B = 4 mm. Therefore, this geometry was chosen to be developed further to explore how much of an improvement on the uniformity of the temperature distribution though the strip edges could be achieved. This was to be done by using a new range of dimensions for A and B. For A these were 0.75 mm and 1.25 mm, and the dimensions for B were 3 mm, 4 mm, and 5 mm.

The temperature contour plots for the second study can be seen on Figure 5.61. On the plot is could be observed that when A = 1.25 mm, there was a greater variance in temperature through the strip edges when compared to when A = 0.75 mm. This was because when A = 1.25 mm it could clearly be seen that there was greater heating at the strip edge centres. However, all the modified edge geometries showed much more uniform temperature distributions than the square edge geometry. Figure 5.62 displays the temperature profile from the centre of the strip face to the strip corner, where the strip centre was at 0 mm on the plot. The plot showed that generally the chamfers where A = 1.25 mm had higher temperatures at the strip edge centres and lower temperatures at the strip corner than the strip edges where A = 0.75 mm. There were lower temperatures at the strip edge corners on the geometries where A = 1.25 mm due to a weaker proximity effect since the corners were a greater distance apart than the geometries where A = 0.75 mm. Therefore, the temperature at the strip edge corner could be increased by decreasing the A dimension.

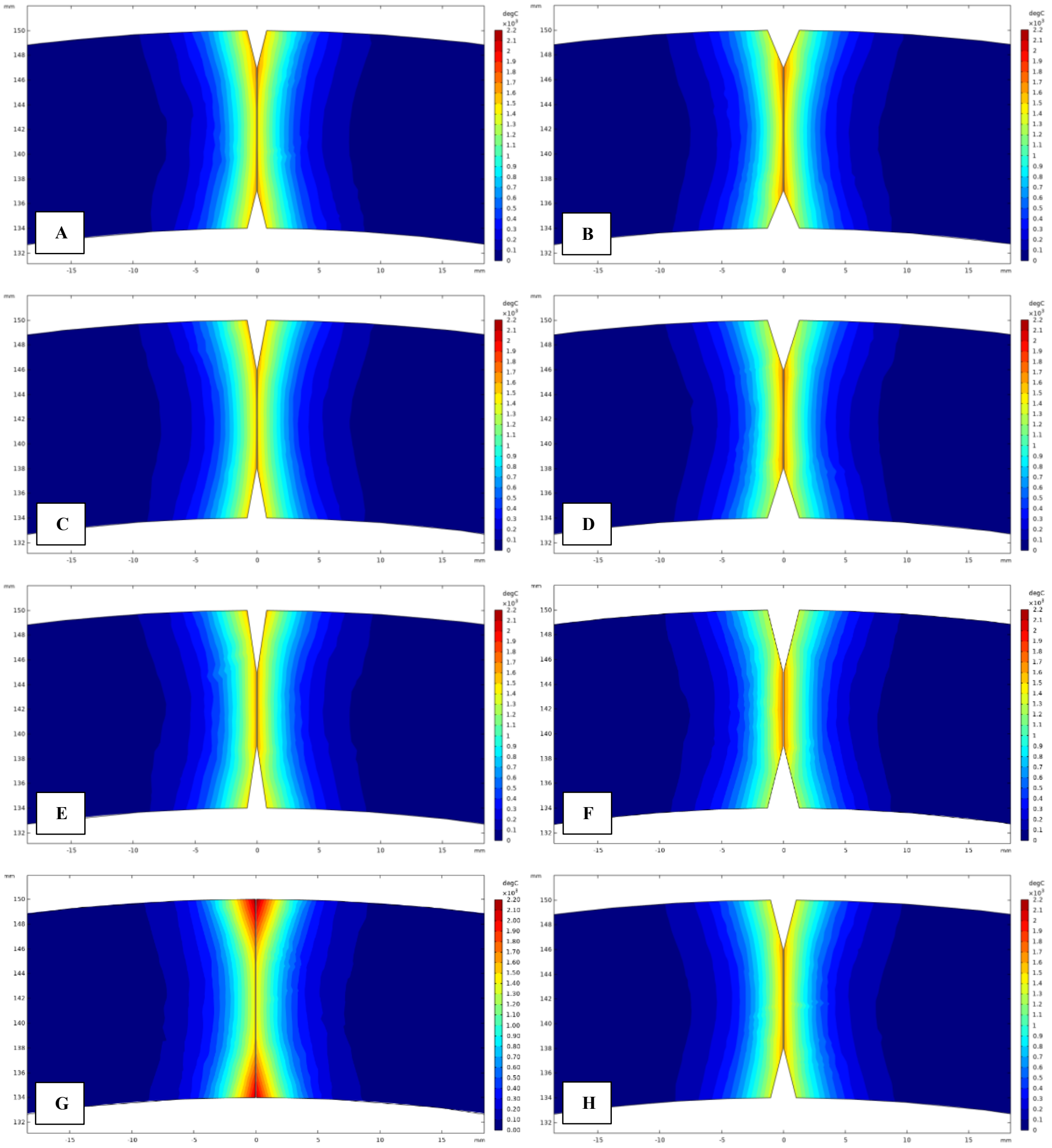

Figure 5.61. Temperature contour plots located 1 mm before vee convergence point. (A) A=0.75 B=3, (B) A=1.25 B=3, (C) A=0.75 B=4, (D) A=1.25 B=4, (E) A=0.75 B=5, (F) A=1.25 B=5, (G) square, and (H) A=1 B=4.

For all the geometries the highest temperature on the strip edge face typically occurred at the corner where the chamfer met the strip edge centre. When A = 1.25 mm the temperature at this location only varied a small amount as the B dimension was changed. However, when A = 0.75 mm the temperature increased in this location as the B dimension decreased. The geometry which produced the most uniform temperature distribution through the strip edge was when A = 0.75 mm and B = 4 mm. The difference between the minimum and maximum temperatures for the geometry with the most uniform temperature profile and that of the square edge geometry were 115 °C and 773 °C respectively. This is a reduction of 658 °C or 85 % in temperature variation across the strip edge face, although the reduction was likely to be less since specific heat was not properly defined above 1400 °C. Figure 5.63 displays the temperature profile across the strip faces for when A = 0.75 mm and B = 4 mm, and the square edge geometry. It clearly displays that altering the geometry of the strip edges can greatly improve the uniformity of the temperature profile.

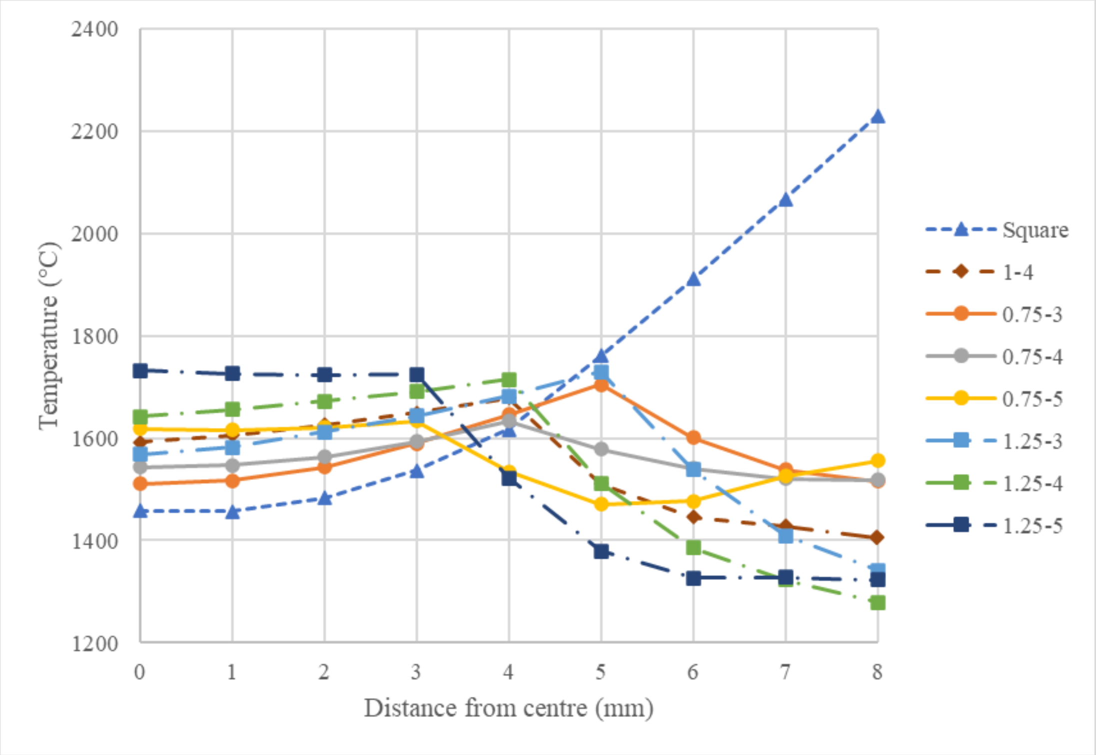

Figure 5.62. Temperature from strip edge corner to strip edge centre.

Since the study used the same input current for all the different edge geometries, the lowest temperature on the strip edge face, when A = 0.75 mm and B = 4 mm, was greater than the minimum required welding temperature. This meant that a smaller input current could be used to achieve welding temperature across the strip edge face with the chosen chamfered geometry. For the square edge geometry to achieve the desired welding temperature an input current of 2750 A was used. The chamfered edge geometry required an input current of 2650 A to achieve the same minimum welding temperature. This was a reduction of 100 A or 3.64 %. A lower input current would result in lower energy inputs for manufacturing. This would lead to a reduction in manufacturing costs as well as having a positive impact on the environment. Therefore, altering the strip edge geometry to achieve a more uniform temperature distribution to improve the weld quality could also give rise to lower manufacturing costs and environmental benefits.

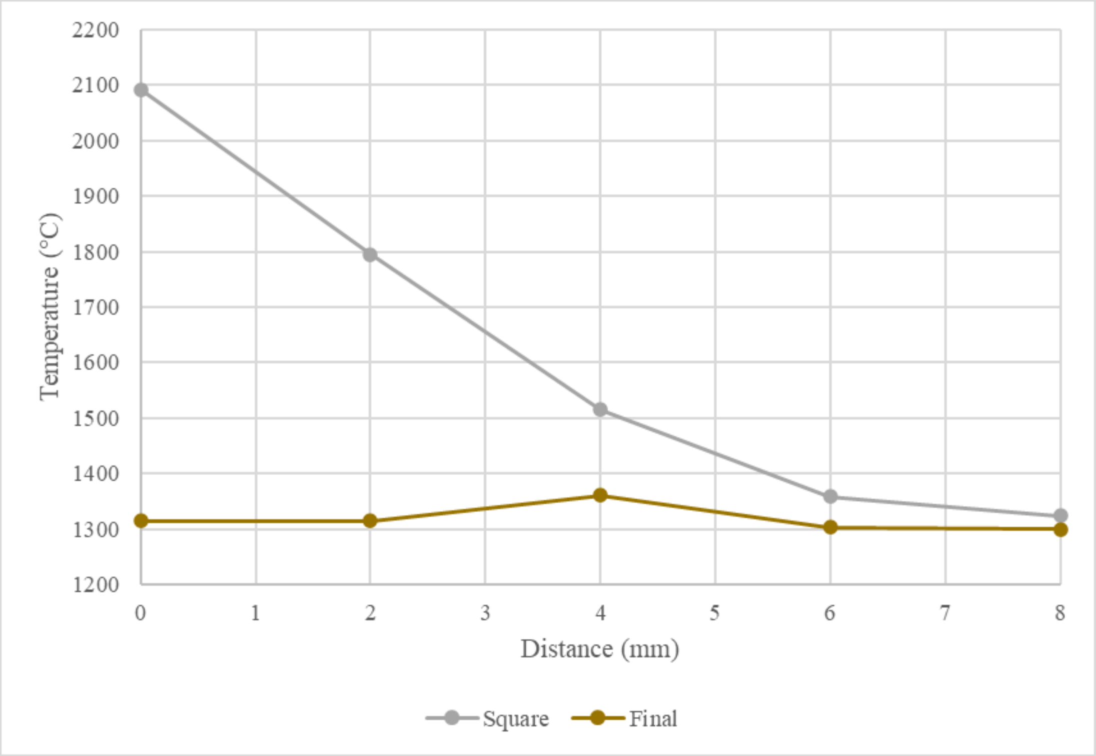

Figure 5.63. Temperature from strip edge corner to strip edge centre for square and final geometries.

5.3.4 Summary

- The frequency and thickness studies both displayed that it was not possible to achieve a uniform temperature distribution through the depth of the strip edges on a thick-walled pipe. This was especially noticeable in the frequency study where there was still a large temperature difference across the strip edges even when a low frequency was used.
- It was found that a more uniform temperature distribution could be achieved through the strip edges by altering the geometry of the strip edges. There was also efficiency benefits observed when altering the strip edge geometry, where the power requirements were reduced by 3.64 %.

6 Discussions

6.1 Weld line microstructure and toughness relationships

Previous HFI welded pipe weld line toughness investigations had not carried out extensive fracture analysis. Without fracture analysis it could not be well understood how the crack was initiating and propagating through the weld line. Therefore, strong relationships between the weld line microstructure and its toughness had not been established. As well as a lack of fracture analysis, the toughness of the weld line had only been assessed using the traditional Charpy impact test. This only measured the absorbed energy associated with the whole of the fracture, which can consequently lead to a false assessment of the toughness [122–124]. Thus, the previous toughness analysis was somewhat limited. The use of Charpy impact testing with an instrumented head provides the absorbed energy at specific fracture events, allowing for a more accurate assessment of the weld line to be accomplished.

Earlier research suggested that M-A was detrimental to the toughness of the weld line of an X65 HFI welded pipe in the AW condition [3]. However, a lack of fracture surface analysis has meant this, and how the constituent may be affecting the toughness of the weld line had not been confirmed. This was important because the literature has shown that M-A constituent does not always affect the toughness of a material, where this was observed in a submerged arc welded joint of a carbon bainitic steel. It was found when the M-A constituent was less than 1 μm in size and with a low volume fraction, it did not have any influence on the toughness of the steel [75]. The microstructural analysis revealed that M-A constituent was present in the AW weld line, where it was large and elongated with some more equiaxed M-A constituent also present. On some occasions the elongated M-A constituent was near 10 μm in length. The M-A islands formed when the weld line cooled to a temperature approximately below 500 °C where it transformed from the small amount of remaining austenite [60]. Both the size and morphology of the constituent can influence the toughness. For instance, in an X100 pipeline steel it was observed that an increase in the size of the M-A constituent, even when the dispersion was consistent, reduced the toughness of the material [72]. Gleeble thermal simulations have also shown that M-A constituent was most detrimental to the toughness of a high strength low alloy steel when it had a large and elongated morphology [74]. Since the M-A constituent observed during microstructural analysis was large and elongated, it was highly likely that it negatively influenced the toughness of the AW weld line. The fracture surface analysis revealed that cleavage fracture was initiating at M-A constituent across the whole of the test temperature range for the AW weld line. Although, it was important to note that this was not the case when large defects or inclusions were present. Therefore, it was observed that there was a hierarchy of cleavage fracture initiating features in the AW weld line, where large inclusions and defects were more effective at promoting cleavage fracture than M-A constituent. However, the fracture analysis still confirmed that M-A constituent was negatively influencing the toughness of the AW weld line by promoting cleavage fracture initiation. The force-time plots, generated by the instrumented head, for the AW weld line had curves with very small stable crack propagation phases following fracture initiation. This demonstrated that it was easy for cleavage fracture to initiate in the AW weld line. Therefore, it could be concluded that M-A constituent was not just initiating cleavage fracture but was also very effective at promoting it.

An increase in grain size leads to an increase in the DBTT [35–37]. This happens because when the grain size increases the stress needed to initiate cleavage fracture decreases [39]. Therefore, it was expected that the coarse grain size produced at the AW weld line would negatively influence the toughness by reducing the stress required to initiate cleavage fracture and by increasing the DBTT. This explained why the AW specimens were highly brittle across the entirety of the test temperature range and no USE region was present on the Charpy impact energy against temperature plot. At the fracture initiation sites on the AW specimens there were large and flat facets present, displaying that cleavage fracture was initiating in locations where there were large grains present. Hence, these fractography observations agreed with the Charpy impact test results. ThermoCalc Prisma simulations displayed that the NbC precipitates would have been fully dissolved at the weld line during welding and that they were only able reprecipitate at the mid-thickness during cooling. It was likely that the precipitates here were much larger and less well dispersed than in the base metal, as under static recrystallisation conditions there were no dislocation cores for them to nucleate at. Therefore, the effect of grain refinement may have been very small where they were able to reprecipitate. Subsequently, the high temperatures and the inability of NbC precipitates to offer grain refinement at the weld line during cooling was the likely reason why there was a large grain present. The fracture and microstructural analysis identified that M-A constituent acting as stress raisers coupled with the coarse grain size reducing the cleavage fracture initiation stress, was the main reason why cleavage fracture was easily initiating in the AW specimens across the entirety of the test temperature range.

Although cleavage fracture was typically initiating at M-A constituent in the AW specimens, this was not always the case. As previously discussed, there was a hierarchy of cleavage fracture initiating features, where large inclusions and defects were the most effective at promoting cleavage fracture. The AW specimen tested at ambient temperature with lowest toughness had a total absorbed energy that was only 61 % of the average for the AW specimens tested at this temperature. There was almost no stable crack propagation phase present on the force-time curve, revealing that cleavage fracture was initiating with ease. When inspecting the fracture surface, it was found that cleavage fracture was initiating at a large defect, which was determined to be a lack of fusion defect. This was most likely caused by a pre-arc which momentarily robbed heat from the strip edges when the current was diverted. The Charpy impact test results and fracture surface analysis agreed that this type of defect was highly detrimental to the toughness of the weld line.

Large inclusions approximately 15 to 20 μm in size were found to be extremely detrimental to the toughness of the AW weld line at -20 °C. Fracture surface analysis revealed that these large inclusions were triggering cleavage fracture initiation. The instrumented head displayed that the fracture initiation energy was extremely low and that the fracture was instantly initiating with cleavage fracture. The total absorbed energy was 11 J for this specimen which was approximately 20 % of the average of the AW specimens tested at this temperature. As well as large inclusions, there were large and flat facets present at the fracture initiation site, from which one can infer large grains were present in that region. The reduction in temperature would have enhanced the influence the inclusions had on the toughness of the material. This was because the inclusions have different thermal expansion coefficients to that of the surrounding matrix [81]. Therefore, as the temperature decreased, residual stresses were generated at the interface between the inclusions and the steel due to the different thermal contractions. This led to a reduction in the energy required to initiate cleavage fracture, explaining why cleavage fracture was able to initiate with ease when large inclusions were present. Since large inclusions and defects cannot be removed by a PWHT, it is of paramount importance that they are not produced during welding as an acceptable toughness cannot be achieved when they are present. However, it was important to remember that the toughness of the AW weld line was much lower than that of the base metal regardless of whether large inclusions or defects were present in the weld line.

The microstructural analysis revealed that Widmanstätten ferrite was present in the AW weld line. Previous research has overlooked the potential role Widmanstätten ferrite may have on influencing the AW weld line toughness [2]. Therefore, the effect of this constituent on the AW weld line toughness needed to be considered. Especially since the literature has shown that the presence of Widmanstätten ferrite reduces the toughness of steel welds [65]. Widmanstätten ferrite was produced in the AW weld line because of the fast-cooling rates. It started to form once the weld cooled to a temperature lower than 600 °C when the diffusional growth of ferrite had slowed so much that the allotriomorphic ferrite had reached a limiting thickness [60]. It nucleated at the ferrite-austenite boundary and grew in the form of wedge-shaped plates which had similar crystallographic orientations [64]. Since the plates grew with similar orientations, the grain boundary angles between the plates were low. The grain boundary angle plays an important role in cleavage crack propagation, where High Angle Grain Boundaries (HAGBs) offer good resistance [43,44]. This is because when a cleavage crack propagates from one grain to the next, the crack must change its surface from the cleavage plane of the first grain to that of the second grain. When the misorientation angle is low the crack is able to propagate easily resulting in a low energy absorption [45,46]. Consequently, Widmanstätten ferrite offers little resistance to cleavage crack propagation due to the Low Angle Grain Boundaries (LAGBs) between the ferrite plates. The instrumented head revealed that the AW weld line had low crack propagation energies and a poor ability to initiate crack arrest, demonstrating that it offered very little resistance to cleavage crack propagation. Hence, it was confirmed that Widmanstätten ferrite had a negative influence on the AW weld line toughness by reducing the weld line's ability to resist cleavage crack propagation.

Previous research has determined that crystallographic texture was a major factor influencing the toughness of the weld line of an X65 HFI welded pipe [3–5]. The studies examined the fraction of grains with their {100} plane orientated within 10 °

parallel to the weld plane. These grains were considered to be orientated for easy fracture since the {100} plane is considered the cleavage plane. Literature has shown that an increase in the fraction of {100} planes aligned parallel to the fracture surface increases the DBTT and helps to promote cleavage fracture propagation [6–8]. The previous X65 studies all displayed that welding produced a high fraction of grains orientated for easy fracture at the weld line when compared to that of the base metal. Consequently, the undesirable texture was concluded to be the main reason for the poor weld line toughness. The EBSD analysis revealed that the percentage of grains orientated for easy fracture in the base metal was approximately 2 %. In the AW weld line this had roughly increased by a factor of 8 to approximately 16 %, dependant on the location within the weld line. The instrumented head data displayed that the base metal had superior crack propagation energies when compared to that of the AW weld line. Therefore, it was confirmed that the strong {100} texture in the AW weld line was extremely detrimental to the weld line's ability to resist cleavage crack propagation.

The texture component maps revealed that it was not just the percentage of grains orientated for easy fracture affecting the toughness. The maps displayed that the grains orientated for easy fracture were large and clustered. The clustering of grains further reduced the toughness of the weld line because cleavage cracks could propagate easily through the weld line from one grain to the next as the misorientation angles between the grains was small. Misorientation distributions produced by EBSD analysis found that the percentage of HAGBs was lower in the AW weld line than that of the base metal. The reduction in the percentage of HAGBs reduces a materials ability to resist cleavage crack propagation [43,44]. This was driven by two factors. Firstly, the clustering of grains orientated for easy fracture, and secondly the presence of Widmanstätten ferrite which grew in plates with similar crystallographic orientations.

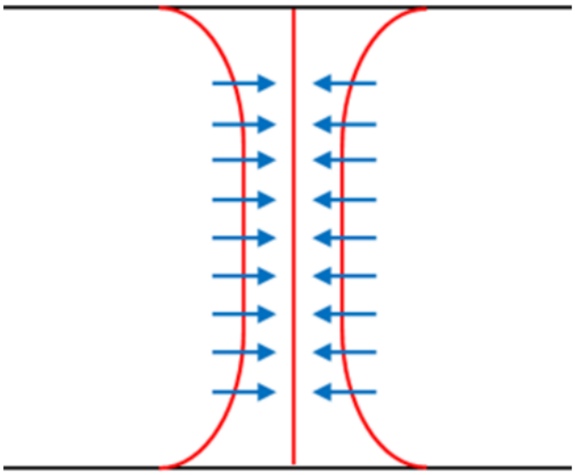

Figure 6.1. Solidification direction during cooling of the weld line.

With the analysis of the {100} texture strongly agreeing with previous literature, it can be confidently said that the role of the {100} plane on the toughness of the weld line of a HFI welded pipe has been well established. However, by what method the texture formed within the weld line had not been considered. The strong {100} texture produced at the weld line was highly likely to have been caused by directional solidification. When a material directionally solidifies, a given crystallographic texture in relation to the solidification direction can be produced. In BCC steels the <100> direction is preferred since it is the most loosely packed direction [51]. Figure 6.1 displays the direction in which the weld line solidified, which was perpendicular to the weld plane. When the <100> direction is perpendicular to the weld plane, then the {100} plane will be parallel to the weld plane. The solidification rate also plays an important role in the intensity of the texture produced, where a sharper {100} texture can be produced when the solidification rate is increased [53]. Since the HFI welding process is associated with fast cooling rates, they likely contributed to producing the strong {100} texture during the directional solidification of the weld line.

Although the role of the {100} plane on the toughness of the weld line has been well established, the role of the {110} plane has not. Literature has shown that promoting cracking along the {110} plane can improve the brittle crack resistance by frequent blunting of the crack tip [48]. This improves the material’s resistance to crack propagation and can also increase the USE [6–8]. In an X65 pipeline steel it was observed that the USE greatly increased when the fraction of {110} planes orientated parallel to the fracture surface was increased [50]. EBSD analysis found that the base metal had a percentage of grains with their {110} plane aligned within 10 ° to the weld plane of approximately 13 %. In the AW weld line this was reduced to roughly 9 % dependant on the location in the weld line. This would have reduced the ability of the AW weld line to resist cleavage fracture propagation. The combination of the increased percentage of grains orientated for easy fracture and the reduction of {110} planes aligned parallel to the weld line was extremely detrimental to the toughness, where it would have reduced the USE and increased the DBTT. These would have also contributed to the absence of the upper shelf region present on the Charpy impact energy against temperature plot. Therefore, it was confirmed that the reduction of {110} texture negatively affected the toughness of the AW weld line.

The literature has shown that the toughness of the weld line on an X65 HFI welded pipe still remains low even after a PWHT. The reasoning was due to the coarse grain size and poor {100} texture remaining at the weld line. However, a lack of fracture analysis and only the use of the basic Charpy impact test has meant how these factors were affecting the toughness had not been well established. On initial investigation of the weld line following a PWHT under SEM, it was expected that the toughness of the weld line would be greatly improved. This was because the M-A constituent promoting cleavage fracture initiation and the Widmanstätten ferrite offering little resistance to cleavage fracture propagation were both completely removed and replaced with allotriomorphic ferrite. However, the large visual improvements in microstructure disagreed with the small improvements in toughness displayed by the Charpy impact test results.

Grain size analysis revealed that the grain size of the weld line remained coarse following a PWHT. This was consistent with previous research. The grain size of the weld line was considerably larger than that of the adjacent AZ. The persistent coarse grain size would have kept the DBTT high as well as keeping the energy required to initiate brittle fracture low. This contributed to the upper shelf region remaining absent on the Charpy impact energy against temperature plot. Fracture analysis revealed that for temperatures of -20 °C and above, cleavage fracture initiation was initiating at large grains. Here the large grains were able to reduce the stress needed to initiate cleavage fracture [39]. The analysis agreed with the literature that the persistent coarse grain size was a factor negatively influencing the toughness of the weld line. Consequently, the fracture analysis confirmed the persistent large grain size was influencing the toughness by helping to promote cleavage fracture initiation and reducing the DBTT of the weld line.

Although the literature has concluded a persistent coarse grain size at the weld line contributed to why the toughness remained poor following a PWHT, it had not been understood why it remained. One possible explanation for the persistent large grain size was structural heredity. This is when the original grain size is recovered after a heat-treatment, and it is most likely to occur when rapid thermal cycles are used [160]. The induction annealing and quenching PWHT used a rapid austenitising thermal cycle. During the PWHT the AZ was rapidly heated by the induction annealers until the whole of the zone had transformed to austenite, and next immediately quenched. The purpose for using a rapid austenitising thermal cycle was to ensure a fine prior austenite grain size was developed. However, coarse ferrite microstructures do not always respond well to this type of heat-treatment [157]. Therefore, it was highly likely that the coarse microstructure of the AW weld line did not respond well to the PWHT. It was also highly likely that the dissolution of the NbC precipitates caused the persistent coarse grain size. As previously discussed, ThermoCalc Prisma simulations predicted that the NbC precipitates were completely dissolved during welding. Literature has shown that they can reprecipitate during a heat-treatment but will be much coarser and less well dispersed than before [117]. Hence it was probable that NbC precipitates were able to form during the PWHT, although they were coarse and poorly dispersed offering little grain refinement effect.

At temperatures of -40 °C and lower, the cleavage fracture initiation in the HT weld line was triggered by small particles. The fracture surface analysis found small voids where particles had debonded at the fracture initiation site. This trigger for cleavage fracture initiation occurring at low temperatures was a result of the different thermal expansion coefficients between the particles and the surrounding steel, which reduced the fracture initiation energy [81]. Consequently, as the temperature reduced cleavage fracture was no longer triggered by large grains but instead by small particles. Therefore, it had been found that the features initiating cleavage fracture at the weld line changed as the temperature was decreased.

It has been observed in previous research that the undesirable {100} texture remains at the weld line following a PWHT [3–5]. EBSD analysis revealed that there was still a large fraction of grains orientated for easy fracture remaining at the weld line. The PWHT was somewhat able to reduce the intensity of grains orientated for easy fracture. However, it was still roughly 5 times greater than that of the base metal. This was approximately 10 % dependant on the location within the weld line. The instrumented head data displayed that the weld line following a PWHT was still extremely poor at resisting crack propagation when compared to that of the base metal. The persistent strong {100} texture explained why the weld line still exhibited a poor resistance to crack propagation. These observations agreed with the previous studies; however, it had not been considered why the undesirable texture remained.

It was highly likely the persisting crystallographic texture was the result of a texture memory effect. This is when the original ferrite crystallographic texture is recovered even after the material has undergone the ferrite → austenite → ferrite transformation. Previous research has suggested that the residual stresses introduced during the ferrite → austenite transformation contributes to the variant selection during the austenite → ferrite transformation. Thus, the original texture of the ferrite is inherited after the ferrite → austenite → ferrite transformation since the expansion axis in the ferrite → austenite transformation matches with the compression axis of the austenite → ferrite transformation. This infers that the variant selection is controlled by residual stresses created during phase transformation [59]. Both the chemistry and the heat-treatment have an influence on the intensity of the effect [56]. The addition of Mn can enhance the texture memory effect. X60 pipeline steel has an approximate Mn wt.% of 1.3 %. Therefore, the presence of Mn would have likely contributed to the effect. However, when fast cooling rates are applied the texture memory effect can occur even when Mn isn't present. Since the weld line was quenched, following induction annealing, the cooling rates would have been fast, subsequently enhancing the memory effect. The peak temperature of the heat-treatment also influences the intensity of the effect, where the greater the peak temperature the lesser the effect [57]. The PWHT used a rapid austenitising thermal cycle, where the weld was immediately quenched as soon as the AZ had fully transformed to austenite. Therefore, the peak temperature during the PWHT was low, making it was easier for the texture memory effect to occur.

The texture component maps revealed that the clustering of grains orientated for easy was removed. This would have improved the weld line's ability to resist cleavage crack propagation since the easy crack propagation paths had been removed. However, the grains orientated for easy fracture were still visibly large. EBSD analysis revealed that the percentage of HAGBs was increased by the PWHT, which was expected to be seen due to the removal of the Widmanstätten ferrite and clustering of grains with similar crystallographic orientations. The increase would have been beneficial to resisting cleavage crack propagation. However, an undesirable crystallographic texture and a coarse grain size still remained at the weld line which nullified the toughness benefit from the increase of HAGBs.

6.2 Microstructural variation through depth of weld line

During the induction heating of the HFI welded pipe manufacturing process it is well known that the temperatures are greatest at the strip edge corners, which results in an hourglass shaped weld profile. Therefore, different thermal cycles are experienced through the depth of the weld line, likely resulting in a varying microstructure through the depth of the weld line. This would consequently mean it is also likely that the toughness of the weld line varies through the depth of the weld. However, previous research has only analysed localised zones of the weld and the fact that the toughness most probably varies though the depth of the weld line has been overlooked [3–5]. Although the potential variation of toughness through the depth of the weld line has not been explored, literature has suggested that improving the uniformity of the heating during welding, by reducing the high temperatures at the strip edge corners, can improve the quality of the weld [9–11]. However, no relationships have been established between the microstructure of the weld line and how this could improve the weld quality.

The microstructural analysis revealed that the microstructure of the AW weld line varied through the depth of the weld. M-A constituent was present through the entirety of the depth of the AW weld line, however the size and the morphology of the constituent changed. At the mid-thickness the M-A constituent was somewhat equiaxed in shape, although there was some elongated M-A present. Towards the outer pipe surfaces the M-A constituent was larger than at the mid-thickness and had an elongated morphology, where some of the constituent was up to 10 μm in length. The size, distribution and morphology play an important role in influencing toughness. An increase in the size of the M-A constituent leads to a reduction in toughness [73]. Also, M-A constituent is most detrimental to toughness when it has an elongated morphology [74]. Since the M-A was largest with an undesirable morphology near the top and bottom of the weld, it would have been much more detrimental to the toughness of the weld line in these areas when compared to that of the mid-thickness.

A variation in grain size was also observed through the depth of the AW weld line. The grain size was finest at the mid-thickness and then increased towards the top and bottom of the weld. Near the inner pipe surface there were large grains present approximately 40 µm in size. These would have been detrimental to the toughness of the weld line in this area since large singular grains can act as local stress raisers, reducing the local toughness associated with it, causing the grain to become a cleavage fracture origin site [152]. The larger grain size towards the top and bottom of the weld meant that the DBTT in these areas was greater than at the mid-thickness [35–37]. Consequently, the stress required to initiate brittle fracture in the areas was lower. The large grain size, coupled with the coarse M-A constituent that had an undesirable morphology, implied that brittle fracture would initiate more easily towards the top and bottom of the weld line than when compared to that of the mid-thickness. NbC precipitates may have played a role in a producing a finer grain at the mid-thickness. This was because ThermoCalc Prisma simulations predicted that the NbC precipitates were fully dissolved at the weld line during welding, and then were only able to reprecipitate at the mid-thickness during cooling. Therefore, they may have been able to offer some grain refinement at the mid-thickness by pinning prior austenite grain boundaries. However, the precipitates here were most likely coarser and less well dispersed than previous, so therefore the grain refinement effect could have been small.

EBSD analysis also revealed that the texture of the weld line changed through the depth of the weld. At the weld line a large percentage of grains orientated for easy fracture were produced. This was when the {100} plane was orientated within 10 ° to the weld plane. An increasing fraction of {100} planes parallel to the fracture surface increases the DBTT and helps to promote cleavage fracture [6–8]. The base metal had a percentage of grains orientated for easy fracture of approximately 2 %. At the mid-thickness of the AW weld line this was 14 %. However, approximately 3 mm above the inner pipe surface it was measured to be 18 %. This demonstrated that the weld line was most resistant to cleavage crack propagation at the mid-thickness.

Microstructural analysis consistently found features through the depth of the AW weld line that displayed that the toughness of the weld line was greatest at the mid-thickness. This was due to its finer grain size, smaller and blockier M-A constituent, and lower percentage of grains orientated for easy fracture. Therefore, by reducing the high temperatures at the strip edge corners, the toughness of the weld line towards the top and the bottom of the weld could be improved by achieving a microstructure similar to that of the weld line at the mid-thickness. This would improve the overall toughness of the weld line; however, it would still be expected to be lower than that of the base metal.

Following the PWHT the coarse grain size and the poor crystallographic texture that remained at the weld line was most likely due to structural heredity and a texture memory effect respectively. The EBSD analysis again revealed that the percentage of grains orientated for easy fracture was the lowest at the mid-thickness of the weld line. Therefore, by lowering the temperature at the strip corners, the grain size and the intensity of grains orientated for easy fracture towards the top and bottom of the weld could be reduced before a PWHT, which would then result in a preferable microstructure following the PWHT. This would enhance the overall toughness of the weld by reducing the percentage of grains orientated for easy fracture as well as the grain size.

The computational modelling demonstrated that it was extremely difficult to improve the uniformity of the temperature distribution through the depth of the strip edges on a 16 mm thick pipe during induction heating by altering the process parameters alone. Thick-walled pipes experience greater temperature differences through the depth of the strip edges when compared to that of thin-walled pipes [12]. Therefore, they are more susceptible to poor weld quality due to non-uniform heating. Previous computational modelling research has shown that the uniformity of the heating can be improved by altering the geometry of the strip edges, although this has only been demonstrated on pipes with a wall thickness of less than 9 mm [9–11]. Though, there have been no claims made why this could not be achieved on heavy walled pipes. These studies claimed that the more uniform temperature distribution could improve weld quality, however they provided no explanation as to why this would lead to improvements.

It was demonstrated using computational modelling that the heating distribution could be made more uniform through the depth of the strip edges on a 16 mm thick HFI welded pipe by altering the geometry of the strip edges. This would improve the toughness of the weld line by reducing the high temperatures towards the strip edge corners since the grain size and undesirable crystallographic texture would be reduced to a level similar to that of the mid-thickness of the weld line. Consequently improving the overall toughness of the weld line.

7 Conclusions

The factors influencing the weld line toughness of an X60 high frequency induction welded pipe were able to be well established. This was achieved by building relationships between the microstructural characterisation, fracture surface analysis and the Charpy instrumented head data. Previous research had investigated the factors affecting toughness, but the findings were somewhat limited as there was not a strong understanding of how fracture was initiating and propagating through the weld line.

Charpy impact testing displayed that the as-welded weld line produced low toughness across the entirety of the test temperature range. Microstructural analysis found martensite-austenite constituent was present in the as-welded weld line. Furthermore, fracture analysis revealed that brittle fracture was initiating at this constituent in areas where a large grain size was present. However, if large inclusions or defects were present this was not the case. Therefore, a hierarchy of cleavage fracture initiating features was observed, where large inclusions and defects were more effective at promoting cleavage fracture than martensite-austenite constituent. Nonetheless, the toughness of the weld line was still poor when large inclusions or defects were not present. The large grain size was attributed to the dissolution of niobium carbide precipitates during welding that were then not able to reprecipitate on subsequent cooling of the weld line. The instrumented head data demonstrated that the as-welded weld line had a poor resistance to cleavage crack propagation. This was a result of the formation of Widmanstätten ferrite and an undesirable texture. The Widmanstätten ferrite offered little resistance to cleavage crack propagation as it grew in similar crystallographic orientations. The undesirable texture comprised of a strong {100} texture which was consistent with previous research. However, it was also found that there was a reduction in {110} texture when compared to that of the base metal. This would have further reduced the weld line’s ability to resist cleavage crack propagation. Texture component maps revealed clusters of grains with {100} orientations. This would have been detrimental to the weld line toughness as there were easy cleavage crack propagation paths. It was identified that the undesirable {100} texture produced was a result of directional solidification.

Following a post weld heat-treatment the toughness of the weld line was still poor and considerably lower than that of the base metal. It was confirmed that this was a result of the persistent large grain size and poor crystallographic texture. The remaining large grain size was possibly caused by the dissolution of niobium carbide precipitates. Here the niobium carbide precipitates were dissolved during welding and may have been able to reprecipitate during the subsequent cooling of the weld and/or the post weld heat-treatment. However, it was highly likely that they were coarse and less well dispersed than previous, offering little grain refinement effect. It may have also been a result of structural heredity which is more likely to occur when rapid heat-treatment cycles are used. The instrumented head data revealed that the weld line still had a poor resistance to cleavage crack propagation. This was attributed to the strong {100} texture remaining at the weld line, since it offered little resistance to cleavage crack propagation. The persistent undesirable {100} texture was considered to be highly likely a result of a texture memory effect.

Literature had suggested that the toughness of the weld line could be enhanced by improving the uniformity of the temperature distribution during welding. However, justification as to why had not been considered. This thesis hypothesised that by reducing the high temperatures at the strip corners during welding it would produce microstructures in these locations that would have a more favourable toughness than typically produced. Consequently, improving the overall toughness of the weld line. During the microstructural analysis it was observed that the weld line microstructure varied through the depth of the weld. It was found that the parts of the weld line which experienced greater heating during welding possessed microstructures that presented themselves as greater sources of poor toughness. This was because they consisted of a coarser grain size, large and elongated martensite-austenite constituent, and a higher percentage of grains orientated for easy fracture. Therefore, the microstructural observations agreed with the hypothesis that by reducing the temperatures at the strip edge corners it would improve the overall toughness of the weld line.

Computational modelling displayed that a uniform temperature distribution could be achieved on a thick-walled pipe by altering the geometry of the strip edges. This was accomplished by adding chamfers to the corners of the strip edges. Therefore, a rational method to improve the weld line toughness of thick-walled high frequency induction welded pipes was achieved. However, this method would need to be trialled and tested physically before determining whether it is a truly viable technique.

8 References

1. Zhang W, Zhao G, Fu Q. Study on the effects and mechanisms of induction heat treatment cycles on toughness of high frequency welded pipe welds. Mater Sci Eng A. 2018;736:276–87.

2. Yan P, Güngö ÖE, Thibaux P, Bhadeshia HKDH. Crystallographic texture of induction-welded and heat-treated pipeline steel. Adv Mater Res. 2010;89–91:651–6.

3. Güngör OE, Yan P, Thibaux P, Liebeherr M, Bhadeshia HKDH, Quidort D. Investigations into the microstructure - Toughness relation in high frequency induction welded pipes. Vol. 2, Proceedings of the Biennial International Pipeline Conference, IPC. 2010.

4. Yan P, Guüngör ÖE, Thibaux P, Bhadeshia HKDH. Induction welding and heat treatment of steel pipes: Evolution of crystallographic texture detrimental to toughness. Sci Technol Weld Join. 2010;15(2):137–41.

5. Yan P, Güngör OE, Thibaux P, Liebeherr M, Bhadeshia HKDH. Tackling the toughness of steel pipes produced by high frequency induction welding and heat-treatment. Mater Sci Eng A. 2011;528(29–30):8492–9.

6. Duan H, Shan Y, Yang K, Shi X, Yan W. Effect of microstructure and crystallographic orientation characteristics on low temperature toughness and fracture behavior of pipeline steels. J Mater Res Technol. 2022;17:3172–85.

7. Ghosh A, Modak P, Dutta R, Chakrabarti D. Effect of MnS inclusion and crystallographic texture on anisotropy in Charpy impact toughness of low carbon ferritic steel. Mater Sci Eng A. 2016;654:298–308.

8. Yang XL, Xu YB, Tan XD, Wu D. Relationships among crystallographic texture, fracture behavior and Charpy impact toughness in API X100 pipeline steel. Mater Sci Eng A. 2015;641:96–106.

9. Han Y, Yu E, Fan Y, Zhao Y. Effects of opening angle on temperature distribution of HFIW pipe. 2010 Int Conf E-Product E-Service E-Entertainment, ICEEE2010. 2010;1–4.

10. Han Y, Yu EL. Numerical analysis of a high-frequency induction welded pipe. Weld J. 2012;91(10):270–7.

11. Ghaffarpour M, Akbari D, Moslemi Naeeni H, Ghanbari S. Improvement of the joint quality in the high-frequency induction welding of pipes by edge modification. Weld World. 2019;63:1561–72.

12. Tazedakis AS, Voudouris NG, Musslewhite M. Manufacturing of 25mm heavy-wall linepipe using the high frequency induction (HFI) welding technique, a challenge for a pipe manufacturer. Proc Bienn Int Pipeline Conf IPC. 2010;

13. Morris JW, Hardy SJ, Lees AW, Thomas JT. Formation of residual stresses owing to tension levelling of cold rolled strip. Ironmak Steelmak. 2001;28(1):44–52.

14. Selejdak J. Influencing factors onto quality of welded pipes. Metalurgija. 2003;42(1):65–7.

15. Babakri KA. Improvements in flattening test performance in high frequency induction welded steel pipe mill. J Mater Process Technol. 2010;210(15):2171–7.

16. Dunlap DC. Evolution of continuous coiled line pipe into the offshore pipeline industry. Precis tube Technol. 2003;

17. Wright J. Principles of High Frequency Induction Tube Welding. Electronic Heating Equipment, Inc. 1997.

18. Runte E. The Brown Boveri Review. Brown Boveri. 1968;12.

19. Wheeler HA. Formulas for the Skin Effect. Proc IRE. 1942;30(9):412–24.

20. Reid JE, Macnae JC. Doubling the effective skin depth with a local source. Geophysics. 1999;64(3):732–8.

21. Johnson HW, Graham M. High-speed Signal Propagation: Advanced Black Magic. 2003.

22. Ciudad D, Cobos P, Sanchez P, Aroc C. RFID in Metal Environments: An Overview on Low (LF) and Ultra-Low (ULF) Frequency Systemsled. Radio Freq Identif Fundam Appl Des Methods Solut. 2010;

23. Kroll M, Birnbaum P, Zeisig J, Kraeusel V, Wagner MFX. Manufacturing of 42SiCr-pipes for quenching and partitioning by longitudinal HFI-Welding. Metals (Basel). 2019;9(6):1–15.

24. B.Grande, Asperheim JI. Factors influencing heavy wall tube welding. Tube Pipe Technol. 2003;85–90.

25. Wright J. Optimizing Efficiency in HF Tube Welding Processes. 1999.

26. Techmański Z, Stępień M, Stępień J. Analysis of Selected Properties of Induction Welded Seamed Tubes. Biul Inst Spaw. 2021;(6):31–6.

27. Varbai B, Adonyi Y, Nagy E, Kristaly F, Mertinger V. Bondline Characterization in High Frequency Welding of Steels. 2020;(December).

28. Techmański Z, Stępień J, Garstka T, Wieczorek P, Golański G, Supernak J. Improving the Energy Efficiency of the Production of Pipes Welded with High-Frequency Induction. Processes. 2023;11(9):1–14.

29. Bharti A. Mismatch defects in ERW steel tubes. 2014;

30. Grande B, Waerstad O, Runeborg P. Weld setup, variable frequency and heat affected zones in hf tube and pipe welding. Tube Pipe Tchnology. 2012;(July):116–9.

31. Cvetkovski S, Brkovski D. Optimising Technology for Production of High Frequency Welded Pipes Made of X60 Steel. Mach Technol Mater. 2016;1(12):13–6.

32. Iatchcva I, Stancheva R, Petkova N. Parameterized study of high-frequency welding system. In 2018.

33. Land A, Vol E. Improving induction tube welding system performance utilizing soft magnetic composites. 2014;(1).

34. Milićević M, Radaković Z. Quality improvement of steel pipes produced by seam welding with new magneto-dielectric impeder. Mater Trans. 2006;47(6):1464–8.

35. Calcagnotto M, Ponge D, Raabe D. Effect of grain refinement to 1µm on strength and toughness of dual-phase steels. Mater Sci Eng A. 2010;527(29–

30):7832–40.

36. Liu Y, Ma Z, Liu X, Zhang Z. Effect of grain size and grain boundary on ductile to brittle transition behavior of Fe-6.5wt.%Si alloy under miniaturized three-point bending tests. Mater Lett. 2023;353(September):135288.

37. Takaki S, Kawasaki K, Kimura Y. Mechanical properties of ultra fine grained steels. J Mater Process Technol. 2001;117(3):359–63.

38. Morris JW. The influence of grain size on the mechanical properties of steel. Nanostructured Mater. 1997;9(1–8):611–4.

39. Inoue T. Brittle fracture stress of ultrafine-grained low-carbon steel. Mater Trans. 2017;58(10):1505–8.

40. Inoue T, Ueji R. Improvement of strength, toughness and ductility in ultrafine-grained low-carbon steel processed by warm bi-axial rolling. Mater Sci Eng A. 2020;786(March):139415.

41. Qiu H, Hanamura T, Torizuka S. Influence of grain size on the ductile fracture toughness of ferritic steel. ISIJ Int. 2014;54(8):1958–64.

42. Hwang B, Kim YG, Lee S, Kim YM, Kim NJ, Yoo JY. Effective grain size and Charpy impact properties of high-toughness X70 pipeline steels. Metall Mater Trans A Phys Metall Mater Sci. 2005;36(8):2107–14.

43. Ghosh A, Kundu S, Chakrabarti D. Effect of crystallographic texture on the cleavage fracture mechanism and effective grain size of ferritic steel. Scr Mater. 2014;81:8–11.

44. Qiao Y, Argon AS. Cleavage cracking resistance of high angle grain boundaries in Fe-3%Si alloy. Mech Mater. 2003;35(3–6):313–31.

45. Chen J, Lu W, Qiao Y. Resistance of grain boundary array to cleavage cracking in free-standing thin film. Mech Mater. 2009;41(2):131–8.

46. Gilman JJ. Propagation of cleavage cracks in crystals. J Appl Phys. 1956;27(11):1262–9.

47. Lan L, Qiu C, Du L. Effective grain size dependence of crack propagation resistance in low carbon steel. Theor Appl Fract Mech. 2023;124(December

2022):103762.

48. Barik RK, Biswal S, Bhandari KK, Ghosh A, Chakrabarti D. Micromechanics of cleavage fracture and the associated tongue formation in ferritic steel. Mater Sci Eng A. 2023;885(July):145616.

49. Joo MS, Suh DW, Bae JH, Bhadeshia HKDH. Role of delamination and crystallography on anisotropy of Charpy toughness in API-X80 steel. Mater Sci Eng A. 2012;546:314–22.

50. Ju JB, Lee JS, Jang J il. Fracture toughness anisotropy in a API steel line-pipe. Mater Lett. 2007;61(29):5178–80.

51. Yoon Y, Yim J, Choi E, Kim J, Oh K, Joo Y. Texture control of 3.04%-Si electrical steel sheets by local laser melting and directional solidification. Mater Lett. 2016;185:43–6.

52. Fu H, Zhang Z, Jiang Y, Xie J. Improvement of magnetic properties of an Fe-6.5 wt.% Si alloy by directional solidification. Mater Lett. 2011;65:1416–9.

53. Zhang X, Zhou Y, Jin T, Sun X, Liu L. Effect of solidification rate on grain structure evolution during directional solidification of a Ni-based superalloy. J Mater Sci Technol. 2013;29(9):879–83.

54. Ardakani MG, Souza ND, Wagner A, Shollock BA, McLean M. Competitive Grain Growth and Texture Evolution during Directional Solidification of Superalloys. Miner Met Mater Soc. 2000;219–28.

55. Wagner A, Shollock BA, McLean M. Grain structure development in directional solidification of nickel-base superalloys. Mater Sci Eng. 2004;374:270–9.

56. Yoshinaga N, Inoue H, Kawasaki K, Kestens L, De Cooman BC. Factors affecting texture memory appearing through α → γ → α transformation in IF steels. Mater Trans. 2007;48(8):2036–42.

57. Romero J, Preuss M, Quinta da Fonseca J. Texture memory and variant selection during phase transformation of a zirconium alloy. Acta Mater. 2009;57(18):5501–11.

58. Yoshinaga N, Kestens L, De Cooman BC. α→γ→α Transformation Texture Formation at Cold-Rolled Ultra Low Carbon Steel Surfaces. Mater Sci Forum. 2005;495–497:1267–72.

59. Yoshinaga N, Ushioda K, Itami A, Akisue O. α+γ and γ Phases Annealing in Ultra Low-Carbon Sheet Steels. ISIJ Int. 1994;34(1):33–42.

60. Bhadeshia H, Honeycombe R. Steels: Microstructure and Properties. 4th ed. Elsevier Ltd; 2017. 377–400 p.

61. Han XL, Wu DY, Min XL, Wang X, Liao B, Xiao FR. Influence of post-weld heat treatment on the microstructure, microhardness, and toughness of a weld metal for hot bend. Metals (Basel). 2016;6(4).

62. Li W, Cao R, Zhu W, Guo X, Jiang Y, Chen J. Microstructure evolution and impact toughness variation for high strength steel multi-pass weld metals with various cooling rates. J Manuf Process. 2021;65(December 2020):245–57.

63. Bhadeshia HKDH. Widmanstätten ferrite. Mater Sci Metall. 2021;

64. Nucleation of Widmanstatten Ferrite.pdf.

65. Costa VM, da Cunha PHCP, Vieira E da R. Impact Toughness Analysis of a High Strength Steel Hardox 450 Welded Joint. Soldag e Insp. 2023;28(Vmc):1–7.

66. Fattahi M, Nabhani N, Vaezi MR, Rahimi E. Improvement of impact toughness of AWS E6010 weld metal by adding TiO2 nanoparticles to the electrode coating. Mater Sci Eng A. 2011;528(27):8031–9.

67. Hu J, Du LX, Zang M, Yin SJ, Wang YG, Qi XY, et al. On the determining role of acicular ferrite in V-N microalloyed steel in increasing strength-toughness combination. Mater Charact. 2016;118:446–53.

68. Cheng H, Fu H, Lin J, Lei Y. Effect of Cr content on microstructure and mechanical properties of carbidic austempered ductile iron. Mater Test. 2018;60(1):31–9.

69. Babu SS. The mechanism of acicular ferrite in weld deposits. Solid State Mater Sci. 2004;8:267–78.

70. Loder D, Michelic SK, Bernhard C. Acicular Ferrite Formation and Its Influencing Factors-A Review. J Mater Sci Res. 2016;6(1):24.

71. Yang JR, Huang CY, Huang CF, Aoh JN. Influence of acicular ferrite and bainite microstructures on toughness for an ultra-low-carbon alloy steel weld metal. J Mater Sci Lett. 1993;12(16):1290–3.

72. Li X, Fan Y, Ma X, Subramanian S V., Shang C. Influence of Martensite-Austenite constituents formed at different intercritical temperatures on toughness. Mater Des. 2015;67:457–63.

73. Li X, Ma X, Subramanian S V., Shang C, Misra RDK. Influence of prior austenite grain size on martensite-austenite constituent and toughness in the heat affected zone of 700MPa high strength linepipe steel. Mater Sci Eng A. 2014;616:141–7.

74. Luo X, Chen X, Wang T, Pan S, Wang Z. Effect of morphologies of martensite–austenite constituents on impact toughness in intercritically reheated coarse-grained heat-affected zone of HSLA steel. Mater Sci Eng A. 2018;710(October 2017):192–9.

75. Lan L, Qiu C, Zhao D, Gao X, Du L. Analysis of martensite-austenite constituent and its effect on toughness in submerged arc welded joint of low carbon bainitic steel. J Mater Sci. 2012;47(11):4732–42.

76. Li S, Zhu G, Kang Y. Effect of substructure on mechanical properties and fracture behavior of lath martensite in 0.1C-1.1Si-1.7Mn steel. J Alloys Compd. 2016;675:104–15.

77. Morito S, Huang X, Furuhara T, Maki T, Hansen N. The morphology and crystallography of lath martensite in alloy steels. Acta Mater. 2006;54:5323–31.

78. Gallardo-Basile FJ, Naunheim Y, Roters F, Diehl M. Lath martensite microstructure modeling: A high-resolution crystal plasticity simulation study. Materials (Basel). 2021;14.

79. Schulz-Beenken AS. Martensite in steels: Its significance, recent developments and trends. J Phys. 1997;7:359–66.

80. Wang J, Li W, Zhu X, Zhang L. Effect of martensite morphology and volume fraction on the low-temperature impact toughness of dual-phase steels. Mater Sci Eng A. 2022;832(November 2021):142424.

81. Yan W, Shan YY, Yang K. Effect of TiN inclusions on the impact toughness of low-carbon microalloyed steels. Metall Mater Trans A Phys Metall Mater Sci. 2006;37(7):2147–58.

82. Mapelli C. Non-metallic inclusions and clean steel. Metall Ital. 2008;100(6):43–52.

83. Lou X, Andresen PL, Rebak RB. Oxide inclusions in laser additive manufactured stainless steel and their effects on impact toughness and stress corrosion cracking behavior. J Nucl Mater. 2018;499:182–90.

84. Ghosh A, Sahoo S, Ghosh M, Ghosh RN, Chakrabarti D. Effect of microstructural parameters, microtexture and matrix strain on the Charpy impact properties of low carbon HSLA steel containing MnS inclusions. Mater Sci Eng A. 2014;613:37–47.

85. Findley KO, Damm EB. The effects of non-metallic inclusions on mechanical properties and performance of steel. Metall Mater Eng.

86. Arreola-Herrera R, Cruz-Ramírez A, Rivera-Salinas JE, Romero-Serrano JA, Sánchez-Alvarado RG. The effect of non-metallic inclusions on the mechanical properties of 32 CDV 13 steel and their mechanical stress analysis by numerical simulation. Theor Appl Fract Mech. 2018;94(August 2017):134–46.

87. Moonngam S, Wangjina P, Viyanit E, Banjongprasert C. Characterizing Oxide Inclusions in Welded Lean Duplex Stainless Steels and Their Influence on Impact Toughness. Materials (Basel). 2023;16(5):1–10.

88. Hill DC, Passoja DE. Understanding the Role of Inclusions and Microstructure in Ductile Fracture. Weld J (Miami, Fla). 1974;53(11):481–5.

89. Sánchez Osio A, Liu S, Olson DL. The effect of solidification on the formation and growth of inclusions in low carbon steel welds. Mater Sci Eng A. 1996;221(1–2):122–33.

90. Kyogoku T, Takamadate C, Hotta K, Tatsuwaki M, Nemoto S. Automatic

Welding Control System of Electric-Resistance Weld Tube Mill. Sumitomo Met. 1983;35(2):193–205.

91. Choi J-H, Chang YS, Kim C-M, Oh J-S, Kim Y-S. Penetrator Formation Mechanisms during High-Frequency. Weld J. 2004;83(1):27–31.

92. Kim CM, Kim JK. The effect of electromagnetic forces on the penetrator formation during high-frequency electric resistance welding. J Mater Process Technol. 2009;209(2):838–46.

93. Haga H, Aoki K, Sato T. The Mechanisms of Formation of Weld Defects in High-Frequency Electric Resistance Welding. Weld J. 1979;104–9.

94. Sofras C, Bouzouni M, Voudouris N, Papaefthymiou S. Investigation of penetrator defect formation during high frequency induction welding in pipeline steels. MATEC Web Conf. 2021;349:04002.

95. Odebiyi OS, Adedayo SM, Tunji LA, Martins O, Odebiyi OS, Adedayo SM, et al. A review of weldability of carbon steel in arc-based welding processes. Cogent Eng. 2019;6(1).

96. Yurioka N. Carbon Equivalent and Multiplying Factor for Hardenability of Steel. :263–8.

97. Communication S. The assessment of carbon equivalent formulas in predicting the properties of steel weld metals. 2010;31:2649–53.

98. En BS. Welding — Recommendations for welding of metallic materials —. 2003;3(1).

99. Komizo Y ich, Fukada Y. CTOD properties and M-A constituent in the HAZ of C-Mn microalloyed steel. Japan Weld Soc. 1988;40:31–40.

100. Kyung H, Yong S, Hwang B, Gil C, Kim NJ, Lee S. Effects of carbon equivalent and cooling rate on tensile and Charpy impact properties of high-strength bainitic steels. Mater Sci Eng A. 2011;530:530–8.

101. Kim KH, Moon IJ, Kim KW, Kang KB, Park BG, Lee KS. Influence of Carbon Equivalent Value on the Weld Bead Bending Properties of High-Strength Low-Alloy Steel Plates. J Mater Sci Technol. 2017;33(4):321–9.

102. Meyer L. History of niobium as a microalloying element. Appl Niobium as a Microalloying Elem. 2001;359–77.

103. Mandal GK, Das SS, Kumar T, Kamaraj A, Mondal K, Srivastava VC. Role of Precipitates in Recrystallization Mechanisms of Nb-Mo Microalloyed Steel. J Mater Eng Perform. 2018;27(12):6748–57.

104. DeArdo AJ. Microalloyed strip steels for the 21st century. Mater Sci Forum. 1998;284–286:15–26.

105. Speer JG, Pavlina EJ. Solubility and precipitation of carbides containing niobium and molybdenum in low alloy steels. Fundam Appl Mo Nb High Perform Steels. 2015;2:85–98.

106. Martín DS, Caballero FG, Capdevila C, De Andrés CG. Austenite grain coarsening under the influence of niobium carbonitrides. Mater Trans. 2004;45(9):2797–804.

107. Cuddy LJ, Raley JC. Austenite Grain Coarsening in Microalloyed Steels. 1989;14(October 1983):1989–95.

108. Portuetxe C De, Sebastian S, Csic C. Austenitic grain size evolution and continuous cooling transformation diagrams in vanadium and titanium microalloyed steels. 1996;31:3847–52.

109. Kumar AS, Kumar BR, Datta GL, Ranganath VR. Effect of microstructure and grain size on the fracture toughness of a micro-alloyed steel. Mater Sci Eng. 2010;527:954–60.

110. Hanamura T, Torizuka S, Tamura S, Enokida S, Takech H. Effect of Austenite Grain Size on Transformation Behavior, Microstructure and Mechanical Properties of 0.1C–5Mn Martensitic Steel. Mater Sci Forum. 2014;783–786(12):1027–32.

111. Wu BB, Wang XL, Wang ZQ, Zhao JX, Jin YH, Wang CS, et al. New insights from crystallography into the effect of refining prior austenite grain size on transformation phenomenon and consequent mechanical properties of ultra-high strength low alloy steel. Mater Sci Eng A. 2019;745(December 2018):126–36.

112. Bodnar RL, Hansen SS. Effects of austenite grain size and cooling rate on Widmanstätten ferrite formation in low-alloy steels. Metall Mater Trans A. 1994;25(4):665–75.

113. Li Y, Crowther DN, Green MJW, Mitchell PS, Baker TN. The Effect of Vanadium and Niobium on the Properties and Microstructure of the Intercritically Reheated Coarse Grained Heat Affected Zone in Low Carbon Microalloyed Steels. 2001;41(1):46–55.

114. Mintz B, Qaban A, Naher S. Further insights on compositional control and heat treatment for improving the impact behaviour of hot-rolled steels containing Nb and Al. Mater Des. 2020;190:108601.

115. Yang JR, Huang CY, Chiou CS. Microstructures of heat-affected zone in niobium containing steels. Vol. 40, Materials Transactions, JIM. 1999. p. 199–208.

116. Haslberger P, Holly S, Ernst W, Schnitzer R. Precipitates in microalloyed ultra-high strength weld metal studied by atom probe tomography. Weld World. 2018;62:713–9.

117. Chen YC, Feng JC, Liu HJ. Precipitate evolution in friction stir welding of 2219-T6 aluminum alloys. Mater Charact. 2009;60(6):476–81.

118. Jiao ZB, Luan JH, Guo W, Poplawsky JD, Liu CT. Effects of welding and post-weld heat treatments on nanoscale precipitation and mechanical properties of an ultra-high strength steel hardened by NiAl and Cu nanoparticles. Acta Mater. 2016;120:216–27.

119. Wang XN, Chen CJ, Wang HS, Zhang SH, Zhang M, Luo X. Microstructure formation and precipitation in laser welding of microalloyed C-Mn steel. J Mater Process Technol. 2015;226:106–14.

120. Hsu PW, Kao FH, Wang SH, Yang JR, Chang HY, Wang YM, et al. Twinned formation in weld metal of titanium bearing nano precipitated high strength steel. Mater Chem Phys. 2012;136(2–3):1103–8.

121. Xu S, Laver A, Gianetto J, Liang J, Tyson WR, Matsuno S. Charpy toughness of ERW seam welds. J Pipeline Eng. 2017;16(3):149–67.

122. Saba N, Jawaid M, Sultan MTH. An overview of mechanical and physical testing of composite materials. Elsevier Ltd; 2019.

123. Rossoll A, Berdin C, Prioul C. Determination of the fracture toughness of a low alloy steel by the instrumented charpy impact test. Int J Fract. 2002;115:205–26.

124. Sudin V V., Kantor MM, Solntsev KA. Features of weld metal brittle fracture in Charpy tests. Struct Integr Procedia. 2020;28:1637–43.

125. Iatcheva I, Gigov G, Kunov G, Stancheva R. Analysis of induction heating system for high frequency welding. Facta Univ. 2012;25(3):183–91.

126. Asperheim JI, Das P, Grande B, Hömberg D, Petzold T. Numerical simulation of high-frequency induction welding in longitudinal welded tubes. 2019;

127. Dughiero F, Forzan M, Pozza C, Sieni E. A translational coupled electromagnetic and thermal innovative model for induction welding of tubes. In: IEEE Transactions on Magnetics. IEEE; 2012. p. 483–6.

128. Nikanorov A, Baake E, Brauer H, Weil C. Approaches for numerical simulation of high frequency tube welding process. Int Conf Heat by Electromagn Sources. 2013;

129. Nikanorov A, Baake E, Neumeyer J. Numerical Simulation and Investigation of High Frequency Tube Welding Process. Appl Mech Mater. 2014;698:245–50.

130. BS EN ISO 148-1:2016 Metallic materials — Charpy pendulum impact test Part 1 : Test method.

131. Pereira LC, Blas JCG de, Griza S, Darwish FAI. Use of instrumented charpy testing on the fracture toughness characterization of metallic materials. Tecnol Met Mater Min. 2021;18:1–11.

132. Wang C, Tong Z, Zhong W, Lin H, Ning G, Zhang C, et al. A method for directly measuring fracture toughness and determining reference temperature for RPV steels by Charpy impact test. Eng Fract Mech. 2021;243.

133. Chaouadi R, Gérard R. Development of a method for extracting fracture

toughness from instrumented Charpy impact tests in the ductile and transition regimes. Theor Appl Fract Mech. 2021;115.

134. Tardif HP, Marquis H. Force measurements in the charpy impact test. Can Metall Q. 1963;2(4):373–98.

135. Serway R, Jr JJ. Physics for Scientists and Engineers with Modern Physics. 2008.

136. Pride TO, Vokos S, McDermott LC. The challenge of matching learning assessments to teaching goals: An example from the work-energy and impulse-momentum theorems. Am J Phys. 1998;66(2):147–57.

137. BS EN ISO 14556:2015 Metallic materials — Charpy V- notch pendulum impact test — Instrumented test method.

138. Specimens P. ASTM-E112-13 (2021) - Standard Test Methods for Determining Average Grain Size. 2021;

139. ISO 6507-1:2018 Metallic materials - Vickers hardness test - Part 1: Test method.

140. Steel T. High Frequency Induction (HFI) Welded line pipe. 2018.

141. Soyer H. Thermal Data for Carbon Steel and Stainless Steel Sections. Fire Des Steel Struct. 2013;319–45.

142. More S, Bindu R. Effect of Mesh Size on Finite Element Analysis of Plate Structure. Int J Eng Sci Innov Technol. 2015;4(3).

143. Kirkwood P. Niobium and Heat Affected Zone Mythology. Proc Int Semin Weld High Strength Pipeline Steel. 2013;23–64.

144. Microalloyed steel precipitate characterization by TEM. Thermo Fish Sci. 2022;

145. Xiao F ren, Cao Y bin, Qiao G ying, Zhang X bing, Liao B. Effect of Nb Solute and NbC Precipitates on Dynamic or Static Recrystallization in Nb Steels. J Iron Steel Res. 2012;19(11):52–6.

146. Tao NR, Wang ZB, Tong WP, Sui ML, Lu J, Lu K. An investigation of surface nanocrystallization mechanism in Fe induced by surface mechanical attrition treatment. Acta Mater. 2002;50:4603–16.

147. Lehto P. Adaptive domain misorientation approach for the EBSD measurement of deformation induced dislocation sub-structures. Ultramicroscopy. 2021;222.

148. Gove KB, Charles JA. The high-temperature hardness of various phases in steel. Met Soc. 1974;279–83.

149. Borisova MZ. Effect of severe plastic deformation and hardening on the properties and failure mechanisms of constructional steel. Mater Sci Forum. 2018;945 MSF(February):579–84.

150. Pussegoda LN, Malik L, Tyson WR. Effects of plastic deformation on fracture toughness of ship plate steels. Can Metall Q. 1997;36(1):39–47.

151. Kammerhofer C, Hohenwarter A, Scheriau S, Brantner HP, Pippan R. Influence of morphology and structural size on the fracture behavior of a nanostructured pearlitic steel. Mater Sci Eng A. 2013;585:190–6.

152. Morrell R. Fractography of Brittle Materials. Meas Good Pract Guid. 2001;(15).

153. Milad M, Zreiba N, Elhalouani F, Baradai C. The effect of cold work on structure and properties of AISI 304 stainless steel. J Mater Process Technol. 2008;203(1–3):80–5.

154. Lee JB, Kang N, Park JT, Ahn ST, Park Y Do, Choi ID, et al. Kinetics of carbide formation for quenching and tempering steels during high-frequency induction heat treatment. Mater Chem Phys. 2011;129:365–70.

155. Wang S, Cao L, Zhang Z. Influence of carbide morphology on the deformation and fracture mechanisms of spheroidized 14CrMoR steel. Metals (Basel). 2019;9.

156. Bhadeshia HKDH. Steels for bearings. Prog Mater Sci. 2012;57:268–435.

157. Grange RA. The rapid heat treatment of steel. Metall Trans. 1971;2:65–78.

158. Umemoto M, Guo ZH, Tamura I. Effect of cooling rate on grain size of ferrite in a carbon steel. Mater Sci Technol. 1987;3:249–55.

159. Jang KN, Kim TK, Kim KT. The effect of cooling rates on carbide precipitate and microstructure of 9CR-1MO oxide dispersion strengthened(ODS) steel. Nucl Eng Technol. 2019;51:249–56.

160. D’yachenko SS. Heredity in phase transformations: Mechanism of the phenomenon and effect on the properties. Met Sci Heat Treat. 2000;42(4):122–7.

161. Galindo-Nava EI, Rivera-Díaz-Del-Castillo PEJ. Understanding the factors controlling the hardness in martensitic steels. Scr Mater. 2016;110:96–100.

162. Berns H, Gavriljuk V. Steel of Highest Fracture Energy. Key Eng Mater. 2007;345–346:421–4.

163. Bodnar RL, Hansen SS. Effects of Widmanstätten ferrite on the mechanical properties of a 0.2 pct C-0.7 pct Mn steel. Metall Mater Trans. 1994;25:763–73.

164. McClintock R, Gibbons H. Mechanical properties of structural materials at low temperature. U.S Department of Commerce. 1960.

165. Shen Z, Zhang L, Tang R, Zhang Q. The effect of temperature on the SSRT behavior of austenitic stainless steels in SCW. J Nucl Mater. 2014;454:274–82.

166. Nichols RK. Common HF Welding Defects. Thermatool Corp.

167. Ramachandran DC, Murugan SP, Moon J, Lee CH, Park Y Do. The Effect of the Hyperstoichiometric Ti/N Ratio Due to Excessive Ti on the Toughness of N-Controlled Novel Fire- and Seismic-Resistant Steels. Metall Mater Trans A Phys Metall Mater Sci. 2019;50(8):3514–27.